



**LARGE-SCALE ADVANCED PROP-FAN  
(LAP)  
BLADE DESIGN**

**By: William E. Sullivan  
Jay E. Turnberg  
John A. Violette**

**HAMILTON STANDARD DIVISION  
UNITED TECHNOLOGIES**

**Prepared for  
National Aeronautics and Space Administration  
NASA-Lewis Research Center  
Contract NAS3-23051**

# CONTENTS

<u>SUBJECT</u>		<u>PAGE</u>
1.0	SUMMARY	1
2.0	INTRODUCTION	3
3.0	REQUIREMENTS AND GOALS	7
3.1	Design Requirements	7
3.1.1	Configuration	7
3.1.2	Flutter Limits	7
3.1.3	Critical Speed Margins	7
3.1.4	Stress Limits	10
	3.1.4.1 Normal Operation	10
	3.1.4.2 Rotor Overspeeds	10
3.1.5	Foreign Object Damage	10
3.1.6	Flight Representative Design	10
3.2	Design Goals	10
3.2.1	Net Prop-Fan Efficiency (isolated nacelle installation)	10
3.2.2	Noise	12
3.2.3	Flutter Margin	12
	3.2.3.1 Stall Flutter	12
	3.2.3.2 Unstalled Flutter	12
3.2.4	Foreign Object Damage (FOD)	12
	3.2.4.1 Minor Impacts	12
	3.2.4.2 Moderate Impacts	12
	3.2.4.3 Major Impacts	12
3.2.5	Blade Design Life and Inherent Reliability	13
3.3	Evaluation Conditions	13
3.3.1	Primary Required Design Conditions	13
3.3.2	Additional Secondary Conditions	13
4.0	DESCRIPTION OF FINAL SR-7L BLADE	17
4.1	Final Design	17

## CONTENTS (Continued)

<u>SUBJECT</u>	<u>PAGE</u>
5.0      FINITE ELEMENT MODELING	25
5.1    Coordinate System	25
5.2    Bond Model	25
5.3    Offset Model	30
5.4    Retention Simulation	33
5.4.1    Retention System Design	33
5.4.2    Hub Design	33
5.4.3    Retention Coordinate System	38
5.4.4    Retention System Model	38
6.0      STEADY-STATE ANALYSIS	43
6.1    Application of Loads	43
6.1.1    Centrifugal Loads	43
6.1.2    Airloads	43
6.2    Finite Element Solution Techniques	52
6.2.1    Differential Stiffening	52
6.2.2    One-Step Plus Differential Stiffening	52
6.2.3    Piecewise Linear Analysis	52
6.3    Pre-Deflection Iterations	56
6.3.1    First Iteration	56
6.3.2    Additional Iterations	57
6.3.3    Final Check of Predeflected Configuration	57
6.4    Final Calculations	57
6.4.1    Conditions Analyzed	61
6.4.2    Blade Shank Loads	61
6.4.3    Deflections	61
7.0      VIBRATORY RESPONSE ANALYSIS	71
7.1    Origin of the Once-Per-Revolution Excitation	71
7.2    Excitation Factor	75
7.3    Calculation of Vibratory Response	75
7.4    Blade Shank Loads	75
7.5    Twist Magnification	78

## CONTENTS (Continued)

<u>SUBJECT</u>	<u>PAGE</u>
8.0        STRESS VS. STRENGTH EVALUATION	81
8.1    Establishing Design Strength Allowables	81
8.2    Method of Combining Steady-State and Vibratory Stresses	81
8.3    High Cycle Fatigue	85
8.4    Low Cycle Fatigue	89
8.5    Stress Contour Plots	93
9.0        RESONANT FREQUENCIES AND MODE SHAPES	119
9.1    Calculation Method	119
9.2    Results	119
9.3    Characterization of Mode Shapes	124
9.3.1    First Mode	124
9.3.2    Second Mode	124
9.3.3    Third Mode	124
9.3.4    Fourth Mode	124
9.3.5    Fifth Mode	130
10.0       STABILITY	131
10.1   Unstalled Flutter Analysis	131
10.1.1   Unstalled Flutter Requirements and Results	132
10.1.2   Stability Determination	136
10.1.3   Stability Discussion	136
10.1.4   Stability Modal Evaluation at Nine Other Conditions	141
10.1.5   Effects of Aerodynamic and Structural Variations	148
10.2   Stall Flutter Evaluation	150
10.2.1   Semi-Empirical Method	150
10.2.2   Empirical Method	152
11.0       FOREIGN OBJECT DAMAGE	159
11.1   Calculation Procedure	159
11.1.1   Flight Condition	159
11.1.2   Bird Impact Model	161

## CONTENTS (Continued)

<u>SUBJECT</u>	<u>PAGE</u>
11.2 Effect of Sweep	161
11.3 Deflection and Stress Results	161
11.4 Establishing "True" Ultimate Spar Strength	168
11.5 Stress/Strength Comparison	168
12.0 AERODYNAMIC AND ACOUSTIC PERFORMANCE	171
13.0 CONCLUSIONS	173
13.1 Stress/Strength Evaluation	173
13.2 Resonant Frequencies	173
13.3 Stability	174
13.4 Foreign Object Damage	174
13.5 Aerodynamic and Acoustic Performance	174
13.6 Weight	175
14.0 REFERENCES	177

## ILLUSTRATIONS

<u>FIGURE</u>		<u>PAGE</u>
2-1	Prop-Fan Blades Untwisted Planform Comparison	4
3-1	SR-7L Design Stability Requirements	8
3-2	Resonant Frequency Requirements	9
3-3	Stress Requirements	11
4-1	Balancing the Final SR-7L Design	18
4-2	SR-7L Aero Characteristics (Deflected: Design/Cruise)	20
4-3	SR-7L Blade Stacking Data (Deflected: Design/Cruise)	21
4-4	Untwisted Plan View	22
4-5	SR-7L Prop-Fan	23
4-6	Features of SR-7L Blade Construction	24
5-1	Global Coordinate System	26
5-2	Global Coordinate System Beta Three-Quarters Angle = $57.57^\circ$ ((Design/Cruise)	27
5-3	Global Coordinate System Beta Three-Quarters = $38.26^\circ$ (Take-Off/Climb)	28
5-4	SR-7L Elements for "Bond" and "Offset" FEA Models	29
5-5	SR-7L "Bond" Model	31
5-6	Offset FEA Model	32
5-7	SR-7L Retention	34
5-8	SR-7L Retention Restraints	35
5-9	Pitch Change Actuator & Blade Trunnion Interface	36
5-10	SR-7L Hub	37
5-11	Local Retention Coordinate System	39
5-12	SR-7L Finite Element Model Restraints	41
6-1	SR-7L Blade "Offset" FEA Model	44
6-2	Aerodynamic Load Distribution Design/Cruise	46
6-3	Aerodynamic Load Distribution Take-Off/Climb	46
6-4	Resolution of Airloads at Typical FEA Station	47
6-5	Conversion of Resultant to Lift and Drag	48
6-6	Distribution of Drag Load at a Typical FEA Station	49
6-7	Center of Pressure Distribution, Design/Cruise	50
6-8	Center of Pressure Distribution, Take-Off/Climb	50
6-9	Distribution of Lift Load at Typical FEA Station	51
6-10	Typical Cumulative Deflection Piecewise Linear Analysis	54
6-11	Piecewise Linear Analysis Typical Differential Stiffness vs. Load	55
6-12	Deflection Error Relative to Desired Design Configuration Single Step Procedure from 7th Position	58
6-13	Deflection Error, First PWLA Results, Relative to Desired Design Configuration	59
6-14	Deflection Error, Second PWLA Results, Relative to Desired Design Configuration	60
6-15	Blade Shank Loads (Positive Direction Shown)	65
6-16	Steady-State Displacements Design/Cruise Condition	66
6-17	Steady-State Rotations Design/Cruise Condition	67

## ILLUSTRATIONS (Continued)

<u>FIGURE</u>		<u>PAGE</u>
6-18	Steady-State Displacements Take-Off/Climb Condition	68
6-19	Steady-State Rotations Take-Off/Climb Condition	69
7-1	Cyclic Aerodynamic Loading	72
7-2	Variable Velocity Air Inflow Acting on SR-7L	73
7-3	Typical Steady-State and Cyclic Loadings	74
7-4	Loading - Aerodynamic - Cyclic	76
7-5	Vibratory Deflection Patterns Due to Forced Response at Design/Cruise Condition	79
7-6	Vibratory Rotation Patterns Due to Forced Response at Design/Cruise Conditions	80
8-1	Design Strength Methodology	82
8-2	Hamilton Standard Design Strength Allowable Compared with "Specimen Only" Design Strength Allowable	83
8-3	Typical Goodman Diagram	84
8-4	SR-7L Blade Spar Stress/Strength Comparison	86
8-5	SR-7L Blade Shell Stress/Strength Comparison	86
8-6	SR-7L Blade Sheath Stress/Strength Comparison (Plated Nickel)	87
8-7	SR-7L Blade Filler Material Stress/Strength Comparison (Foam - 8 lbs/cu ft)	87
8-8	Low Cycle Fatigue Stress Evaluation	90
8-9	Modified Goodman Diagram for Low Cycle Fatigue	91
8-10	Design/Cruise High Cycle Fatigue Combined Effective Stress (Percent of Design Allowable) Spar, Face Side	95
8-11	Design/Cruise High Cycle Fatigue Combined Effective Stress (Percent of Design Allowable) Spar, Camber Side	96
8-12	Design/Cruise High Cycle Fatigue Spanwise Stress (Percent of Design Allowable) Shell, Face Side	97
8-13	Design/Cruise High Cycle Fatigue Chordwise Stress (Percent of Design Allowable) Shell, Face Side	98
8-14	Design/Cruise High Cycle Fatigue Shear Effective Stress (Percent of Design Allowable) Shell, Face Side	99
8-15	Design/Cruise High Cycle Fatigue Spanwise Shell, Camber Side (Percent of Design Allowable)	100
8-16	Design/Cruise High Cycle Fatigue Chordwise Stress (Percent of Design Allowable) Shell, Camber Side	101
8-17	Design/Cruise High Cycle Fatigue Shear Stress (Percent of Design Allowable) Shell, Camber Side	102
8-18	Design/Cruise High Cycle Fatigue Combined Effective Stress (Percent of Design Allowable) Foam, Face Side	103
8-19	Design/Cruise High Cycle Fatigue Combined Effective Stress (Percent of Design Allowable) Foam, Camber Side	104
8-20	Design/Cruise High Cycle Fatigue Combined Effective Stress (Percent of Design Allowable) Sheath, Face Side	105

## ILLUSTRATIONS (Continued)

<u>FIGURE</u>		<u>PAGE</u>
8-21	Design/Cruise High Cycle Fatigue Combined Effective Stress (Percent of Design Allowable) Sheath, Camber Side	106
8-22	Take-Off/Climb High Cycle Fatigue Combined Effective Stress (Percent of Design Allowable) Spare, Face Side	107
8-23	Take-Off/Climb High Cycle Fatigue Combined Effective Stress (Percent of Design Allowable) Spar, Camber Side	108
8-24	Take-Off/Climb High Cycle Fatigue Spanwise Stress (Percent of Design Allowable) Shell, Face Side	109
8-25	Take-Off/Climb High Cycle Fatigue Chordwise Stress (Percent of Design Allowable) Shell, Face Side	110
8-26	Take-Off/Climb High Cycle Fatigue Shear Stress (Percent of Design Allowable) Shell, Face Side	111
8-27	Take-Off/Climb High Cycle Fatigue Spanwise Effective Stress (Percent of Design Allowable) Shell, Camber Side	112
8-28	Take-Off/Climb High Cycle Fatigue Chordwise Stress (Percent of Design Allowable) Shell, Camber Side	118
8-29	Take-Off/Climb High Cycle Fatigue Shear Stress (Percent of Design Allowable) Shell, Camber Side	114
8-30	Take-Off/Climb High Cycle Fatigue Combined Effective Stress (Percent of Design Allowable) Foam, Face Side	115
8-31	Take-Off Climb High Cycle Fatigue Combined Effective Stress (Percent of Design Allowable) Foam, Camber Side	116
8-32	Take-Off/Climb High Cycle Fatigue Combined Effective Stress (Percent of Design Allowable) Sheath, Face Side	117
8-33	Take-Off/Climb High Cycle Fatigue Combined Effective Stress (Percent of Design Allowable) Sheath, Camber Side	118
9-1	Calculated Modal Frequencies	122
9-2	SR-7L Blade Resonant Frequencies (For Additional 8 Conditions Analyzed)	123
9-3	Normalized Mode Shape Cruise Condition SR-7L Mode 1	125
9-4	Normalized Mode Shape Cruise Condition SR-7L Mode 2	126
9-5	Normalized Mode Shape Cruise Condition SR-7L Mode 3	127
9-6	Normalized Mode Shape Cruise Condition SR-7L Mode 4	128
9-7	Normalized Mode Shape Cruise Condition SR-7L Mode 5	129
10-1	SR-7L Flight Envelope Airspeed vs. Altitude	133
10-2	SR-7L Design Requirements Unstalled Flutter	134
10-3	Unstalled Flutter Stability Summary by Condition Number	137
10-4	SR-7L Damping Prediction at the D1 Condition	138
10-5	SR-7L Root Locus Plot for Mode 3 at Condition D1	139
10-6	Effect of Unsteady Airloads on SR-7L Freq. for Condition D1	140



## ILLUSTRATIONS (Continued)

<u>FIGURE</u>		<u>PAGE</u>
10-7	The Effect of Unsteady Airloads on the Third Natural Mode Shape for the D1 Flight Condition	142
10-8	SR-7L Damping at Condition D2	143
10-9	SR-7L Damping at Condition 1A	143
10-10	SR-7L Damping at Condition 1B	144
10-11	SR-7L Damping at Condition 1C	144
10-12	SR-7L Damping at Condition	145
10-13	SR-7L Damping at Condition 5	145
10-14	SR-7L Damping at Condition 6	146
10-15	SR-7L Damping at Condition 7	146
10-16	SR-7L Damping at Condition 8	147
10-17	Effect of Changes in the Structure and Aerodynamics on the Stability of the SR-7L Prop-Fan	149
10-18	Damping Prediction Including the Effect of an Aerodynamic Blade Tip Loss on Condition D1	151
10-19	SR-7L Stall Flutter Stability	153
10-20	SR-7L Stall Flutter Stability	154
10-21	SR-7L Stall Flutter Stability	155
10-22	Stall Flutter Design Chart	156
11-1	Spanwise Bird Impact Location	160
11-2	Bird Impact Model for Take-Off Condition	162
11-3	Load at Impact Site vs. Time After Impact	163
11-4	Deflection at Impact Site vs. Time After Impact	164
11-5	Flatwise Deflection vs. Blade Radius at Various Times After Impact	165
11-6	Torsional Deflection vs. Blade Radius at Various Times After Impact	166
11-7	Maximum Blade Stress vs. Bird Weight	169

## 1.0 Summary

This report covers the design and structural analysis of the blade for the SR-7L Large-Scale Advanced Prop-Fan (LAP). Blade stresses, resonant frequencies, stability, aerodynamic and acoustic performance, and results of foreign object impact analyses are reviewed against requirements and goals. The SR-7L is a large scale 2.75 meter (nine foot) diameter test model of a Prop-Fan, so called because it combines the operating efficiency of the turboprop with the higher speed and altitude capabilities of the turbofan. Relative to standard propellers, Prop-Fans have higher disk loadings, more blades, and thinner blades whose tips are swept rearward to decrease relative tip Mach number. The Prop-Fan shows promise of operation at cruise speeds of Mach 0.8 and altitudes of 9,150 meters (30,000 feet) with fuel savings of as much as 40 percent over current turbofan propulsion systems.

Design requirements for the SR-7L blade were established to define the basic configuration, stress limits for normal and overspeed operations, critical speed frequency margins, stability/flutter boundaries, and protection against surface erosion. Recognizing that LAP is a research and not a production program, additional goals were established which are desirable but not mandatory. These goals set standards for aerodynamic efficiency and noise levels, expanded stability boundaries to account for frequency degradation, and resistance to foreign object impact damage. Goals were also imposed to ensure safe operation at anticipated high speed wind tunnel test conditions and at selected flight and ground operating conditions.

The steady-state and dynamic structural evaluations of the blade were conducted with finite element analyses. Iterations were conducted to determine the proper static shape of the blade, ensuring that it will deflect to the desired aerodynamic shape at the design/cruise condition. Non-linearities, due to changes in centrifugal load arising from blade deflections, were evaluated with a piecewise linear analysis which applied air and centrifugal loads to the finite element model in small, successive steps, updating the geometry to account for deflections between steps. Forced response analyses were conducted by applying cyclic airloads to the blade in its steady-state deflected position. A comparison of combined stresses, from the steady and cyclic analyses, to material allowables for high and low-cycle fatigue, shows the SR-7L blade meets all requirements and goals for high-cycle fatigue, and all requirements and most goals for low cycle fatigue, resulting in adequate life for planned SR-7L tests.

The first five blade resonant frequencies and mode shapes of the SR-7L blade were predicted using a deflected, pre-stiffened, finite element model. A comparison of resonant frequencies against the first five integer-order (integer multiples of design rotational speed, 1-P, 2-P, 3-P, 4-P, and 5-P) avoidance bands shows that all frequency placement requirements are met except for a minor infringement of the second mode on the 3-P band at the

design/cruise condition only. All frequency goals for other operating conditions were met, except for the first mode in reverse which infringes on a 2-P zone, expanded for ground operation.

Unstalled flutter stability was evaluated using an aeroelastic stability analysis specifically developed for Prop-Fans. The SR-7L blade meets all requirements and goals for unstalled flutter stability. Stall flutter stability will have to be determined through careful monitoring during planned static thrust tests on a whirl rig and/or on the aircraft, since two methods, one semi-empirical and one purely empirical, give opposite results.

A three-dimensional, interactive, blade impact analysis was performed on the SR-7L blade to investigate the resistance of the blade to the impact of a 1.814 kilograms mass (four pound) bird at the 80 percent radial station near the leading edge with the aircraft assumed to be flying at 185 kilometers per hour (100 knots). The analysis showed that both the aluminum spar and fiberglass shell meet the requirements for major impacts.

Aerodynamic and acoustic performance were calculated for the SR-7L blade. The efficiency and near field noise level at the design/cruise condition satisfy the design goals. The take-off/climb condition efficiency is slightly less than the design goal. The far field noise level for take-off and approach is satisfactory if a cut-back power level is used during take-off.

## 2.0 Introduction

In 1975, at the request of Congress, NASA established the Aircraft Energy Efficiency (ACEE) Program directed at reducing fuel consumption of commercial subsonic air transports. Besides saving fuel, the technology developed under the program would help U.S. aircraft manufacturers retain their dominant role in the world commercial aircraft market. One element of the ACEE Program offering the greatest potential fuel savings is the Advanced Turboprop Program (ATP)(reference 1). Turboprops, with their inherently higher propulsive efficiency, have provided efficient transportation for years at speeds up to about Mach 0.6 and altitudes around 6,100 meters (20,000 feet). However, in order to be compatible with the current and future commercial aircraft operational structure, future turboprop-powered aircraft will be required to cruise at speeds of Mach 0.7 and 0.8 and at altitudes of 9,150 meters (30,000 feet) and higher, while maintaining a comfortable cabin environment.

Early aircraft engine studies have shown that the inherent efficiency advantage of turboprop propulsion systems over turbofan systems at low speed may be extended to these higher speeds by the use of a highly loaded, multi-bladed, swept-tip propeller. This type of propeller is sometimes called a Prop-Fan. Turboprop aircraft with a Prop-Fan type of propeller have the potential of obtaining fuel savings of 15 to 20 percent relative to turbofans with an equivalent level of core engine technology. This translates into a 30 to 40 percent fuel savings relative to current in-service turbofan-powered aircraft.

The objective of the Advanced Turboprop Program (ATP) is to develop the technology required for efficient, reliable, and acceptable operation of advanced turboprop (or Prop-Fan) powered aircraft at cruise speeds up to Mach 0.8 while maintaining cabin comfort levels (noise and vibration) comparable to those of modern turbofan-powered aircraft.

Initial work under the ATP developed a fundamental aerodynamic performance data base on small-scale propeller models and the feasibility of the high speed (Mach 0.7 to 0.8) turboprop concept was established. High levels of aerodynamic performance were demonstrated in tests with these models between 1976 and 1981. However, it is generally accepted by the aircraft industry that an advanced large-scale propeller must ultimately be tested in the real flow environment afforded by a flight test program to demonstrate technology readiness for commercial applications.

In 1981, the structural feasibility of designing several configurations of large-scale Prop-Fan blades was explored. These were 3.36 meters (eleven feet) in diameter and were the same in external shape as the model blades tested. As illustrated in figure 2-1, one had no sweep, one had moderate sweep and was studied in two activity factors (chord widths), and one had a large amount of sweep. Results of this study are reported in reference 2.

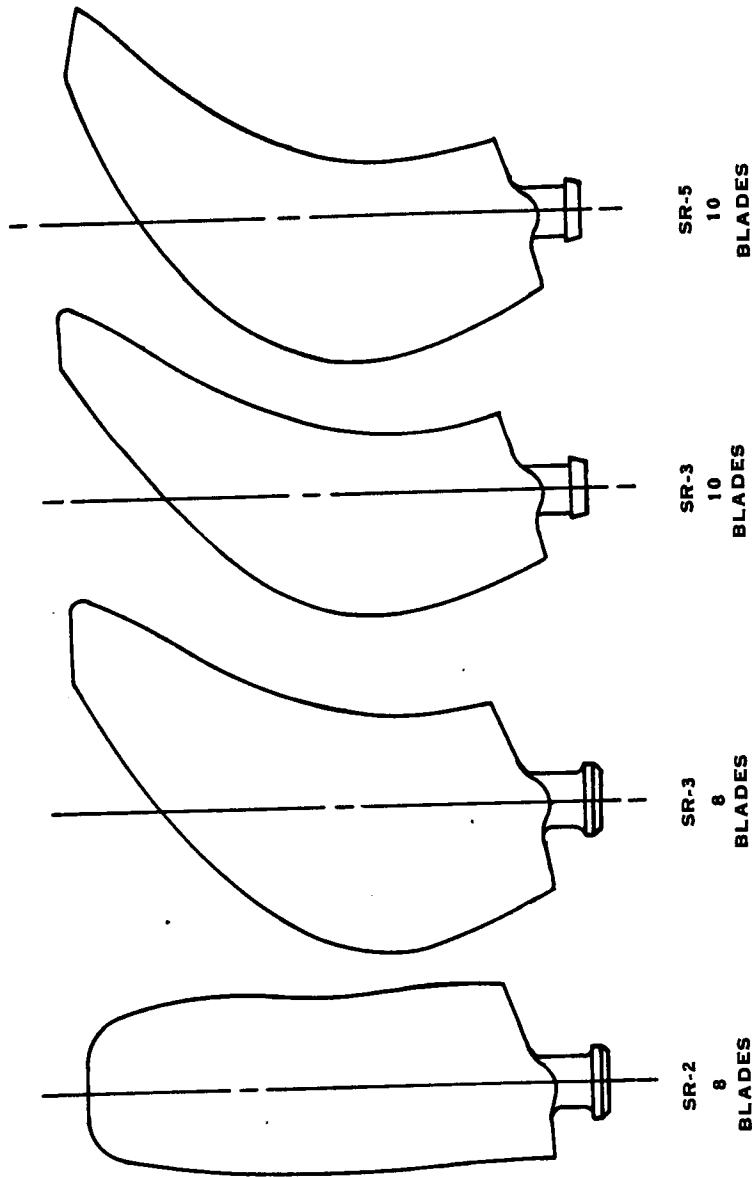


**FIGURE 2-1. PROP-FAN BLADES UNTWISTED  
PLANFORM COMPARISON**

## 2.0 (Continued)

A supplementary task to the study of large-scale Prop-Fans was the design of a 2.75 meter (nine foot) diameter, flight worthy, Prop-Fan, whose blade construction would be representative, within existing blade manufacturing technology, of full-size Prop-Fans in the 3.7 to 5 meter (12 to 16 ft) diameter range. The subsequent detail design, manufacturing, and testing of that Prop-Fan evolved into the LAP program, an acronym for Large-Scale Advanced Prop-Fan. Iterations leading to an acceptable preliminary blade design were conducted in 1982 and are summarized in reference 2.

The report which follows is limited to the description and evaluation of the blade used in the final detail design phase of the LAP program, conducted in 1983. This blade is suitable for testing in the ONERA S1 Wind Tunnel (Modane, France) and for proposed flight test portions of the Prop-Fan Test Assessment (PTA) (ref. 3) program planned for 1986 and 1987, respectively. This blade is sufficiently large and of such a construction that test data obtained will be closely representative of a full-scale blade in the 3.7 to 5 meter (12 to 16 foot) diameter range.

### 3.0 Requirements and Goals

The design objectives for the SR-7L blade are divided into requirements and goals. The requirements are objectives which must be satisfied in the design process. The goals are additional objectives that are desired but need not be satisfied. Four conditions were used to assure the structural adequacy of the design with respect to the requirements. After this was achieved, eight additional conditions were evaluated. Satisfying the requirements for these eight additional conditions was not mandatory.

#### 3.1 Design Requirements

The design requirements can be divided into six categories. These categories, along with the requirements of each, follow:

##### 3.1.1 Configuration

No. of blades per rotor..... 8  
Tip diameter..... 2.75 m. (9 ft.)  
Tip speed..... 244 mps (800 fps)  
Activity factor..... 227.3  
Direction of rotation, aft looking forward.. counter-clockwise

##### 3.1.2 Flutter Limits

The Prop-Fan assembly shall be free of flutter instabilities over a normal flight profile shown in figure 3-1 for a representative aircraft installation for normal operating conditions.

##### 3.1.3 Critical Speed Margins

For the two-per-revolution (2-P) excitation at 244 meters per second (800 feet per second), tip rotational speed, the critical speed margin shall be a minimum of ten percent of propeller speed and resonant frequency. As indicated in figure 3-2, this margin shall be reduced inversely as the exciting order is increased from 3-P to 5-P. No 1-P critical speeds shall be permitted in the operating speed range and the minimum 1-P margin shall be 40 percent of the maximum Prop-Fan operating speed. For ground operation, the 2-P critical speed margin shall be a minimum of twenty percent of the propeller speed and frequency. These margins shall include the effect of blade angle on frequency.

ALTITUDE, THOUSANDS OF METERS

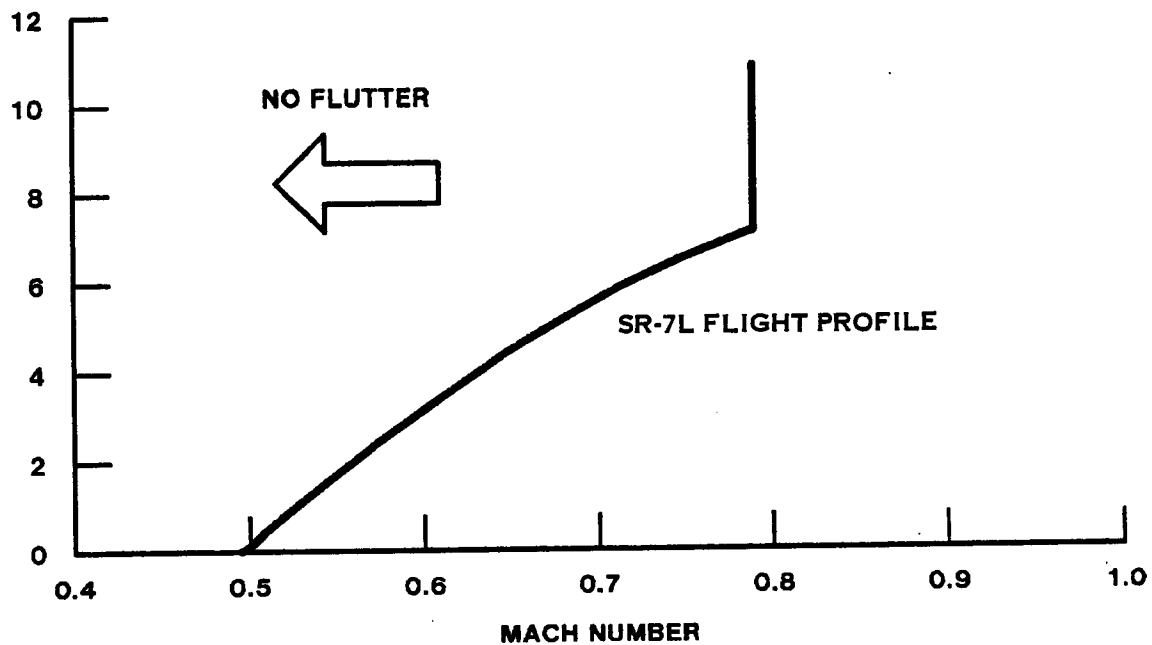


FIGURE 3-1. SR-7L DESIGN STABILITY REQUIREMENTS



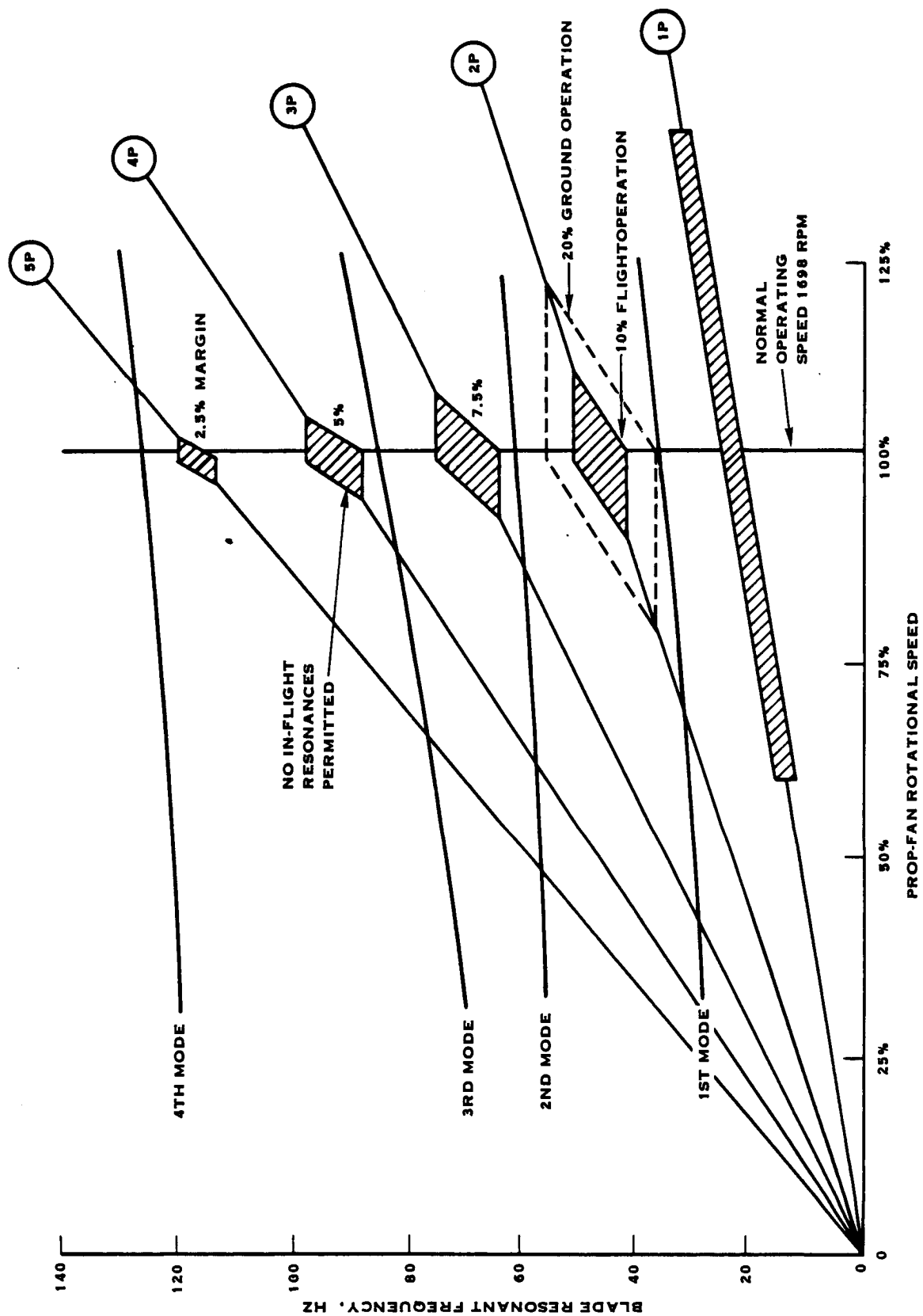


FIGURE 3-2. RESONANT FREQUENCY REQUIREMENTS

#### 3.1.4 Stress Limits

Figure 3-3 shows a typical Goodman diagram which illustrates the relationship between the blade operating conditions evaluated and the required stress limits for these conditions.

##### 3.1.4.1 Normal Operation

All structural components of the blade shall be free of higher than allowable combined stresses during both the design/cruise and take-off/climb conditions. The high cycle fatigue stress limits for these conditions are based on  $10^8$  cycles as shown in figure 3-3, while the low cycle fatigue stress limits are based on 50,000 start-stop cycles.

##### 3.1.4.2 Rotor Overspeeds

The blade shall be capable of operating to 125 percent (1.5 times the normal centrifugal load) of the maximum operating speed with no inelastic deformation. That is, all material stresses must fall below the yield strength as shown in figure 3-3.

The blade shall be capable of operating to 140 percent (2.0 times the normal centrifugal load) of the maximum operating speed with some allowable inelastic deformation, but no material separation (metal or composite). All material stresses must fall below the ultimate tensile strength as shown in figure 3-3.

#### 3.1.5 Foreign Object Damage

The outer portion of the blade leading edge shall be covered with a partial chord width metal sheath for protection against erosion, such as from rain and sand.

#### 3.1.6 Flight Representative Design

The blade shall be designed to have weight and structural characteristics that are representative of anticipated Prop-Fan systems for future aircraft applications.

### 3.2 Design Goals

The design goals can be divided into five categories. These categories, along with the goals of each, follow:

#### 3.2.1 Net Prop-Fan Efficiency (isolated nacelle installation)

Design point cruise (forward velocity) = 0.8 Mach no.,

Altitude = 10,675 meters (35,000 feet)...78.6 percent

Take-off (forward velocity = .2 Mach no.).....52.0 percent

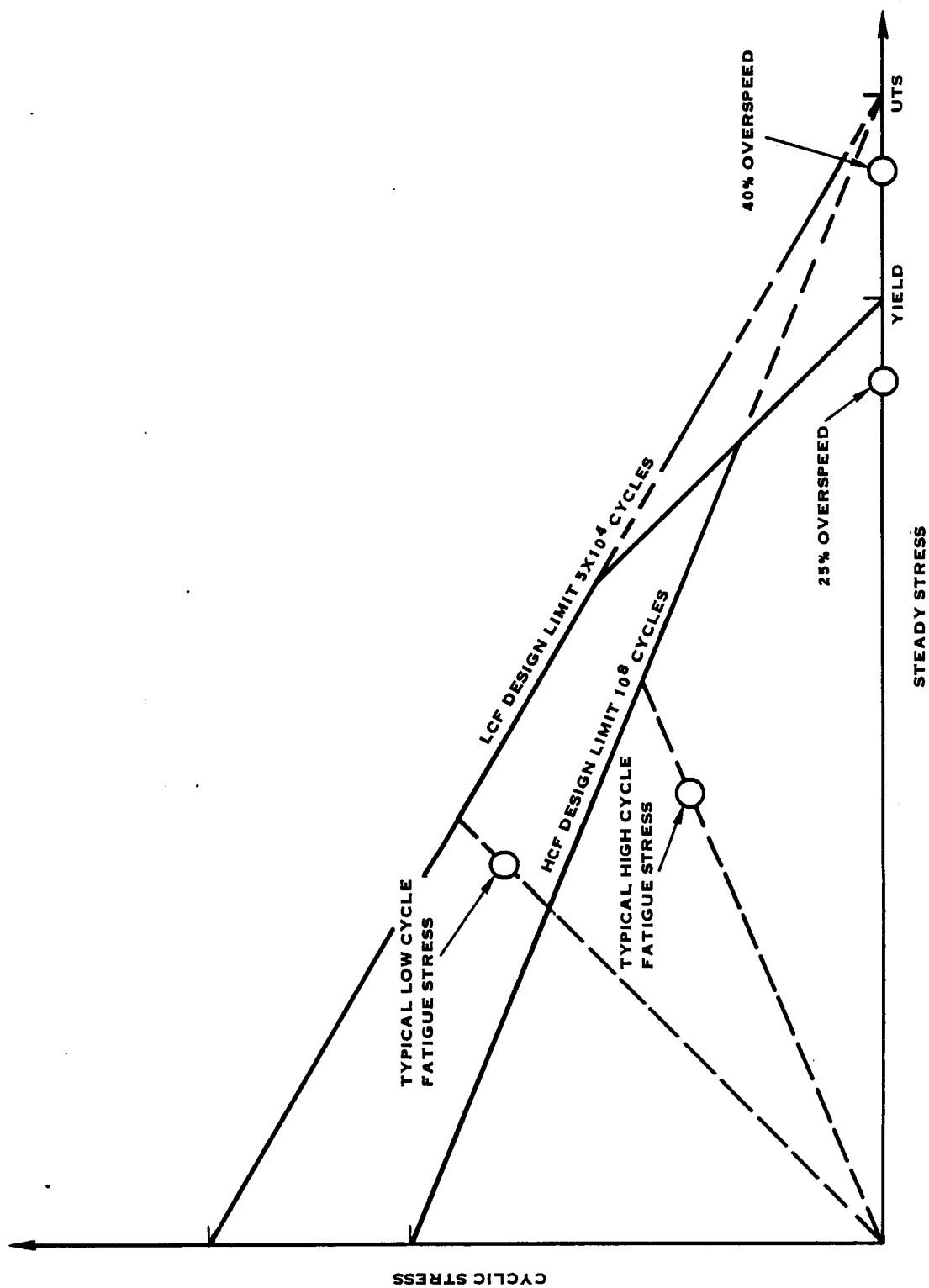


FIGURE 3-3. STRESS REQUIREMENTS

### 3.2.2 Noise

Near field, design point cruise, free field

maximum sideline at 0.8D (overall sound pressure level)...144 dB

Far field (take-off or approach) ....FAR-36 minus 10 EPN dB

### 3.2.3 Flutter Margin

#### 3.2.3.1 Stall Flutter

The Prop-Fan shall be free of stall flutter at 100 percent of design take-off power at 100 percent design speed and take-off conditions (Mach no. = 0.0 to 0.2). The Prop-Fan shall also be free of stall flutter in reverse thrust.

#### 3.2.3.2 Unstalled Flutter

The Prop-Fan shall be free of unstalled high speed flutter over the normal flight profile (see fig. 3-1) and range of power loadings at 15 percent degradation in natural frequencies.

### 3.2.4 Foreign Object Damage (FOD)

#### 3.2.4.1 Minor Impacts

Minor impacts are those due to sand, small stones, and birds up to .113 kilogram (four ounces). No structural damage allowed to the blade shell or sheath. Operation will continue without impediment.

#### 3.2.4.2 Moderate Impacts

Moderate impacts are those due to 5.1 centimeter (two inch) hailstones and birds up to .907 kilogram (two pounds). Damage can include loss of material or airfoil distortion. Operation shall continue at 76 percent power for five minutes. No fragments (metal or composite) shall be lost which can penetrate the aircraft fuselage pressure shell. Roughness shall be tolerable and the rotor unbalance force due to damage to one or more blades shall be kept below 22,240 newtons (5,000 pounds).

#### 3.2.4.3 Major Impacts

Major impacts are those due to a single bird up to 1.814 kilograms (four pounds). Damage can include loss of material or airfoil distortion. The ability to feather the Prop-Fan must be maintained. Shutdown must be accomplished without catastrophic effects on the airframe structure. The rotor unbalance force due to damage to one or more blades shall be kept below 111,200 newtons (25,000 pounds). No fragments (metal or composite) shall be lost which can penetrate the aircraft fuselage pressure shell.

### 3.2.5 Blade Design Life and Inherent Reliability

Replacement life with scheduled maintenance.....35,000 hours

Mean time between unscheduled removals  
(8 blade set).....50,000 hours

### 3.3 Evaluation Conditions

#### 3.3.1 Primary Required Design Conditions

A description of the conditions for the primary design requirement evaluation is given in table 3-1. These four conditions were used to determine the structural adequacy of the design. Analysis at these conditions will be reported in detail in sections 6 through 12.

#### 3.3.2 Additional Secondary Conditions

In addition to the primary required design conditions listed in table 3-1, eight additional secondary conditions listed in table 3-2 were examined to determine the suitability of the design for a broader test envelope. Although it was not mandatory that the design requirements of these additional conditions be satisfied, it was agreed that if the results of the evaluations placed severe limitations on the planned test program, blade design revisions would have to be considered.

Case one consists of three conditions for the simulation of the ONERA S1 Wind Tunnel tests. In the ONERA S1 Wind Tunnel, a full load blade test is planned, along with an investigation into the effects of cascade and coupling phenomena on the blade. However, due to power limitations in the wind tunnel, only a two bladed Prop-Fan configuration can be tested at full load. In order to investigate the effects of the cascade and coupling phenomena, four-blade and eight-blade Prop-Fan configurations will be tested separately at partial load.

Table 3-1

PRIMARY REQUIRED DESIGN CONDITIONS  
ANALYZED TO ASSURE STRUCTURAL ADEQUACY

Case	D1	D2	D3	D4
Condition	Design/ Cruise	Take-off/ Climb	25 pct. overspeed	40 pct. overspeed
Power loading, kw/meter <sup>2</sup> (HP/foot <sup>2</sup> )	253 (32.0)	586 (74.1)	0.0 (0.0)	0.0 (0.0)
Forward velocity, Mach no.	0.80	0.20	2**	2**
Altitude, meters (feet)	10,675 (35,000)	sea level	2**	2**
Tip speed, meters/second (feet/second)	244 (800)	244 (800)	305 (1,000)	342 (1,120)
Rotation speed, rev./min.	1,698	1,698	2,122	2,371
Excitation factor	4.5	4.5	0.0	0.0
Beta 3/4, degrees	57.57	38.26	57.57	57.57
Power, kilowatts (horsepower)	1,906 (2,592)	4,413 (6,000)	2**	2**
Thrust, newtons (pounds)	6,490 (1,459)	33,649 (7,565)	2**	2**

1\* based on blade tip diameter squared.

2\*\* Overspeed conditions were evaluated as 125% and 140% design/cruise RPM, while maintaining airloads and blade angle setting of the design/cruise condition.

Table 3-2

## ADDITIONAL SECONDARY CONDITIONS EVALUATED

Case	1A	1B	1C	2	3	4	5	6	7	8
Condition	ONERA 8 Blade	ONERA 4 Blade	ONERA 2 Blade	Static Thrust	Reverse Thrust	Cruise Lo RPM	Cruise Hi RPM	Climb Mid Alt.	Dive Mid Alt.	Dive High Alt.
Power loading,* kw/meter <sup>2</sup> (HP/foot <sup>2</sup> )	103 (13.0)	103 (13.0)	103 (13.0)	586 (74.1)	117 (14.8)	198 (25.0)	316 (40.0)	527 (66.7)	0.0 (0.0)	0.0 (0.0)
Forward velocity, Mach no.	0.80	0.80	0.80	0.00	0.00	0.80	0.85	0.50	0.60	0.80
Altitude, meters (feet)	4,270 (14,000)	4,270 (14,000)	4,270 (14,000)	sea level	sea level	10,675 (35,000)	10,675 (35,000)	3,050 (10,000)	6,100 (20,000)	10,675 (35,000)
Tip speed, meters/second (feet/second)	244 (800)	244 (800)	244 (800)	244 (800)	244 (800)	183 (600)	256 (840)	244 (800)	244 (800)	244 (800)
Rotational speed, rev./minute	1698	1698	1698	1698	1698	1273	1783	1698	1698	1698
Excitation factor	4.5	4.5	4.5	0.0	0.0	4.5	4.5	4.5	0.0	0.0

\*based on blade tip diameter squared.

#### 4.0 Description of Final SR-7L Blade

##### 4.1 Concept Evolution

A moderately swept, eight-blade geometry, based on the SR-3 full-scale feasibility configuration shown previously in figure 2-1, was judged to be the best starting point for the 2.75 meter (nine foot) diameter blade. Internal construction consisted of a solid aluminum spar and fiberglass shell which is a service-proven combination.

The feasibility study predicted that this type design would have good aerodynamic performance, adequate critical speed margin, and satisfactory stress margins in all structural components. However, the SR-3 design was predicted to be susceptible to aeroelastic instability, or flutter, at the high speed end of the flight profile, as were all the large-scale swept blades studied.

Internal analytical study had shown that high speed flutter was directly related to the amount of torsion-bending coupling in the blades normal vibratory modes. The greater the torsion-bending coupling in a blade mode the more susceptible that blade mode is to flutter. (Ref. 4). A preliminary study had shown that torsional content could be reduced, and stability thus increased, by restacking the blade tip geometry to a more favorable position "off" the theoretical helix established by the airflow. This caused a slight performance loss and noise increase but was deemed necessary for stability.

Unfortunately, it was found that stacking the blade tip "off" helix to increase stability resulted in blade steady stresses that were unacceptably high. Therefore, many iterations were performed on this original concept, including changes in thickness, chord width, stacking, internal construction, materials, etc. to obtain an acceptable design. A detailed description of these iterations is contained in reference 2..

##### 4.2 Final Design

The final blade design is a careful balance of performance, stress, and stability characteristics as shown in figure 4-1. The original tip sweep was reduced and resulted in a small drop in performance, but this loss was required to increase blade stability while maintaining an adequate stress margin. The offset was changed to further increase stability with a small decrease in stress margin. Stress margin was recovered at a slight cost in performance by increasing the airfoil thickness at the mid-region of the blade.



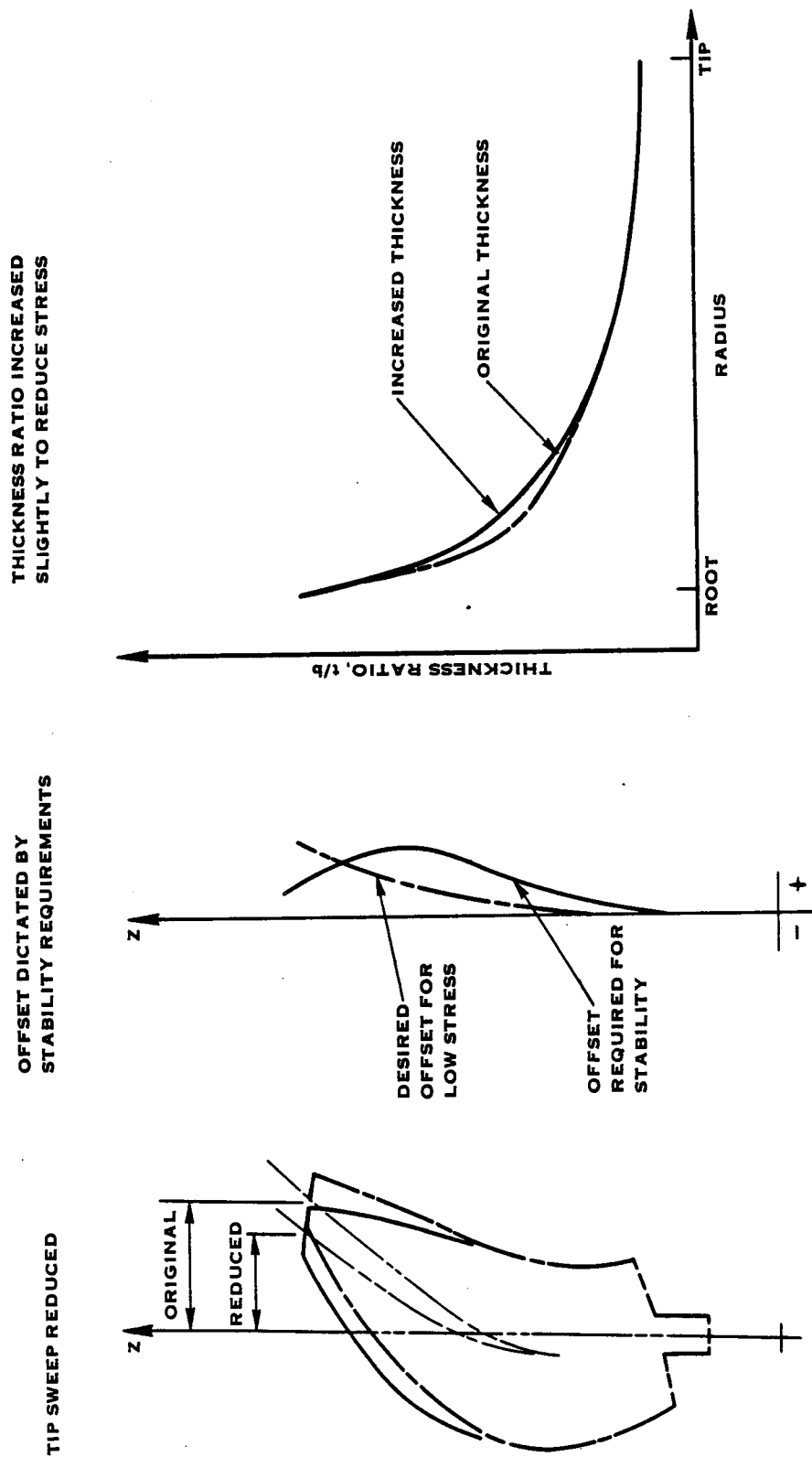


FIGURE 4-1. BALANCING THE FINAL SR-7L DESIGN

The aerodynamic characteristics of the final design are shown in figure 4-2 and the blade stacking data is shown in figure 4-3. The untwisted planform of the blade is projected in figure 4-4. Several computer-drawn views of an assembled SR-7L Prop-Fan are shown in figure 4-5.

Features of the blade construction are shown in figure 4-6. These include a central aluminum spar which forms the structural "backbone" of the blade, a multi-layered glass-cloth-reinforced plastic shell which overhangs the leading and trailing edge of the spar, and a partial chord-width nickel sheath which covers the leading edge of the outer two-thirds of the blade. Remaining internal cavities are filled with low-density rigid foam. The outboard portion of the spar is intentionally moved toward the leading edge to increase stability by reducing overhung mass in the tip trailing edge, while at the same time increasing the integrity of the leading edge from the standpoint of foreign object damage.

Although some improvements in sweep/stress/stability trade-offs were predicted through the use of advanced composites, it was decided not to include these in the final blade design. Their use would require the development of new manufacturing technology, both in terms of suitable construction methods and processes, and lengthy development of design allowables to reflect the manufacturing process.

It was felt that the scope of the program would be best served by remaining with the service-proven combination of an aluminum spar enveloped with a fiberglass shell for which processes and stress allowables are well known.

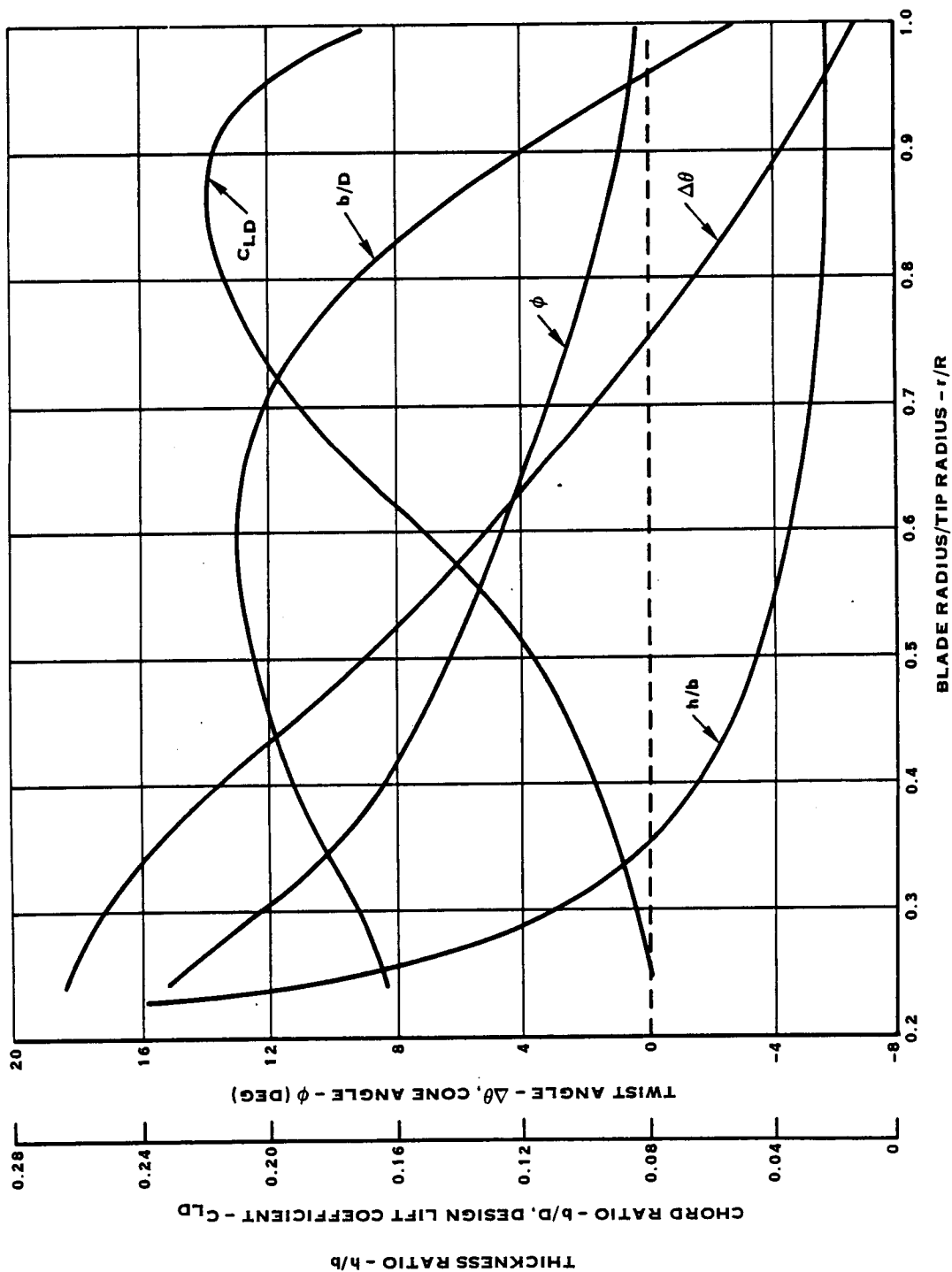


FIGURE 4-2. SR-7L AERO CHARACTERISTICS  
(DEFLECTED: DESIGN/CRUISE)

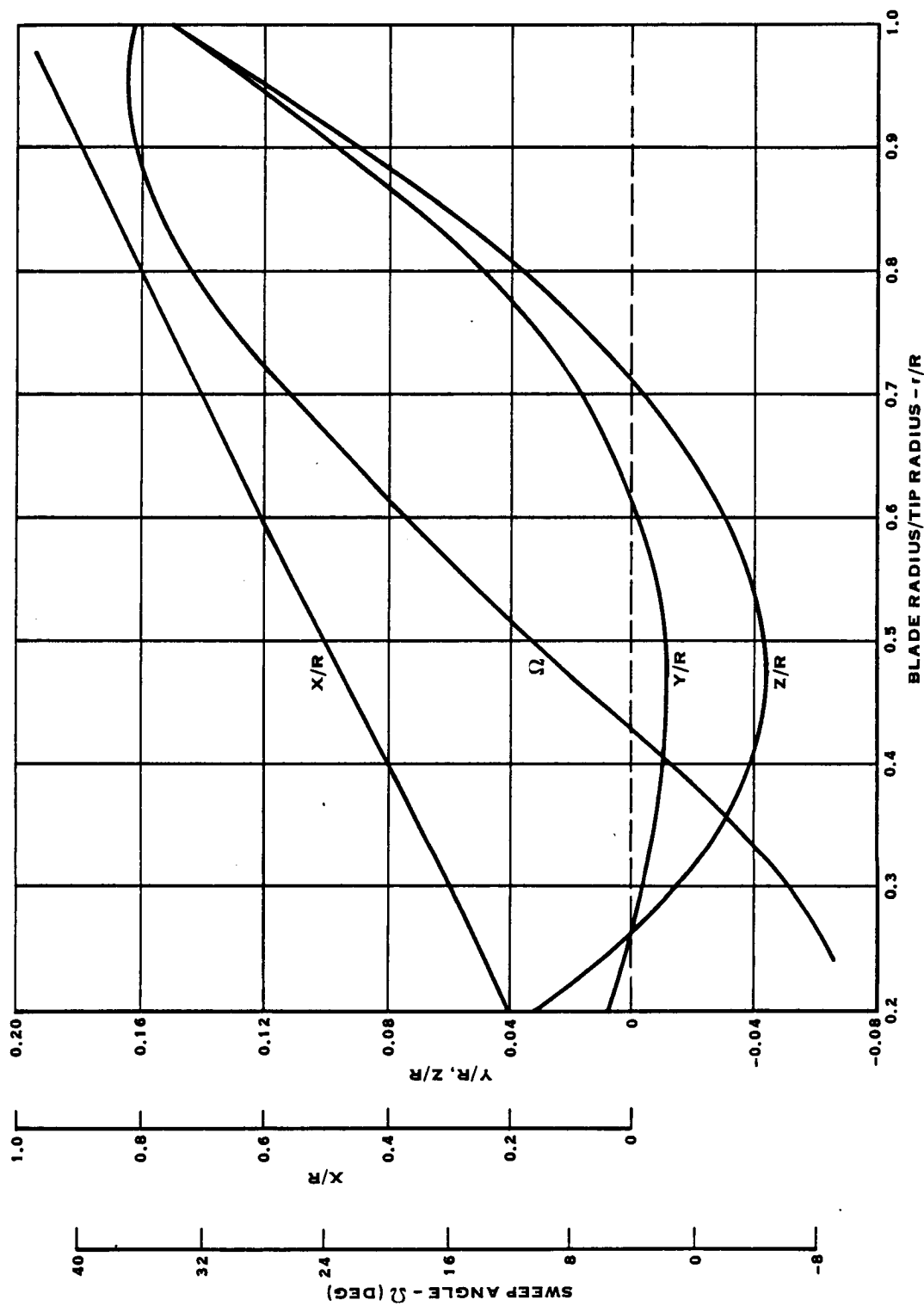


FIGURE 4-3. SR-71 BLADE STACKING DATA (DEFLECTED: DESIGN/CRUISE)

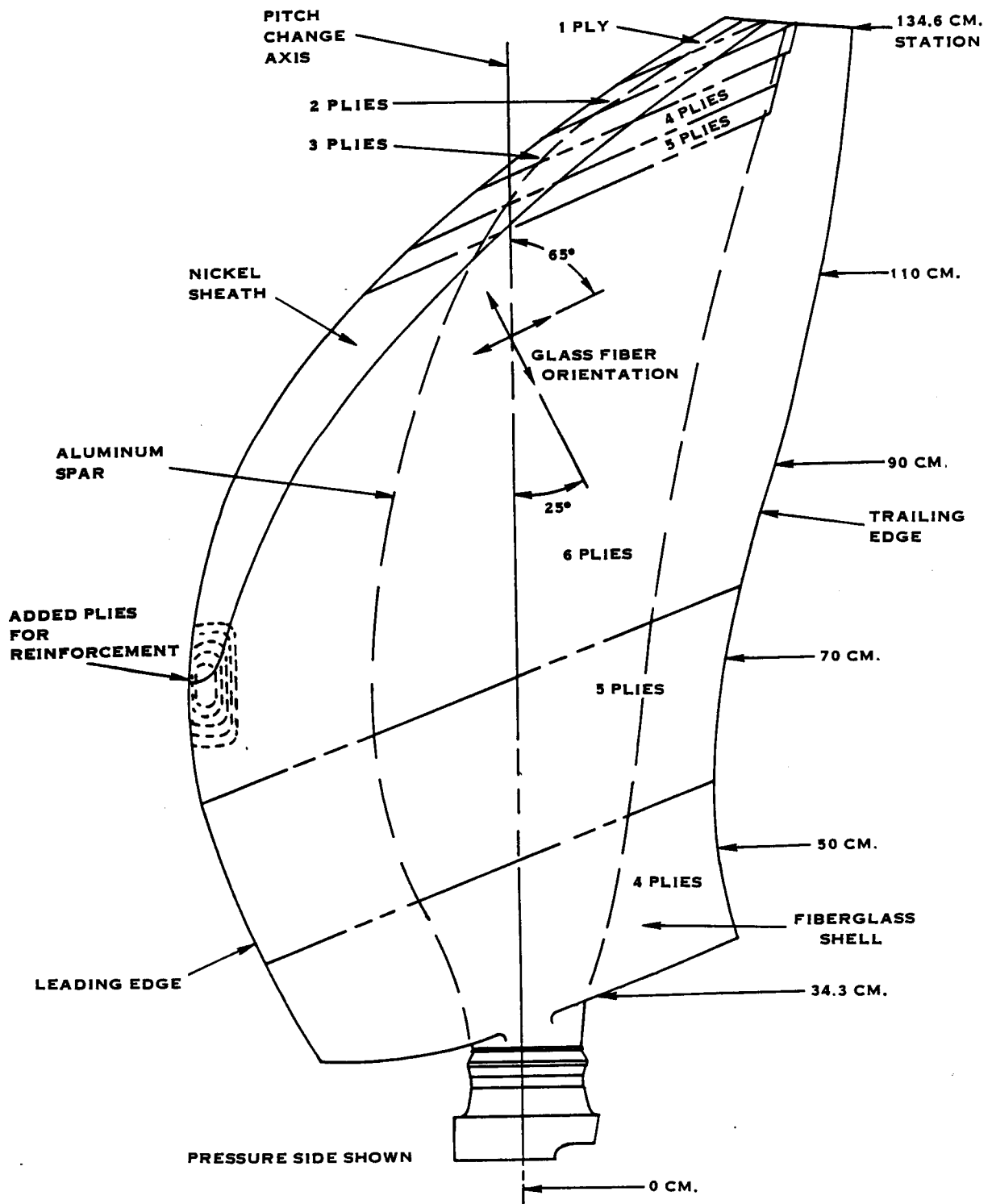


FIGURE 4-4. UNTWISTED PLAN VIEW

ORIGINAL PAGE IS  
OF POOR QUALITY

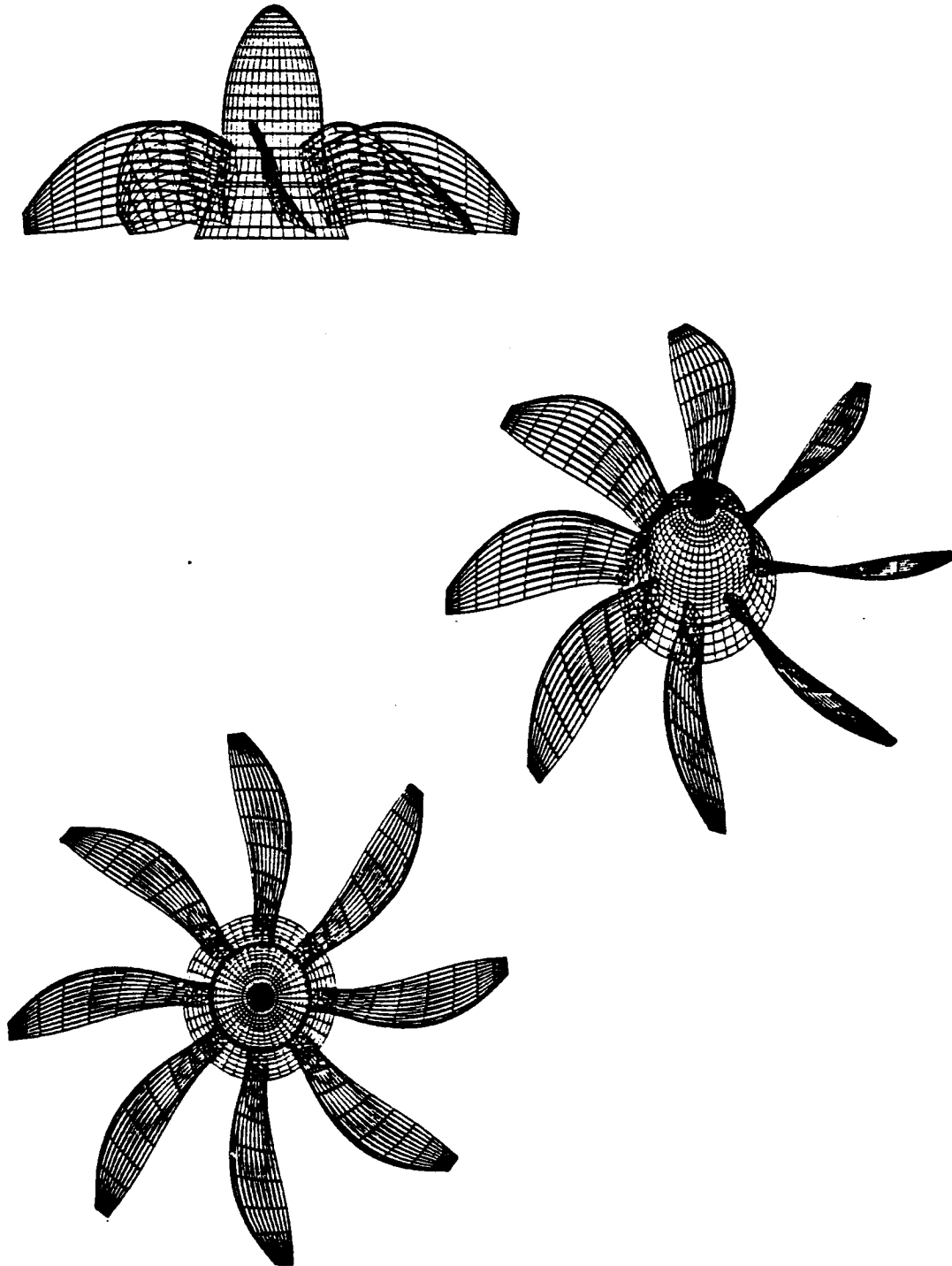


FIGURE 4-5. SR-7L PROP-FAN

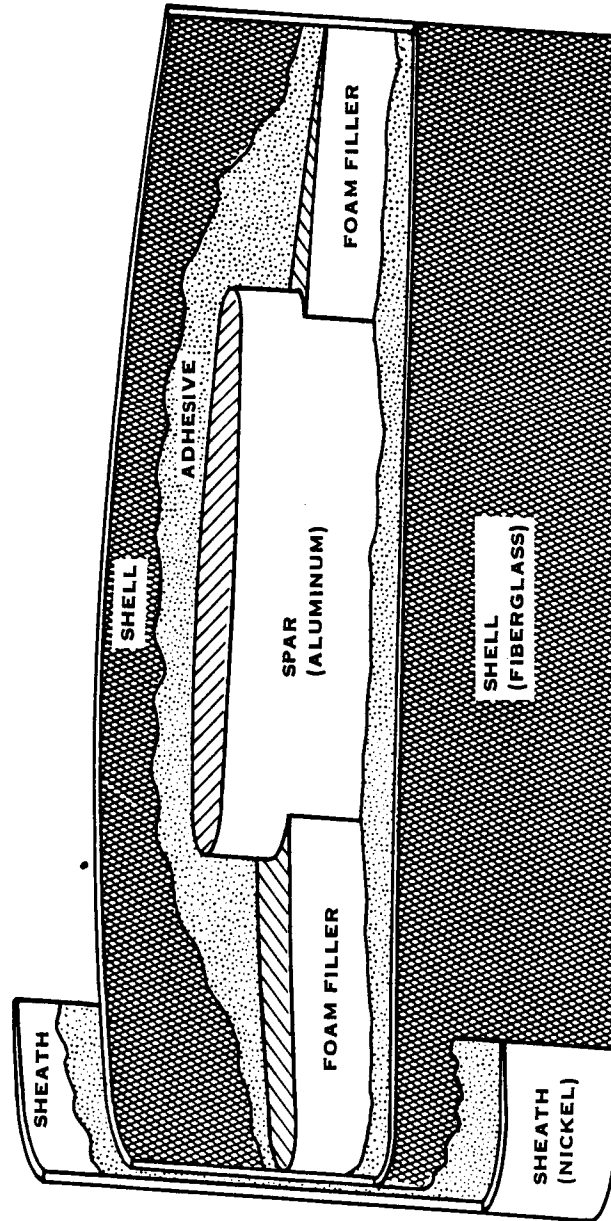


FIGURE 4-6. FEATURES OF SR-7L BLADE CONSTRUCTION

## 5.0 Finite Element Modeling

Because of the swept geometry of the blade, considerable attention was given to the analytical techniques to be used in the design process. An in-house finite element analysis (FEA) code (Ref. 5) was used to represent the three-dimensional blade structure. During preliminary design iterations, the blade was modeled with a relatively course mesh of triangular plate elements, three layers deep through the thickness of the blade. Once an acceptable preliminary design was achieved, a finer mesh FEA model was constructed.

### 5.1 Coordinate System

To help define the position, geometry, restraints, loading, and reactions of the blade model, and to relate these to other models or calculations, or to the actual Prop-Fan system, the global coordinate system shown in figure 5-1 was established. This is a right-handed cartesian system where the Y-axis is colinear with the Prop-Fan rotation axis and is positive in the direction of flight, the X-axis is in the plane of rotation, and the Z-axis, also in the plane of rotation, is colinear with the pitch change axis of a typical blade and is positive toward the blade tip.

The blade model was constructed with respect to this coordinate system in the design/cruise position with a pitch angle setting, Beta three-quarters, of 57.57 degrees as shown in figure 5-2. The blade angle setting or "Beta" angle is usually specified at a radial location three-fourths of the distance from the axis of rotation to the blade tip and when so specified is the "Beta" three-quarters angle.

For an operating condition with an angular setting other than 57.57 degrees (for example, the take-off/climb condition has an angle of 38.26 degrees) the Prop-Fan axis of rotation is changed relative to the global system by specifying new direction cosines defining the direction of the rotation vector, as illustrated in figure 5-3. Therefore, for any operating condition the coordinates of any point on the blade are the same, although that point's relation to the Prop-Fan axis of rotation may vary.

### 5.2 Bond Model

The detail design blade model had a fine mesh of triangular three-dimensional plate elements. As shown in figure 5-4, two outer layers on each side of the blade (face and camber) were used to represent the fiberglass shell and the leading edge nickel sheath, while a central layer was used to represent the internal aluminum spar and leading and trailing edge foam filler (shell cavity) regions.



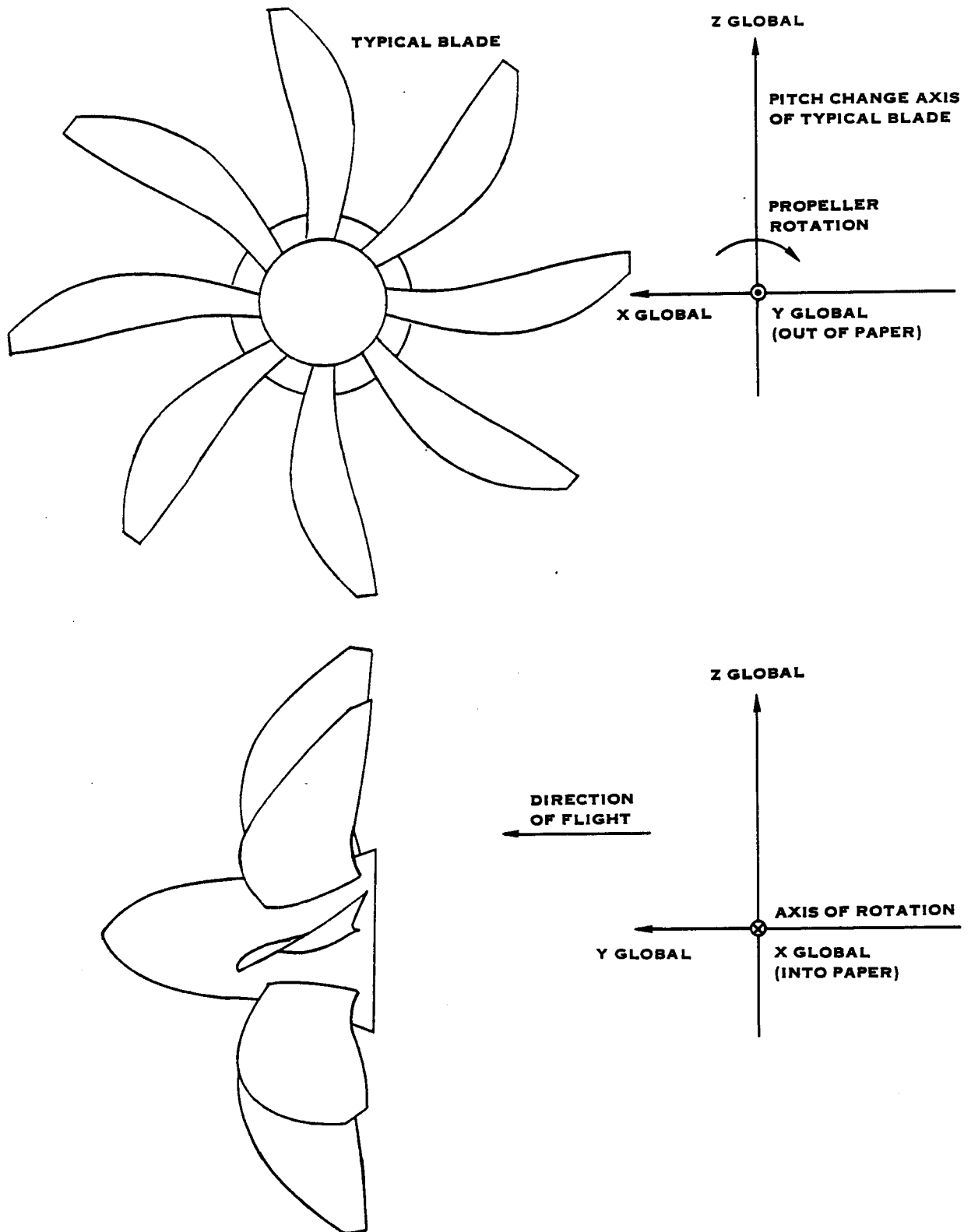


**FIGURE 5-1. GLOBAL COORDINATE SYSTEM**

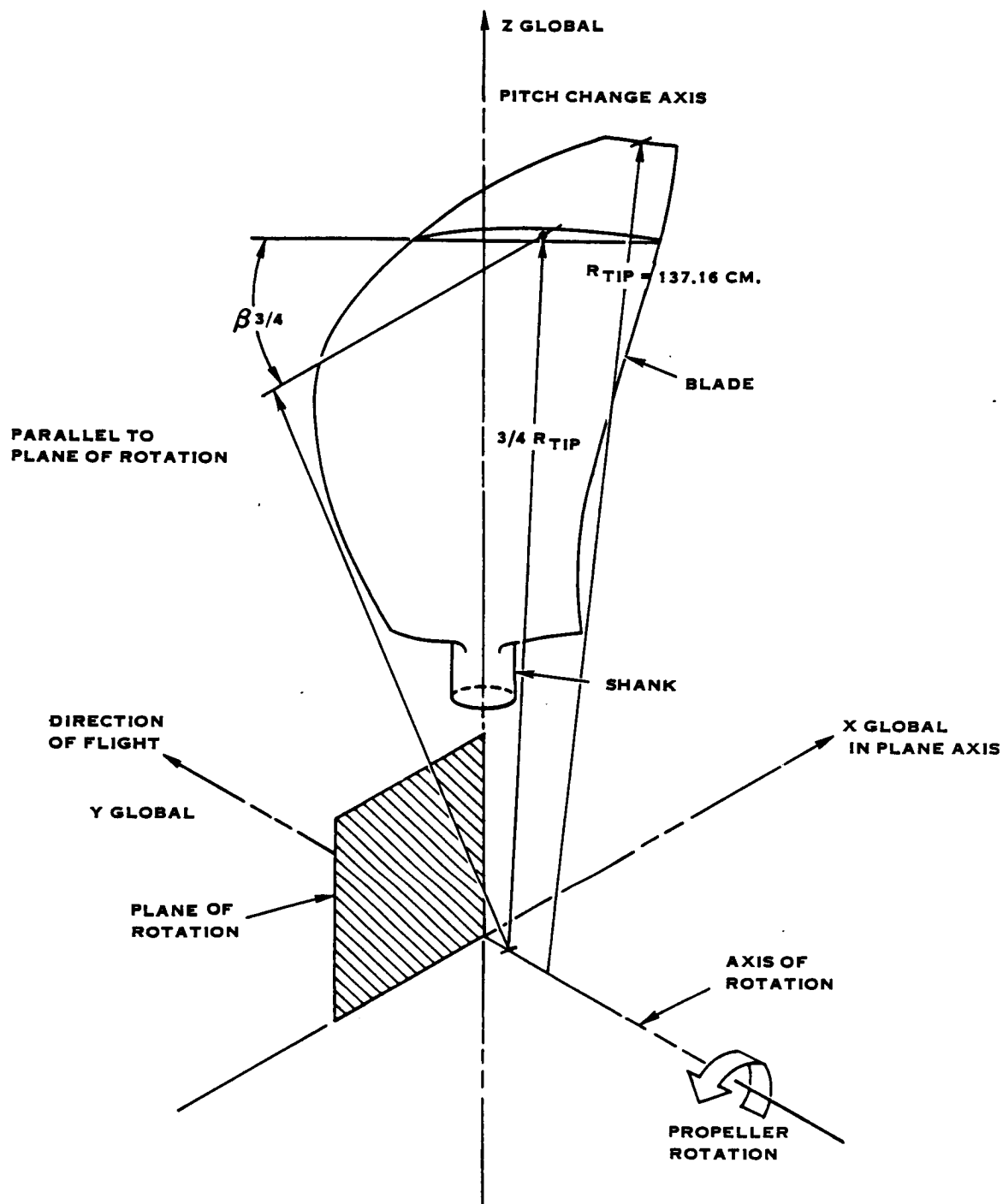


**FIGURE 5-2 GLOBAL COORDINATE SYSTEM BETA THREE-QUARTERS  
ANGLE=57.57° (DESIGN/CRUISE)**

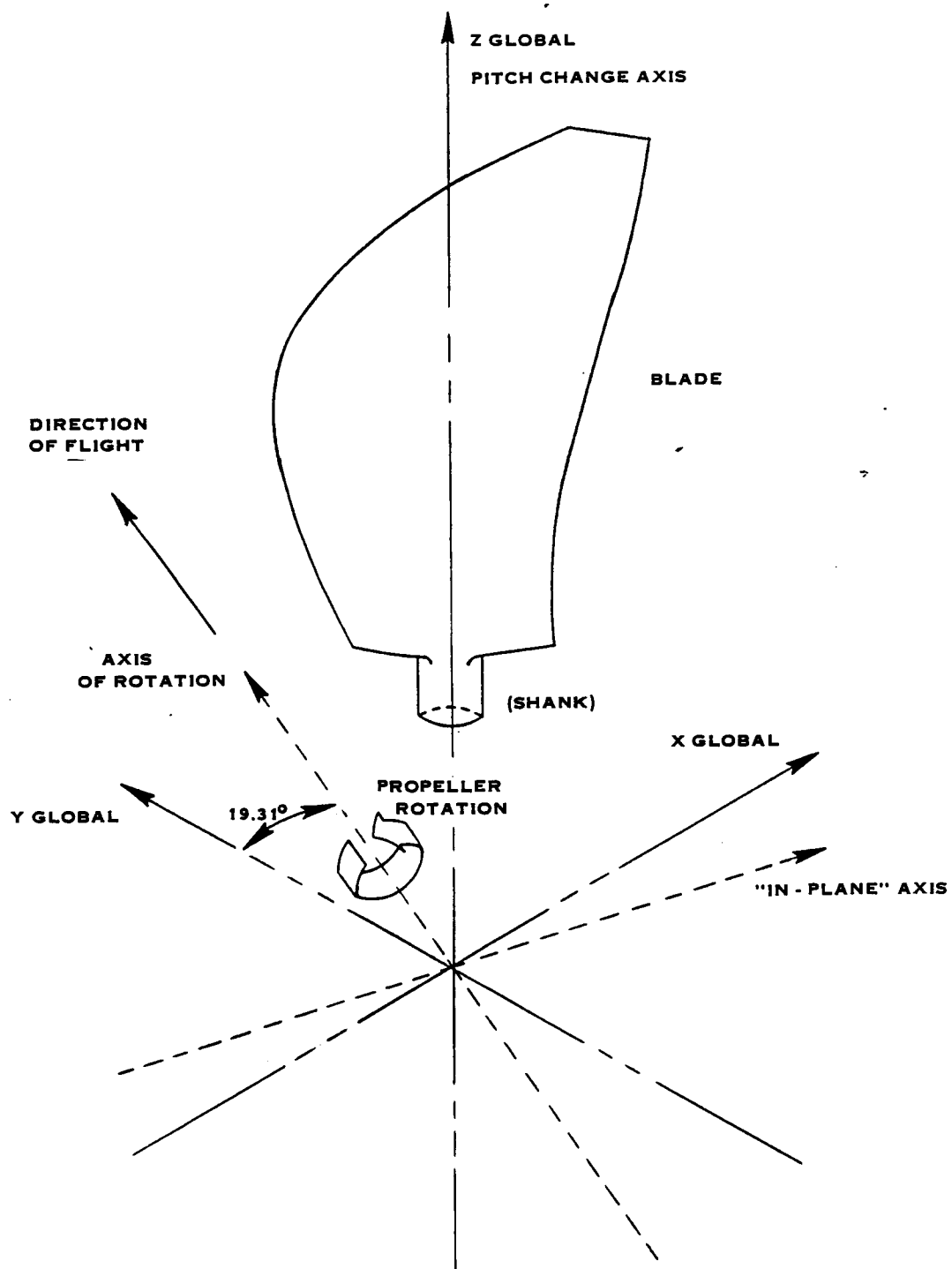


**FIGURE 5-3. GLOBAL COORDINATE SYSTEM  
BETA THREE - QUARTERS =  $38.26^\circ$   
(TAKE-OFF/CLIMB)**

ORIGINAL PAGE IS  
OF POOR QUALITY

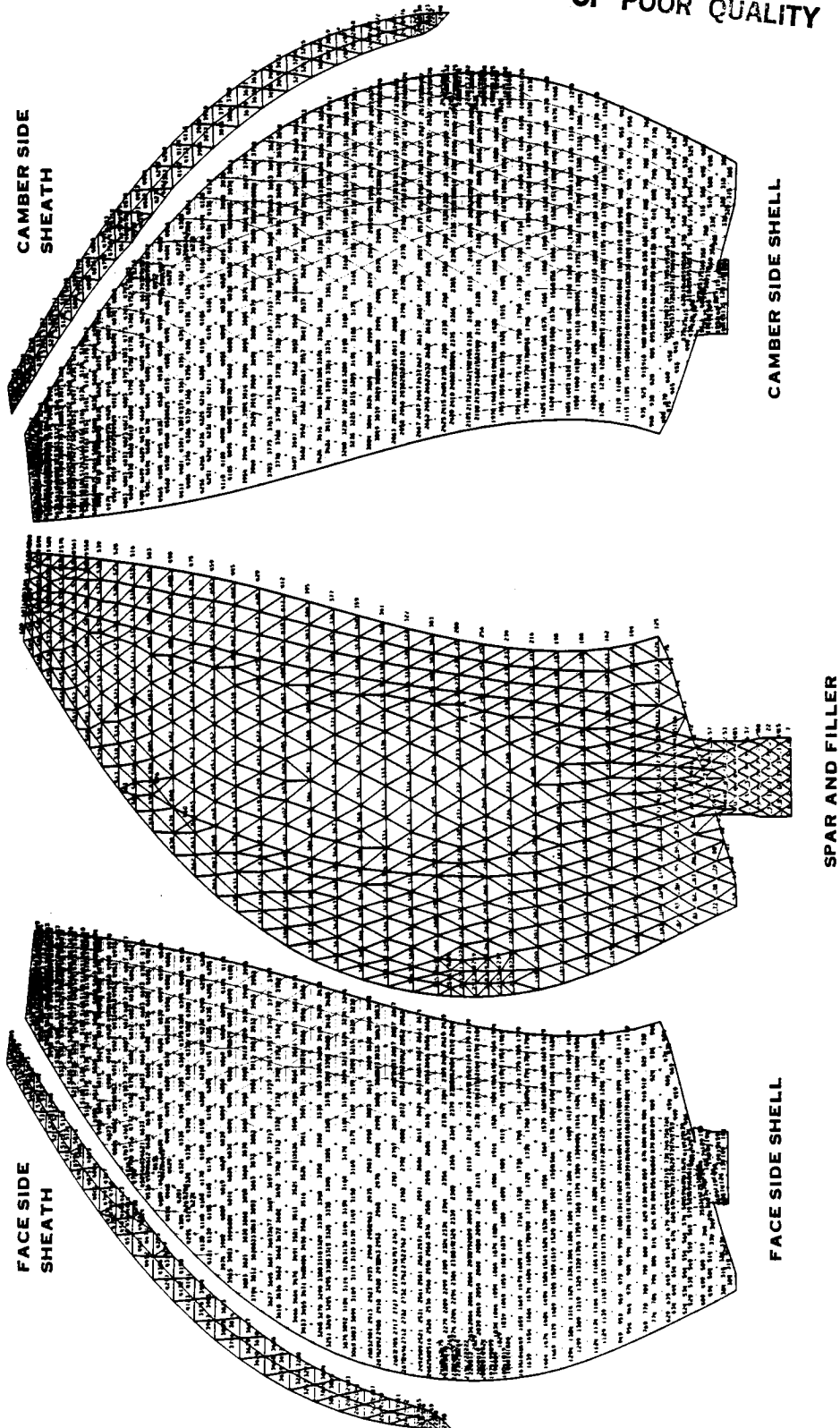


FIGURE 5-4. SR-7L ELEMENTS FOR "BOND" AND "OFFSET" FEA MODELS

These five layers in turn were "tied" together with bond elements at each corresponding grid point of the individual layers as shown in figure 5-5. These bond elements are non-continuous elastic links whose size and shape influence the shear, tension, compression, and bending motions occurring between mutual layers during the solution process. They proved useful in monitoring adhesive and foam filler stresses throughout the blade.

This FEA bond model yielded the desired information for the design/cruise steady-state operating condition. However, the bond model proved extremely lengthy to solve because the bond elements introduce a large number of degrees of freedom. The cost and time required for steady-state response, forced vibratory response, and resonant frequency solutions for 14 operating conditions would have been prohibitive. The complex bond model was therefore revised by removing the bond elements and converting it to an offset model.

### 5.3 Offset Model

In the offset model, shown in figure 5-6, the four outer layers of the model, which represent the shell and sheath, were offset from the central layer, which represents the spar and foam filler, by using an option in the FEA code which enables it to reduce the five layers to an equivalent central layer using rigid link connections between layers, thereby greatly reducing matrix solution time. Translations and rotations from the displacement matrix are then applied internally to each layer through the rigid link connections to obtain proper element strains and stresses for each material layer prior to being output from the FEA code.

As seen in table 5-1, the solution time for the resulting offset model was one-tenth that of the bond model. Stresses and deflections were nearly identical to those of the bond model for the design/cruise case.

This supports the view that the foam and adhesive flexibilities are important only in regard to local edge stressing of these components. The structural influence of these components on the overall assembly is adequately modeled by the rigid link representation. Adhesive stresses were not available from the offset model, but these had been found to be well below the material allowables for the case analyzed with the bond model. Therefore, the offset model was used as the finite element model in the detailed design process.

ORIGINAL PAGE IS  
OF POOR QUALITY

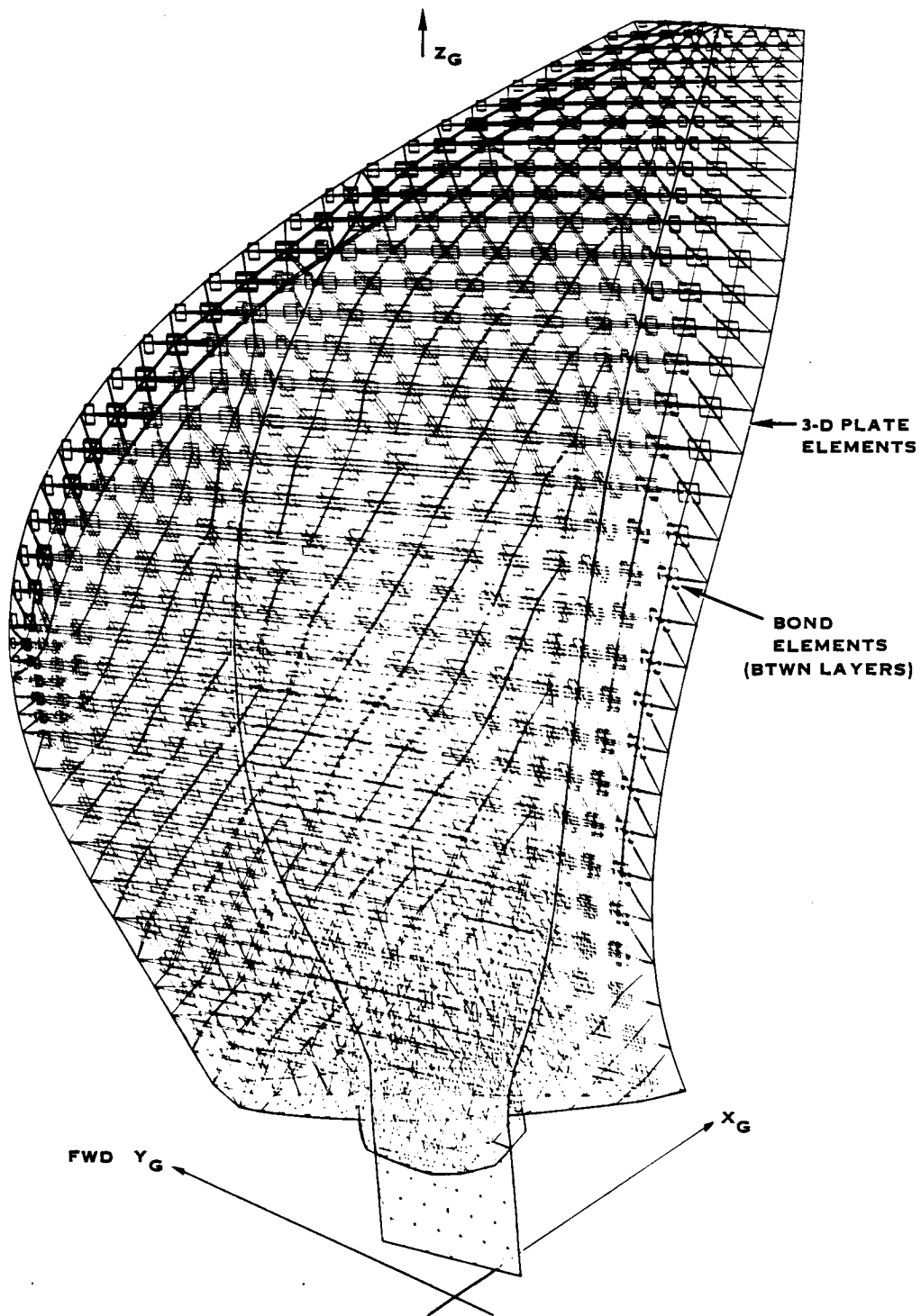


FIGURE 5-5. SR-7L "BOND" FEA MODEL

ORIGINAL PAGE IS  
OF POOR QUALITY

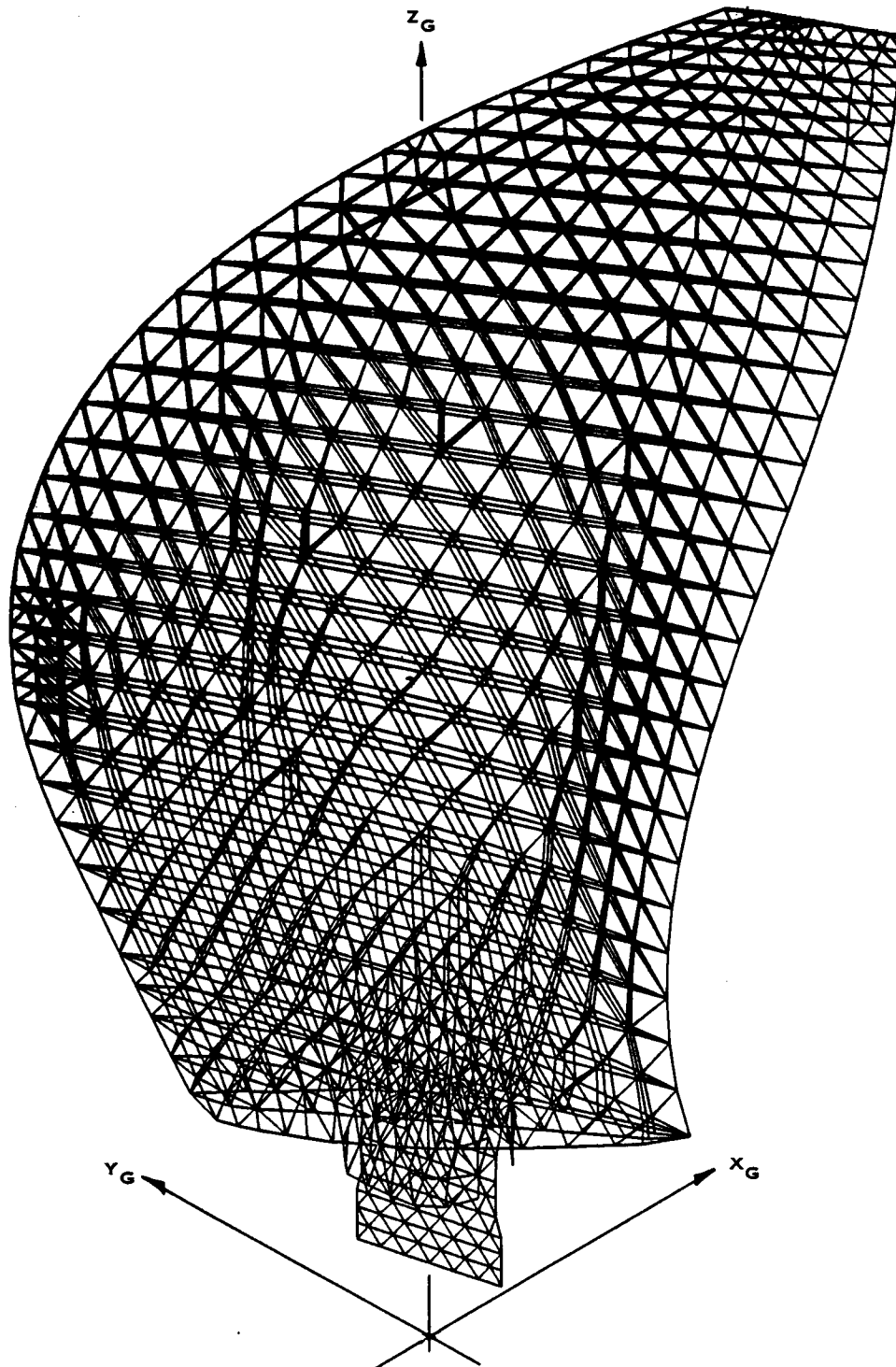


FIGURE 5-6. OFFSET FEA MODEL

Table 5-1

## COMPARISON OF MODEL STATISTICS

<u>Item</u>	<u>Bond Model</u>	<u>Offset Model</u>
Number of Nodes (Net)	1,725	608
Degrees of Freedom	10,350	3,648
Maximum Wavefront	420	138
Number of Elements	4,650	3,350
CPU, 1 Step + K-Diff.	10 Hrs., 30 Min.	33 Min.
CPU, Piecewise Linear	47 Hrs. (Estimated)	2 Hrs., 40 Min.
CPU, Frequencies	PROHIBITIVE	12 Min.

Note: CPU Computer Times are Per Case on an IBM 370 Computer

#### 5.4 Retention Simulation

##### 5.4.1 Retention System Design

The blade will be retained in the hub by a ring of ball bearings, set in through-hardened steel races on the blade shank and integral, hardened races in the hub as illustrated in figure 5-7.

All blade translations and rotations with respect to the hub, shown in figure 5-8, are restrained by this retention system, except the blade shank is free to rotate in the hub about the pitch change axis (which is normal to the plane of the balls) to allow blade pitch change motion.

The pitch control mechanism, which controls blade pitch through the trunnion and roller assembly attached to the blade shank, as shown in figure 5-9, is designed to resist blade rotation about the pitch change axis or to rotate the blade to a new position when required, under all operating conditions.

##### 5.4.2 Hub Design

As seen in figure 5-10, the hub can be thought of as two rings, the forward ring and the aft ring, connected by "bridges". The cylindrical opening between the rings and bridges is called a hub "arm" and contains a blade retention. The two rings are the primary load-carrying members of the hub while the bridges maintain the position of the rings with respect to each other and transfer the blade loads they support to the rings.

Because of this construction, the hub is stiffer with respect to bending loads applied normal to the plane of rotation (out-of-plane), which are transferred directly to the rings, than with loads applied in the plane of rotation (in-plane), which are transferred to the rings through the bridges. Also, the flexibility of the hub and the small kinematic motions



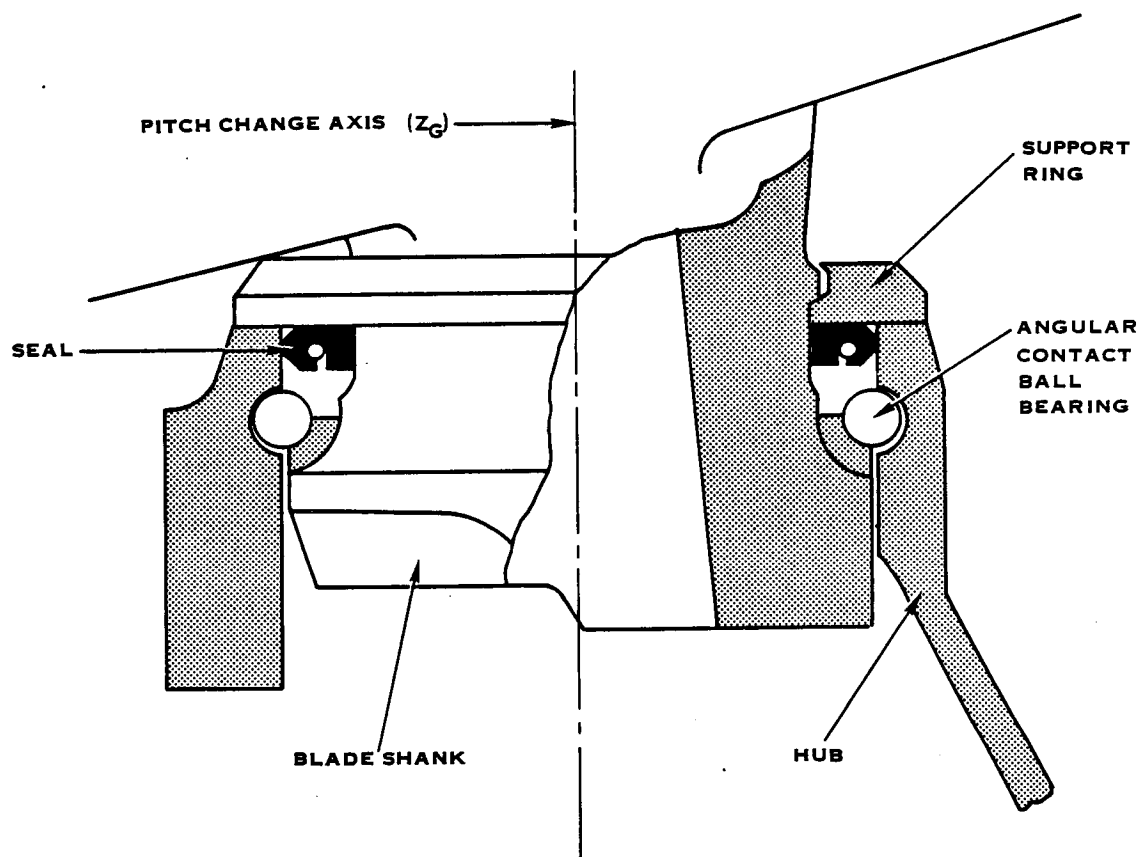


FIGURE 5-7. SR-7L RETENTION

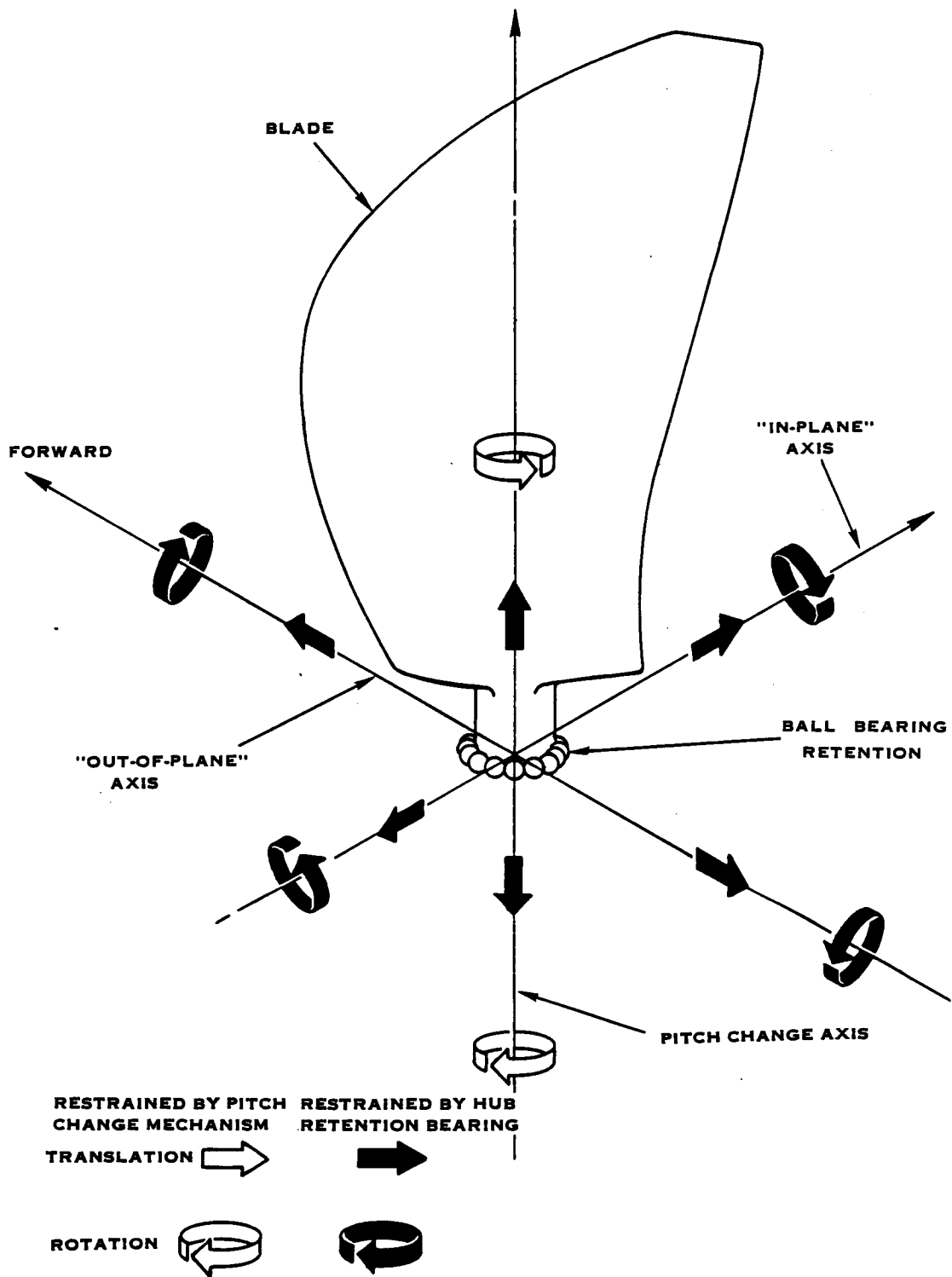


FIGURE 5-8. SR-7L RETENTION RESTRAINTS

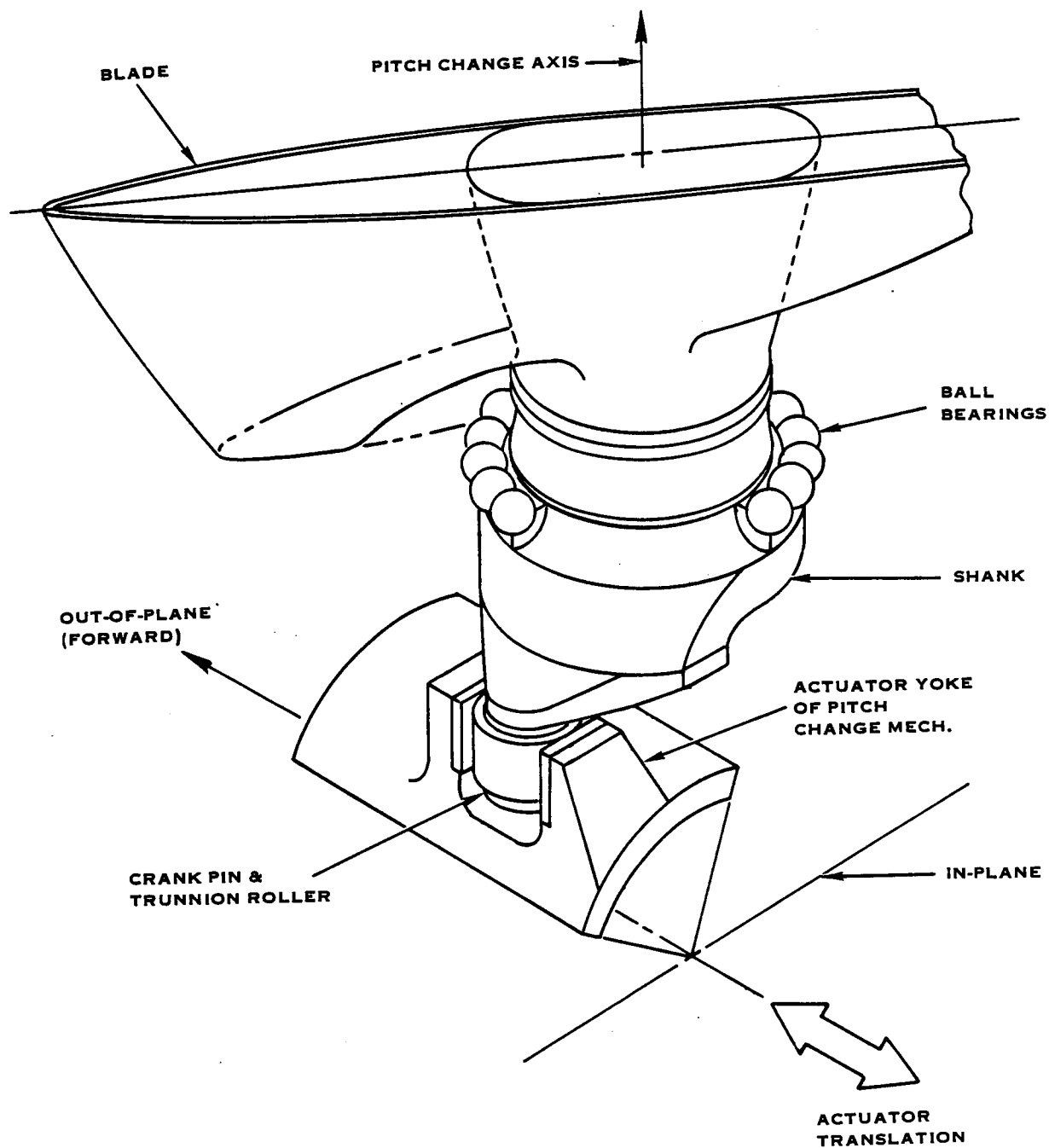


FIGURE 5-9. PITCH CHANGE ACTUATOR & BLADE TRUNNION INTERFACE

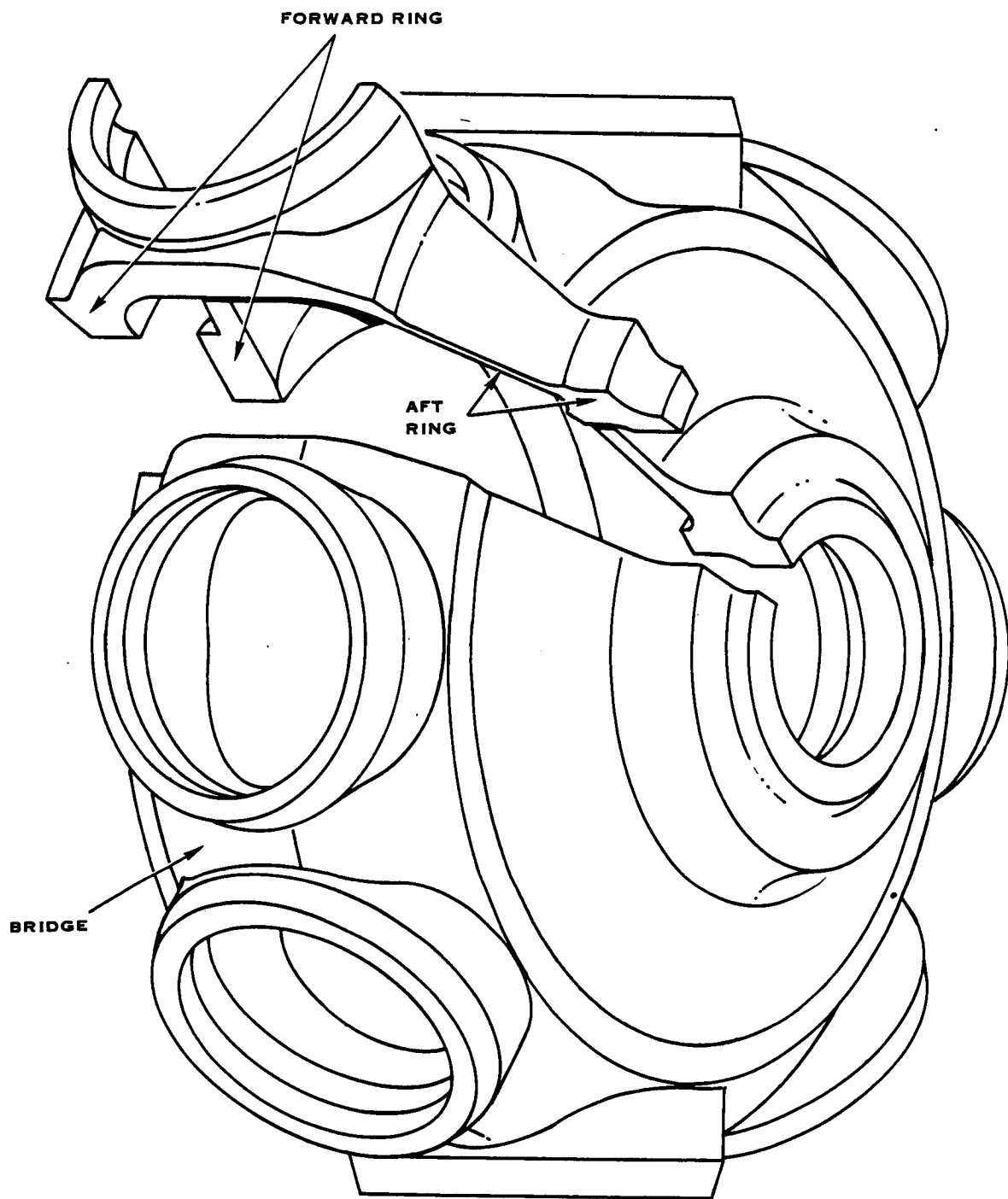


FIGURE 5-10. SR-7L HUB

characteristic of an angular contact ball bearing, particularly with respect to bending moments, cause the blade shank to "pivot" at a point somewhat below the plane of the balls. The design of the hub is covered in reference 6.

#### 5.4.3 Retention Coordinate System

A local coordinate system was defined relative to the Prop-Fan rotation axis to help define the retention system modeling. As seen in figure 5-11, the local Y-axis is parallel to the axis of rotation and also points in the direction of flight, the local Z-axis is colinear with the pitch change axis and points toward the blade tip. The origin of the local retention coordinate system is located below the plane of the bearing at a point corresponding to the base of the blade shank, approximating the "pivot" point, to account for the flexibility of the hub and bearing as described in section 5.4.2 above.

#### 5.4.4 Retention System Model

In order to obtain the compliance simulation necessary for static, modal, and forced response analyses, the blade retention was modeled using a system of spring elements and multi-point constraints. Each spring element was given a spring rate, position, and orientation such that the system of spring elements would reflect the compliance of the actual blade retention. The spring rates to be simulated are listed in table 5-2.

Table 5-2

TABLE OF SPRING RATES TO BE SIMULATED

<u>Type of Load</u> <u>Resisted</u>	<u>Description of Load</u>	<u>Spring Rate to be Simulated</u>
Axial	Total centrifugal pull load	$26.2 \times 10^8$ newtons/meter ( $22.4 \times 10^6$ pounds/inch)
Twisting	About pitch change axis	$22.6 \times 10^6$ newton-meters/radian ( $200 \times 10^6$ inch-pounds/radian)
Bending	About out-of-plane axis	$1.5 \times 10^6$ newton-meters/radian ( $13.4 \times 10^6$ inch-pounds/radian)
Bending	About in-plane axis	$1.15 \times 10^6$ newton-meters/radian ( $10.2 \times 10^6$ inch-pounds/radian)



Translations along the local X and Y-axis are fully restrained at the local coordinate system origin (node 4 of the model), effectively creating a pivot point at the node. An illustration of the remaining restraints is shown in figure 5-12, along with the equivalent spring rates used.

Bending deflections in the plane of rotation and in a plane normal to it are restrained by four axial spring elements working through moment arms defined by multi-point constraints. These constraints are part of the FEA code and can connect nodes at a distance from each other with a rigid link. Springs are attached at each of these distant nodes. The spring rates are selected to reflect the stiffness characteristics of the hub and retention with respect to bending loads.

Translations along the pitch change axis (local Z-axis) are caused by centrifugal pull loads on the blade; these translations are restrained in part by the four parallel axial spring elements described above. However, these spring elements do not reflect the total stiffness of the hub and retention with respect to centrifugal loads and, therefore, another axial spring element was attached to node 4 of the model to complete the required stiffness.

Rotations about the pitch change axis (local Z-axis) would be restrained by the pitch control mechanism in the actual assembly. A torsional spring element was also attached to node 4 of the model to simulate the effect of the pitch change mechanism.

The diagram illustrates a blade shank model, which is a triangular mesh structure. A vertical dashed line represents the "PITCH CHANGE AXIS (COLINEAR WITH GLOBAL Z)". Two axes are defined at the center of the mesh: the "'IN-PLANE' AXIS (NORMAL TO ROTATION VECTOR)" and the "'OUT-OF-PLANE' AXIS (PARALLEL TO ROTATION VECTOR)". A specific node is labeled "NODE 4". Four "TYPICAL RIGID LINK" are shown, each 6.85 CM long, connecting the mesh to external constraints. These links are attached to four fixed points, each with a "MULTI-POINT CONSTRAINT ATTACHED TO NODE 4". The constraints are labeled as follows:
 

- Top-left:  $K_{INP}$  AXIAL  $1.44 \times 10^8$
- Top-right:  $K_{CTR}$  AXIAL  $19.6 \times 10^8$
- Bottom-left:  $K_{CTR}$  TORSION  $22.6 \times 10^8$
- Bottom-right:  $K_{INP}$  AXIAL  $1.44 \times 10^8$

 The links are also labeled with "KOOP AXIAL  $1.87 \times 10^8$ ".

NOTES:

- 1) NODE 4 IS ALSO RESTRAINED FROM TRANSLATING ALONG THE GLOBAL X AND Y AXES
- 2) AXIAL SPRING RATES ARE NEWTONS PER METER; TORSIONAL SPRING RATE IS NEWTONS-METERS PER RADIAN

**FIGURE 5-12. SR-7L FINITE ELEMENT MODEL RESTRAINTS**



## 6.0 Steady-State Analysis

There were four operating conditions to be analyzed to comply with the design requirement. These conditions were: design/cruise, take-off/climb, 25 percent overspeed, and 40 percent overspeed (reference section 3.3.1 table 3-1).

In addition to the four design requirement conditions, ten other operating conditions were analyzed (reference section 3.3.2 table 3-2). These conditions were the three ONERA S1 Wind Tunnel conditions, static and reverse thrust conditions, cruise at low and high rotational speeds, mid-altitude climb, and two dive conditions at mid and high altitude.

### 6.1 Application of Loads

The Prop-Fan blade is affected by two major types of loads: centrifugal and air. Centrifugal loads arise from the blade rotating about the axis of rotation. Airloads arise from the blade moving through the air.

The blade angle setting, or "Beta" angle, is usually specified at a radial location three-fourths of the distance from the axis of rotation to the blade tip and when so specified is the "Beta three-quarters" angle. The airloads can be resolved at the blade retention to a force and moment acting against the direction of rotation, a force and moment acting in the direction of flight, and a moment about the pitch change axis.

#### 6.1.1 Centrifugal Loads

Centrifugal loads arise from the rotation of the Prop-Fan about the axis of rotation, which is not necessarily colinear with the global Y axis as explained in section 5.1. For this reason, direction cosines defining the angle of the axis of rotation with respect to the local X and Y axes were included in the calculation. Centrifugal loads are then developed internally in the analysis about this relative axis.

#### 6.1.2 Airloads

The airloads used in this analysis were the result of aerodynamic calculations (using lifting line theory) based on the flight condition analyzed using standard atmospheric conditions at the altitude required.

A view of the blade model, figure 6-1, shows that the blade is divided into many radial stations. Each station, in turn, is comprised of several grid points. The airloads are applied as discrete loads at the appropriate grid points.

ORIGINAL PAGE IS  
OF POOR QUALITY

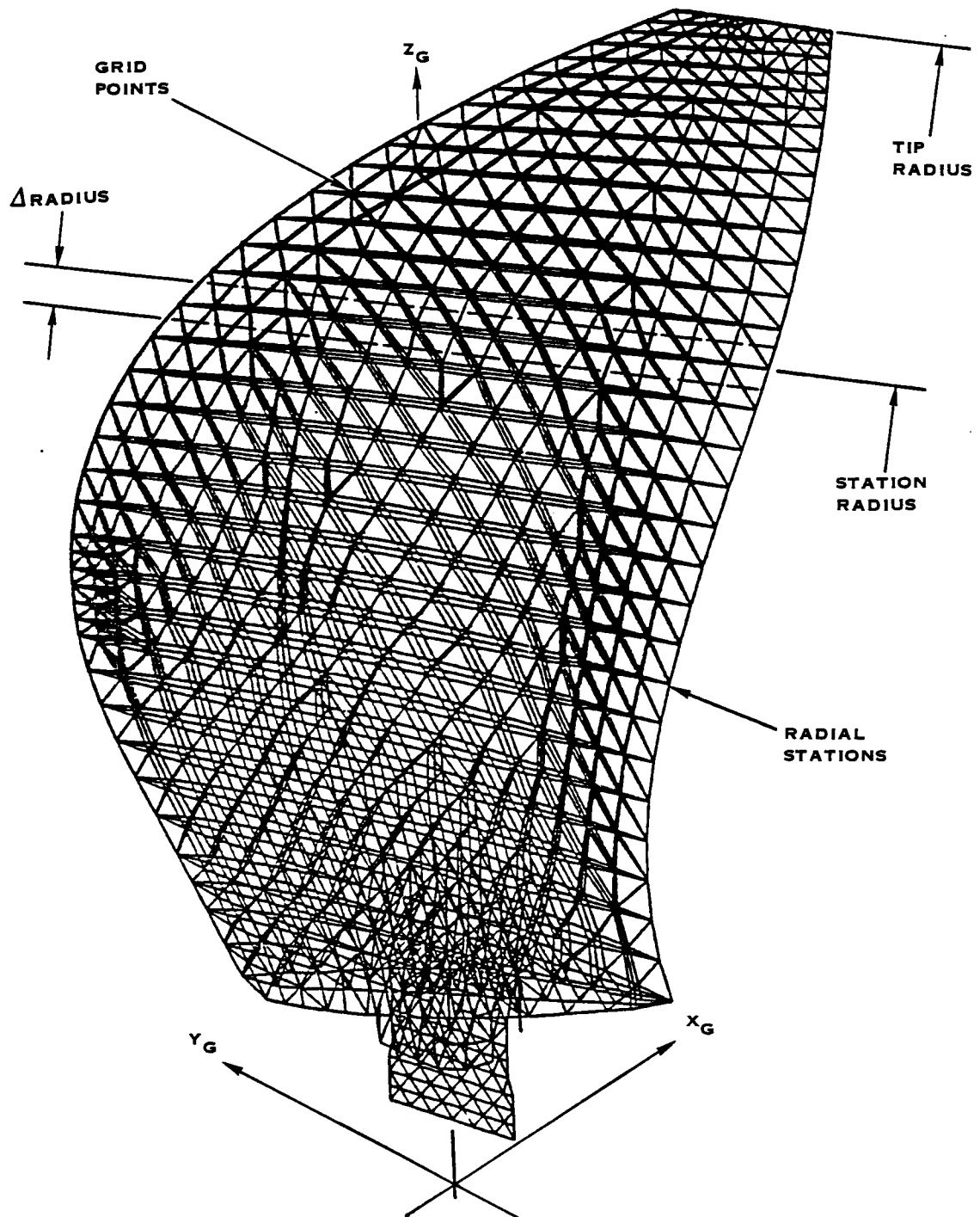


FIGURE 6-1. SR-7L BLADE "OFFSET" FEA MODEL

Airloads are obtained from aerodynamic calculations in the form of in-plane and out-of-plane distributions relative to non-dimensional radial positions. Sample distributions for the steady-state design/cruise and take-off/climb conditions are plotted in figures 6-2 and 6-3. These distributions are integrated at each increment of span to obtain the discrete in-plane and out-of-plane loads at each FEA radial station.

The in-plane and out-of-plane loads at each radial station are then resolved into loads perpendicular to and parallel to the blade chord, representing lift and drag respectively, as shown in figures 6-4 and 6-5.

Assuming a uniform distribution, each drag load (parallel to the blade chord) is divided among the grid points at the appropriate radial station depending on the spacing of the grid points. Figure 6-6 shows that the more removed a grid point is from the others, the greater the share of load it will bear.

The lift loads (perpendicular) loads are distributed somewhat differently than the drag loads. Provisions are made to obtain a chordwise load distribution which preserves the center-of-pressure at each radial station, while maintaining the required blade thrust and torque reactions at the hub for the specific condition. The location of the center-of-pressure varies radially along the blade span as shown in figures 6-7 and 6-8 for the design/cruise and take-off/climb conditions.

The typical center-of-pressure effect is approximated with a "skewed normal" distribution of lift load around the center-of-pressure at each radial station as shown in figure 6-9. This distribution will yield a zero moment about the aerodynamic center of pressure. Also shown is the assignment of the forces among the grid points at the radial station. Again, as was shown in figure 6-6, the more removed a grid point is from its neighbors, the more load it must bear.

Each grid point now has associated with it two forces: one force parallel to the blade chord and the other perpendicular to the chord. Since the finite element analysis requires forces to be defined in the directions of the global coordinate system, the parallel and perpendicular forces at each grid point are resolved into forces acting in the directions of the global coordinate system axes. Once the forces are in terms of the global coordinate system, the aerodynamic loads are ready to be included in the analysis. A computer code is available which accepts the in-plane and out-of-plane airloads and center of pressure locations, as well as the finite element model grid table and resolves/distributes the loads on the grid points according to the blade angle specified. A final check is made to assure that the total loads match the required blade thrust and torque loads for the specified condition.

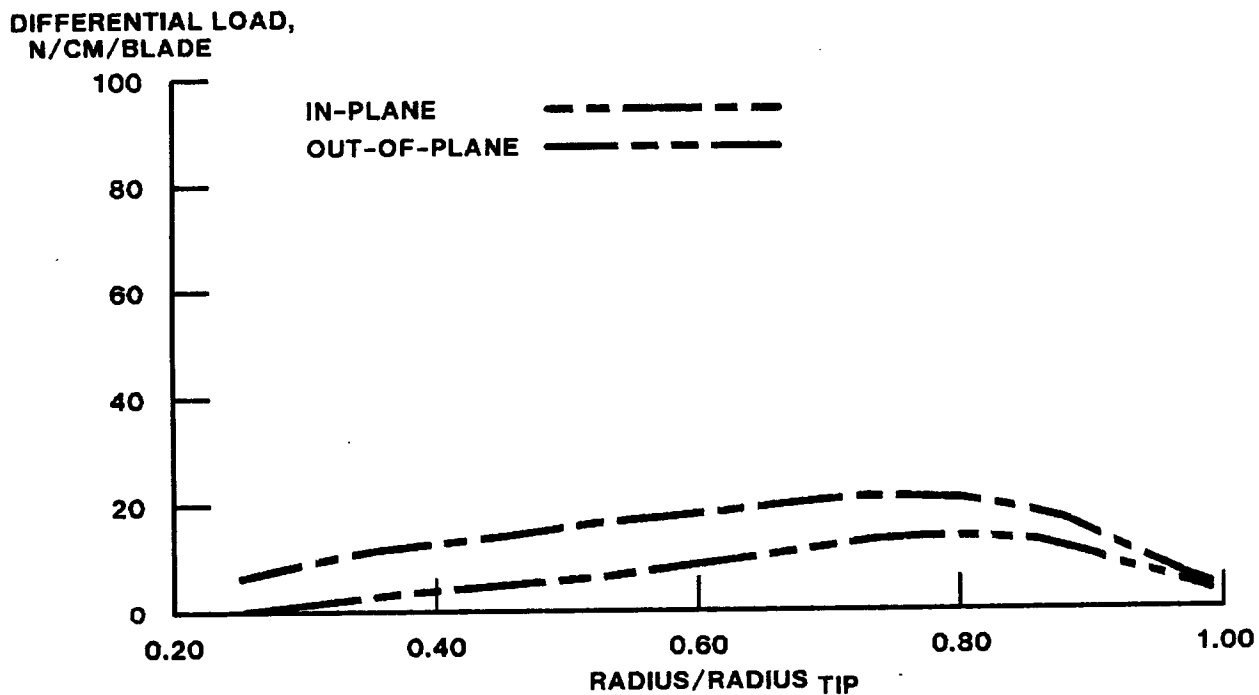


**FIGURE 6-2. AERODYNAMIC LOAD DISTRIBUTION  
DESIGN/CRUISE**

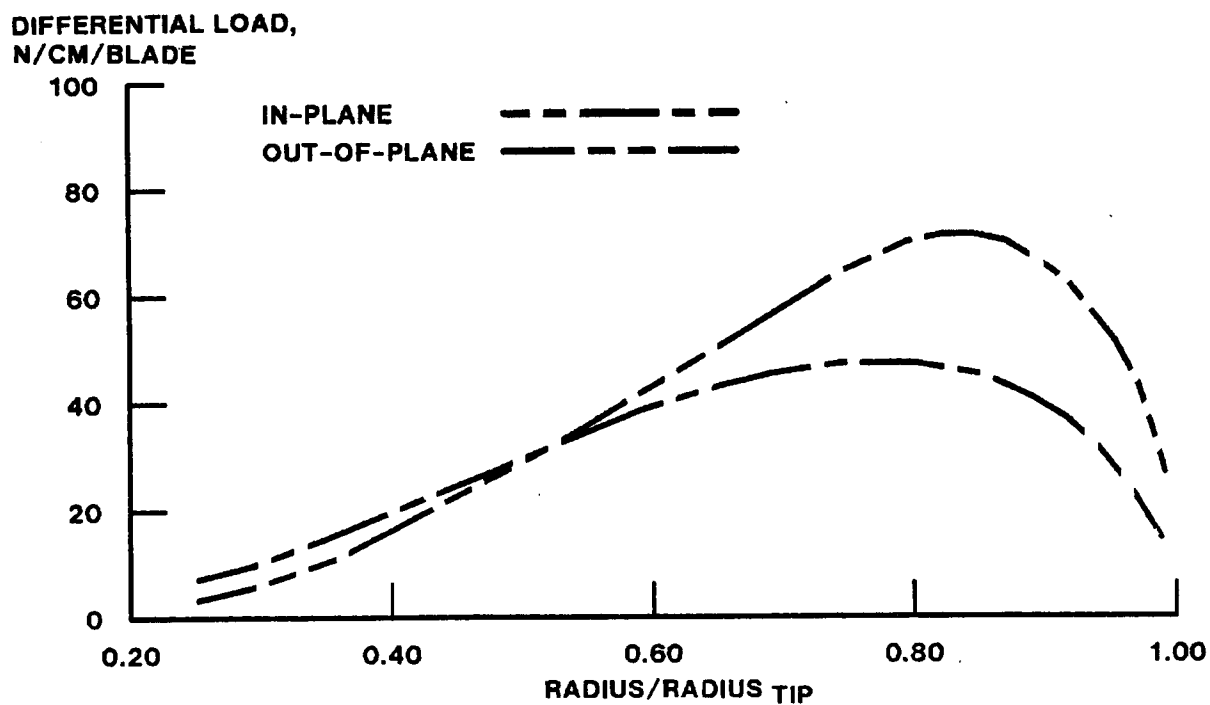


**FIGURE 6-3. AERODYNAMIC LOAD DISTRIBUTION  
TAKE-OFF/CLIMB**

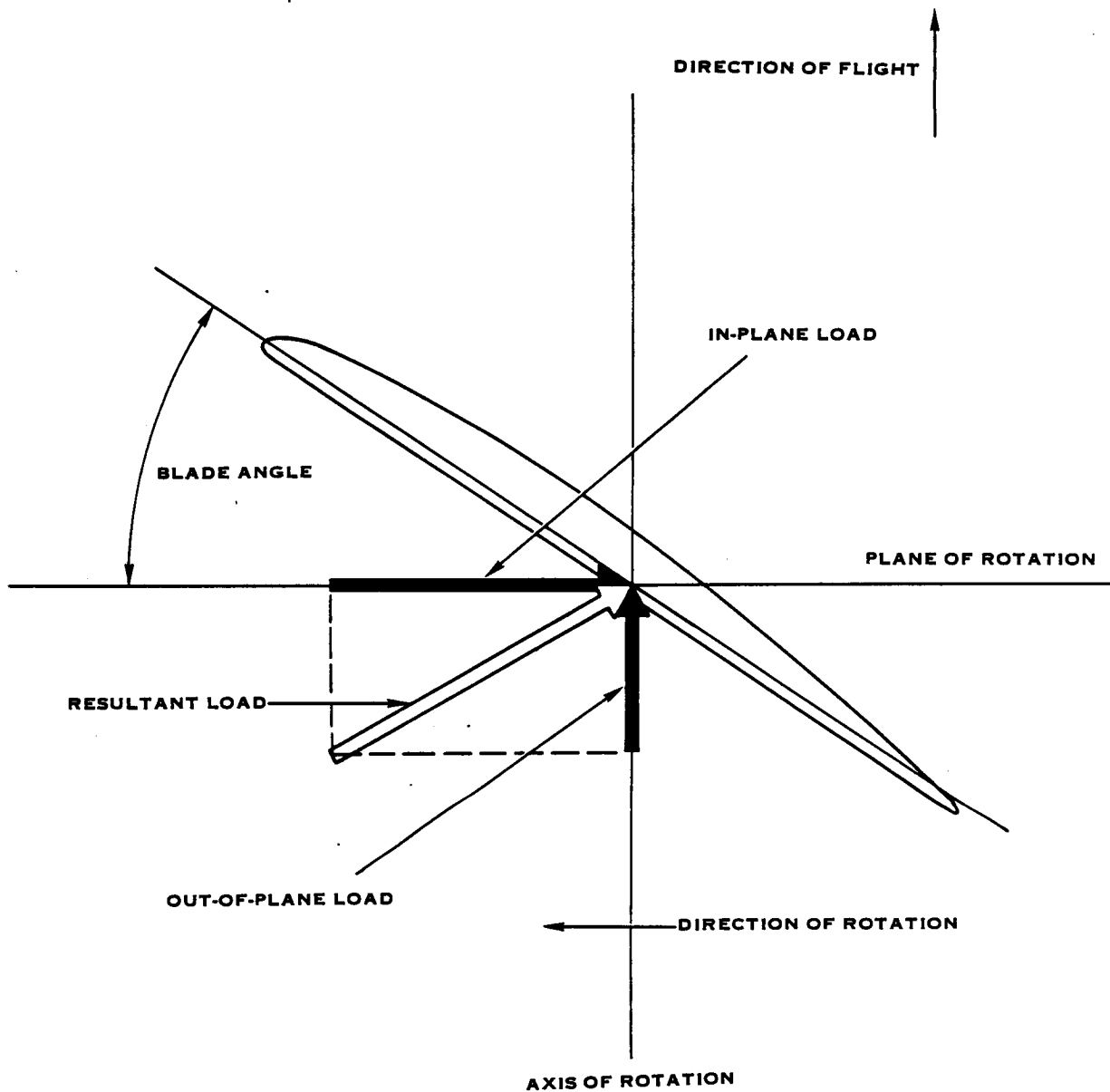


FIGURE 6-4. RESOLUTION OF AIRLOADS AT TYPICAL FEA STATION

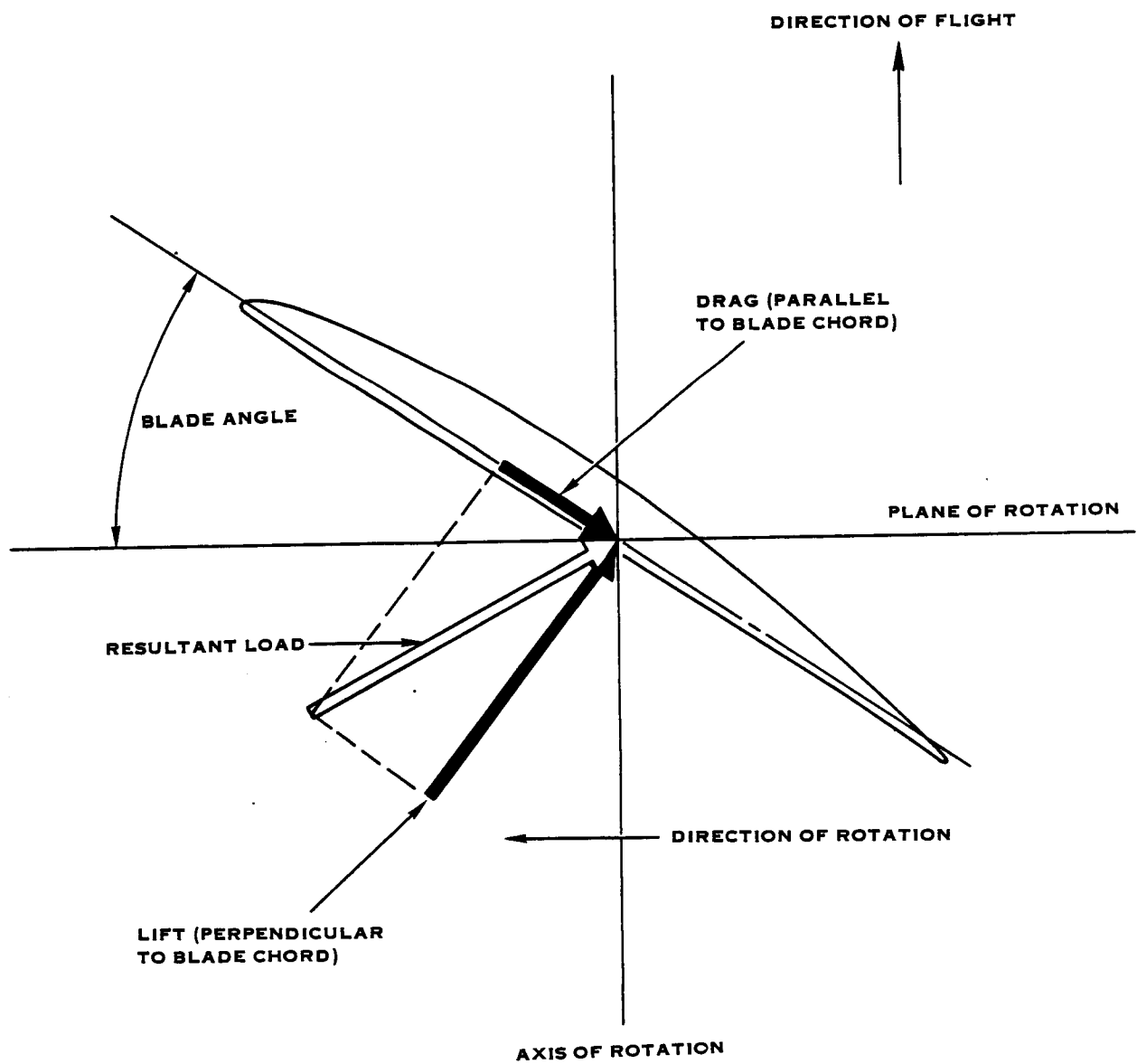


FIGURE 6-5. CONVERSION OF RESULTANT TO LIFT AND DRAG

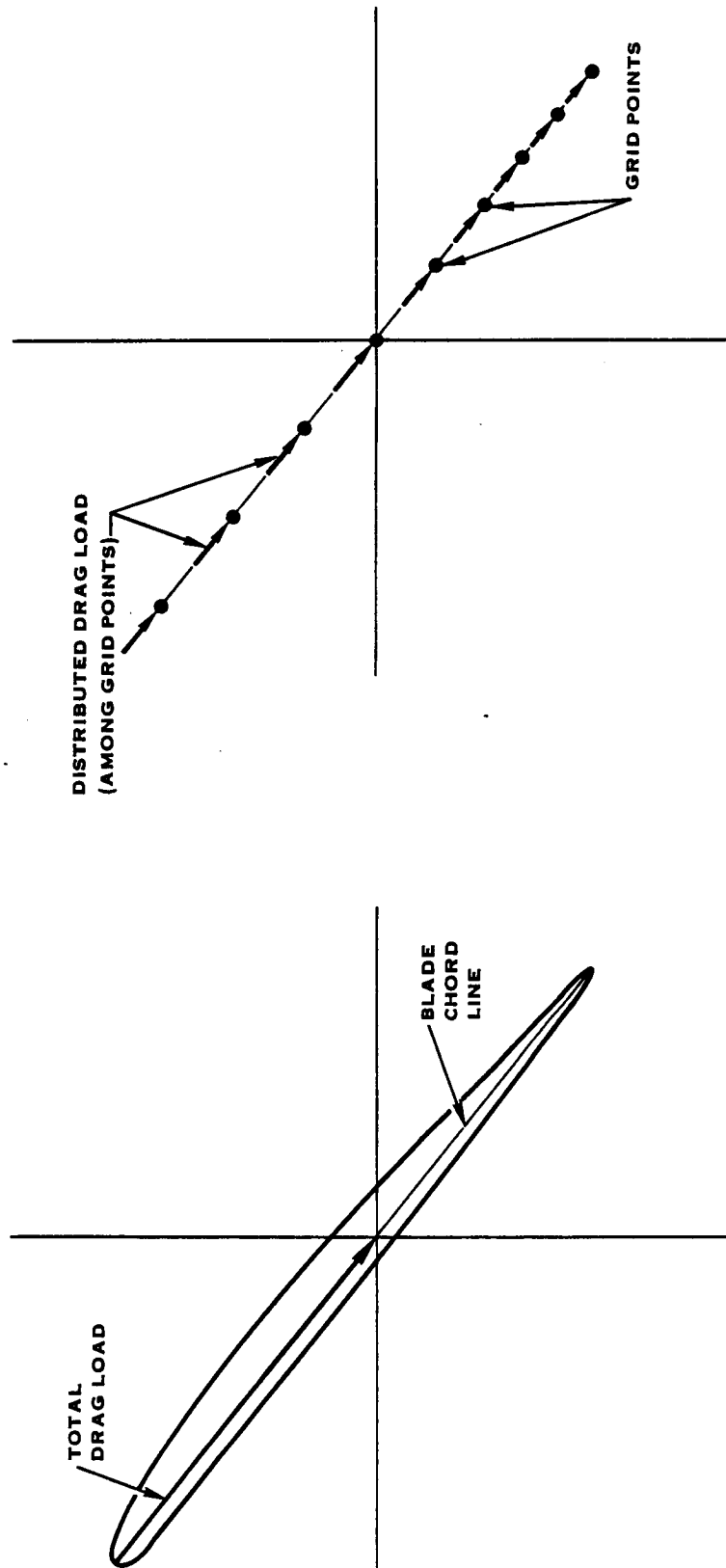


FIGURE 6-6. DISTRIBUTION OF DRAG LOAD AT A TYPICAL FEA STATION

PERCENT BLADE CHORD  
FROM LEADING EDGE

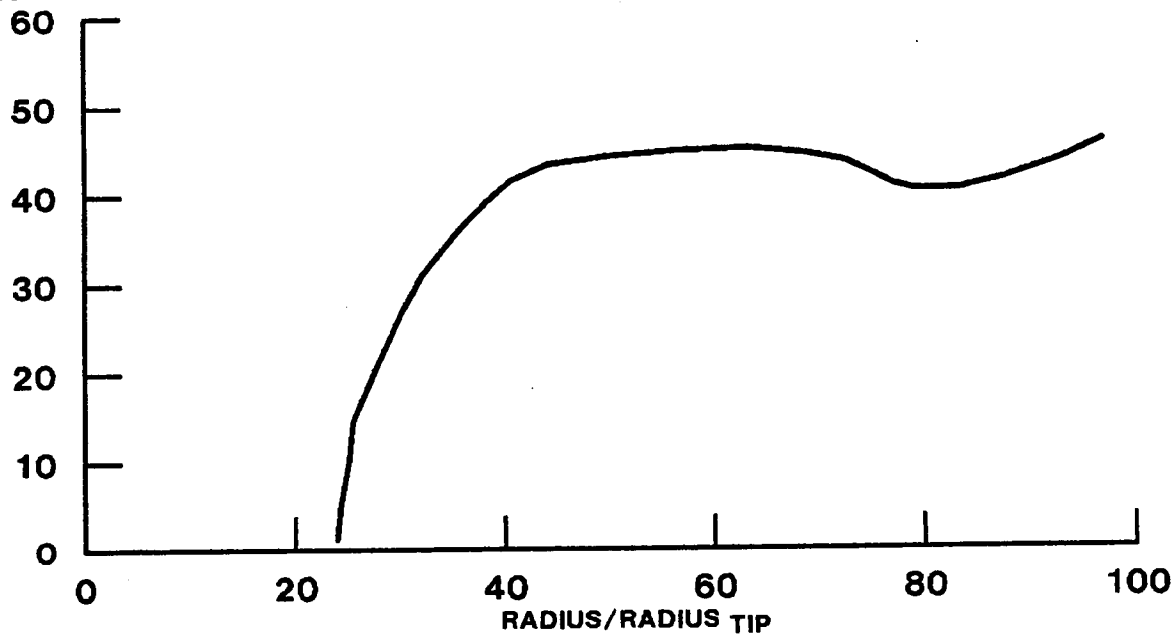


FIGURE 6-7. CENTER OF PRESSURE DISTRIBUTION, DESIGN/CRUISE

PERCENT BLADE CHORD  
FROM LEADING EDGE

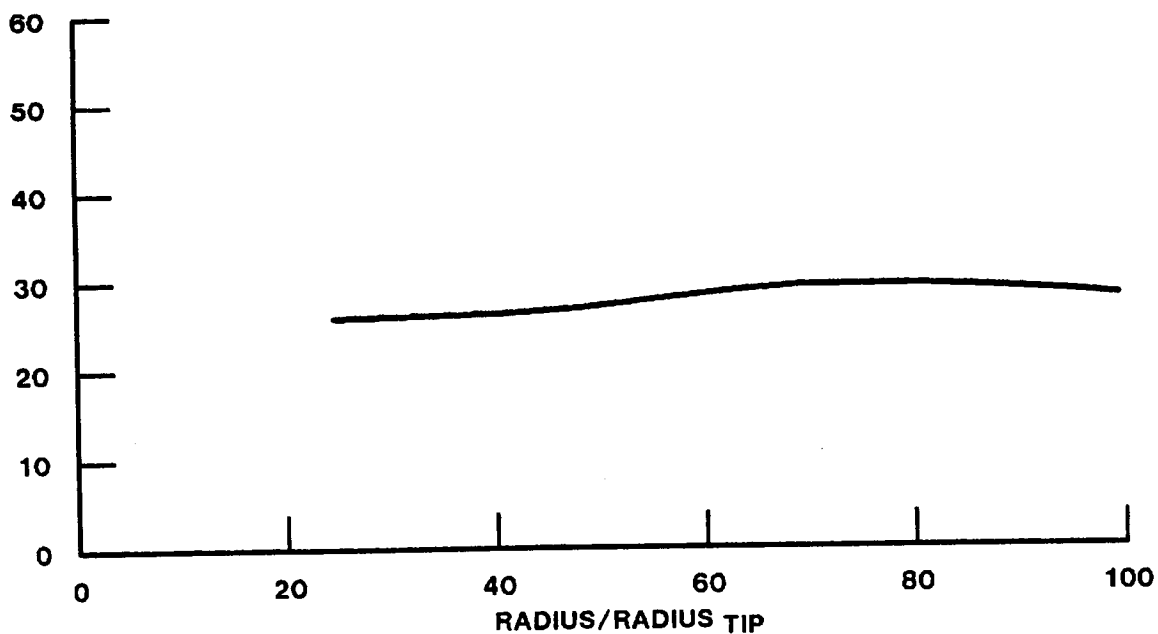


FIGURE 6-8. CENTER OF PRESSURE DISTRIBUTION, TAKE-OFF/CLIMB



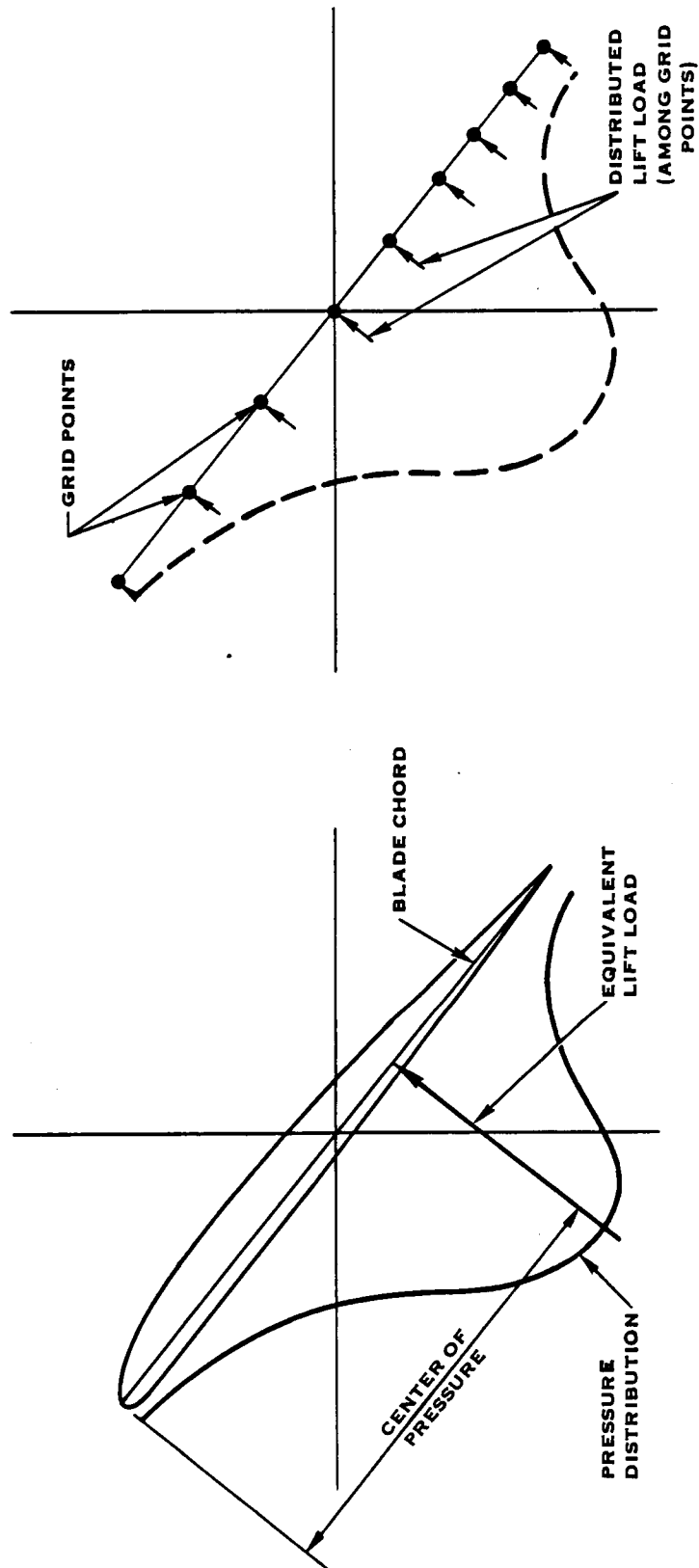


FIGURE 6-9. DISTRIBUTION OF LIFT LOAD AT TYPICAL FEA STATION

## 6.2 Finite Element Solution Techniques

An in-house Finite Element Analysis (FEA) code was used for the steady-state stress analysis of all conditions analyzed. For the pre-deflection or "roughing-in" iterations a one-step analysis was used. For the final design calculations a piecewise linear analysis was used. In order to better account for the effect of in-plane and out-of-plane blade deflections on the application of centrifugal loads, both techniques use differential stiffening.

### 6.2.1 Differential Stiffening

Differential Stiffening is often called a "cross-coupling" effect because element bending stiffness is increased or decreased as the axial or membrane stresses increase or decrease, respectively. Additionally, the in-house FEA code recognized the directionally dependent softening, or "de-stiffening", of element stiffnesses relative to motion in the tangential and radial directions in a centrifugal force field. These latter effects are included and stored as a part of the differential stiffening matrix, and are used to increase the accuracy of the calculations.

### 6.2.2 One-Step Plus Differential Stiffening

The one-step plus differential stiffening analysis is actually a two step calculation. First, the blade is analyzed by the in-house FEA code to obtain the differential stiffening matrix described above. Next, the blade is analyzed by the same code; however, this time the differential stiffening matrix calculated in the first step is included to increase the accuracy of the analysis of the second step. This analysis was used in the preliminary pre-deflection iterations in the blade design.

### 6.2.3 Piecewise Linear Analysis

To better account for the non-linear response of the blade to applied air-loads and centrifugal loads, a Piecewise Linear Analysis (PWLA) technique was used to predict the response of the blade. For most stiff or lightly-loaded structures, the deflections under load are negligible and the shape is essentially unchanged due to the applied loads. As a result, the structural response to the loads is assumed to be linear. However, for the thin and highly-loaded Prop-Fan blade, the deflections under load are sufficient to change the blade shape and position which, in turn, alters the centrifugal forces on deflected blade elements and also alters the assembled elemental stiffness matrix. As a result, the response of the blade to the loads is non-linear.

The PWLA technique applies the loads incrementally. Each incremental load is small enough that the blade response to each increment is essentially linear. Also, the centrifugal loads are updated with each step to account for the change in blade shape and position at each step, and a new differential stiffening matrix is calculated.

As the calculation progresses through the incremental load steps, the loads and deflections of each increment are summed. Figure 6-10 shows a typical plot of cumulative deflections obtained from a piecewise linear analysis of a Prop-Fan blade.

The greater accuracy of the PWLA over that of the one-step plus differential stiffening comes at a much greater cost because the entire FEA model must be solved at each step. In order to take full advantage of the accuracy of the PWLA, as many as ten solution steps may be necessary whereas for the one-step, only two solutions are required.

For the initial step of the PWLA process, the unloaded position of the blade model is used. The blade is analyzed using only a small percentage of the total air and centrifugal loads. The differential stiffening matrix of this load step is calculated as a function of membrane stress.

The unloaded position of the blade is analyzed again for stresses and deflections using the first incremental load. However, this time the differential stiffening calculated in the first analysis is included. The incremental stresses and deflections of this calculation are saved; also saved is an updated differential stiffening matrix.

For the next and all subsequent solution steps a new blade shape is calculated by adding the summed deflections of the previous solution steps to the original blade shape. The differential stiffening for each new step is extrapolated linearly from the stiffening change between the last two steps. Linear extrapolation is a reasonable approach because the step size is small and differential stiffening has only a secondary effect on the solution. Figure 6-11 is a typical plot of differential stiffening versus the incremental load steps, including an example of linear extrapolation.

The new blade shape is analyzed for stresses and deflections using the finite element code along with the new incremental load and the extrapolated differential stiffening. The incremental stresses and deflections are added to those of the previous load steps. The new differential stiffening is calculated and saved to be used in the next extrapolation. This incremental load step calculation procedure is repeated until the total blade loads have been applied.

**PERCENT TIP DEFLECTION**

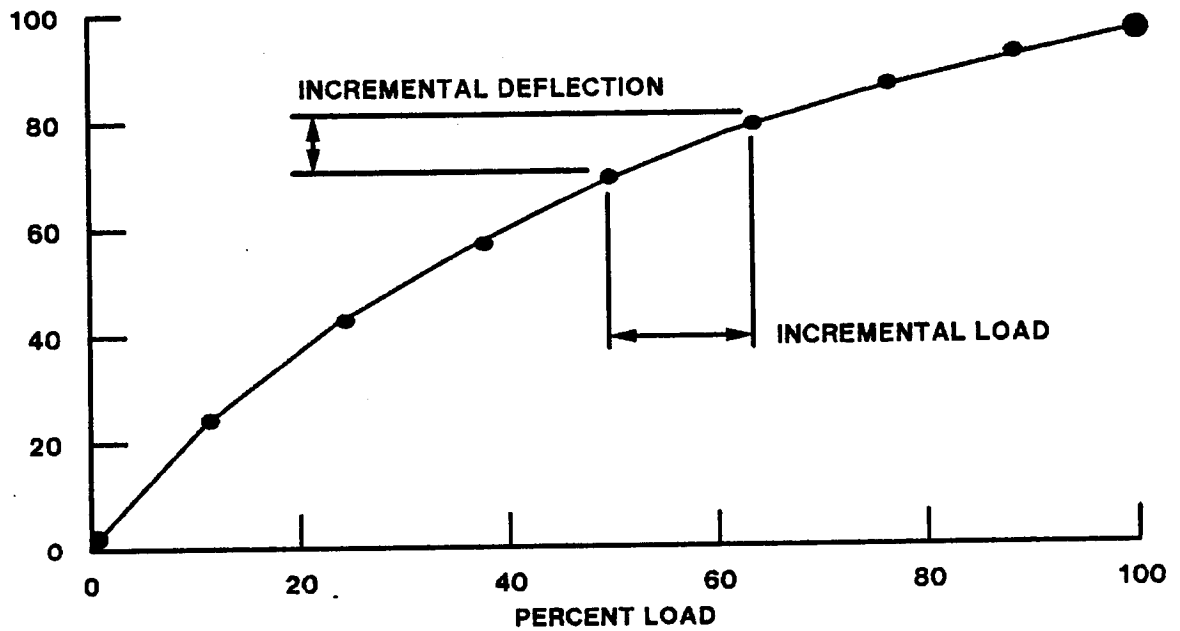


**FIGURE 6-10. TYPICAL CUMULATIVE DEFLECTION  
PIECEWISE LINEAR ANALYSIS**

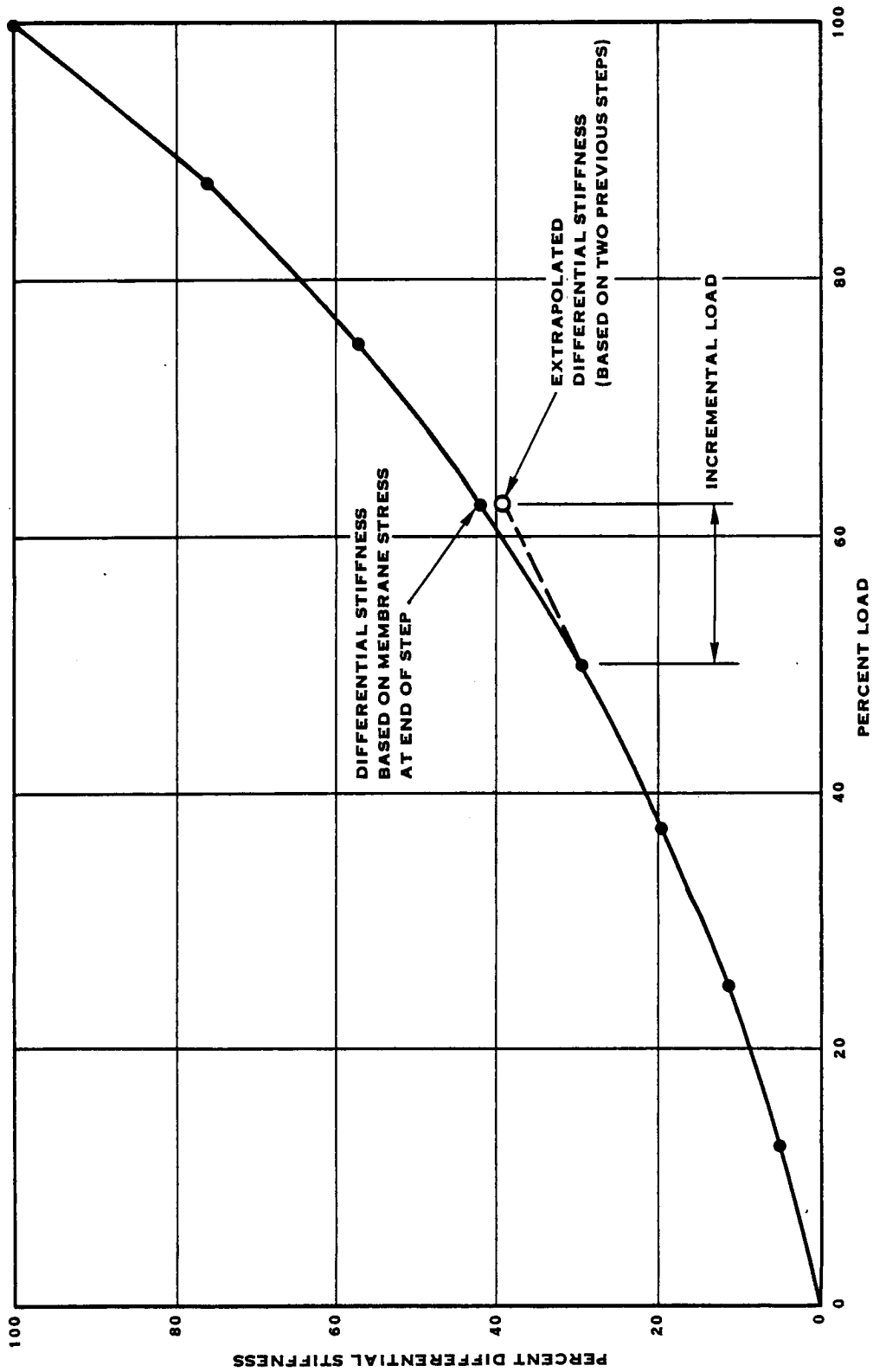


FIGURE 6-11. PIECEWISE LINEAR ANALYSIS  
TYPICAL DIFFERENTIAL STIFFNESS VS. LOAD

### 6.3 Pre-Deflection Iterations

The deflection and twist changes in a blade due to aerodynamic and centrifugal loads can affect both the aerodynamic and mechanical characteristics of the blade. In a wide, thin, swept blade, such as the SR-7L blade, three-dimensional distortions can be significant. To maintain aerodynamic efficiency, these distortions must be accommodated when defining the static, unloaded shape to which the blade will be manufactured. Determining this static shape is called "pre-deflecting" the blade. Unfortunately, the deflections of only one operating condition can be closely matched. For the SR-7L, the condition selected is design/cruise. Once the static shape is established, it is used as the basis for determining deflections at all other operating conditions. It is important to establish the steady-state deflected shape of the blade for each condition because it affects not only the aerodynamics but also the dynamic response of the blade, the frequencies, mode shapes, and stability. The process of establishing the static shape of the SR-7L blade was an iterative one which is described below.

#### 6.3.1 First Iteration

The desired aerodynamic and mechanical configuration was defined at the design/cruise condition. For initial "roughing-in" iterations a series of one-step plus differential stiffening analyses were used.

A finite element model of the desired configuration at the design/cruise condition was first constructed and a preliminary analysis conducted to determine differential stiffening effects due to aerodynamic and centrifugal loads. The differential stiffening was then included in a second analysis to obtain a good estimate of deflection from the desired position. The global deflections of all grid points were then subtracted from their desired design position to obtain a predeflected finite element model. This, then, was the first estimate of the unloaded, or static, blade position.

If the function of blade deflection versus applied loads were linear, then the blade would deflect from the first estimated unloaded position to the desired design position with the application of the original design loads. However, it is not linear because centrifugal loads change with blade deflection.

A repetition of the calculation procedure, using differential stiffening from the first estimated static position, resulted in a significant difference between the desired design position and the newly deflected position. Thus, further iterations were required to obtain the proper unloaded position.

### 6.3.2 Additional Iterations

For each iteration, a new static position was defined by subtracting the latest global deflection of each grid point from the desired design position. The result was a new predeflected configuration which became the new unloaded blade model. This process continued until the deflected, loaded configuration closely matched the original desired configuration. A check of the resulting "error" (deflected vs desired) was made each time with a resolved deflection contour plot. Seven iterations were performed to obtain a proper predeflected, unloaded shape with a maximum deflection error at the leading edge of the blade tip of .023 centimeter (.009 inch). Therefore, this shape was called static position seven. The "error" contour plot from position seven is illustrated in figure 6-12.

### 6.3.3 Final Check of Predeflected Configuration

A piecewise linear finite element analysis (PWLA), that is, an analysis that loads the blade in incremental steps as described in section 6.2.3, was performed starting from static position seven. Because of the much greater solution time required for the PWLA technique, the PWLA was not used for the first seven "roughing-in" iterations described above.

The translations and rotations calculated using the PWLA differed somewhat in some locations from those calculated with the one-step analysis, both starting from the static position seven blade shape. The maximum deflection error became .259 centimeter (.102 inch) at the trailing edge near the blade tip as shown in figure 6-13. A second PWLA iteration was performed to determine if these discrepancies could be reduced.

As in the earlier iterations, the new deflections were subtracted from the desired design configuration to create a new unloaded blade shape, and the second PWLA was performed. The .259 centimeter (.102 inch) discrepancy between the calculated deflected shape and the design deflected shape was reduced. However, as shown in figure 6-14, a new maximum deflection error of .422 centimeter (.166 inch) at the leading edge of the blade near the tip was found.

Before continuing with lengthy, costly PWLA iterations, the impact on aerodynamic performance of the moderate discrepancies between the position seven PWLA deflected blade and the original design blade was evaluated. The evaluation showed no detectable difference in aerodynamic performance due to the discrepancies; therefore, the static position seven blade was used as the SR-7L static blade model.

## 6.4 Final Calculations

Fourteen conditions were analyzed for steady-state reactions, deflections, and stresses. The reactions are summarized as blade shank loads in section 6.4.2, and the deflections are reported in section 6.4.3. The stresses are

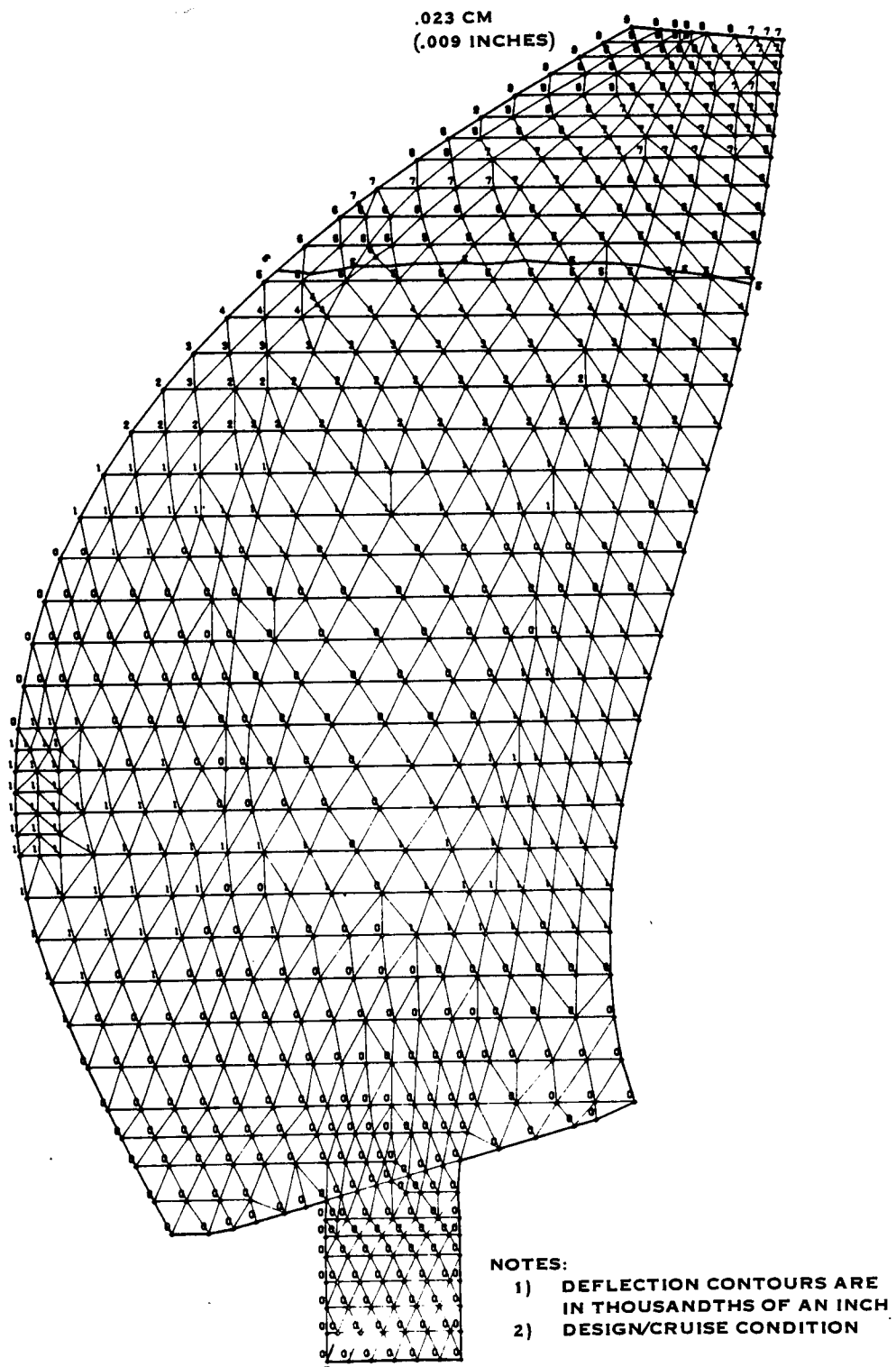


FIGURE 6-12. DEFLECTION ERROR RELATIVE TO DESIRED DESIGN CONFIGURATION  
SINGLE STEP PROCEDURE FROM 7TH POSITION



ORIGINAL PAGE IS  
OF POOR QUALITY

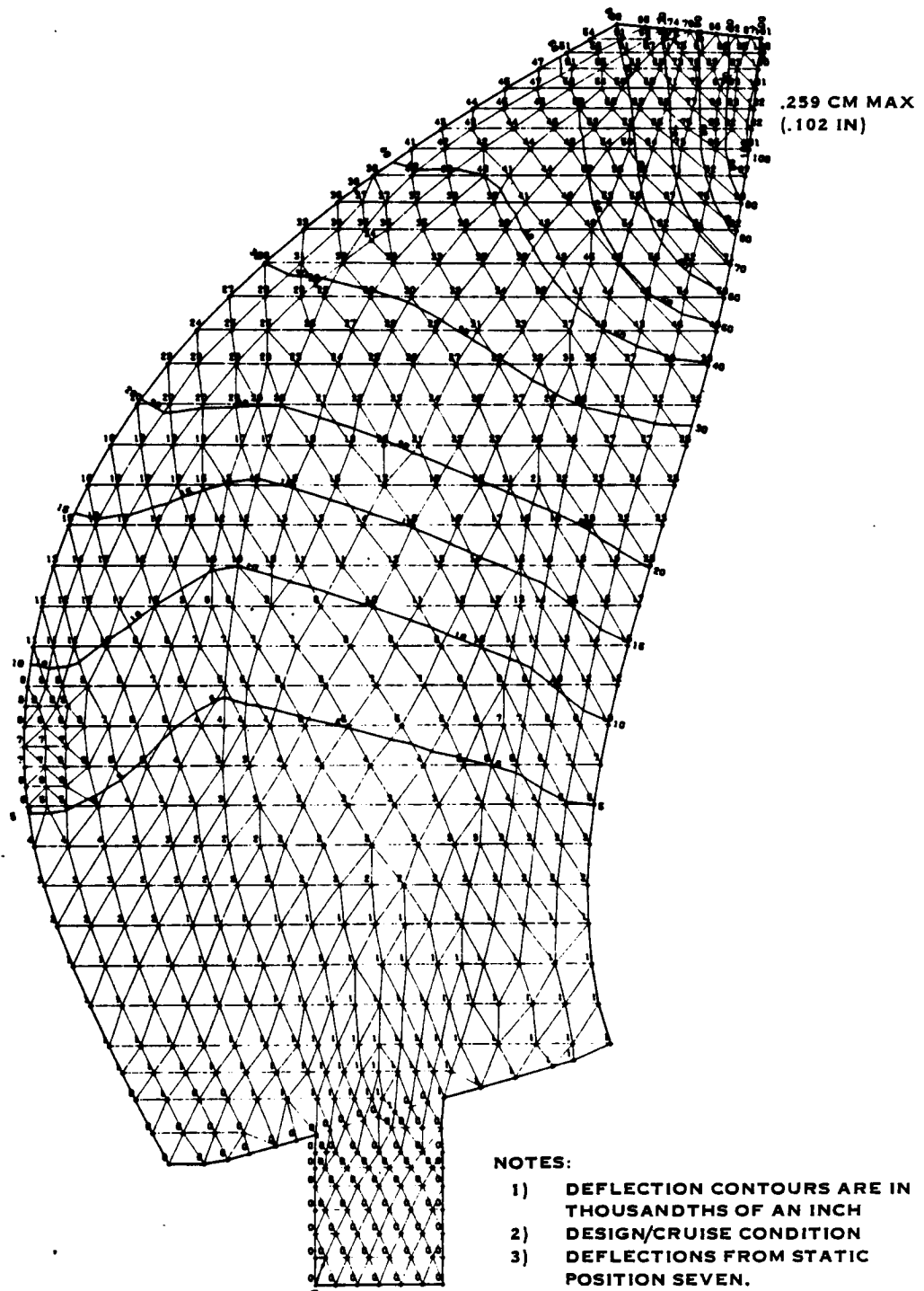


FIGURE 6-13. DEFLECTION ERROR, FIRST PWLA RESULTS, RELATIVE TO DESIRED DESIGN CONFIGURATION

ORIGINAL PAGE IS  
OF POOR QUALITY

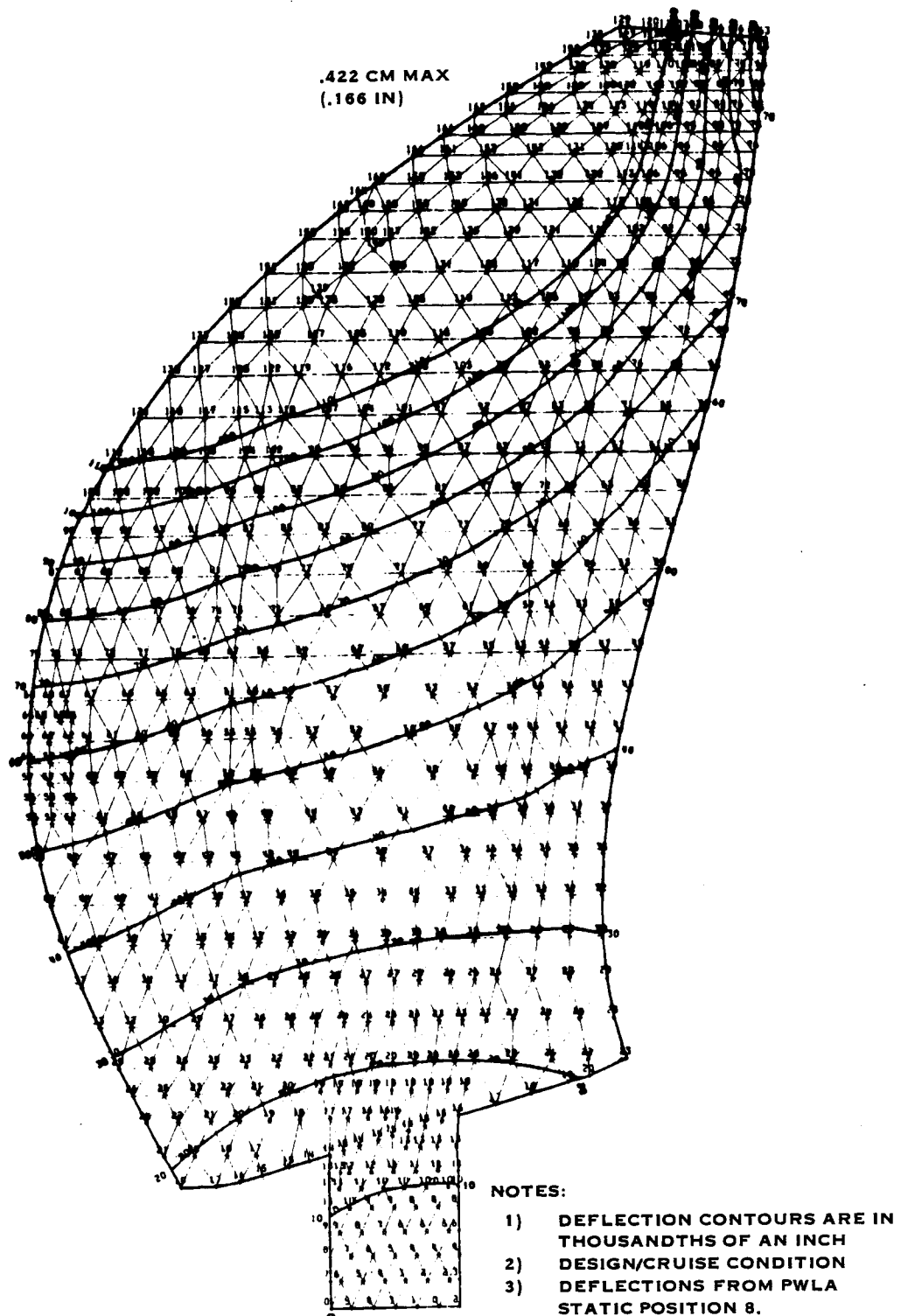


FIGURE 6-14. DEFLECTION ERROR, SECOND PWLA RESULTS, RELATIVE TO DESIRED DESIGN CONFIGURATION.

combined with the vibratory stresses discussed in section 7 (Vibratory Response Analysis) for comparison to design allowables, and are not tabulated in this section.

#### 6.4.1 Conditions Analyzed

Table 6-1 lists the steady-state conditions analyzed along with the analysis technique used.

#### 6.4.2 Blade Shank Loads

The blade shank loads, as calculated using the offset model with the calculation technique listed in table 6-1, are summarized in table 6-2.

#### 6.4.3 Deflections

Translation and rotation contours are plotted in figures 6-16 and 6-17 for the design/cruise condition, and in figures 6-18 and 6-19 for the take-off/-climb condition. Note that all translations have been resolved normal to the chord at the three-quarter radius station.

A summary of the calculated blade deflections using the offset model and the calculation technique listed in table 6-1 is shown in table 6-3.

Table 6-1

#### LIST OF CONDITIONS ANALYZED

<u>No.</u>	<u>Condition</u>	<u>Analysis</u>
Primary required design conditions:		
D1	Design/Cruise	Piecewise Linear
D2	Take-Off/Climb	Piecewise Linear
D3	25% Overspeed	One-Step Plus Differential Stiffening
D4	40% Overspeed	One-Step Plus Differential Stiffening
Additional secondary conditions:		
1A	ONERA, 8 Blade	One-Step Plus Differential Stiffening
1B	ONERA, 4 Blade	One-Step Plus Differential Stiffening
1C	ONERA, 2 Blade	Piecewise Linear
2	Static Thrust	One-Step Plus Differential Stiffening
3	Reverse Thrust	One-Step Plus Differential Stiffening
4	Cruise, Low RPM	One-Step Plus Differential Stiffening
5	Cruise, Hi RPM	One-Step Plus Differential Stiffening
6	Climb, Mid Altitude	One-Step Plus Differential Stiffening
7	Dive, Mid Altitude	One-Step Plus Differential Stiffening
8	Dive, High Altitude	One-Step Plus Differential Stiffening

Table 6-2

## BLADE SHANK STEADY-STATE LOAD SUMMARY

(See Figure 6-15 For Directions of Positive Forces and Moments)

No.	Condition	Centrifugal, newtons (pounds)	CTM Plus ATM*	Shear, newtons Out-Of-Plane	(pounds) In-Plane
D1	Design/Cruise	353,000 (79,400)	2,000 (17,700)	792 (178)	8,340 (1,875)
D2	Take-Off/Climb	353,000 (79,400)	2,169 (19,200)	4,137 (930)	8,629 (1,940)
D3	25% Overspeed	556,000 (125,000)	3,186 (28,200)	0 (0)	8,807 (1,980)
D4	40% Overspeed	694,000 (156,000)	4,011 (35,500)	0 (0)	10,408 (2,340)
1A	ONERA, 8 Blade	353,000 (79,400)	2,282 (20,200)	178 (40)	6,983 (1,570)
1B	ONERA, 4 Blade	353,000 (79,400)	2,180 (19,300)	534 (120)	7,962 (1,790)
1C	ONERA, 2 Blade	353,000 (79,400)	1,977 (17,500)	1,334 (300)	10,008 (2,250)
2	Static Thrust	353,000 (79,400)	2,203 (19,500)	4,937 (1,110)	7,873 (1,770)
3	Reverse Thrust	359,000 (80,600)	-102 (-900)	-427 (-96)	2,980 (670)
4	Cruise, Low RPM	201,000 (45,200)	881 (7,800)	592 (133)	6,316 (1,420)
5	Cruise, Hi RPM	390,000 (87,600)	2,226 (19,700)	876 (197)	9,207 (2,070)
6	Climb, Mid Altitude	353,000 (79,400)	2,327 (20,600)	2,384 (536)	9,652 (2,170)
7	Dive, Mid Altitude	355,000 (79,800)	2,610 (23,100)	-80 (-18)	4,759 (1,070)
8	Dive, High Altitude	354,000 (79,500)	2,395 (21,200)	-93 (-21)	5,604 (1,260)

\* Centrifugal plus Aerodynamic Twisting Moments, newton-meters (inch-pounds)

Table 6-2 (Continued)

<u>No.</u>	<u>Condition</u>	<u>Total Bending Moment, newton-meters (inch-pounds)</u>	<u>Angle,* degrees*</u>
D1	Design/Cruise	1,141 (10,100)	285.8
D2	Take-Off/Climb	1,932 (17,100)	224.3
D3	25% Overspeed	2,497 (22,100)	308.0
D4	40% Overspeed	2,937 (26,000)	307.9
1A	ONERA, 8 Blade	1,909 (16,900)	294.6
1B	ONERA, 4 Blade	1,604 (14,200)	285.7
1C	ONERA, 2 Blade	1,107 (9,800)	251.3
2	Static Thrust	2,034 (18,000)	220.9
3	Reverse Thrust	5,027 (44,500)	261.6
4	Cruise, Low RPM	169 (1,500)	206.0
5	Cruise, Hi RPM	1,243 (11,000)	282.3
6 (12,500)	Climb, Mid Altitude	1,412	233.0
7	Dive, Mid Altitude	3,028 (26,800)	287.9
8	Dive, High Altitude	2,485 (22,000)	296.2

\* Angle, Beta, measured from plane of rotation (see figure 6-15)

Table 6-3

No. M	Condition	BLADE DEFLECTION SUMMARY			
		Rotations*, Degrees		Translations**, Cm. (in.)	
		Mid Tip	T.E. 3/4 r/R	Mid Tip	L.E. 3/4 r/R
D1	Design/ Cruise	3.0	-1.0	-0.81 (-0.32)	1.45 (0.57)
D2	Take-Off/ Climb	2.2	-1.1	-2.01 (-0.79)	0.71 (0.28)
D3	25% Over- speed	4.4	-0.9	-0.36 (-0.14)	2.34 (0.92)
D4	40% Over- speed	5.1	-0.8	-0.48 (-0.19)	2.67 (1.05)
1A	ONERA, 8 Blade	4.2	-0.5	-0.38 (-0.15)	1.83 (0.72)
1B	ONERA, 4 Blade	4.2	-0.5	-0.56 (-0.22)	1.68 (0.66)
1C	ONERA, 2 Blade	3.5	-0.9	-1.04 (-0.41)	1.30 (0.51)
2	Static Thrust	1.9	-1.0	-1.96 (0.77)	0.69 (0.27)
3	Reverse Thrust	-0.4	-3.4	.5.31 (2.09)	3.61 (1.42)
4	Cruise, Low RPM	2.0	-1.1	-0.97 (-0.38)	0.71 (0.28)
5	Cruise, Hi RPM	3.5	-0.7	-0.97 (-0.38)	1.47 (0.58)
6	Climb, Mid Altitude	3.1	-0.9	-2.31 (-0.91)	0.91 (0.36)
7	Dive, Mid Altitude	3.9	-0.4	-0.13 (-0.05)	2.01 (0.79)
8	Dive, High Altitude	4.0	-0.5	-0.23 (-0.09)	1.93 (0.76)

\* Positive (global) rotations are in a direction which decreases blade angle setting

\*\* Translations are perpendicular to chord @ 3/4 radius station(3/4 r/R)

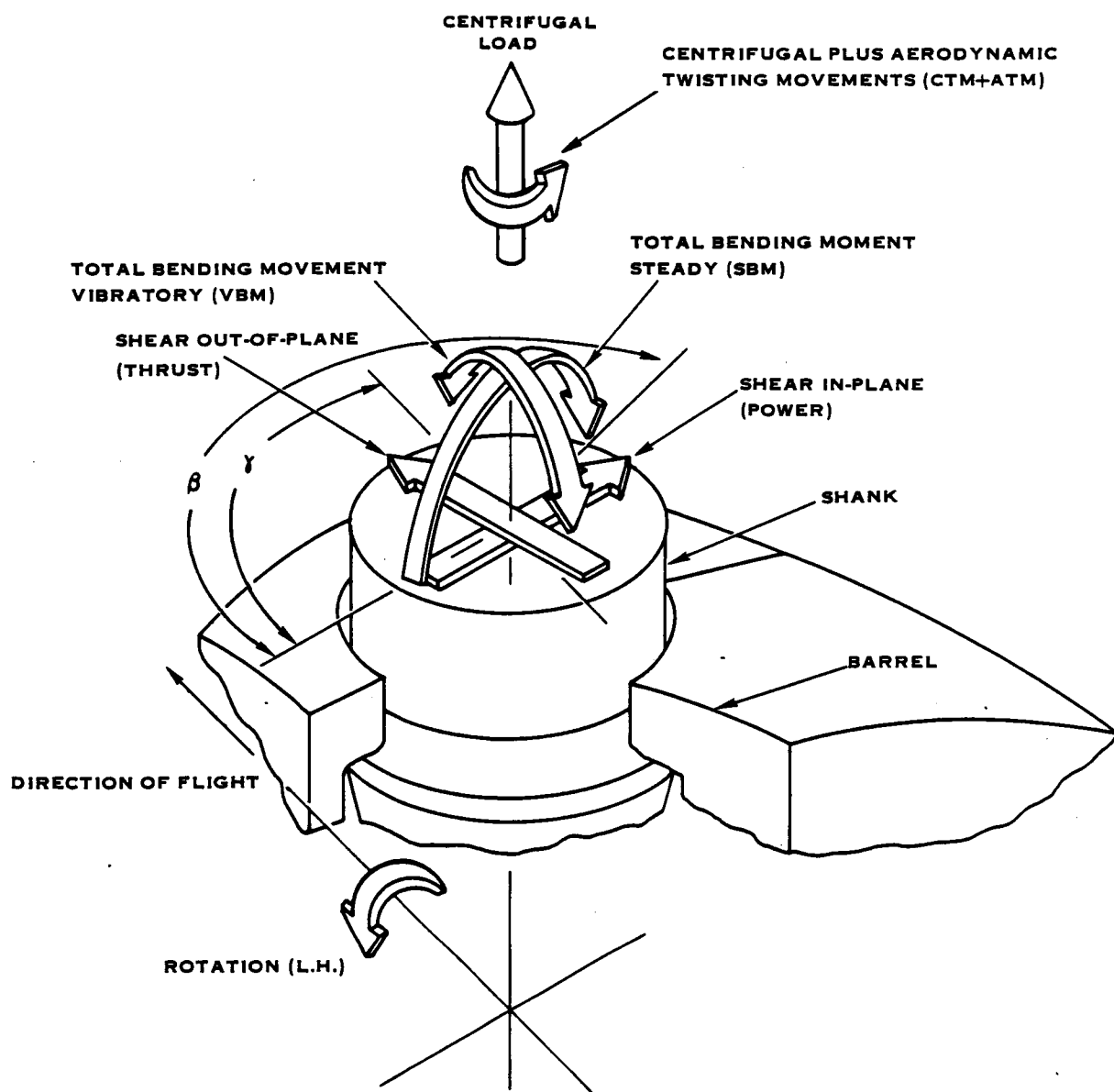


FIGURE 6-15, BLADE SHANK LOADS (POSITIVE DIRECTION SHOWN)

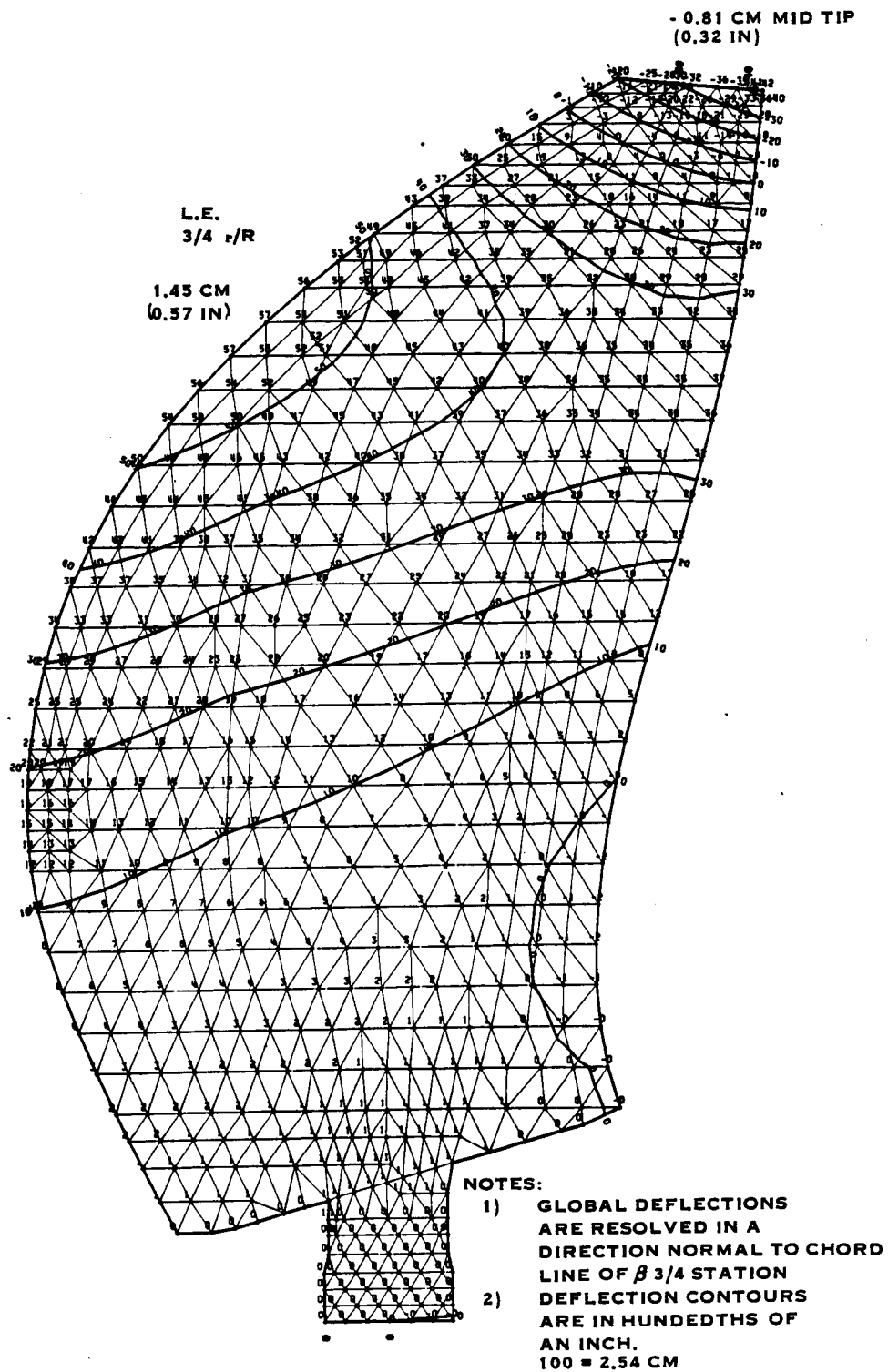


FIGURE 6-16. STEADY-STATE DISPLACEMENTS DESIGN/CRUISE CONDITION



ORIGINAL PAGE IS  
OF POOR QUALITY

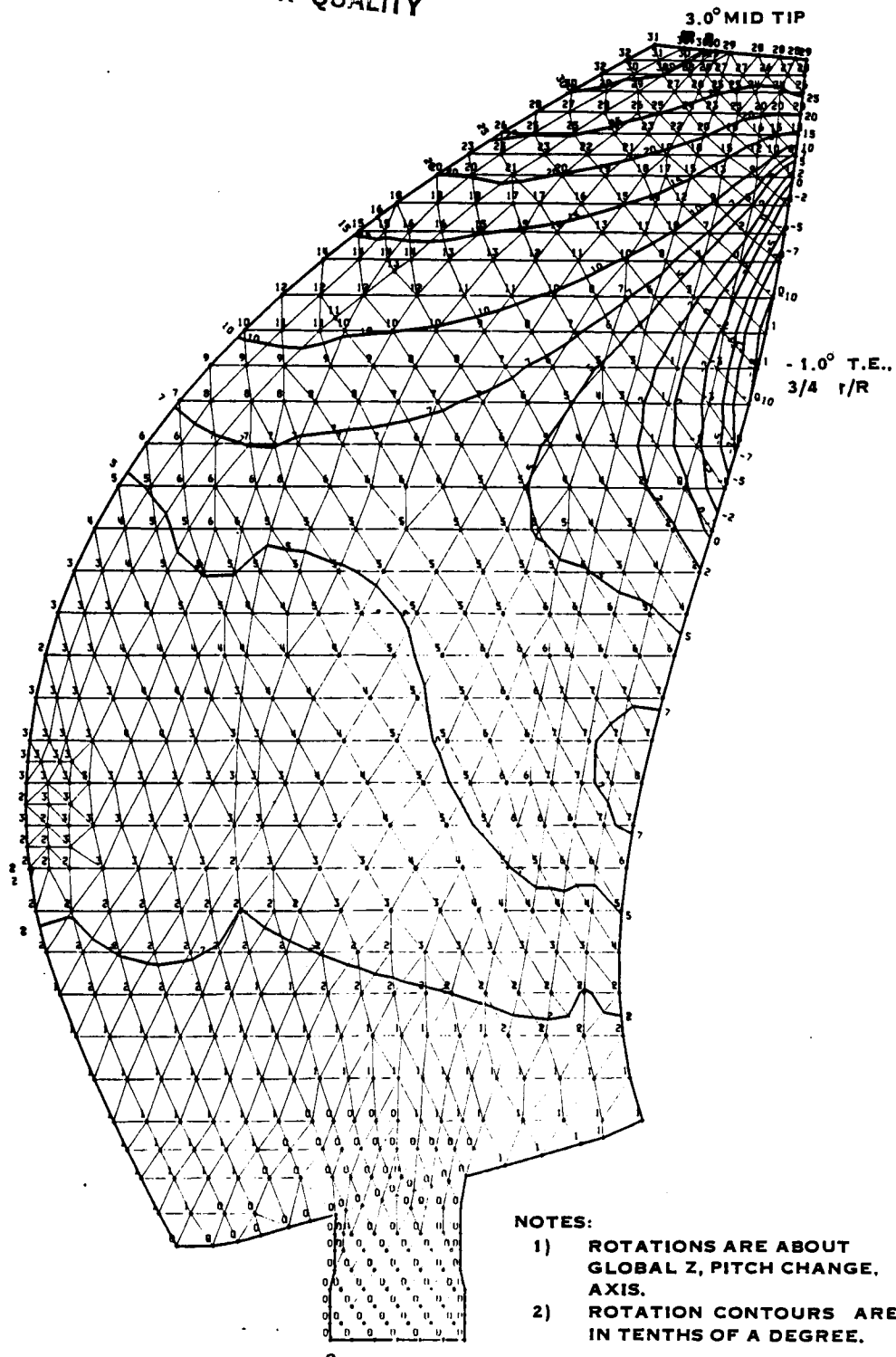


FIGURE 6-17. STEADY-STATE ROTATIONS DESIGN/CRUISE CONDITION

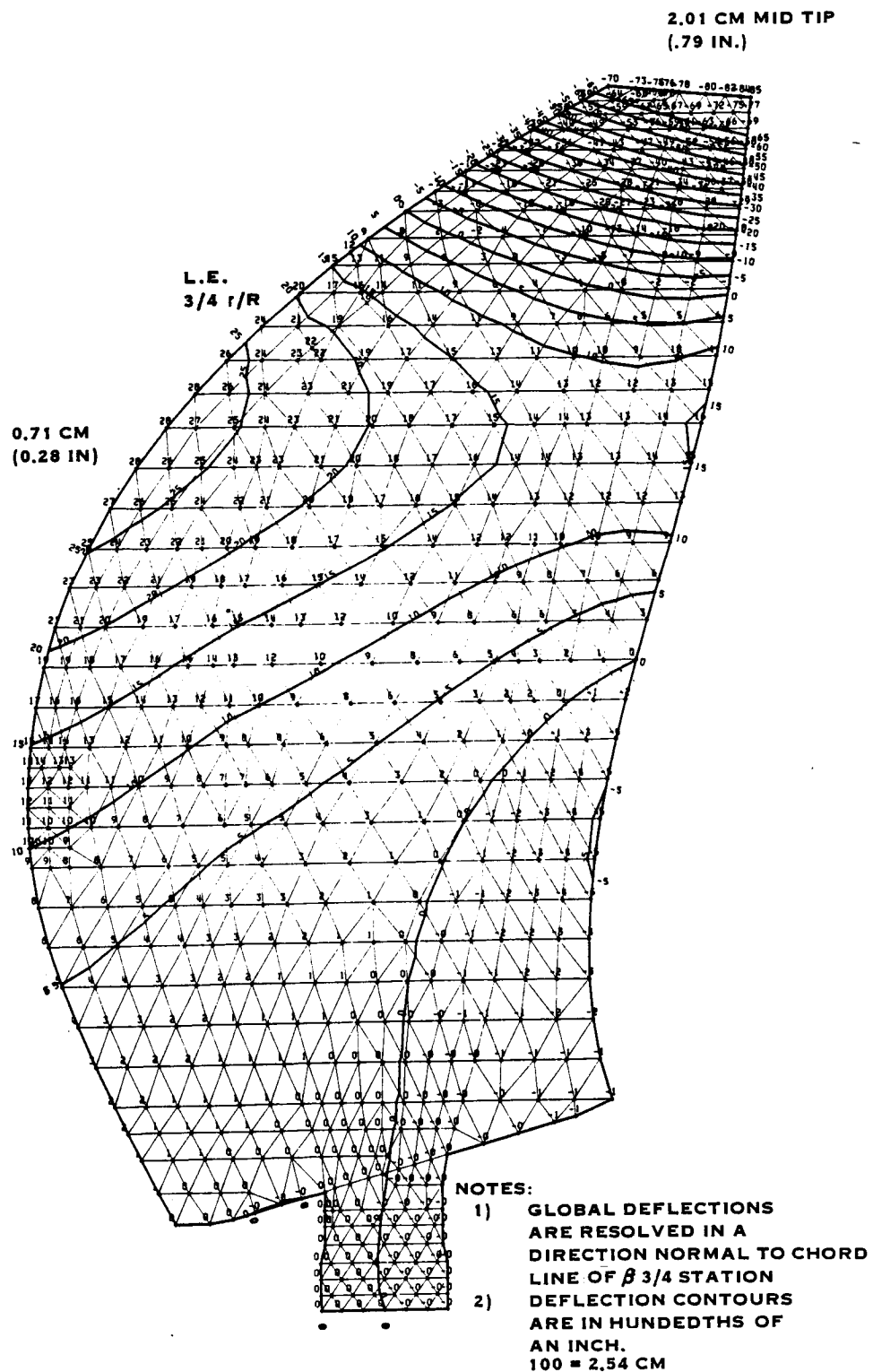


FIGURE 6-18. STEADY-STATE DISPLACEMENTS TAKE-OFF/CLIMB CONDITION

ORIGINAL PAGE IS  
OF POOR QUALITY

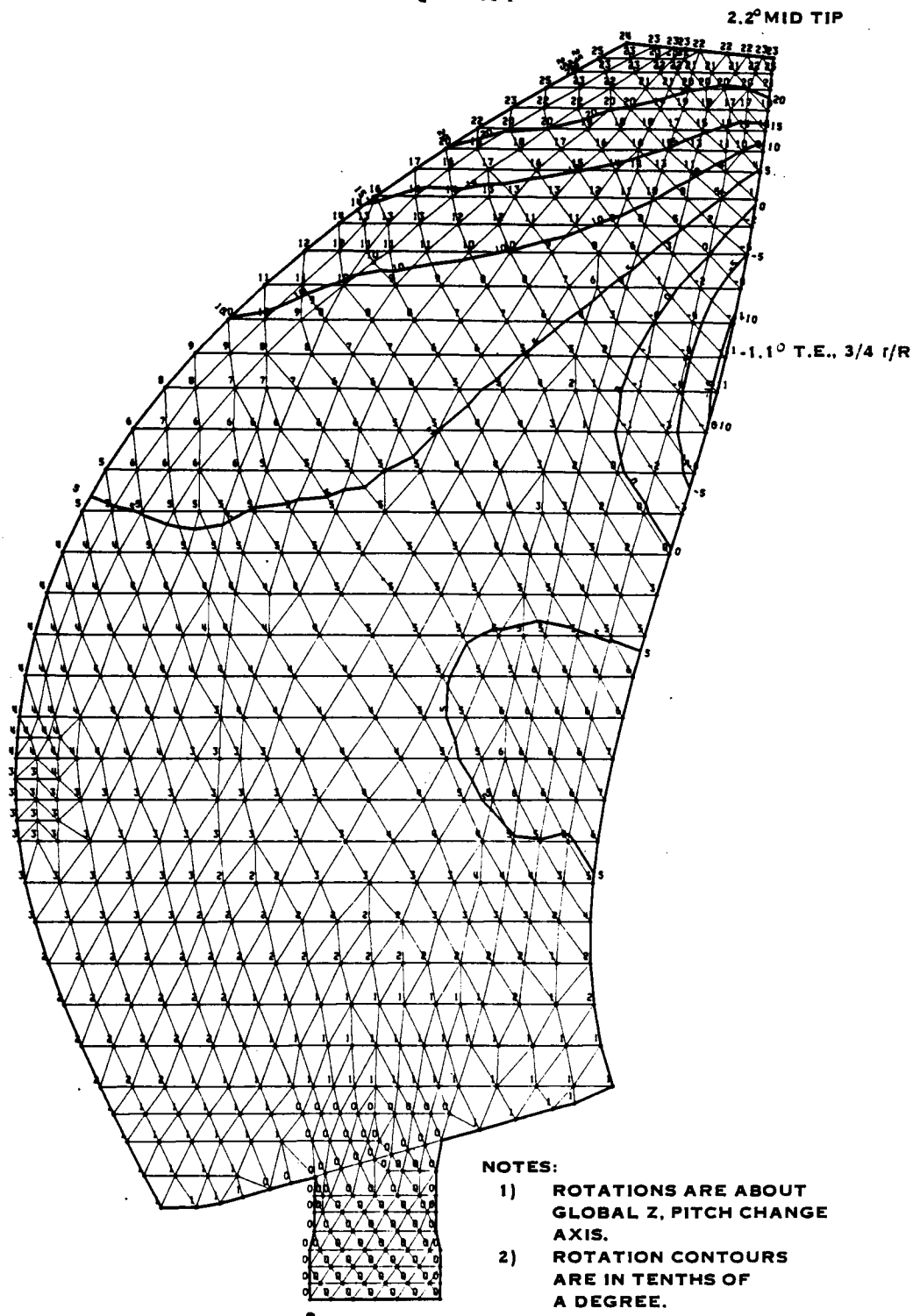


FIGURE 6-19. STEADY-STATE ROTATIONS TAKE-OFF/CLIMB CONDITION

## 7.0 Vibratory Response Analysis

A vibratory response analysis was performed for a once-per-revolution, or 1-P, aerodynamic excitation for eight of the fourteen design conditions. These conditions were: design/cruise, take-off/climb, the three ONERA S1 Wind Tunnel conditions, the low and high rotational speed cruise conditions, and the 0.5 Mach number climb. See table 3-1 of section 3.3.1 and table 3-2 of section 3.3.2 for parameters associated with these conditions.

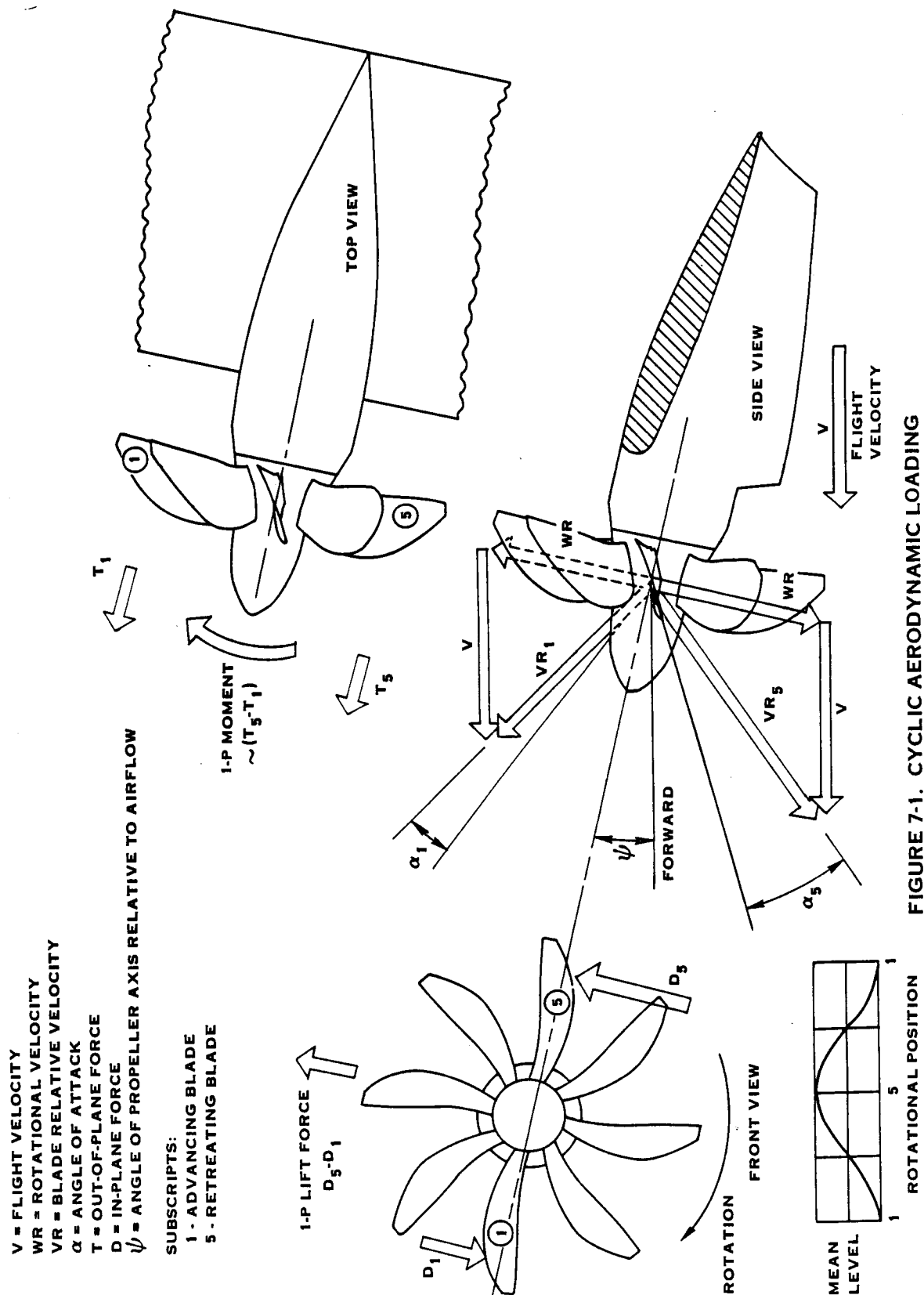
### 7.1 Origin Of The Once-Per-Revolution Excitation

The once-per-revolution (1-P) excitation occurs because of the angle ( $\psi$ ) which the propeller axis of rotation makes with the forward direction of the aircraft, particularly during the climb condition, as illustrated in figure 7-1.

This results in a difference in the relative angle of attack of two horizontal blades shown in the front view. That is, the advancing blade 1 sees a reduced angle of attack ( $\alpha_1$ ), while the retreating blade 5 sees an increased angle of attack ( $\alpha_5$ ). In the top and bottom positions, the angle of attack is equal. Therefore, a single blade experiences a sinusoidal variance in the load during each revolution. The difference in load between blades 5 and 1 results in a small constant vertical force as shown in the front view, while the difference in thrust results in a propeller shaft bending moment as seen in the top view. Additionally, depending on the installation and the proximity of the Prop-Fan to a wing engine inlet, and/or fuselage, the Prop-Fan can operate in a flow field of varying velocity. This is more pronounced if the wing has considerable sweep as shown in figure 7-2.

These factors add to the 1-P excitation and, in the case of the inlet and wing, a slight amount of 2-P excitation may also be present. An example of cyclic loading superimposed on the steady loads that occur during a typical flight is shown in figure 7-3. The primary component of the cyclic load is due to the 1-P vibration, and distortions of the 1-P sinusoidal wave form are due to the higher order (n-P) vibrations.

It is possible to adjust the tilt angle ( $\psi$ ) of the Prop-Fan shaft to achieve a balance in inflow angle between extremes of flight conditions as shown in figure 7-4, and thus to minimize the highest 1-P cyclic loads.



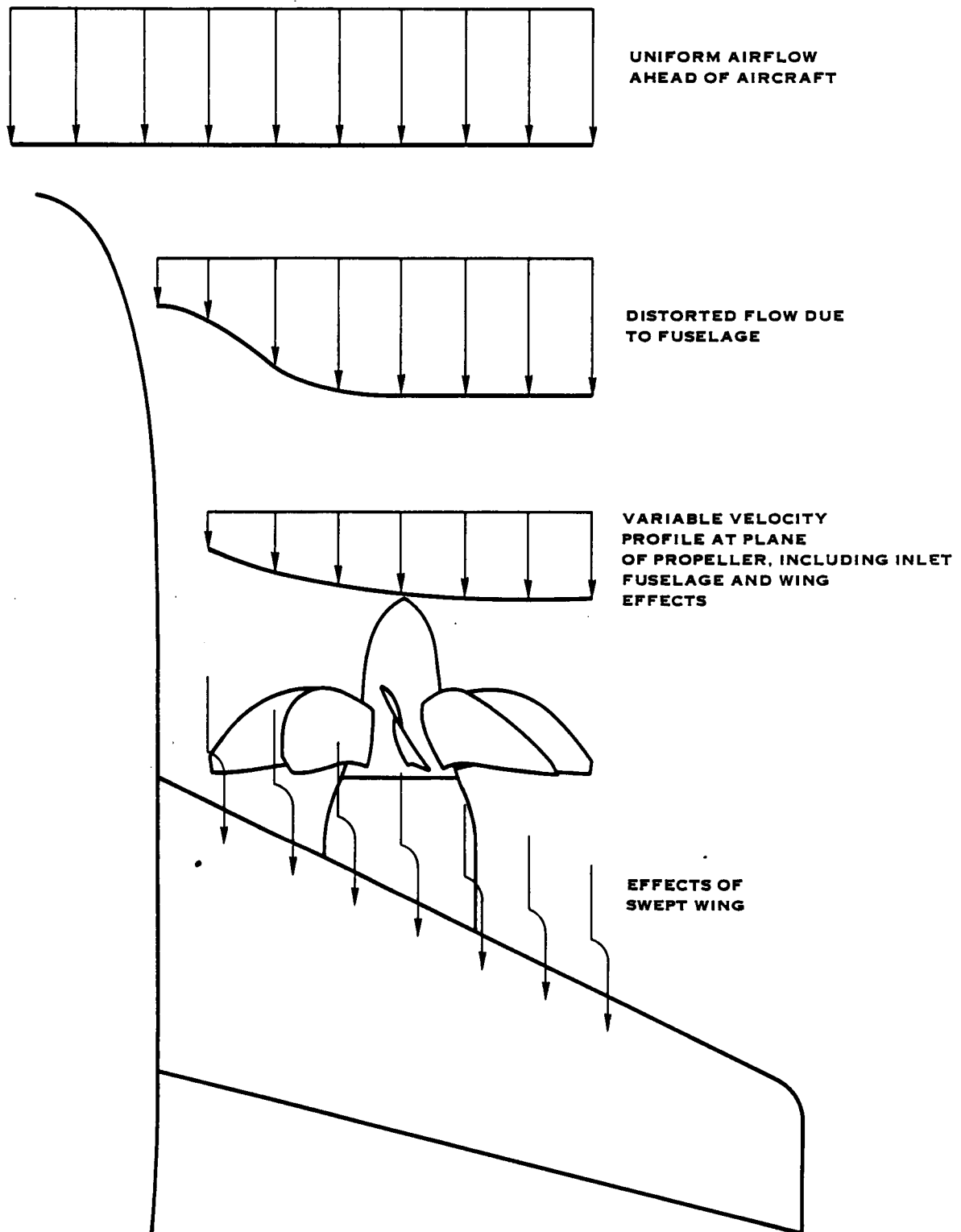
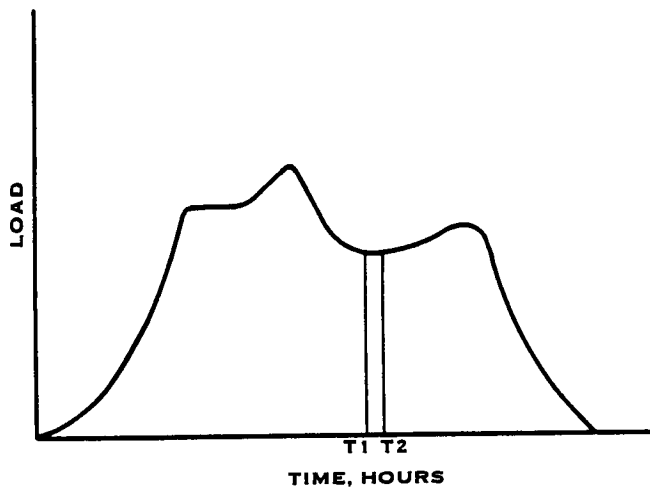
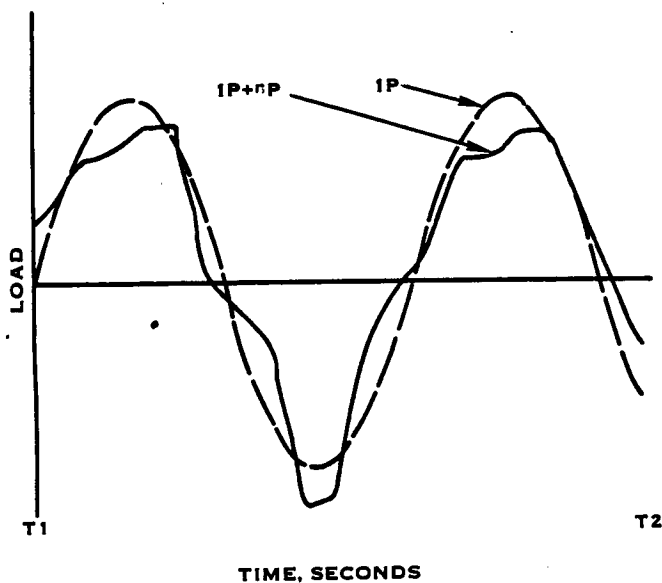


FIGURE 7-2. VARIABLE VELOCITY AIR INFLOW ACTING ON SR-7L



**TYPICAL START-STOP CYCLE:  
ALL "STEADY" LOADS VARY AS  
OPERATING CONDITIONS CHANGE**



**TYPICAL 1-P CYCLIC RESPONSE  
WITH HIGHER ORDER (n-P) COMPONENTS:  
AT ANY "STEADY" OPERATING  
CONDITION THERE ARE SUPERIMPOSED  
HIGH FREQUENCY/LOW AMPLITUDE  
LOAD VARIATIONS**

**FIGURE 7-3. TYPICAL STEADY-STATE AND CYCLIC LOADINGS**

## 7.2 Excitation Factor

In accordance with the design requirements, cyclic airloads corresponding to a 4.5 excitation factor were used for the vibratory response analysis. For a standard propeller, the excitation factor is a measure of the severity of the once-per-revolution aerodynamic excitation, and is a function of the air in-flow angle to the propeller axis and the equivalent airspeed squared as shown in figure 7-4. Normally, propeller excitation factors range from 1.5 to about 2.5. The excitation factor used in this analysis is considerably higher to reflect the worst case flow fields of conceptual Prop-Fan installations for a highly loaded sweep wing mounted tractor configuration (Ref. 7) and consists of a value of 3.3 for the pure 1-P excitation, plus an allowance of 1.2 to account for possible higher order excitations (n-P).

## 7.3 Calculation Of Vibratory Response

For each of the eight conditions, a finite element code was used to evaluate the vibratory response based on several calculation parameters which included: the cyclic airloads based on the 4.5 excitation factor at a frequency corresponding to the once-per-revolution vibration, the differential stiffening from the appropriate steady-state analysis, and the appropriate blade model at the deflected position.

The finite element program applied the cyclic air loads to the stiffened, deflected model and calculated the maximum stress and deflection at each grid point. These stresses are combined with the steady-state stresses of section 6 (Steady State Analysis) for comparison to design allowables on Goodman diagrams in section 8 (Stress versus Strength Evaluation) and are not tabulated in this section.

## 7.4 Blade Shank Loads

The calculated vibratory blade shank loads for the eight conditions analyzed are summarized in table 7-1.



$$EF = \Psi \left[ \frac{V_e}{348} \right]^2$$

$V_e$  = EQUIVALENT AIRSPEED IN KNOTS

$\Psi$  = RELATIVE ANGLE OF PROPELLER  
AXIS TO AIRFLOW

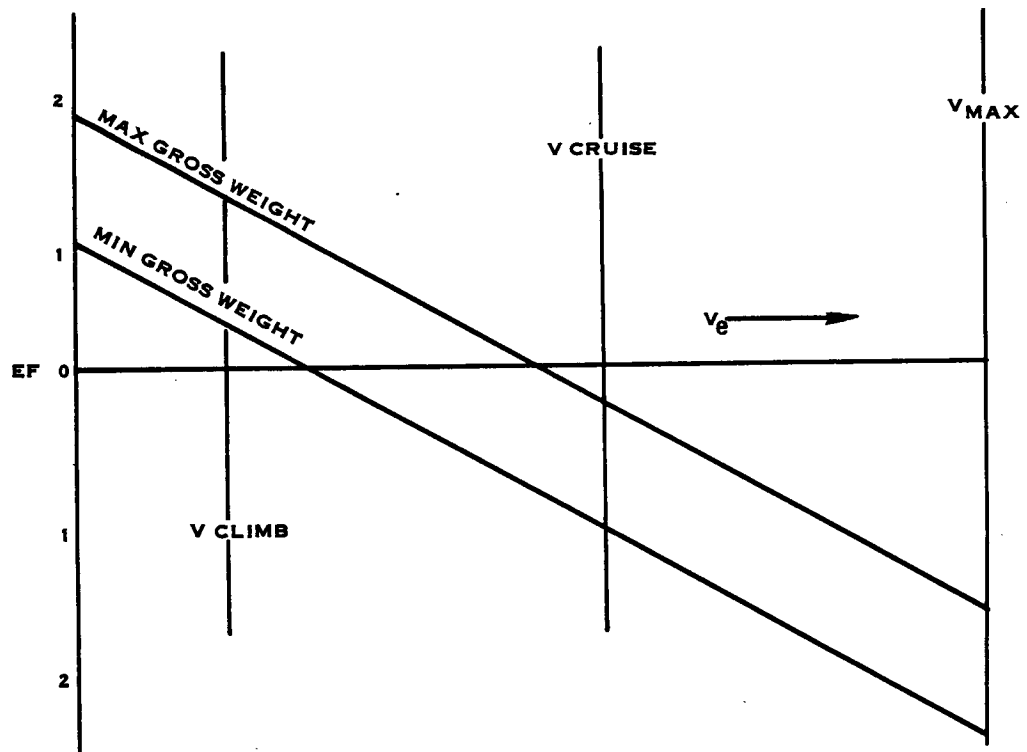


FIGURE 7-4. LOADING - AERODYNAMIC - CYCLIC

Table 7-1

## BLADE SHANK VIBRATORY LOAD SUMMARY

No.	Condition	Total Bending Moment,	Angle,* degrees*
		newton-meters (inch-pounds)	
D1	Design/Cruise	1,718 (15,200)	160.8
D2	Take-Off/Climb	3,187 (28,200)	142.1
1A	ONERA, 8 Blade	1,627 (14,400)	159.3
1B	ONERA, 4 Blade	2,249 (19,900)	159.7
1C	ONERA, 2 Blade	2,769 (24,500)	160.4
4	Cruise, Low RPM	2,452 (21,700)	164.6
5	Cruise, Hi RPM	1,559 (13,800)	162.2
6	Climb, Mid Altitude	1,932 (17,100)	153.9

\* Angle, Gamma, measured from plane of rotation (see Figure 6-15)

## 7.5 Twist Magnification

After the blade was analyzed and the deflections calculated, the deflection patterns of the blade due to the once-per-revolution excitation were checked for potential twist magnification. Twist magnification occurs when the blade deflects about its pitch change axis such that the aerodynamic angle of attack of the blade increases and, as a result, the cyclic air loads on the blade increase. The increased airloads will cause greater blade twist, and this increase in twist will result in still greater airloads. Eventually, the blade reaches a new condition of equilibrium between airloads and deflection.

Deflection patterns for the blade are shown in figures 7-5 and 7-6. Notice that the translational deflection patterns (figure 7-5), which are resolved normal to the chord at the three-quarter radius station, are essentially horizontal, indicating no torsional response. As further proof, the grid point rotations about the pitch change axis (figure 7-6) show very little twist change. This appears to be a benefit of sweeping the blade rearward; that is, the greater load on the tip, which is swept rearward, falls behind the torsional axis of the mid-portion of the blade, thus reducing the potential for twist magnification.

If the deflection patterns showed a potential for twist magnification, then the blade would have to be reanalyzed with new airloads which would correspond to the new twisted position. However, no potential for twist magnification was seen in the SR-7L blade as a result of the once-per-revolution excitation.

ORIGINAL PAGE IS  
OF POOR QUALITY

-1.27 CM MID TIP  
(0.50 IN)

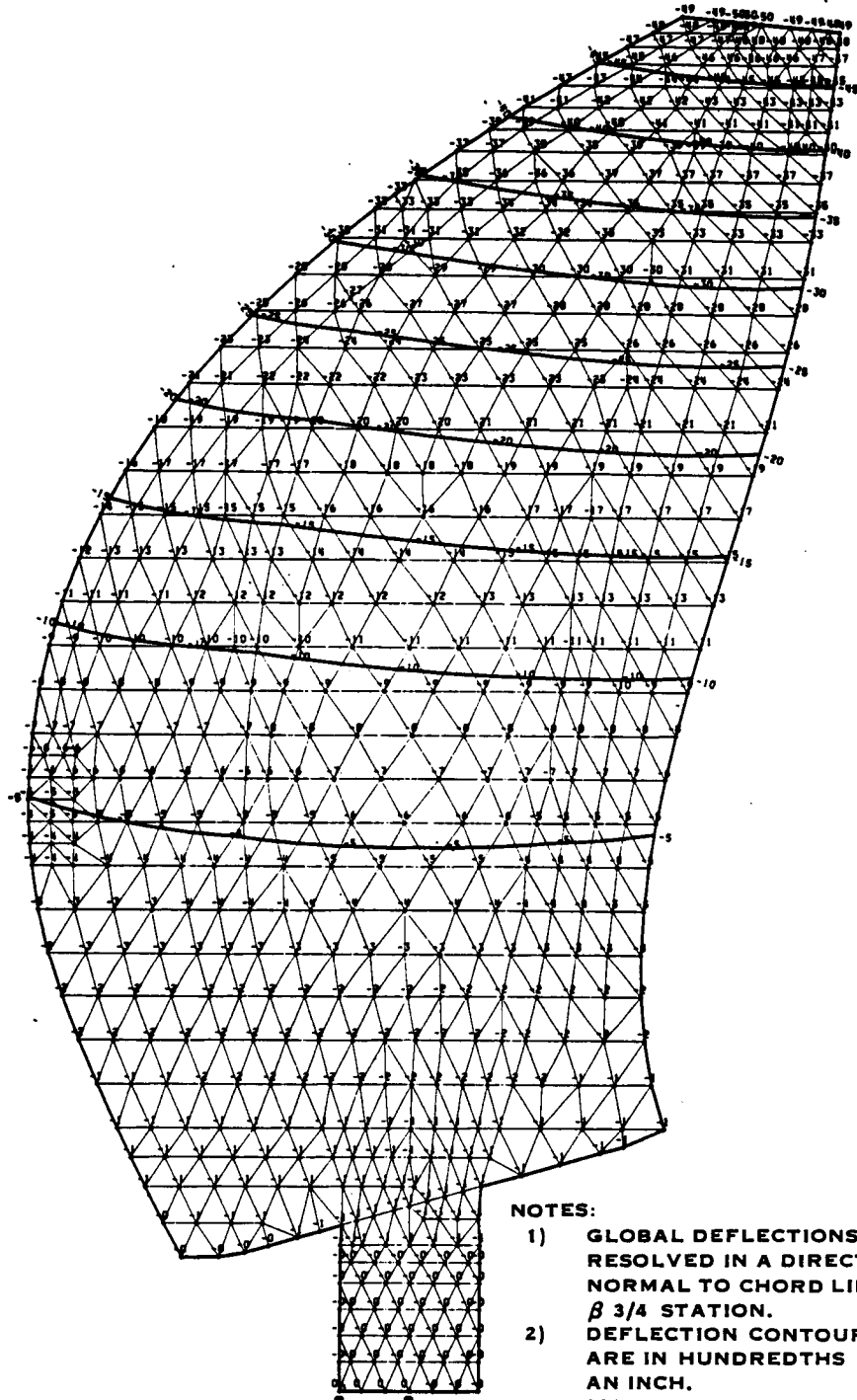


FIGURE 7-5. VIBRATORY DEFLECTION PATTERNS DUE TO FORCED RESPONSE AT DESIGN/CRUISE CONDITION

ORIGINAL PAGE IS  
OF POOR QUALITY

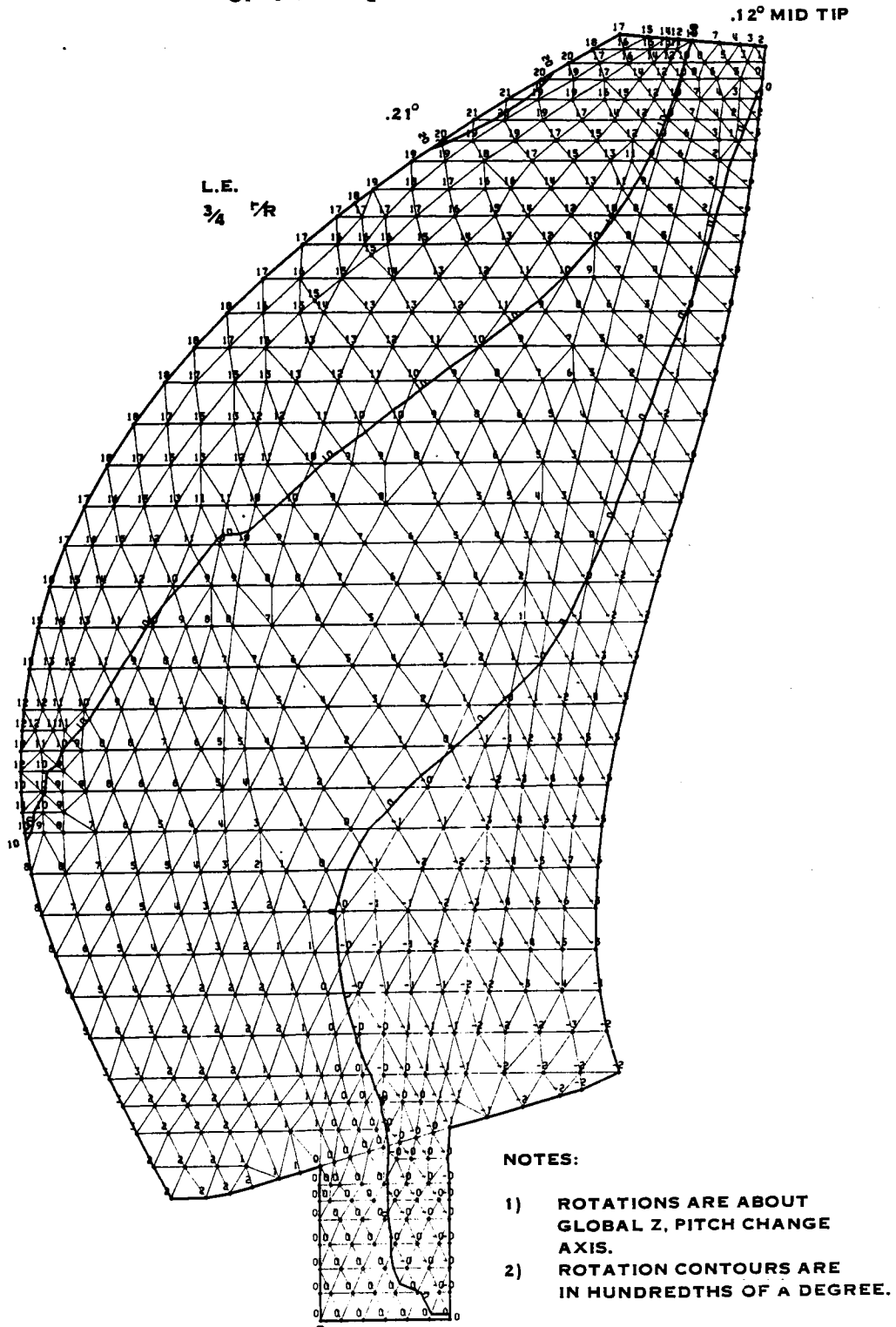


FIGURE 7-6. VIBRATORY ROTATION PATTERNS DUE TO FORCED RESPONSE AT DESIGN/CRUISE CONDITIONS

## 8.0 Stress vs. Strength Evaluation

### 8.1 Establishing Design Strength Allowables

Hamilton Standard's many years of experience in establishing safe design strength allowables for critical aircraft propeller structures is unsurpassed and is directly applicable to Prop-Fans.

The methodology used to establish design strength allowables is illustrated in figures 8-1 and 8-2.

Propeller blades, in addition to experiencing low cyclic fatigue due to high steady centrifugal and aerodynamic loads, are subjected to high cyclic loads which are a major fatigue life consideration. Over a billion cycles of significant high cycle fatigue stress during the useful life is not uncommon. Through experience, it was recognized that laboratory fatigue test specimens alone cannot provide adequate definition of the fatigue strength of a full-scale structure due to such things as size difference, processing variations and hardware geometry. Hamilton Standard has conducted numerous and extensive fatigue tests on full-scale propeller blades and hubs, as produced and after various service exposure times. Blades tested have been both solid and hollow structures encompassing metal alloys as well as fiberglass-reinforced plastics. These test results have not only provided valuable assessment of the fatigue strength of the specific structures being tested, but also, when coupled with specimen fatigue data and service experience, have provided an invaluable basis for extrapolation of fatigue allowables for new designs. The application of the newer fracture mechanics methodologies by themselves can lead to unconservative design allowables for low cycle fatigue (LCF) and high cycle fatigue (HCF) life in service environments. The blade for the SR-7 program has been designed with the allowables developed from this vast data base of test and experience. Since all safety factors are accounted for in the establishment of these design allowables, the SR-7L blade has been designed directly to these limits.

### 8.2 Method Of Combining Steady-State and Vibratory Stresses

After completing both the steady-state and vibratory response analyses, the next step was to combine the 1-P vibratory stresses with the steady-state stresses to provide a structural evaluation of blade components. This was done for each of the cyclic load conditions analyzed.

A Goodman diagram was used to show the relationship of the combined stress of the vibratory response and the steady-state analysis with the design allowable limit. Figure 8-3 shows a calculation point plotted on a typical Goodman diagram.

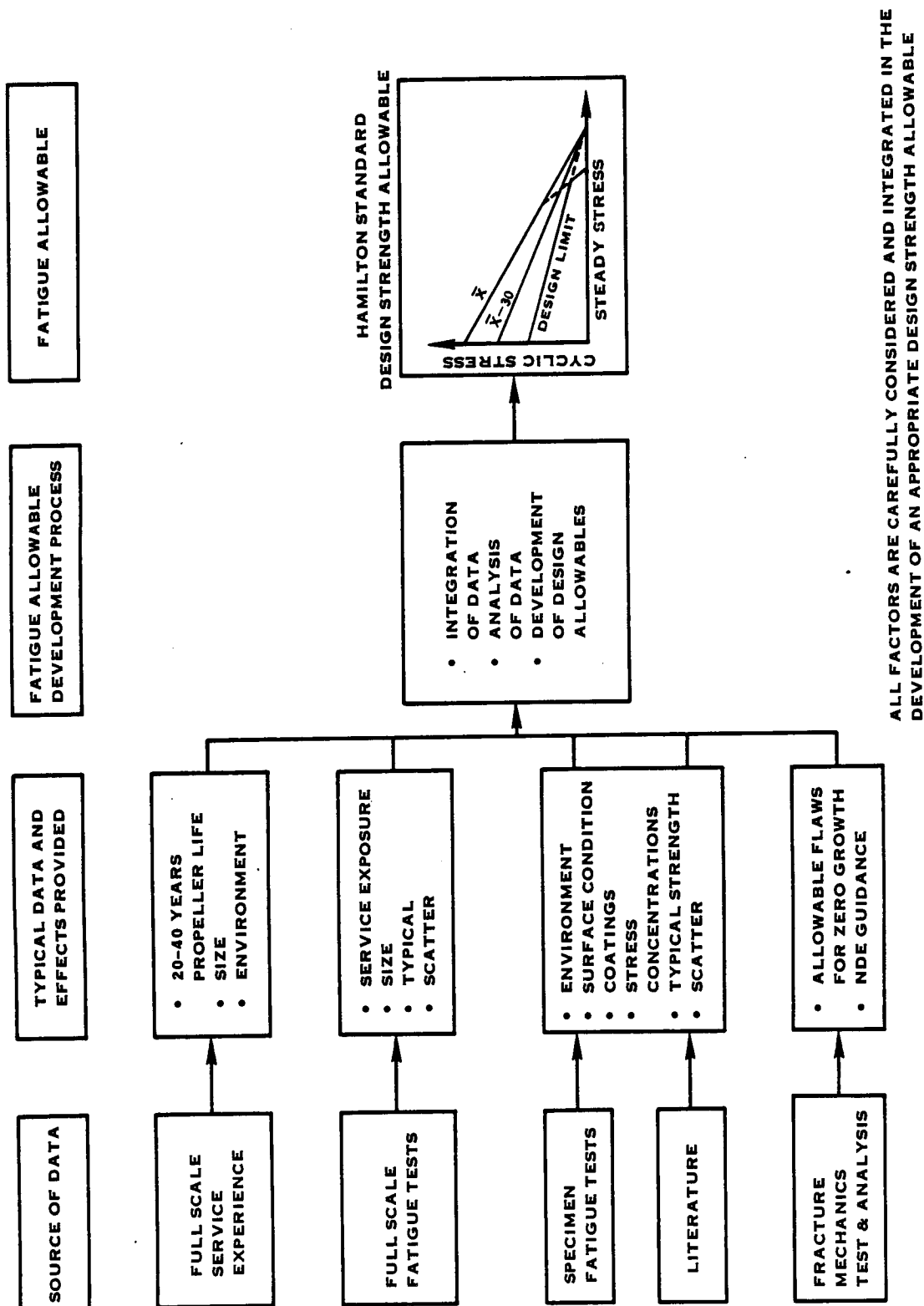


FIGURE 8-1. DESIGN STRENGTH METHODOLOGY

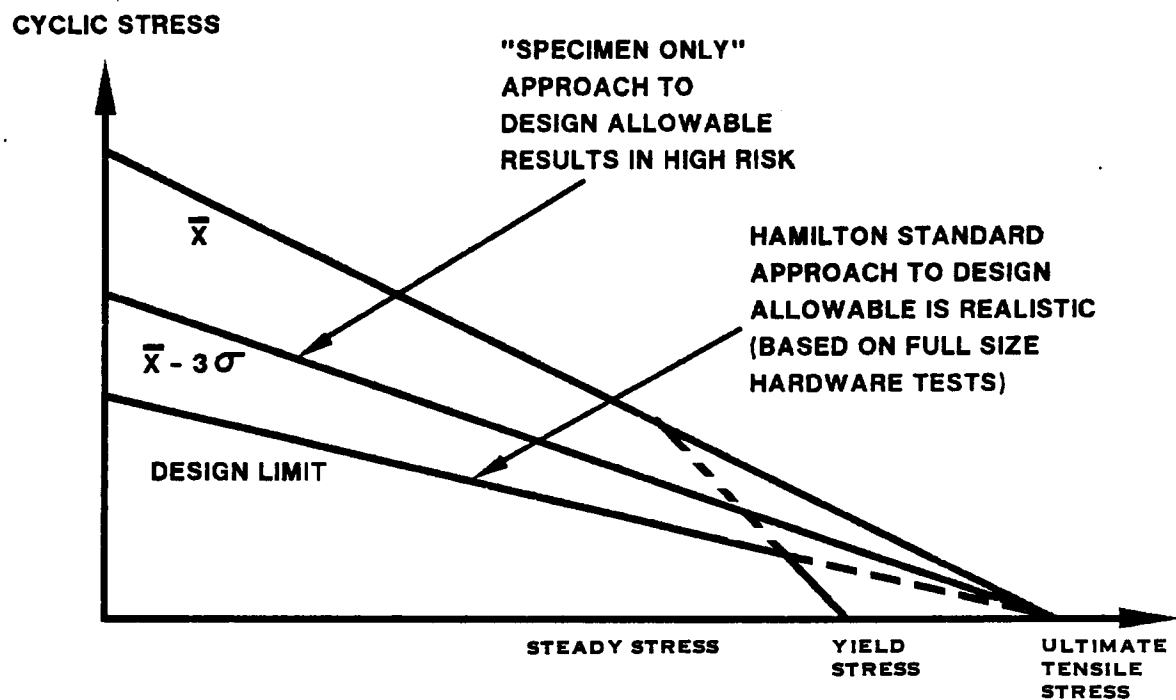


FIGURE 8-2. HAMILTON STANDARD DESIGN STRENGTH ALLOWABLE COMPARED WITH "SPECIMEN ONLY" DESIGN STRENGTH ALLOWABLE



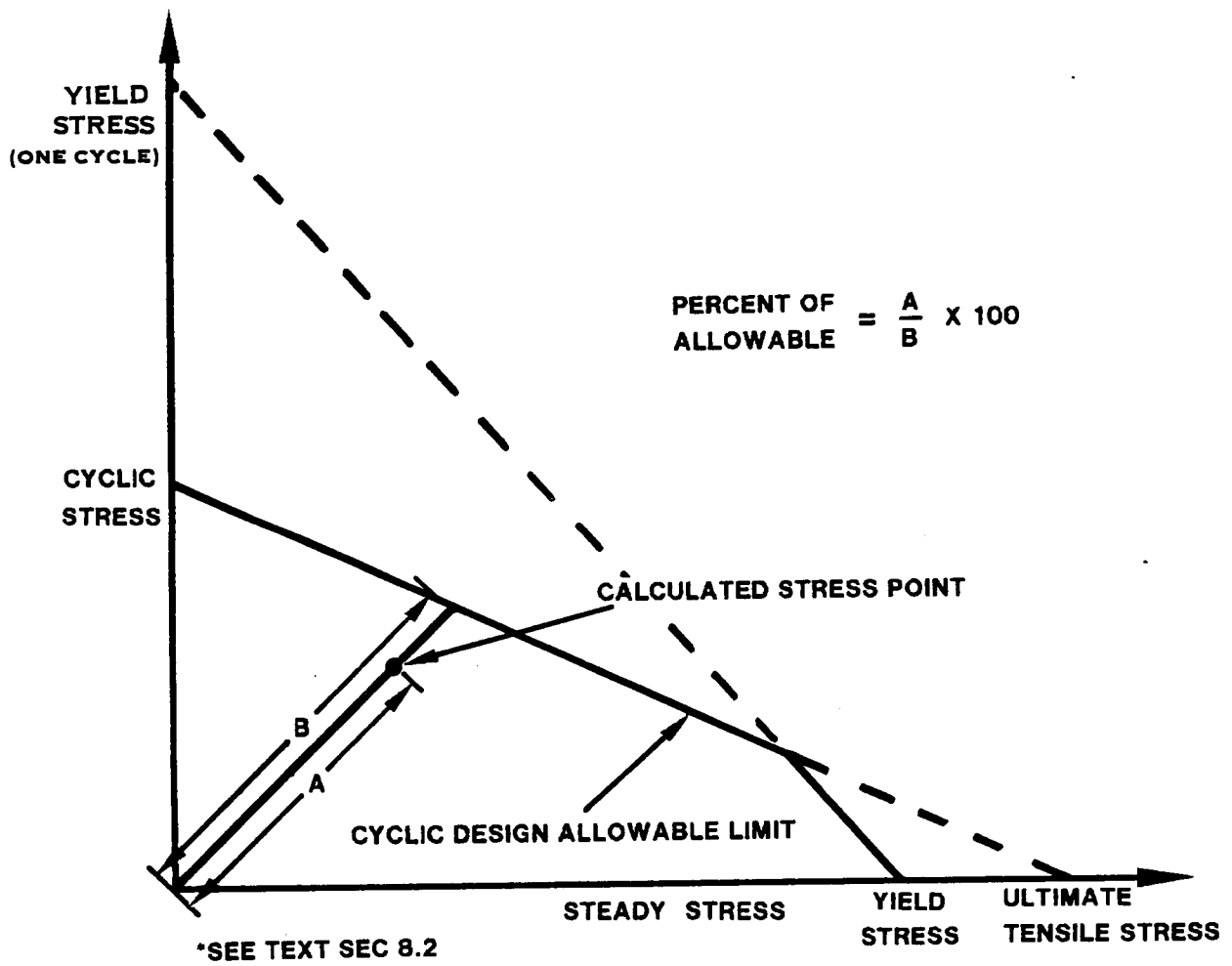


FIGURE 8-3. TYPICAL GOODMAN DIAGRAM

Line A can be constructed on the Goodman diagram which connects a calculation point with the origin of the diagram. Line B can then be drawn coincident with the first line from the origin until it intersects the design limit line. The percent of the first line (origin to calculation point) with respect to the second line (origin to design allowable limit) represents the percent of the allowable limit of the combined stress state at that calculation point. This is a convenient method of expressing combined stresses, especially when evaluating results by means of contour plots. This method is used on all stress/strength contour plots presented in this section.

### 8.3 High Cycle Fatigue

High cycle fatigue is associated with the application of cyclic stress over a relatively long period of time. The application of this cyclic stress will often be in combination with a steady stress which may be much greater in magnitude. As discussed in section 8.2, a Goodman diagram can be used to evaluate the effect of a cyclic stress acting in a steady stress field, with respect to design allowable limits. The steady stress field was calculated as part of the Steady-State Analysis (section 6). The cyclic stress levels were calculated for the 1-P excitation with an allowance for higher order excitations as described in the Vibratory Response Analysis (section 7). For this evaluation, each of the blade components (spar, shell, sheath, and foam filler) is required to withstand at least  $10^8$  cycles under this combined stress condition.

The point with the highest percent of allowable limit from each of the four required conditions (design/cruise, take-off/climb, 25% overspeed, and 40% overspeed) is shown plotted on Goodman diagrams for each of the blade structures as follows:

<u>Figure No.</u>	<u>Structure</u>	<u>Stress</u>
8-4	Spar	Maximum Effective
8-5	Shell	Maximum of Spanwise or Chordwise
8-6	Sheath	Maximum Effective
8-7	Foam Filler	Maximum Effective

A maximum effective stress is shown for the spar, sheath, and foam filler, while the maximum of the spanwise or chordwise stress is shown for the shell. A more complete explanation of effective stress may be found in section 8.5 along with examples of stress contour plots for the design/cruise and take-off/climb conditions. The maximum percent of allowable limit for each of the conditions analyzed is listed in table 8-1.

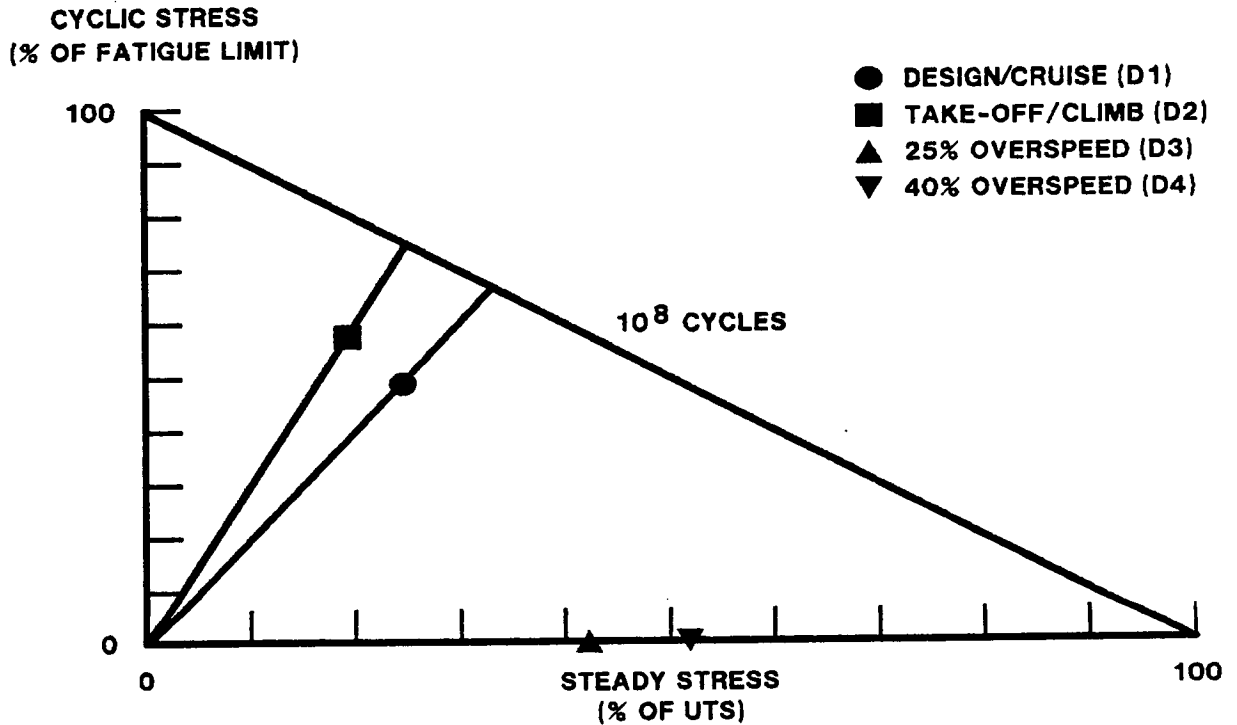


**FIGURE 8-4. SR-7L BLADE SPAR STRESS/STRENGTH COMPARISON  
(ALUMINUM 7075-T73)**

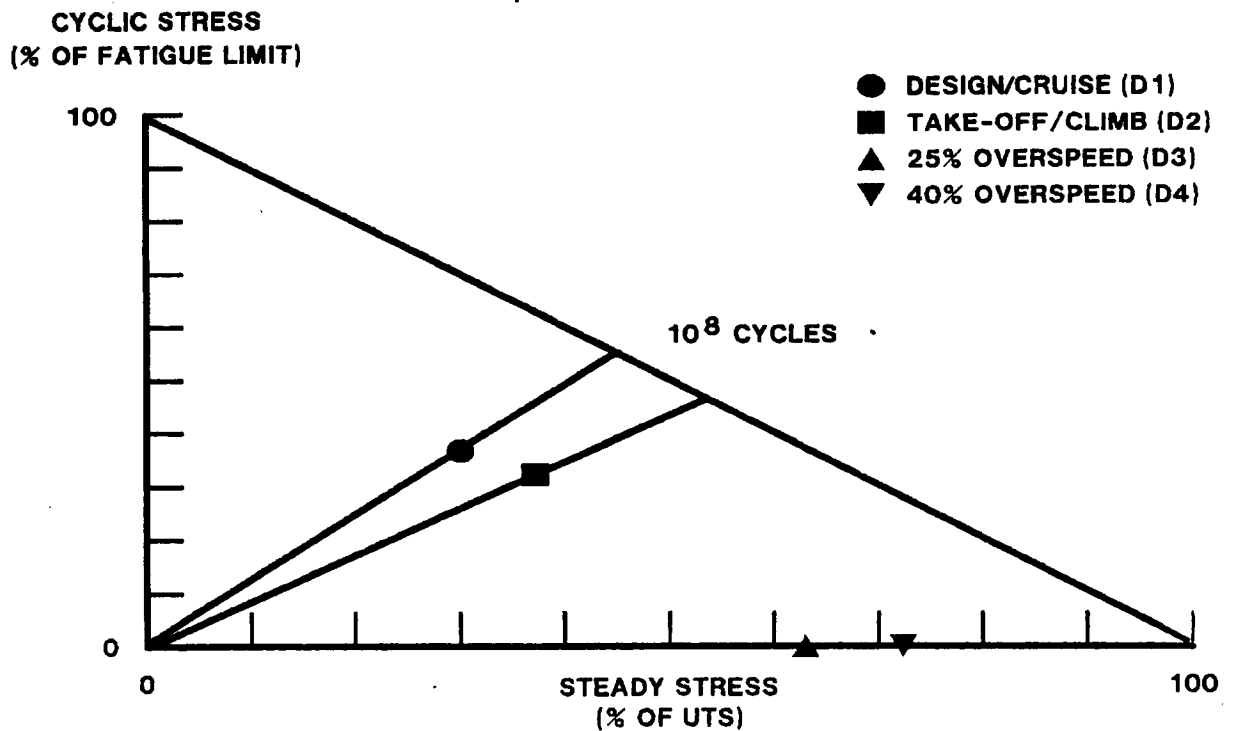


**FIGURE 8-5. SR-7L BLADE SHELL STRESS/STRENGTH COMPARISON  
(FIBERGLASS ± 45° WOVEN 181 CLOTH)**

CYCLIC STRESS  
(% OF FATIGUE LIMIT)

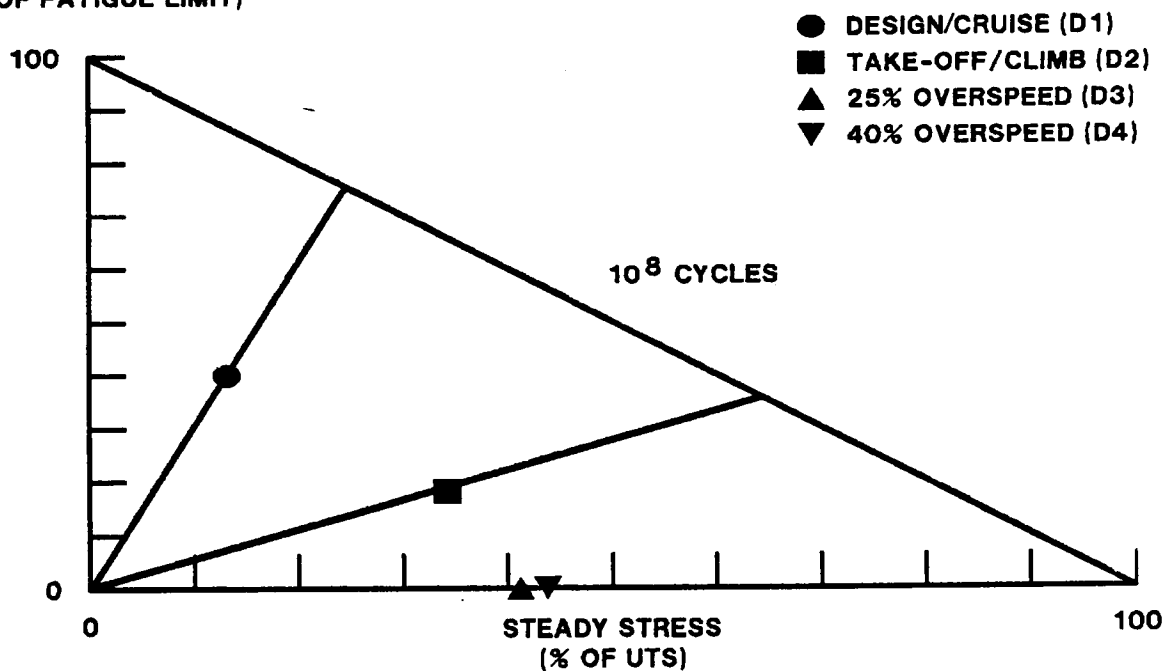


FIGURE 8-6. SR-7L BLADE SHEATH STRESS/STRENGTH COMPARISON (PLATED NICKEL)

CYCLIC STRESS  
(% OF FATIGUE LIMIT)

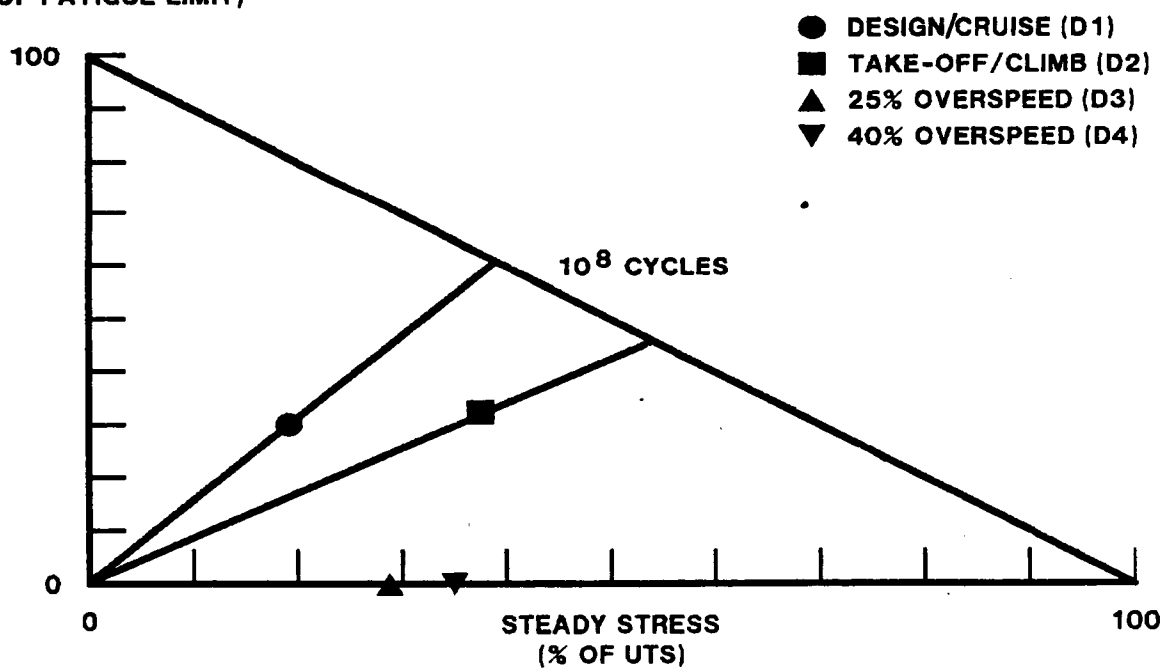


FIGURE 8-7. SR-7L BLADE FILLER MATERIAL STRESS/STRENGTH COMPARISON  
(FOAM - 8 LBS/CU FT)

Table 8-1

## HIGH CYCLE FATIGUE STRESS/STRENGTH COMPARISON

Percent of Allowable Limit\*

<u>No.</u>	<u>Condition</u>	<u>Spar</u>	<u>Shell</u>	<u>Foam filler</u>	<u>Sheath</u>
D1	Design/Cruise	74	67	50	53
D2	Take-off/Climb	76	64	60	53
D3	25% Overspeed	42	61	29	41
D4	40% Overspeed	52	74	35	44
1A	ONERA, 8 Blade	33	76	58	41
1B	ONERA, 4 Blade	86	87	77	46
1C	ONERA, 2 Blade	97	93	86	49
2	Static Thrust	26	65	22	35
3	Reverse Thrust	43	67	18	79
4	Cruise, Low RPM	100	85	63	81
5	Cruise, Hi RPM	70	64	44	49
6	Climb, Mid Altitude	77	67	57	58
7	Dive, Mid Altitude	30	61	24	34
8	Dive, High Altitude	30	60	25	35

\* Percent of allowable limit measured diagonally on Goodman diagram and based on  $10^8$  cycles endurance limit

#### 8.4 Low Cycle Fatigue

Low cycle fatigue (LCF), sometimes referred to as "start-stop" cycles, is associated with alternating between an unstressed state and the maximum stress state. For the low cycle fatigue stresses, the steady and cyclic stresses (presented in sections 6 and 7, respectively) are combined to determine the maximum tensile or compressive stress, shown in figure 8-8.

For LCF evaluation, the steady and cyclic stresses are each assumed equal to half of this maximum value, and are then plotted on a modified Goodman diagram, as shown in figure 8-9, for comparison to the material allowable limits. For the low cycle fatigue conditions, each of the blade components must withstand at least  $5 \times 10^4$  stress cycles under this combined stress condition.

The highest percent of allowable limit for each of the conditions analyzed is listed in table 8-2 for each of the blade components.

Table 8-2

#### LOW CYCLE FATIGUE STRESS/STRENGTH COMPARISON

Percent of Allowable Limit\*  
(Cycles to Allowable if Less Than 50,000)

No.	Condition	Spar	Shell	Foam filler	Sheath
D1	Design/Cruise	56	73	57	54
D2	Take-off/Climb	50	64	52	60
D3	25% Overspeed	71	102(20,000)	67	58
D4	40% Overspeed	86	125 (80)	81	62
1A	ONERA, 8 Blade	58	81	67	50
1B	ONERA, 4 Blade	60	76	69	50
1C	ONERA, 2 Blade	60	77	71	53
2	Static Thrust	43	110 (1,300)	50	50
3	Reverse Thrust	71	113 (600)	41	113 (20,000)
4	Cruise, Low RPM	48	68	48	47
5	Cruise, Hi RPM	58	74	58	51
6	Climb, Mid Altitude	52	96	53	63
7	Dive, Mid Altitude	49	102(25,000)	55	48
8	Dive, High Altitude	49	101(35,000)	58	49

- \* Percent of allowable limit based on 50,000 start-stop cycles  
 Zero to max stress =  $(SS+CYC)/2 \pm (SS+CYC)/2$   
 SS = Steady stress  
 CYC = Cyclic stress

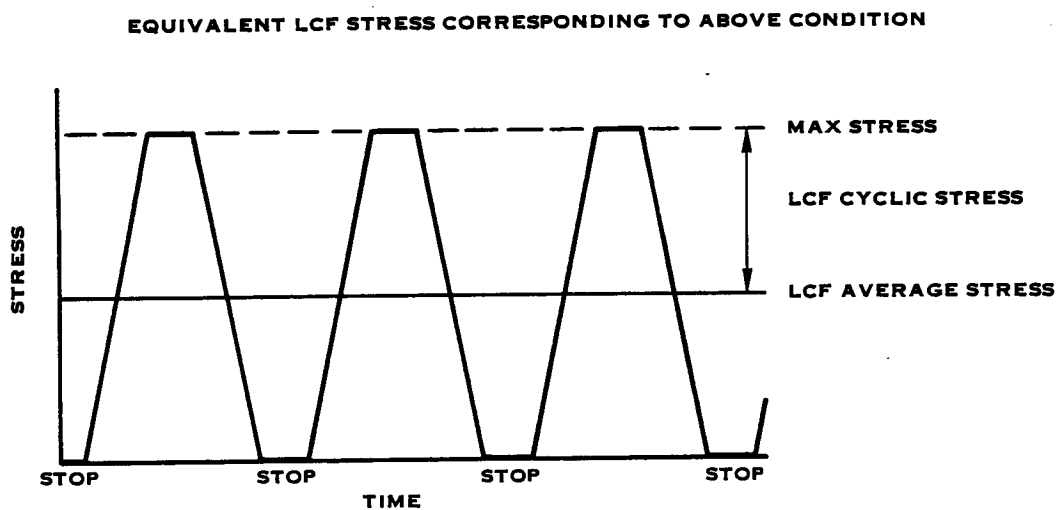
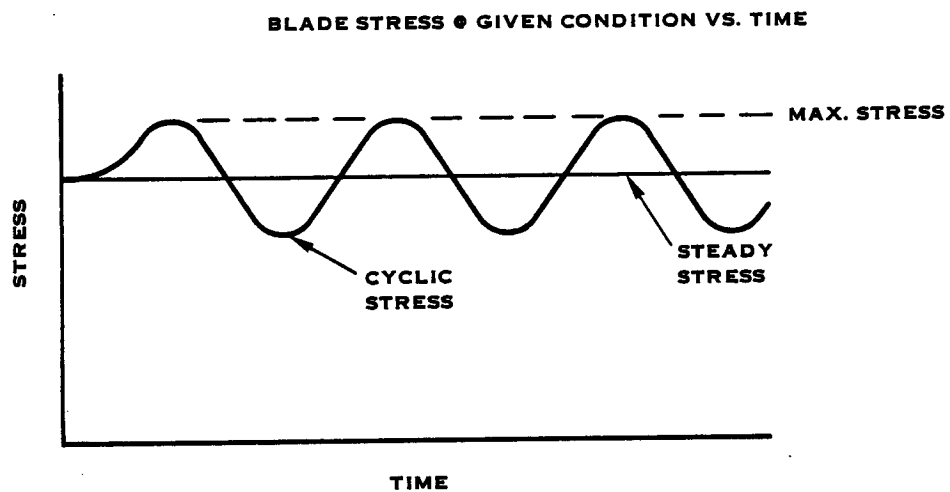


**FIGURE 8-8. LOW CYCLE FATIGUE STRESS EVALUATION**

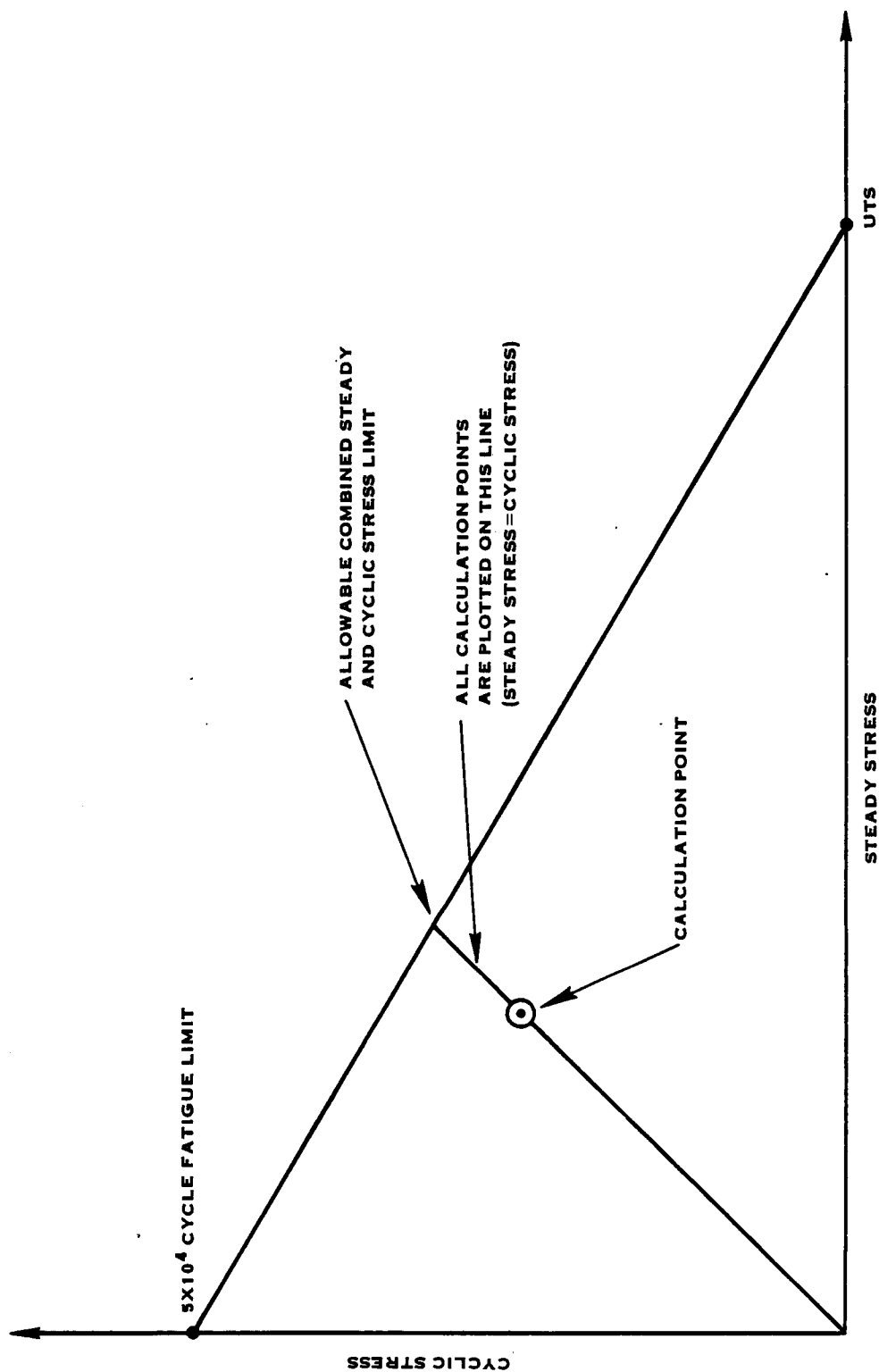


FIGURE 8-9. MODIFIED GOODMAN DIAGRAM FOR LOW CYCLE FATIGUE



Of the four design requirement conditions (design/cruise, take-off/climb, and the two overspeed conditions), the two overspeed conditions have maximum combined shell stresses which are beyond the allowable limit for 50,000 start-stop cycles. The shell is two percent beyond the allowable for the 25 percent overspeed condition, and 25 percent beyond the allowable for the 40 percent overspeed condition. In terms of allowable start-stop cycles, the 25 percent overspeed condition can withstand 20,000 cycles and the 40 percent overspeed condition can withstand 80 cycles. Despite the apparent limitation in allowable start-stop cycles, the two overspeed conditions are well within the design requirements specified in section 3.1.4.2 for rotor overspeeds, and do not represent any limitation in the anticipated test program. The fact that the SR-7L blade can withstand 80 start-stop cycles to 40 percent overspeed is another indication that, if necessary, it can safely operate in an overspeed condition. Also, reaching the shell cycle limit implies only a gradual reduction in modulus and not an abrupt failure. Evidence of a change in modulus may appear as a slight crazing, visible in the fiberglass resin at the shell surface.

Of the ten design goal conditions, four have maximum combined shell stresses beyond the allowable limit, and one has the maximum combined sheath stress beyond the allowable limit. The conditions with shell stresses beyond the allowable are static thrust, reverse, and the two dive conditions. The mid-altitude dive condition is two percent beyond the allowable and the high-altitude dive condition is one percent beyond the allowable. In other words, the shell can withstand 25,000 mid-altitude dives or 35,000 high-altitude dives. For the aircraft for which the Prop-Fan is intended, setting a goal of 25,000 dives would still be a very conservative estimate; therefore, the inability to withstand 50,000 dives is not considered a limitation.

For the static thrust condition, the maximum shell combined stress is ten percent beyond the allowable limit. This overstress condition is not of great concern, however, for three reasons. First, the shell can withstand about 1300 static thrust start-stop cycles, which is an adequate number of cycles for the anticipated test program. Second, the maximum stress occurs in a chordwise direction, in a very localized area, near the spar/shell/root junction on the camber side leading edge, while the rest of the shell is well below the allowable limit. Third, the FEA modeling may not fully represent the true chordwise stiffness of the shell structure in this region since the shell is simply "cut off" at the base, while the actual shell is closed at the base where the shell wraps around the root of the leading edge airfoil. The real shell will have greater chordwise stiffness in this area and the closure will act as a bulkhead to relieve chordwise stressing. Static thrust testing is planned to take place early in the test program. During the test, the stress in this area of the shell can be closely monitored to determine the actual stress state.

The maximum shell combined stress for the reverse condition is 13 percent beyond the combined stress allowable limit. This means that the shell can withstand about 600 reverse start-stop cycles, and although this should be adequate for the anticipated test program, it could represent a test limitation. The overstressed area is large, well-defined, and is centered over the shell/spar junction at about the one-third radius station on the camber side of the blade. If one were designing a full-size blade based on the results of this analysis, it would be possible to restack the blade in the overstressed area to reduce the stress. There would be a minimal change in stability since the restacking would be limited to the lower third of the blade, and stability is more sensitive to changes in the outboard portion of the blade.

The condition where the maximum combined sheath stress exceeds the allowable limit is reverse. The maximum sheath stress is 13 percent beyond the allowable, and the sheath can withstand 20,000 cycles. The maximum stress occurs on both the face and camber sides of the sheath, toward the leading edge, and just below the mid-span region. Although this is a condition of concern, the shell, which can withstand only 600 reverse cycles, already represents a more severe limitation to the reverse condition for the test program. Again, if a full size blade were being designed based on this analysis, the high sheath stress in the reverse condition could be corrected.

## 8.5 Stress Contour Plots

By way of illustration, stress contour plots for HCF evaluation are presented as the percent of the allowable limit (as defined in section 8.2) for each of the blade components (spar, shell, sheath, and foam filler) for the design/cruise and take-off/climb conditions. Similar plots were made for all other operating conditions to evaluate HCF and LCF stress levels. Since the spar, sheath, and foam filler are isotropic materials, the spanwise, chordwise, and shear stresses at each element are combined into maximum and minimum principle stresses, and from these a maximum effective stress is obtained. The effective stress corresponds to a state of pure tensile stress as is obtained from a tensile test specimen. This stress is plotted as a percent of the design allowable. The shell, however, being a woven composite, is an anisotropic material. Therefore, the stresses at each element are not combined into an effective stress, but are presented as spanwise, chordwise, and shear stresses as a percent of the design allowable limit. The figure numbers corresponding to the design/cruise and take-off/ climb conditions are summarized in Tables 8-3 and 8-4, respectively.

Table 8-3

## SUMMARY OF STRESS CONTOUR PLOTS FOR DESIGN/CRUISE CONDITION

<u>Figure No.</u>	<u>Blade Component</u>	<u>Blade Side</u>	<u>Stress Contour Plotted (As a Percent of Design Limit)</u>
8-10	Spar	Face (pressure)	Effective
8-11	Spar	Camber (suction)	Effective
8-12	Shell	Face	Spanwise
8-13	Shell	Face	Chordwise
8-14	Shell	Face	Shear
8-15	Shell	Camber	Spanwise
8-16	Shell	Camber	Chordwise
8-17	Shell	Camber	Shear
8-18	Sheath	Face	Effective
8-19	Sheath	Camber	Effective
8-20	Foam Filler	Face	Effective
8-21	Foam Filler	Camber	Effective

Table 8-4

## SUMMARY OF STRESS CONTOUR PLOTS FOR TAKE-OFF/CLIMB CONDITION

<u>Figure No.</u>	<u>Blade Component</u>	<u>Blade Side</u>	<u>Stress Contour Plotted (As a Percent of Design Limit)</u>
8-22	Spar	Face (pressure)	Effective
8-23	Spar	Camber (suction)	Effective
8-24	Shell	Face	Spanwise
8-25	Shell	Face	Chordwise
8-26	Shell	Face	Shear
8-27	Shell	Camber	Spanwise
8-28	Shell	Camber	Chordwise
8-29	Shell	Camber	Shear
8-30	Sheath	Face	Effective
8-31	Sheath	Camber	Effective
8-32	Foam Filler	Face	Effective
8-33	Foam Filler	Camber	Effective

ORIGINAL PAGE IS  
OF POOR QUALITY

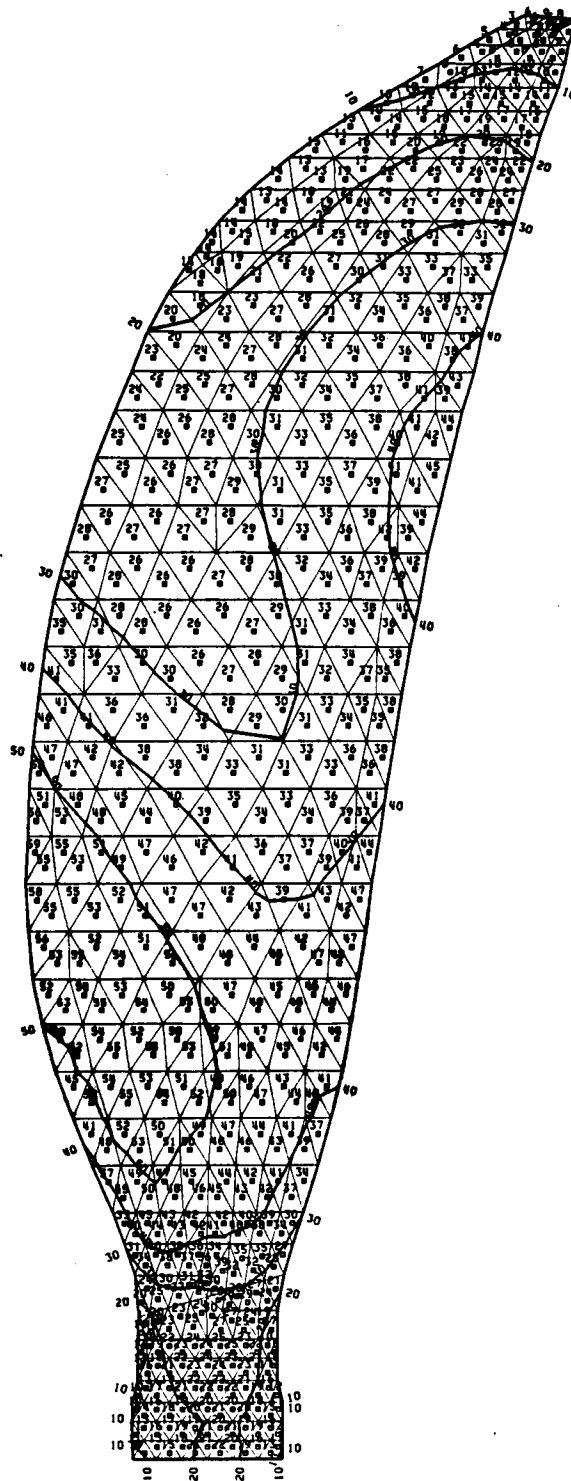


FIGURE 8-10. DESIGN/CRUISE HIGH CYCLE FATIGUE COMBINED EFFECTIVE STRESS  
(PERCENT OF DESIGN ALLOWABLE) SPAR, FACE SIDE

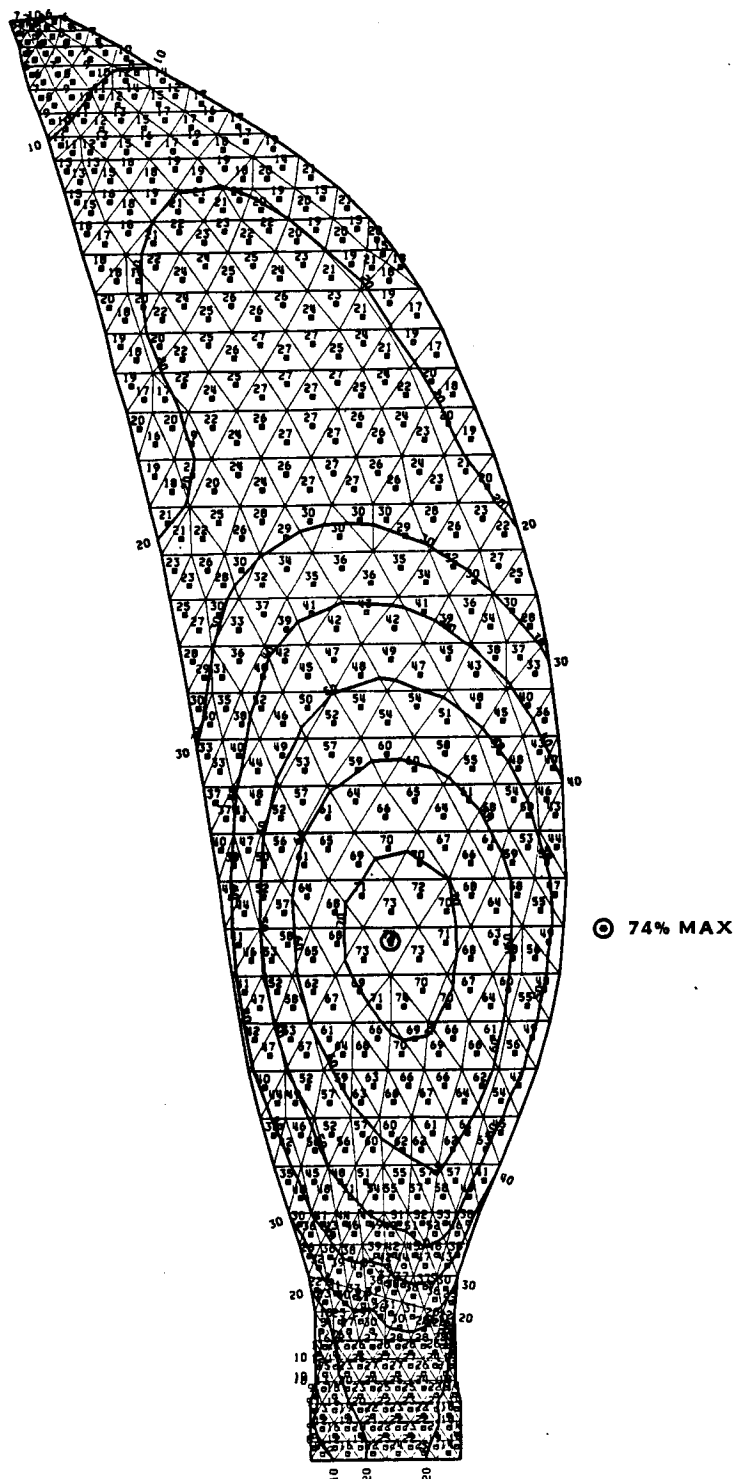


FIGURE 8-11. DESIGN/CRUISE HIGH CYCLE FATIGUE COMBINED EFFECTIVE STRESS (PERCENT OF DESIGN ALLOWABLE) SPAR, CAMBER SIDE

ORIGINAL PAGE IS  
OF POOR QUALITY

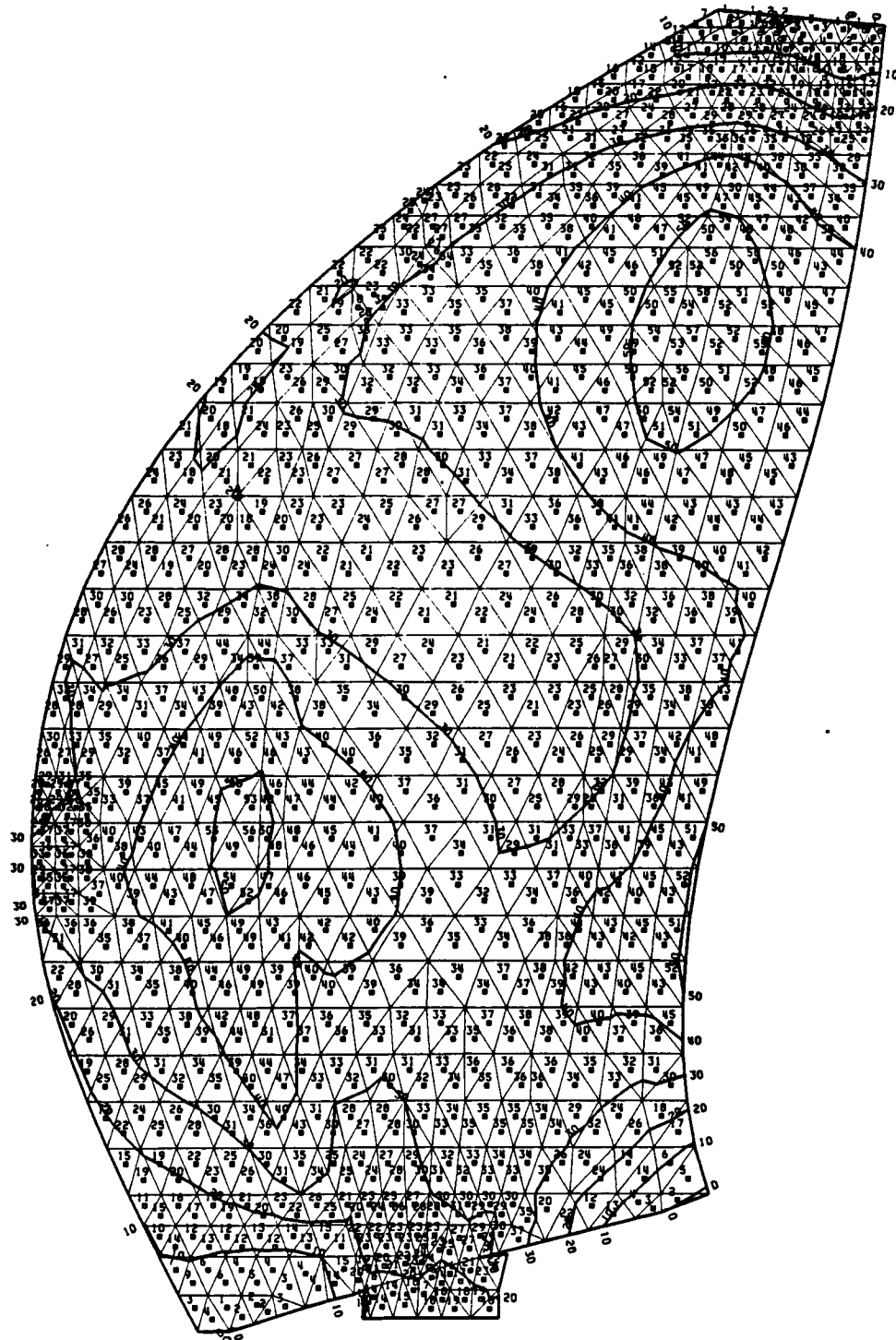


FIGURE 8-12. DESIGN/CRUISE HIGH CYCLE FATIGUE SPANWISE STRESS  
(PERCENT OF DESIGN ALLOWABLE) SHELL, FACE SIDE

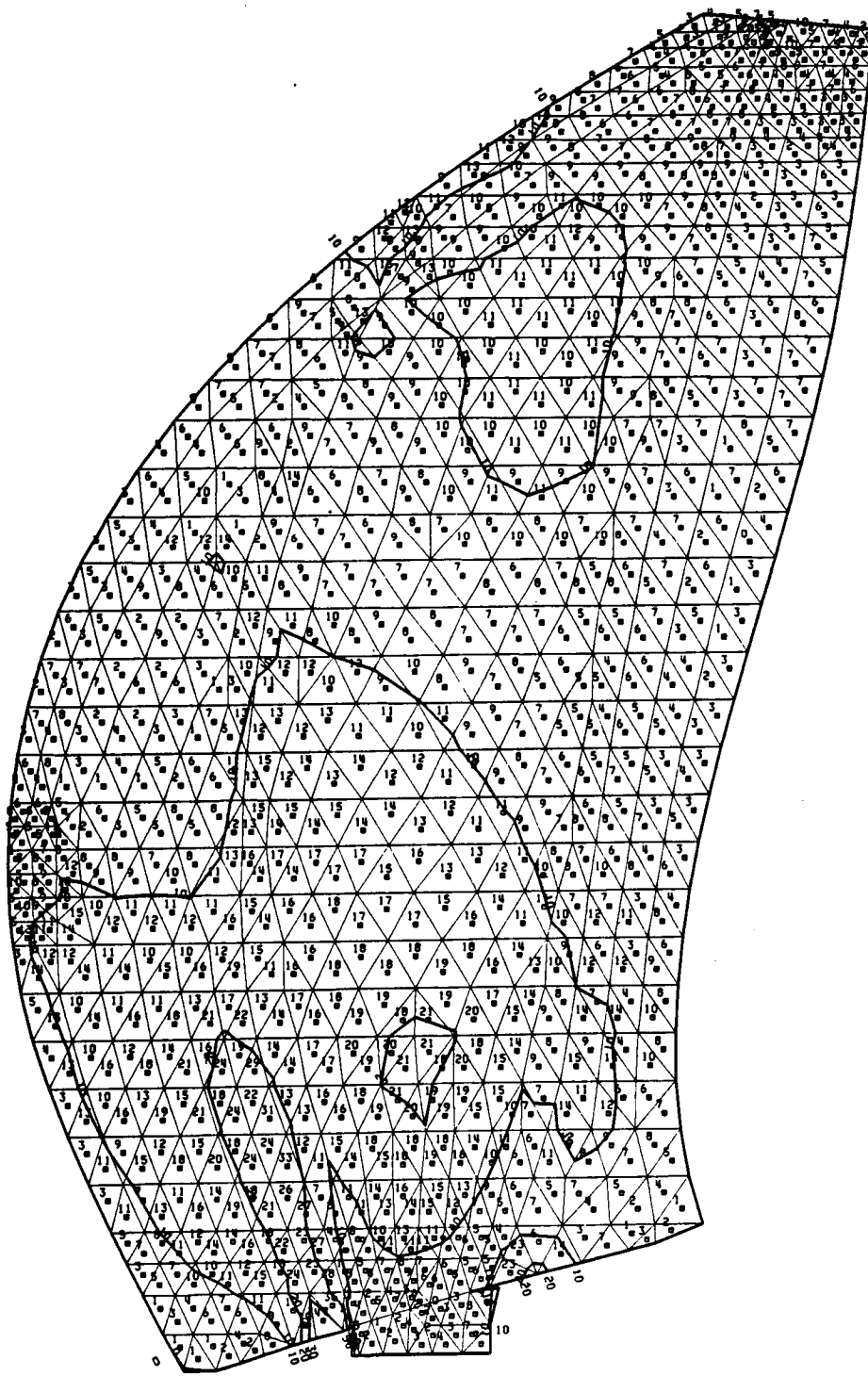


FIGURE 8-13. DESIGN/CRUISE HIGH CYCLE FATIGUE CHORDWISE STRESS  
(PERCENT OF DESIGN ALLOWABLE) SHELL, FACE SIDE

ORIGINAL PAGE IS  
OF POOR QUALITY

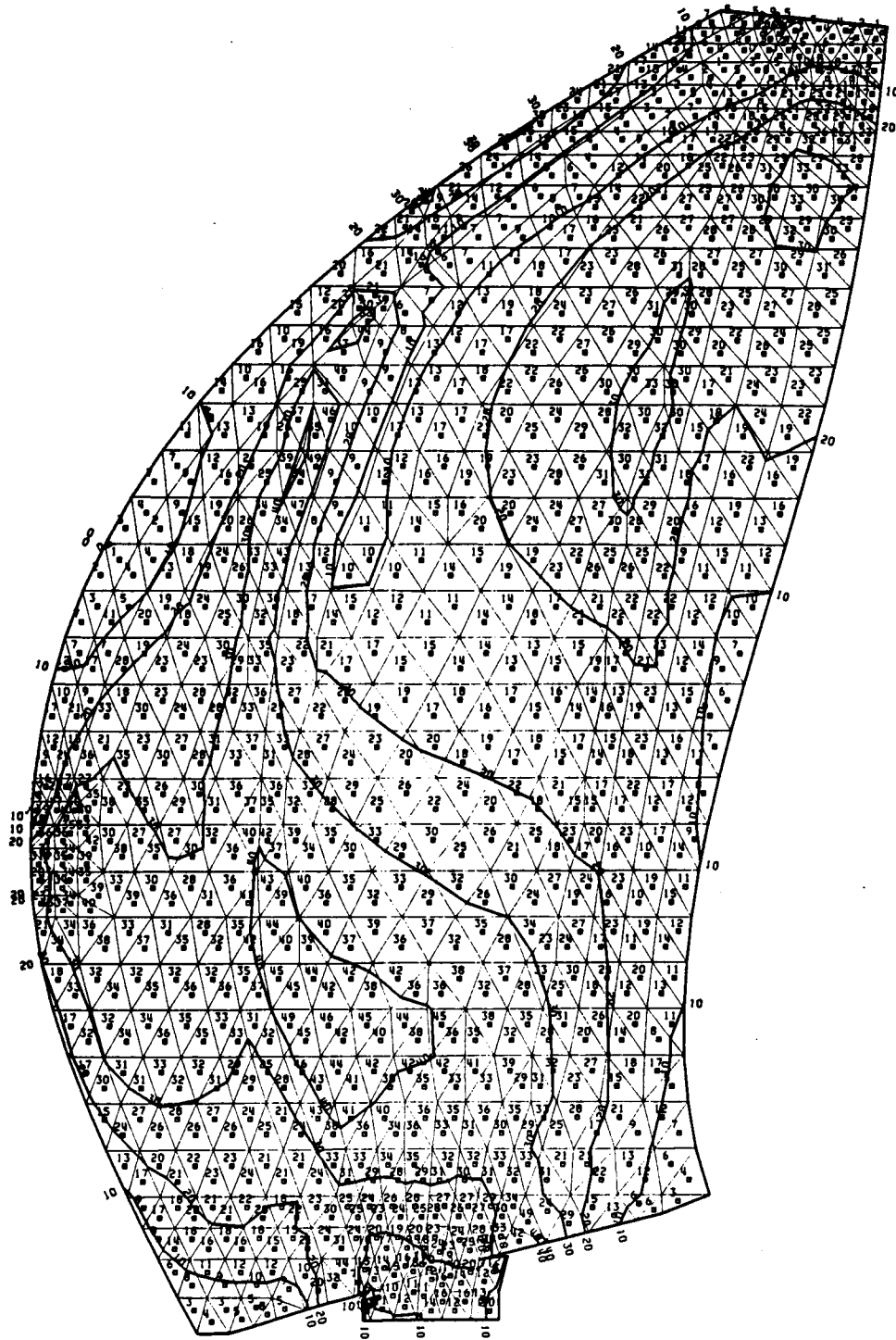


FIGURE 8-14. DESIGN/CRUISE HIGH CYCLE FATIGUE SHEAR EFFECTIVE STRESS  
(PERCENT OF DESIGN ALLOWABLE) SHELL, FACE SIDE



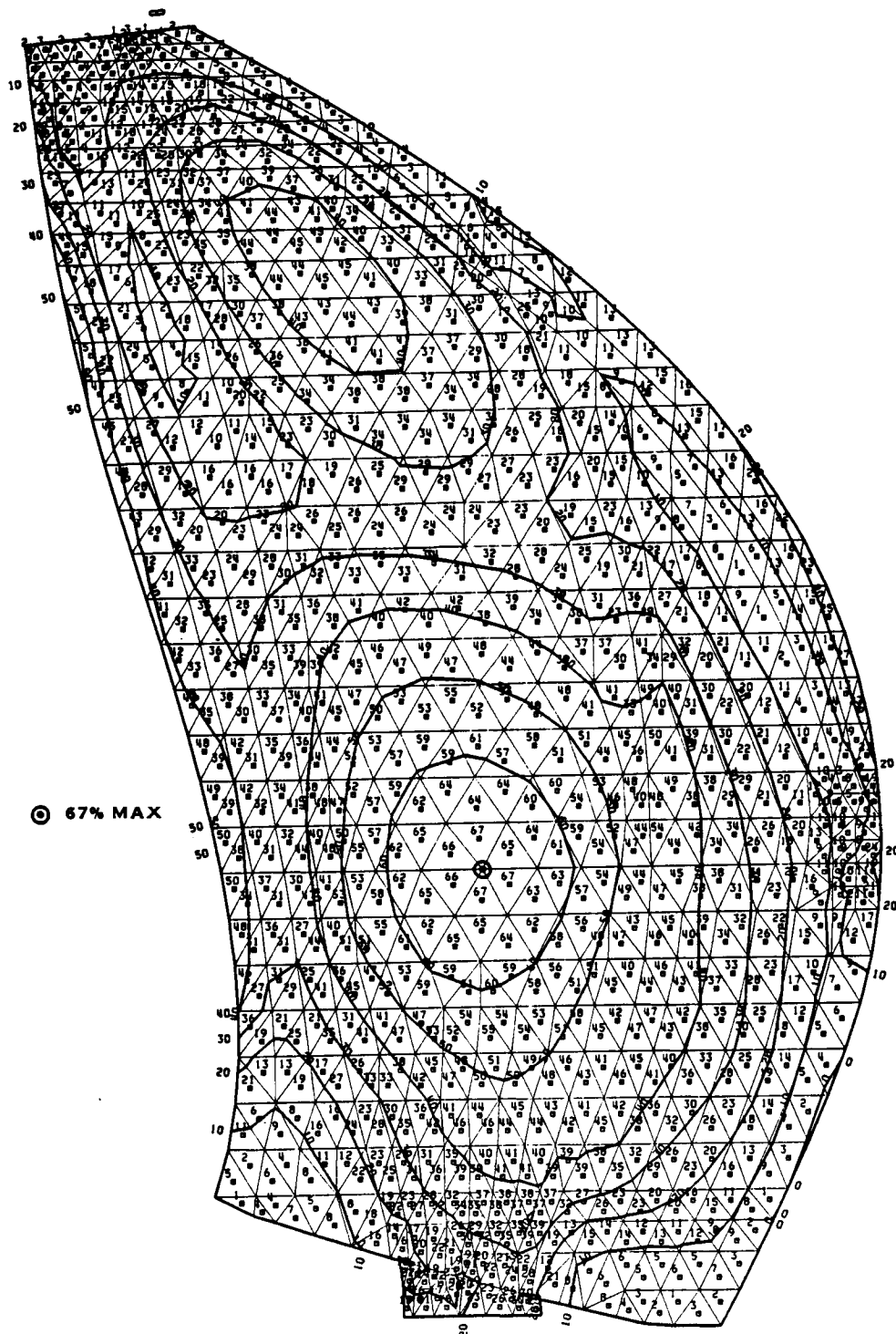


FIGURE 8-15. DESIGN/CRUISE HIGH CYCLE FATIGUE SPANWISE SHELL,  
CAMBER SIDE (PERCENT OF DESIGN ALLOWABLE)

ORIGINAL PAGE IS  
OF POOR QUALITY

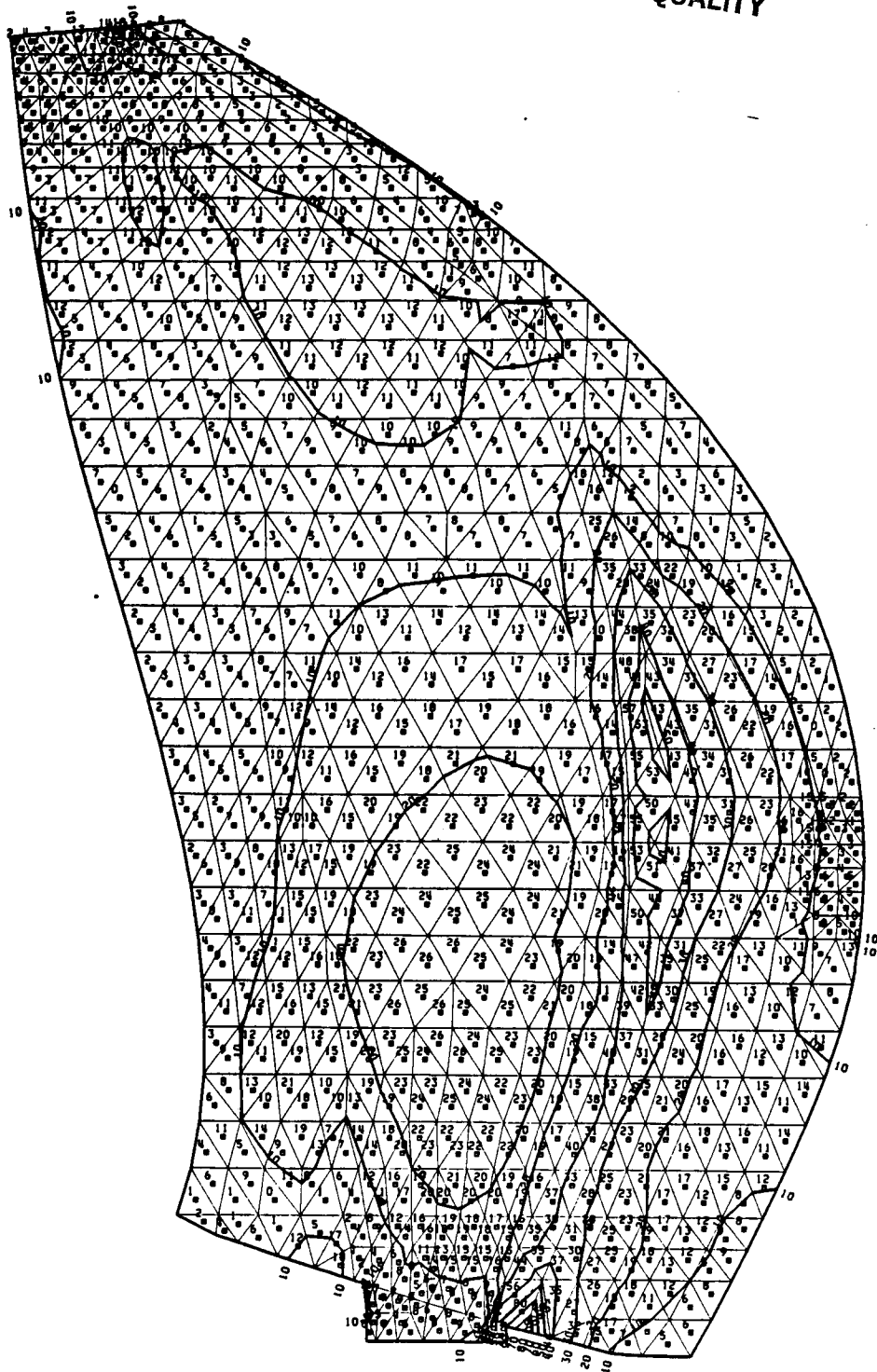


FIGURE 8-16. DESIGN/CRUISE HIGH CYCLE FATIGUE CHORDWISE STRESS  
(PERCENT OF DESIGN ALLOWABLE) SHELL, CAMBER SIDE

ORIGINAL PAGE IS  
OF POOR QUALITY

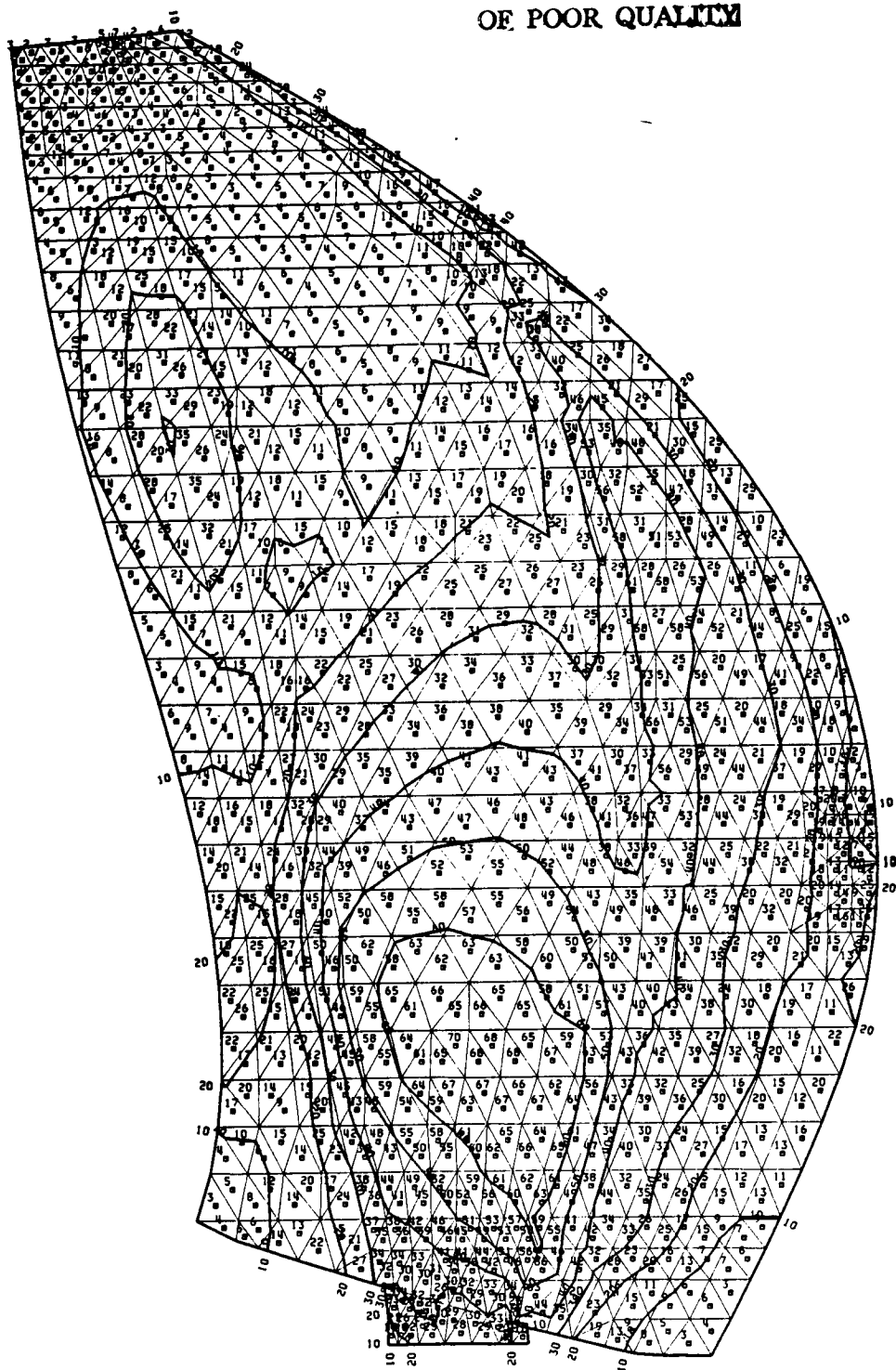


FIGURE 8-17. DESIGN/CRUISE HIGH CYCLE FATIGUE SHEAR STRESS  
(PERCENT OF DESIGN ALLOWABLE) SHELL, CAMBER SIDE

ORIGINAL PAGE IS  
OF POOR QUALITY

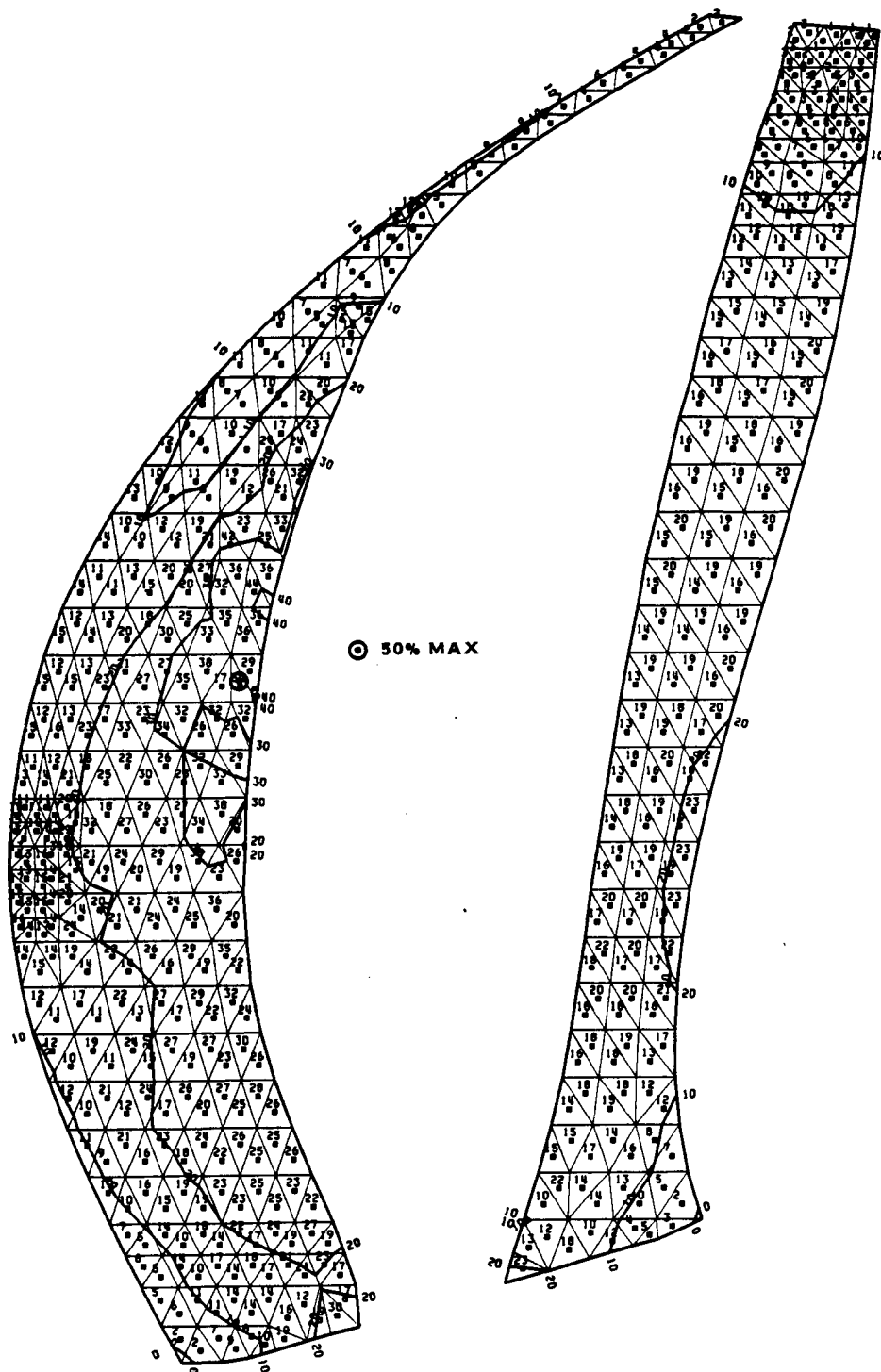


FIGURE 8-18. DESIGN/CRUISE HIGH CYCLE FATIGUE COMBINED EFFECTIVE STRESS  
(PERCENT OF DESIGN ALLOWABLE) FOAM, FACE SIDE

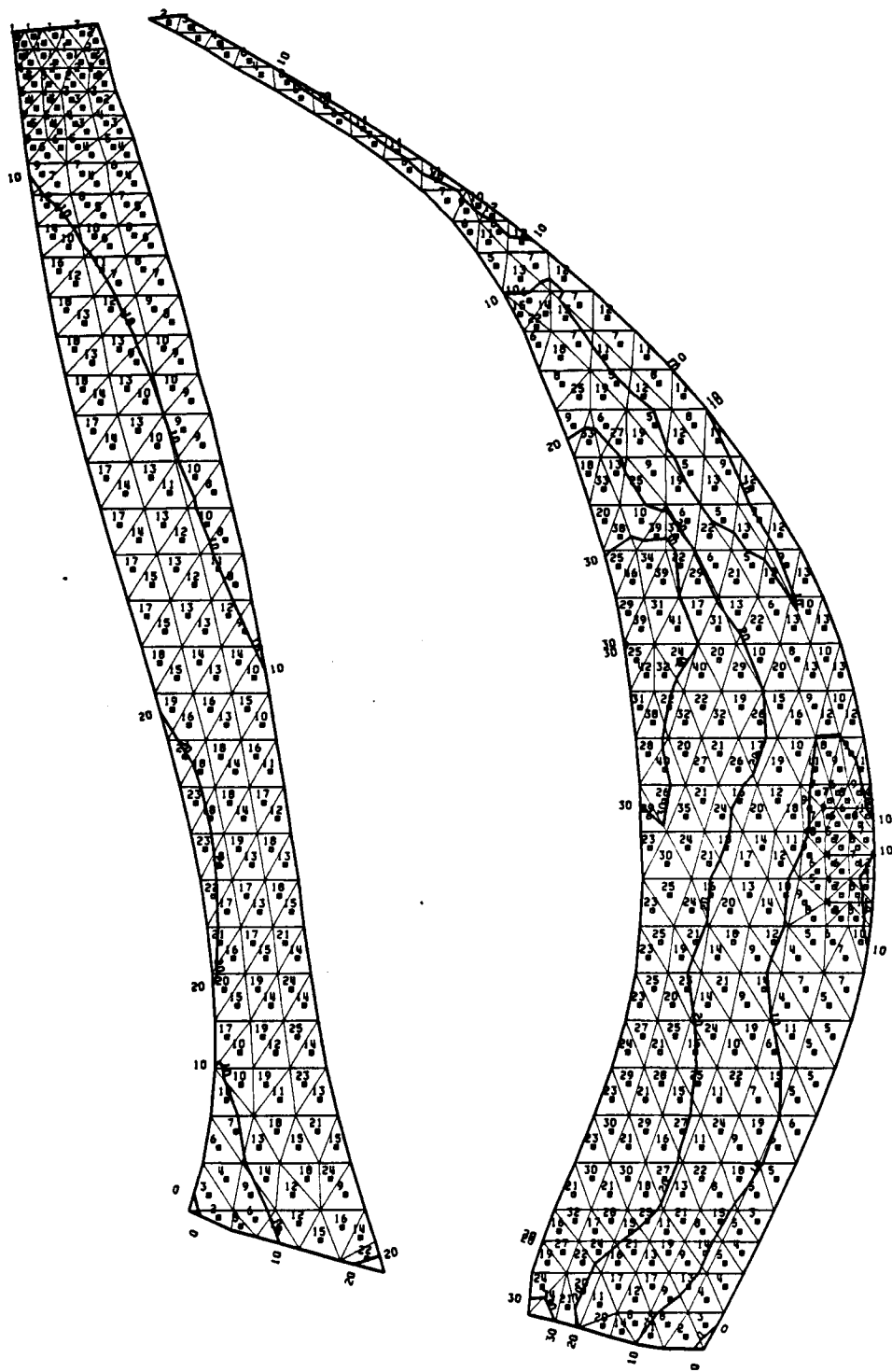


FIGURE 8-19. DESIGN/CRUISE HIGH CYCLE FATIGUE COMBINED EFFECTIVE STRESS (PERCENT OF DESIGN ALLOWABLE) FOAM, CAMBER SIDE

ORIGINAL PAGE IS  
OF POOR QUALITY

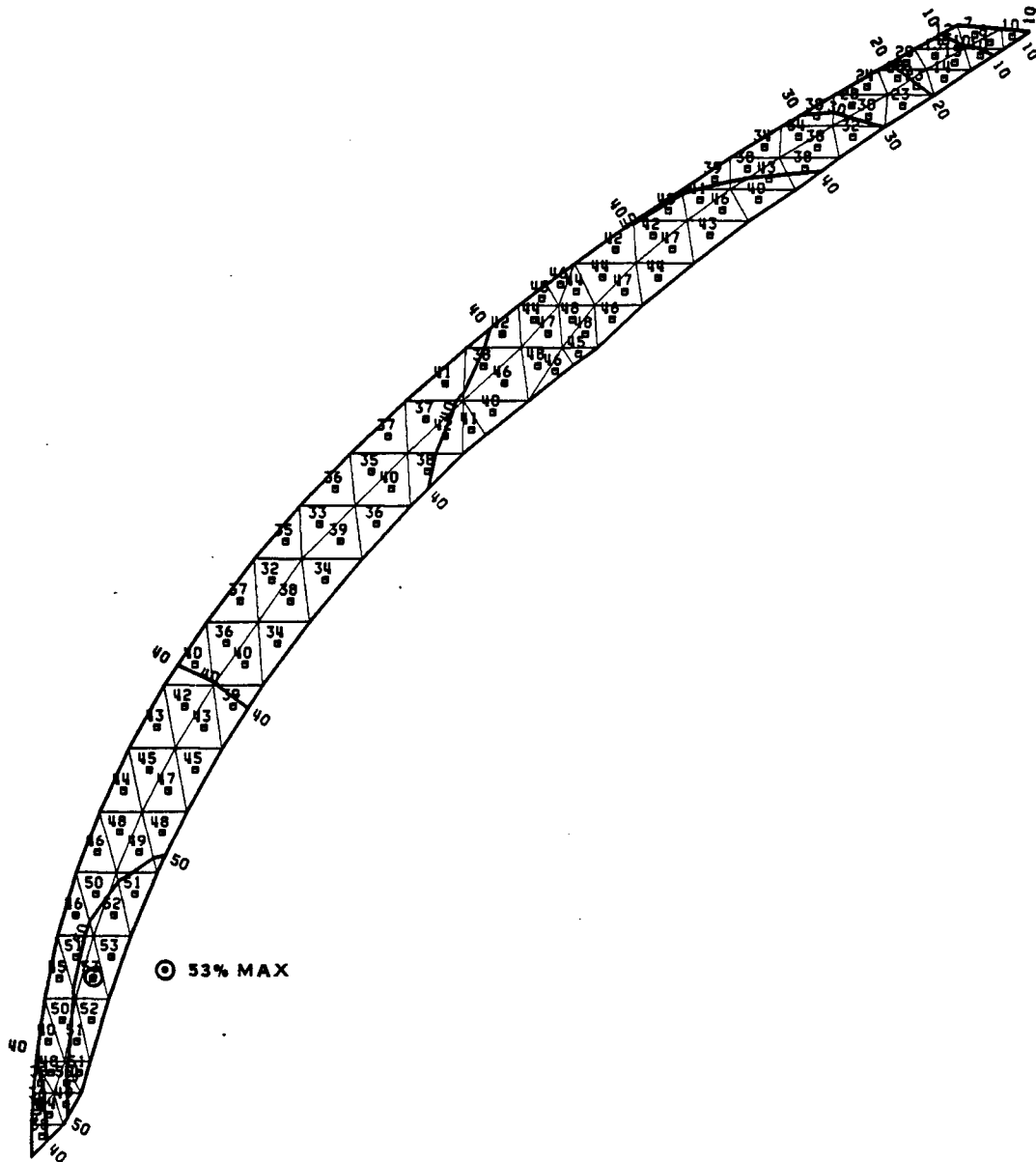


FIGURE 8-20. DESIGN/CRUISE HIGH CYCLE FATIGUE COMBINED EFFECTIVE STRESS  
(PERCENT OF DESIGN ALLOWABLE) SHEATH, FACE SIDE

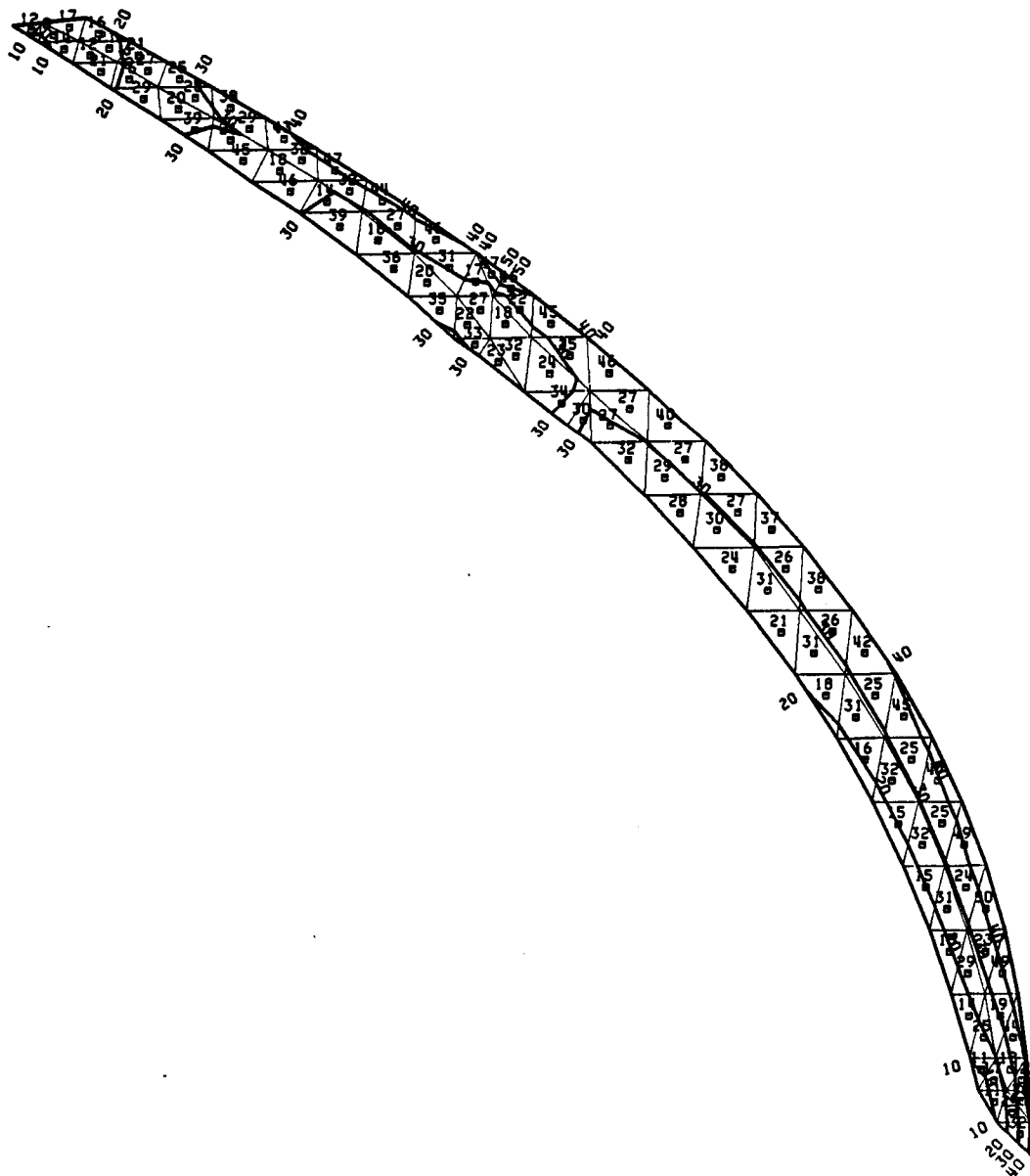


FIGURE 8-21. DESIGN/CRUISE HIGH CYCLE FATIGUE COMBINED EFFECTIVE STRESS (PERCENT OF DESIGN ALLOWABLE) SHEATH, CAMBER SIDE

ORIGINAL PAGE IS  
OF POOR QUALITY

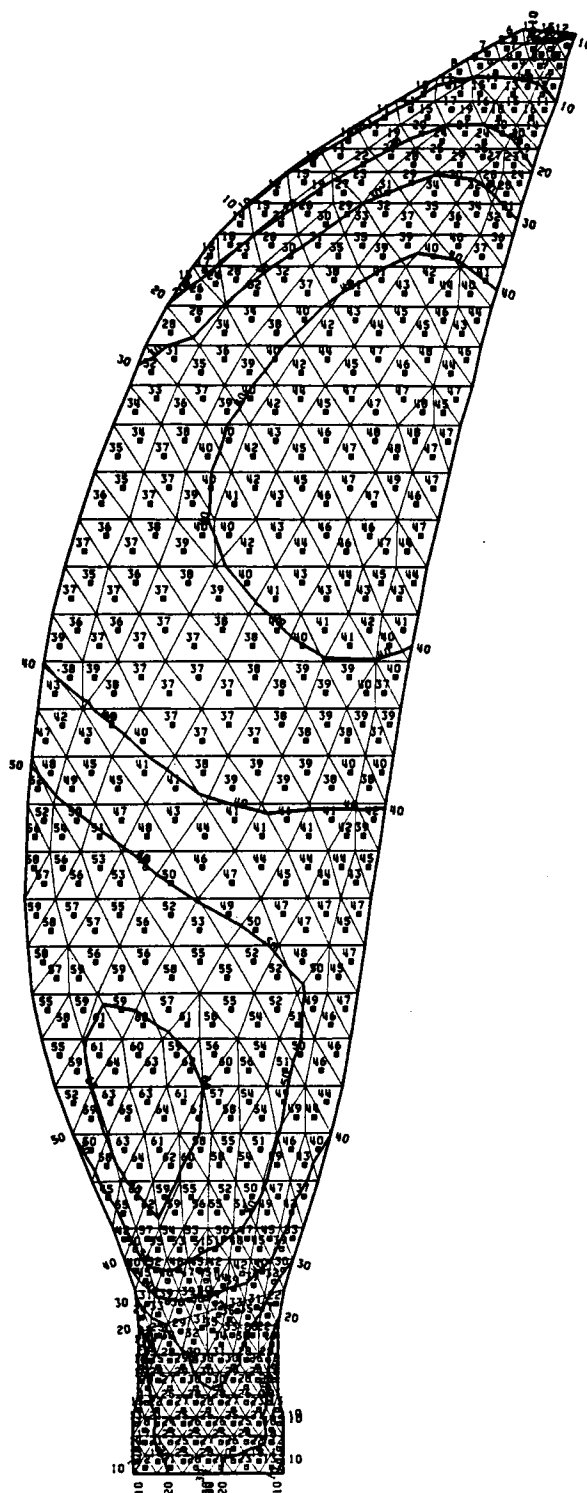


FIGURE 8-22. TAKE-OFF/CLIMB HIGH CYCLE FATIGUE COMBINED EFFECTIVE STRESS  
(PERCENT OF DESIGN ALLOWABLE) SPAR, FACE SIDE



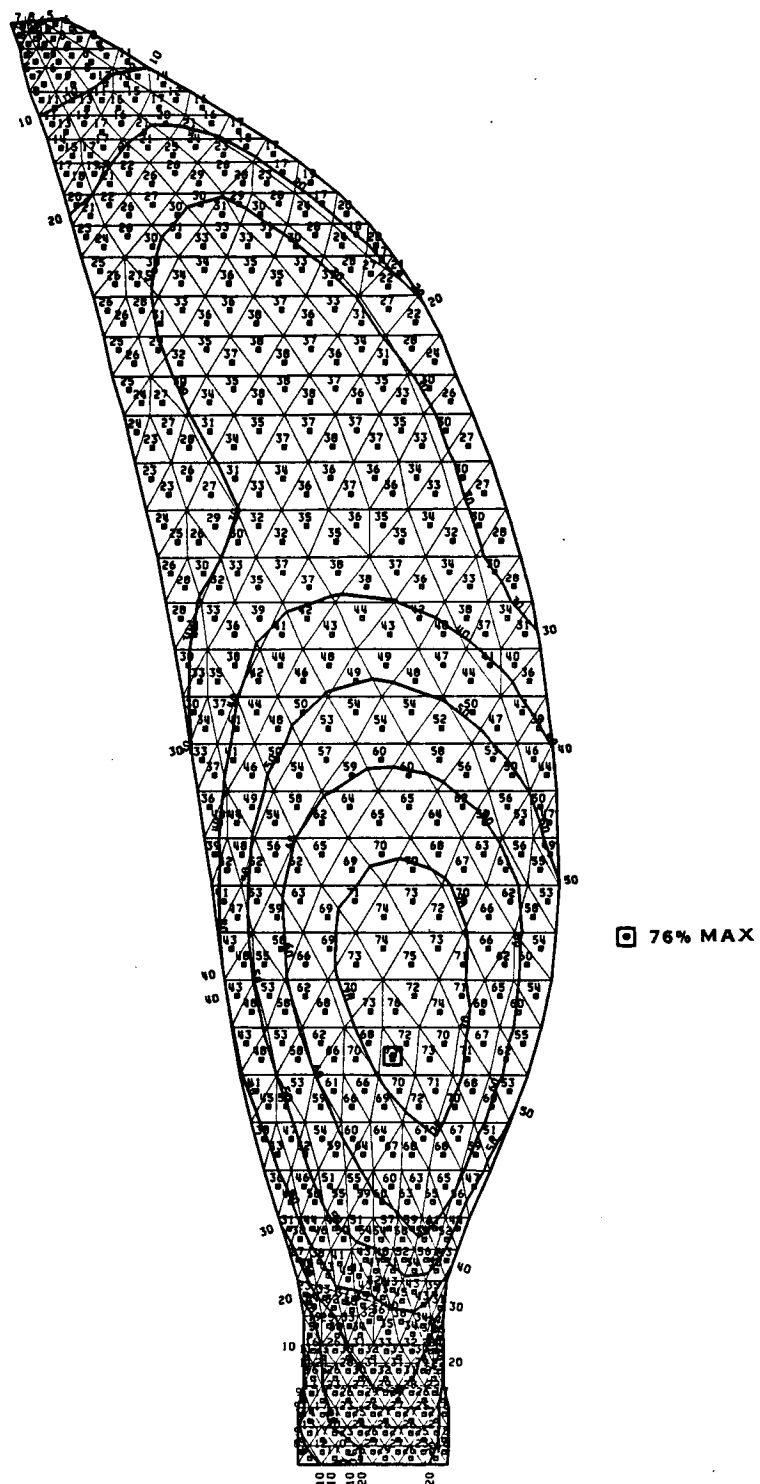


FIGURE 8-23. TAKE-OFF/CLIMB HIGH CYCLE FATIGUE COMBINED EFFECTIVE STRESS (PERCENT OF DESIGN ALLOWABLE) SPAR, CAMBER SIDE

ORIGINAL PAGE IS  
OF POOR QUALITY

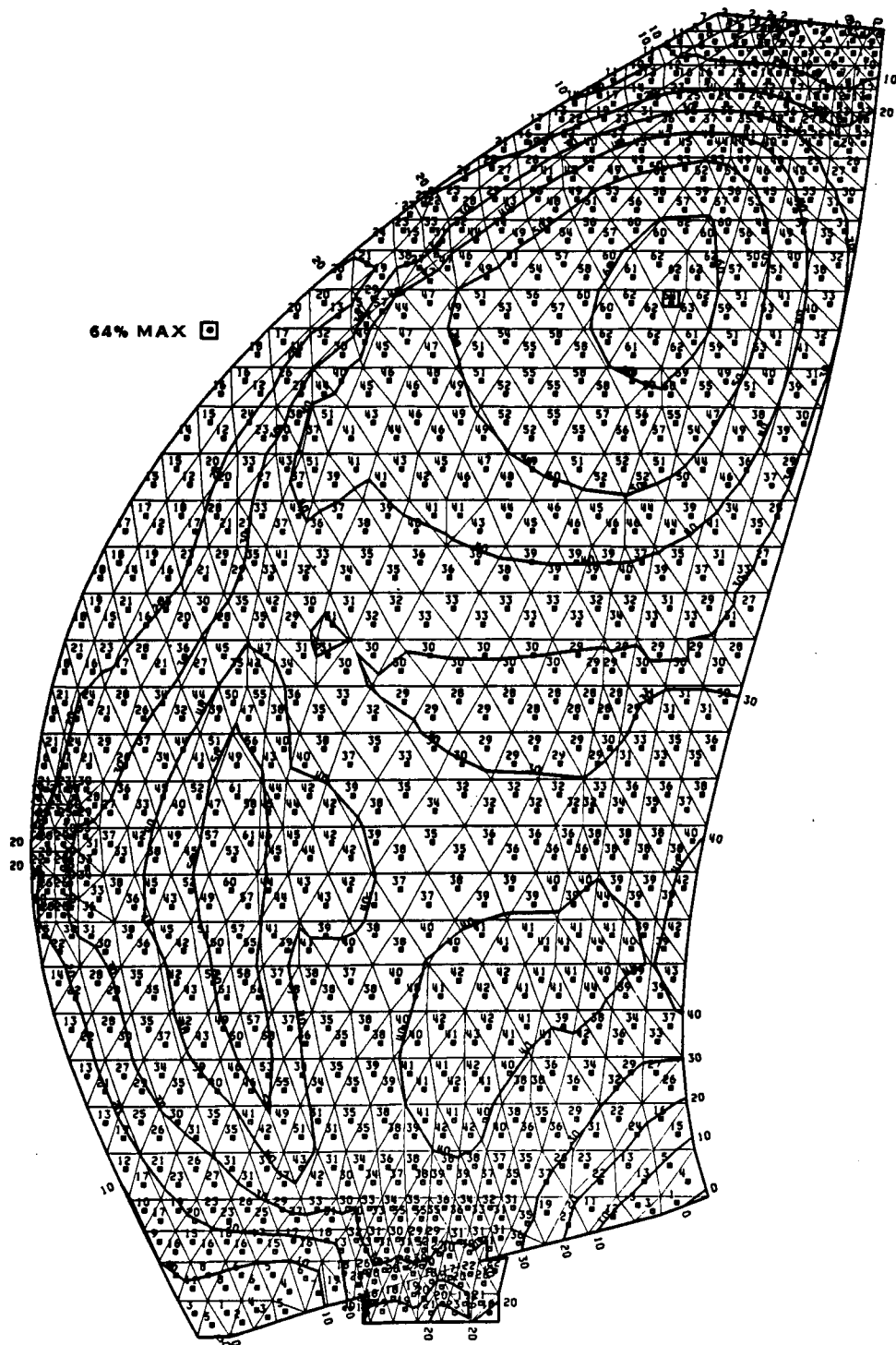


FIGURE 8-24. TAKE-OFF/CLIMB HIGH CYCLE FATIGUE SPANWISE STRESS  
(PERCENT OF DESIGN ALLOWABLE) SHELL, FACE SIDE

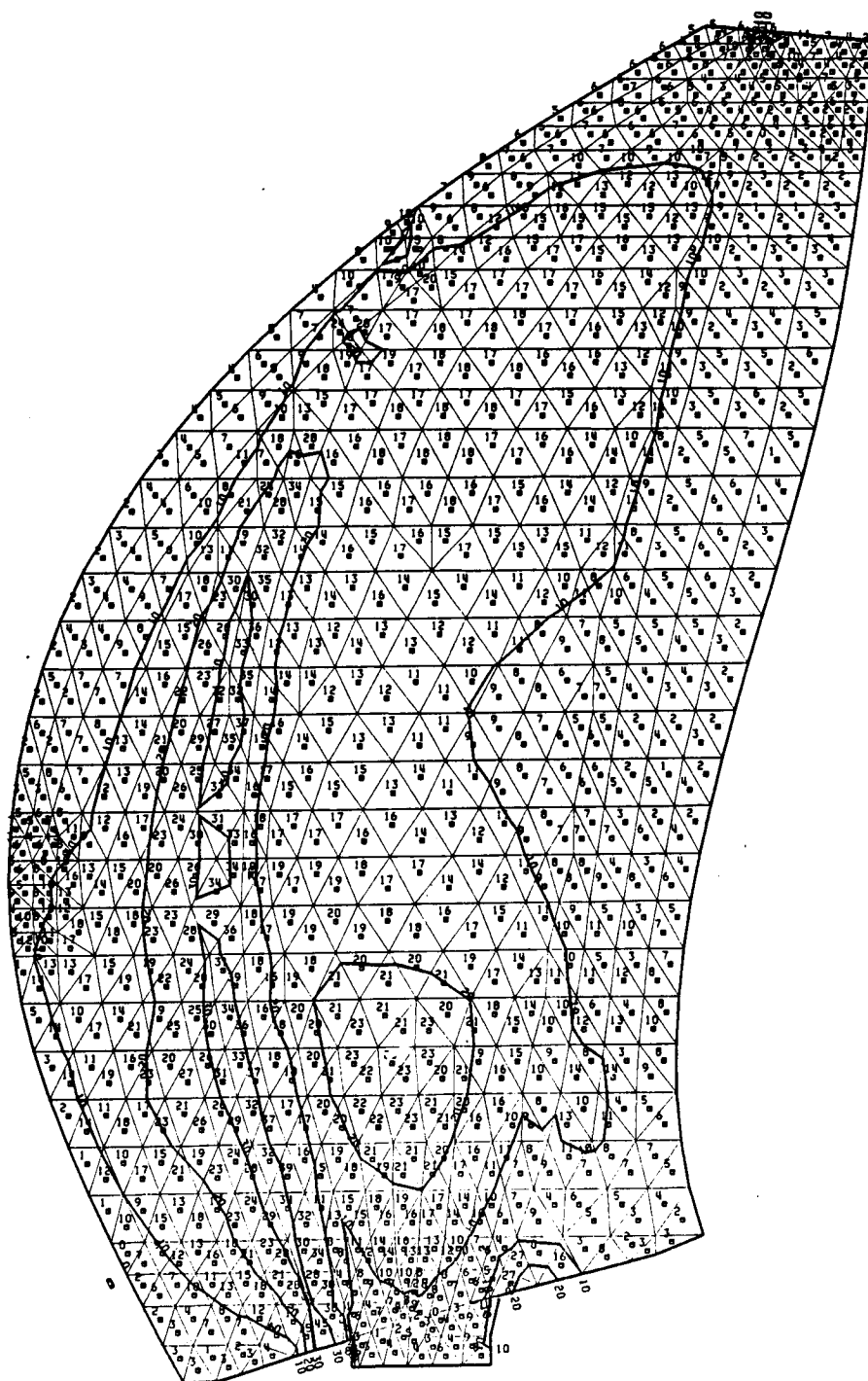


FIGURE 8-25, TAKE-OFF/CLIMB HIGH CYCLE FATIGUE CHORDWISE STRESS  
(PERCENT OF DESIGN ALLOWABLE) SHELL, FACE SIDE

ORIGINAL PAGE IS  
OF POOR QUALITY

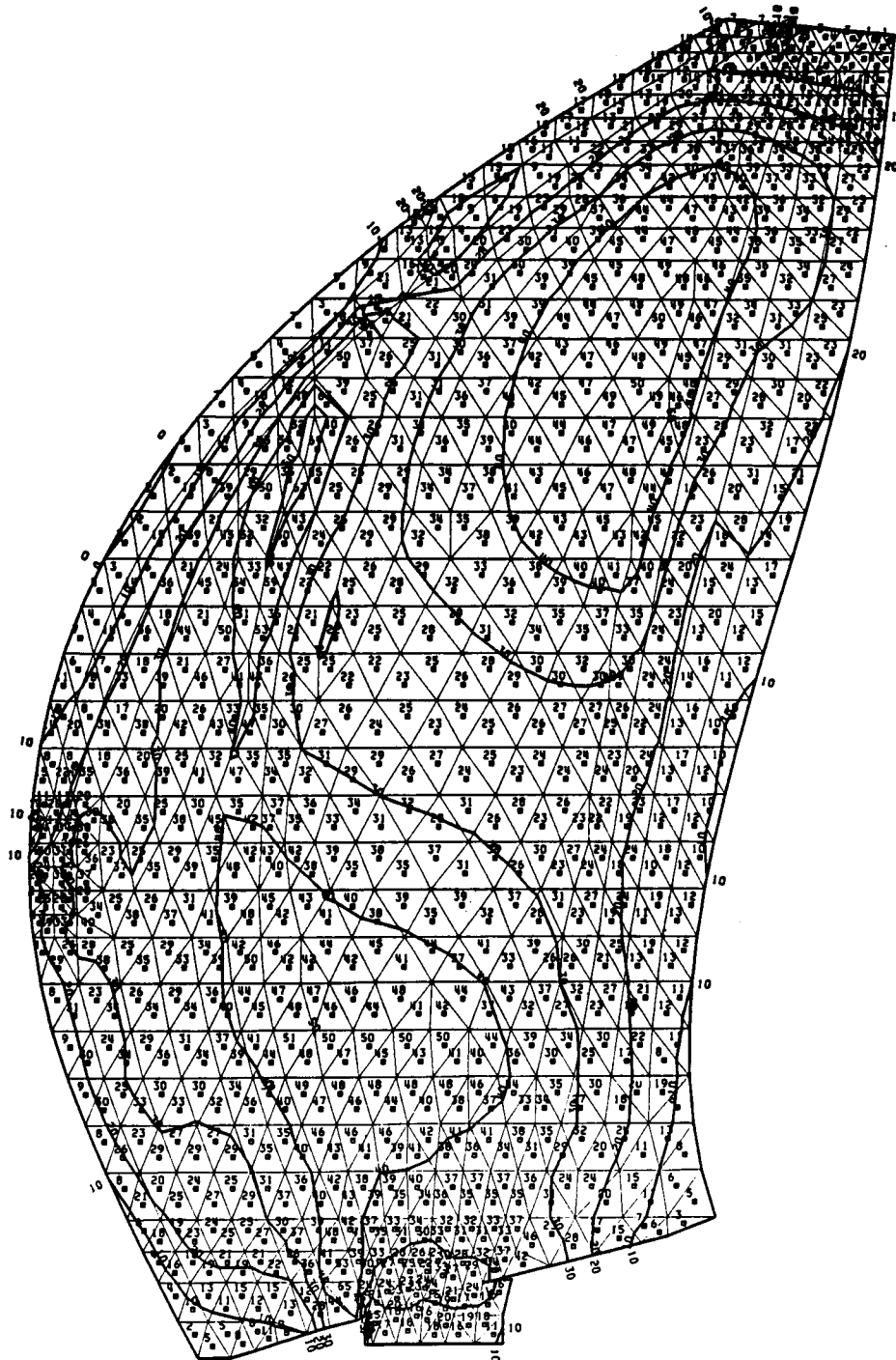


FIGURE 8-26. TAKE-OFF/CLIMB HIGH CYCLE FATIGUE SHEAR STRESS  
(PERCENT OF DESIGN ALLOWABLE) SHELL, FACE SIDE

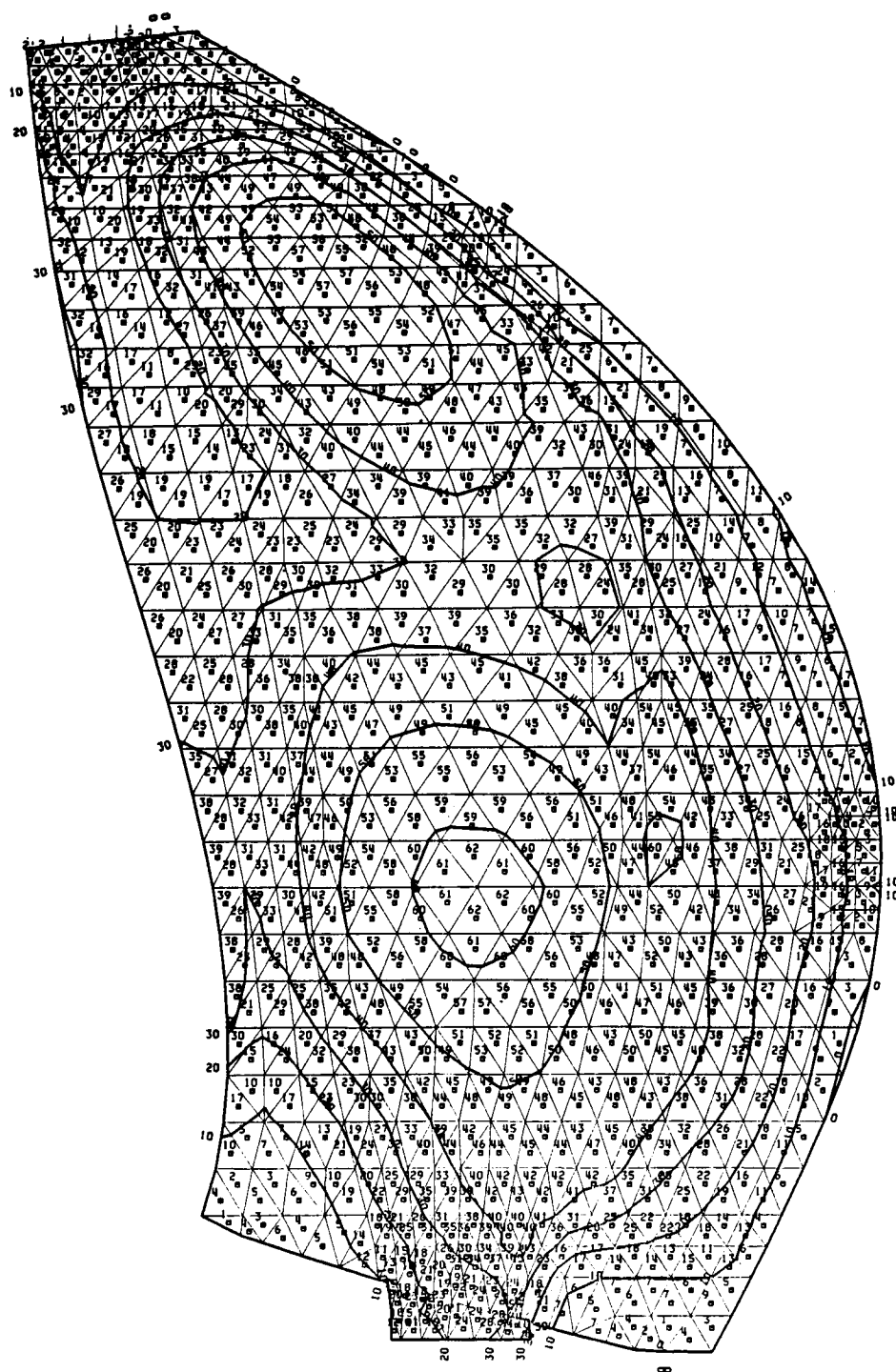


FIGURE 8-27. TAKE-OFF/CLIMB HIGH CYCLE FATIGUE SPANWISE EFFECTIVE STRESS (PERCENT OF DESIGN ALLOWABLE) SHELL, CAMBER SIDE

ORIGINAL PAGE IS  
OF POOR QUALITY

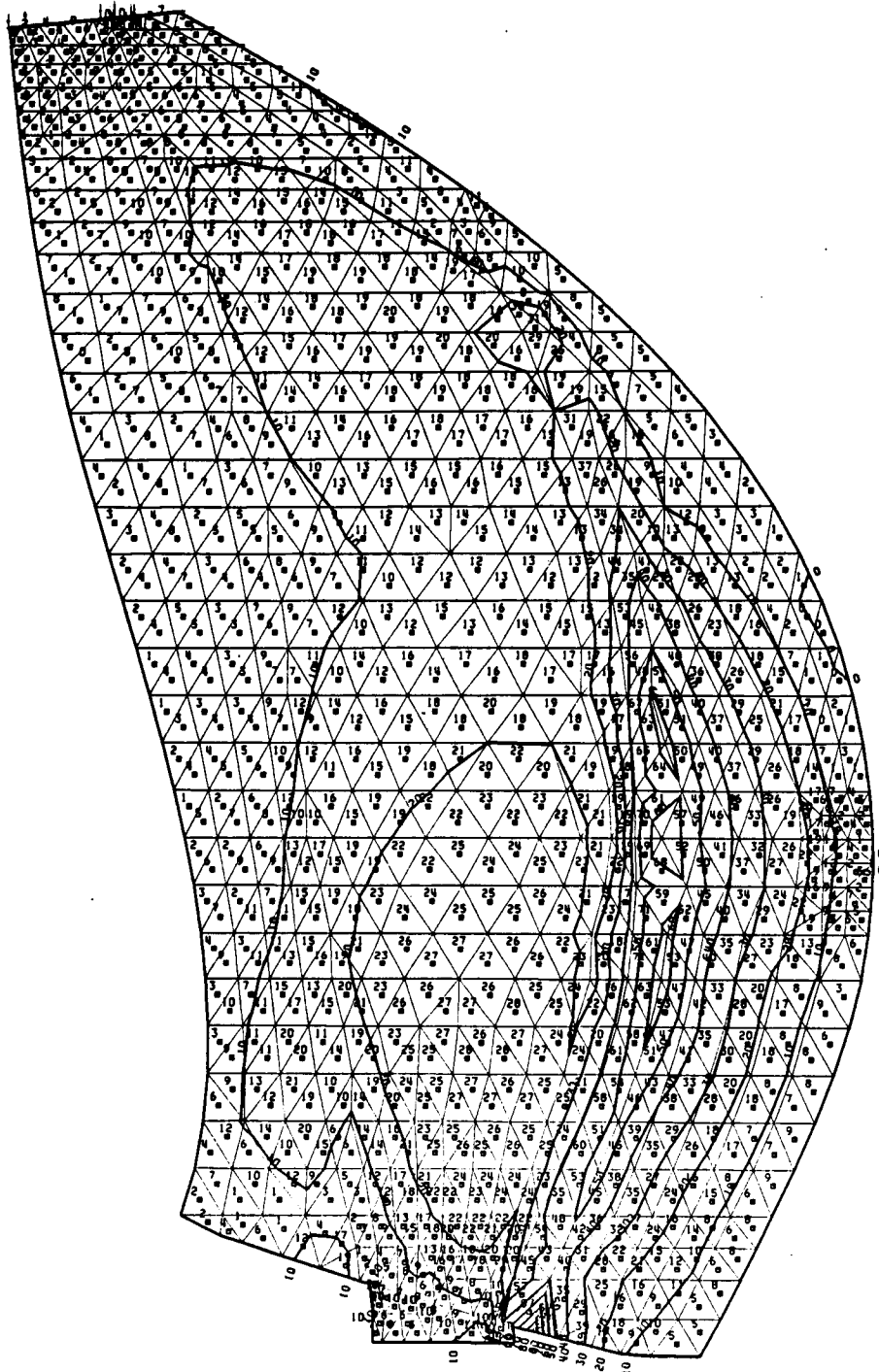


FIGURE 8-28. TAKE-OFF/CLIMB HIGH CYCLE FATIGUE CHORDWISE STRESS  
(PERCENT OF DESIGN ALLOWABLE) SHELL, CAMBER SIDE

ORIGINAL PAGE IS  
OF POOR QUALITY

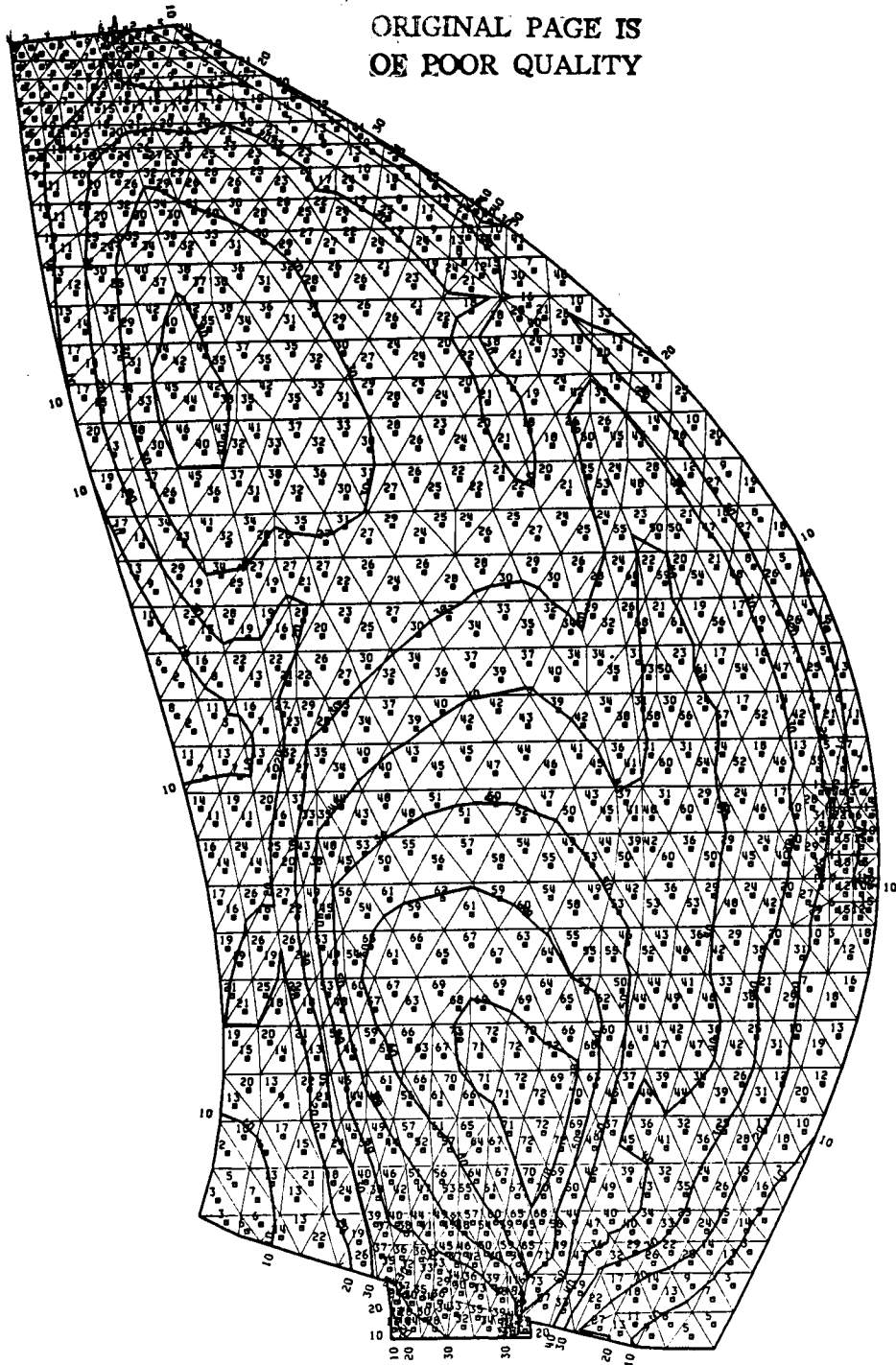


FIGURE 8-29. TAKE-OFF/CLIMB HIGH CYCLE FATIGUE SHEAR STRESS  
(PERCENT OF DESIGN ALLOWABLE) SHELL, CAMBER SIDE

ORIGINAL PAGE IS  
OF POOR QUALITY

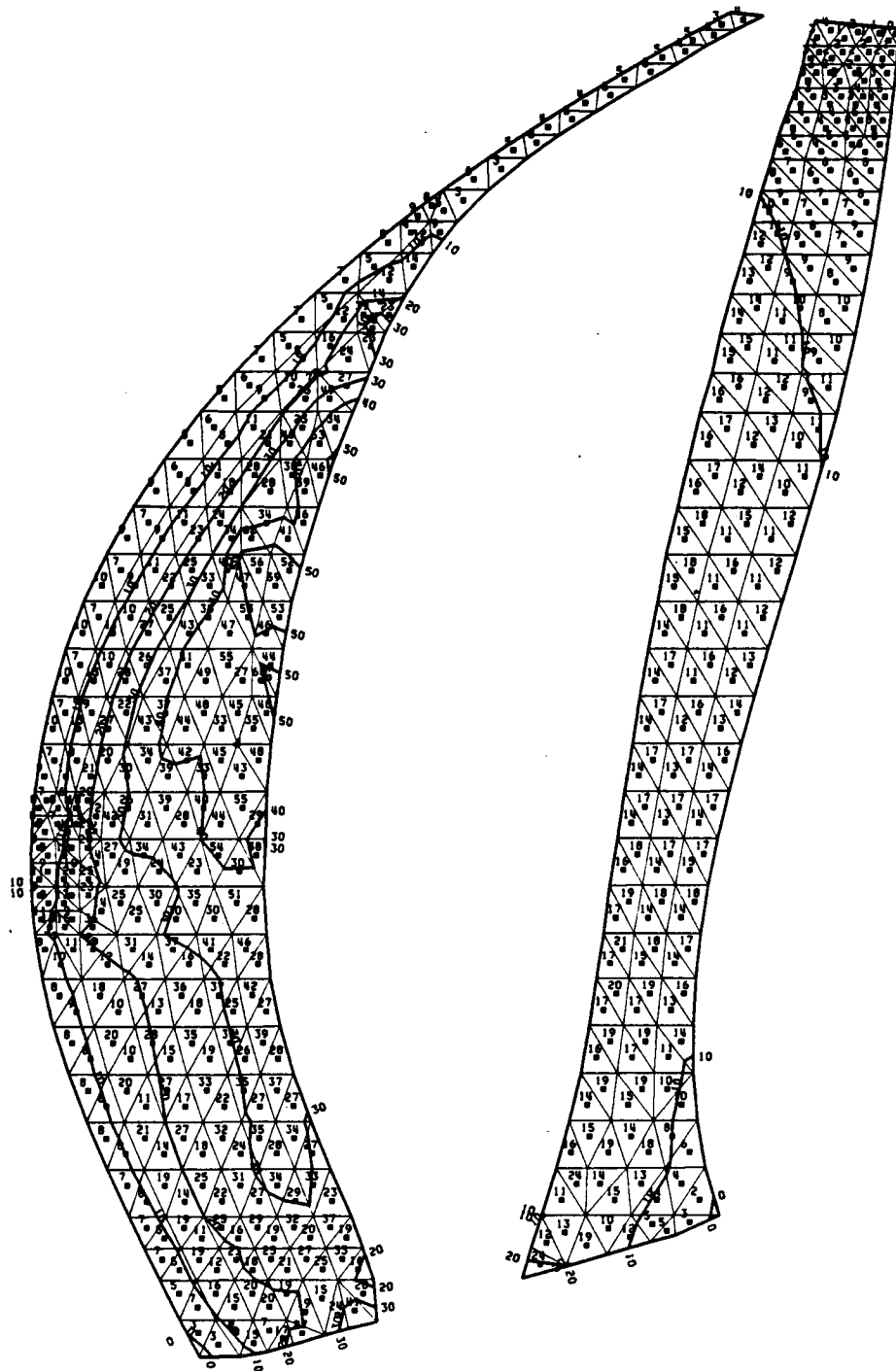


FIGURE 8-30. TAKE-OFF/CLIMB HIGH CYCLE FATIGUE COMBINED EFFECTIVE STRESS  
(PERCENT OF DESIGN ALLOWABLE) FOAM, FACE SIDE



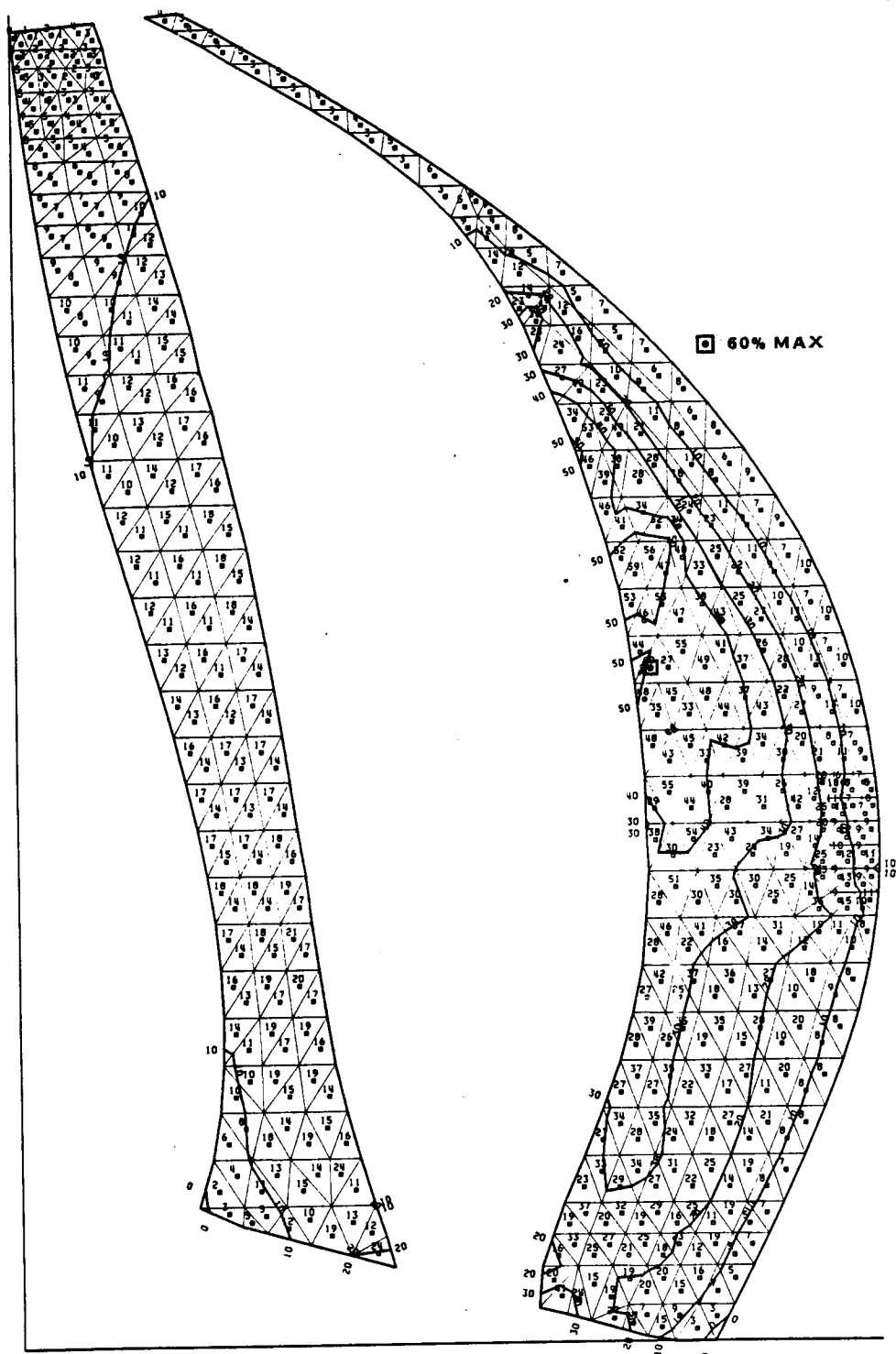


FIGURE 8-31. TAKE-OFF-CLIMB HIGH CYCLE FATIGUE COMBINED EFFECTIVE STRESS (PERCENT OF DESIGN ALLOWABLE) FOAM, CAMBER SIDE

ORIGINAL PAGE IS  
OF POOR QUALITY

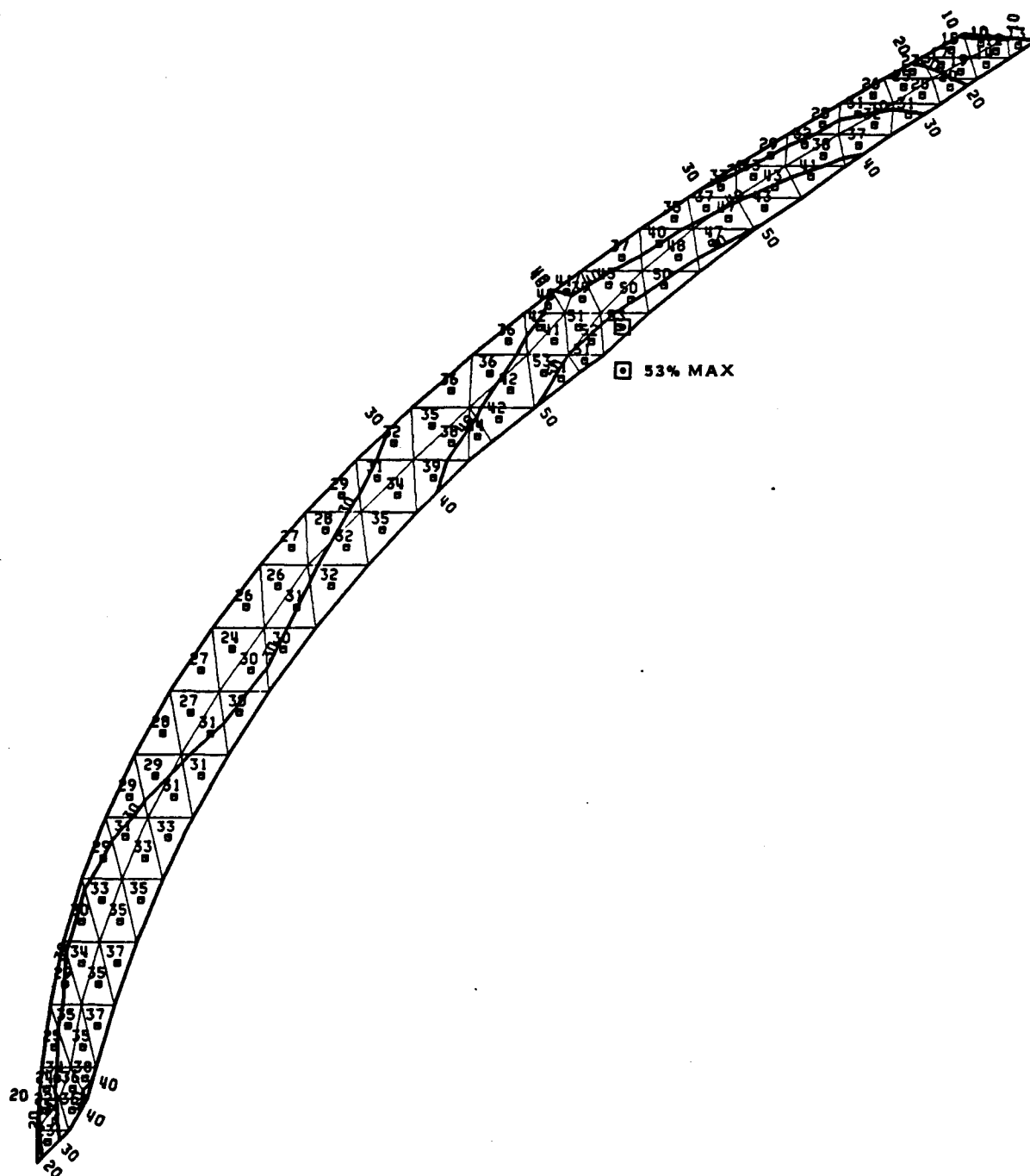


FIGURE 8-32. TAKE-OFF/CLIMB HIGH CYCLE FATIGUE COMBINED EFFECTIVE STRESS  
(PERCENT OF DESIGN ALLOWABLE) SHEATH, FACE SIDE

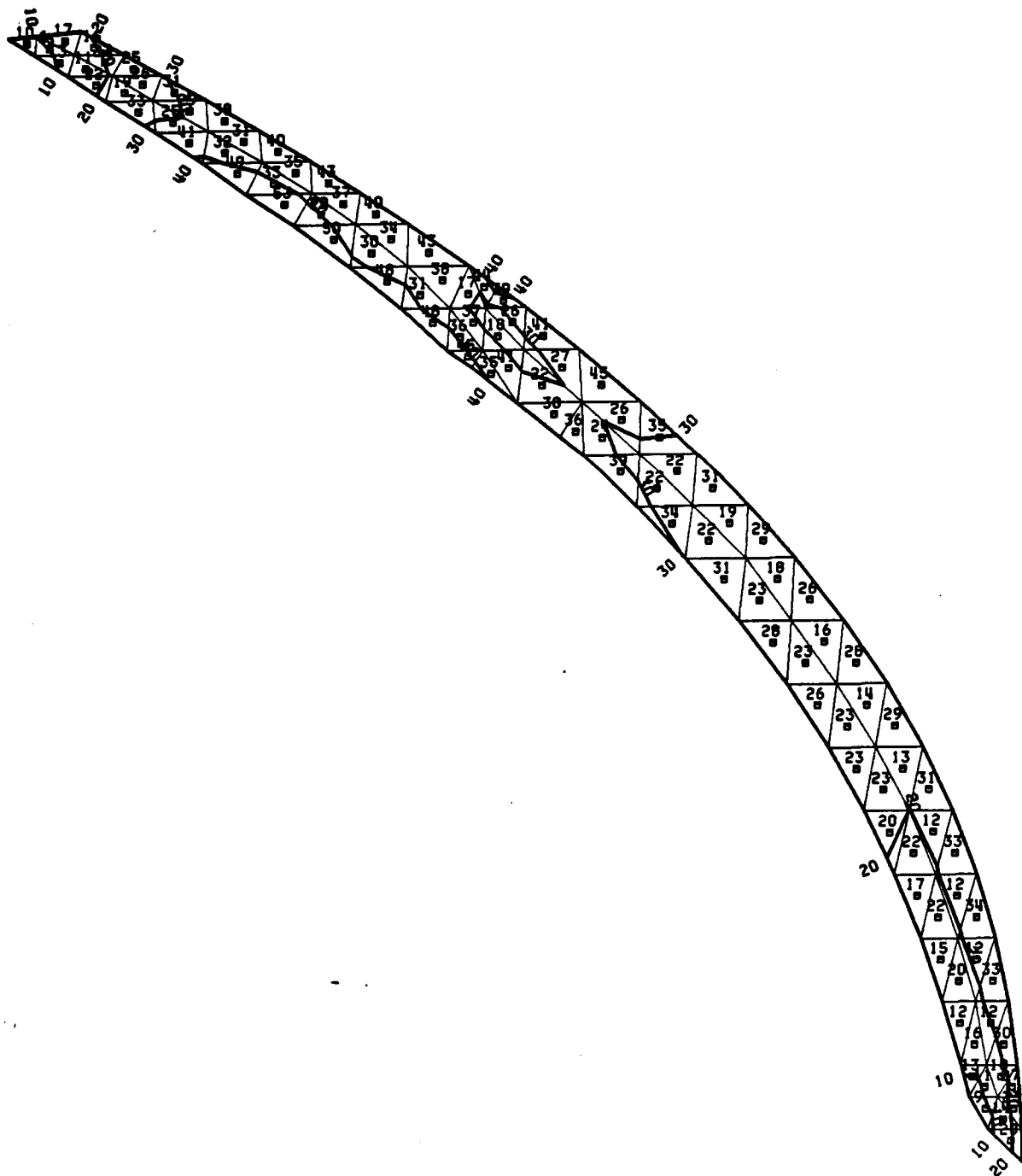


FIGURE 8-33. TAKE-OFF/CLIMB HIGH CYCLE FATIGUE COMBINED EFFECTIVE STRESS (PERCENT OF DESIGN ALLOWABLE) SHEATH, CAMBER SIDE

## 9.0 Resonant Frequencies and Mode Shapes

The prediction and placement of resonant frequencies of Prop-Fan blades are important aspects of the design analysis process. The first few integer orders of design rotational speed are important areas to avoid resonance because excitation forces for these are highest, decreasing inversely as P-order increases. Dynamic magnification, if insufficiently damped, could cause undesirable vibration and stresses. Furthermore, for an eight-bladed propeller, the 2-P, 3-P, 4-P, and 5-P modes of vibration are reactionless, that is, vibration loads at the blade shank are reacted internally through the hub, and no component of vibration is transmitted to the propeller shaft. Thus the pilot has no direct sensory feedback of the vibratory condition of the propeller. For this reason, specific bands of resonant frequency avoidance are specified. These frequency avoidance bands decrease in size with increasing P-order since the magnitude of the excitation decreases as P-order increases. Strain gages will be mounted on the blade surface such that undesirable vibratory levels, should they occur, can be detected and avoided during operation.

The vibratory mode shapes corresponding to the predicted resonant frequencies at various operating conditions are also important from the standpoint of evaluating susceptibility of the blade to low speed stalled flutter and high speed unstalled flutter. The use of these vibratory modes in determining flutter is discussed in section 10.

For the SR-7L blade, the first five resonant frequencies and corresponding mode shapes were predicted for the design/cruise and take-off/climb conditions previously listed in table 3-1 of section 3.3.1 and for all the conditions in table 3-2 of section 3.3.2.

## 9.1 Calculation Method

Because the NASTRAN eigenvalue solver is faster than the determinant search method used by the in-house finite element code (BESTRAN), the NASTRAN solver was used for this analysis. For each of the conditions analyzed, the mass and stiffness matrices, and the differential stiffening matrix were generated with the in-house code for the blade finite element model in its deflected position under load. These were then implanted in the NASTRAN eigenvalue solver to calculate the resonant frequencies and mode shapes. The differential stiffening matrix, which is described briefly in section 6.2.1, included negative stiffening terms for vibration in the in-plane and radial directions for a deflected rotating blade.

## 9.2 Results

A listing of the first five modal frequencies for each of the twelve conditions analyzed is given in table 9-1.

Table 9-1

## SR-7L BLADE RESONANT FREQUENCY SUMMARY

Frequencies in Hz

<u>No.</u>	<u>Condition</u>	<u>Mode</u>				
		<u>1</u>	<u>2</u>	<u>3</u>	<u>4</u>	<u>5</u>
D1	Design/Cruise	43.2	80.1	101.0	148.2	168.6
D2	Take-off/Climb	45.7	77.2	103.2	147.5	170.4
1A	ONERA, 8 Blade	43.4	79.6	100.9	149.8	167.1
1B	ONERA, 4 Blade	43.4	79.7	100.8	149.6	167.2
1C	ONERA, 2 Blade	43.4	79.9	101.2	149.4	168.7
2	Static Thrust	46.4	76.3	103.1	148.4	169.6
3	Reverse Thrust	50.1	73.7	94.3	138.1	148.7
4	Cruise, Low RPM	38.8	77.6	95.6	143.2	155.9
5	Cruise, Hi RPM	44.0	80.7	101.9	149.0	169.4
6	Climb, Mid Altitude	44.1	78.9	102.0	148.8	169.5
7	Dive, Mid Altitude	44.7	77.0	102.2	150.1	168.6
8	Dive, High Altitude	44.0	77.3	101.6	149.5	168.2

The calculated modal frequencies for the required design conditions of design/cruise and take-off/climb are also plotted on a Campbell diagram in figure 9-1. The Campbell diagram includes the integer order resonance avoidance bands specified in the design requirements. Static frequencies are also shown. These frequencies were calculated with a clamped blade shank, and therefore are not shown connected with the other modes that were calculated at speed.

As can be seen from the diagrams, all resonance placement requirements have been met except for the second mode in the design/cruise condition which infringes slightly on the 3-P avoidance band. This is not of great concern since the second mode is edgewise, and is sensitive to retention stiffness. A reduction in frequency will accompany a reduction in stiffness. Planned measurements of static blade frequencies early in the test program will help identify potential problems. Generally, when there has been a deviation in propeller blade frequency or stiffness from that predicted, past propeller experience has shown it to be toward the low side. In other words, measured frequency and/or stiffness has been less than that predicted. Thus, the 3-P infringement during cruise is of less concern on the low side of the avoidance band than on the high side. As mentioned above, SR-7L blade vibratory stresses will be monitored during testing such that 3-P resonance problems could be quickly identified. Besides, at this time, it is difficult to project any source of 3-P load excitations for the SR-7L installation.

Figure 9-2 shows the relationship between each of the first five calculated modal frequencies of the ten additional analysis conditions with respect to the 2-P through 5-P resonance avoidance bands. Meeting resonance for these conditions was a goal and not a requirement. However, most resonant frequencies clear the avoidance bands comfortably. The second mode, again, infringes slightly on the 3-P band. As mentioned above, placing the second mode, which is edgewise, at the lower bound of the 3-P avoidance band is not of great concern.

A second area of possible concern is ground operation. The static thrust case first mode infringes slightly on the expanded avoidance zone for ground operation, but the first mode in reverse shows a significant violation of the expanded zone. Resonances in reverse are affected by blade angle setting, that is, the blade angle setting of -10 degrees is such that the first mode vibration is predominantly bending in the stiff, out-of-plane direction, hence the increase in frequency. The motion of the second mode, which is edgewise however, is predominantly in the reduced stiffness, in-plane direction, hence the reduced frequency. Effects on higher modes are difficult to identify because they are altered by large steady-state tip deflections due to airload reversal, as well as angle setting effects. Blade strain gage responses in the reverse and static thrust conditions should be closely monitored during rig testing in order to characterize these modes before testing on an aircraft. If unacceptable stress levels due to dynamic magnification cannot be avoided, these conditions may need to be tested at lower power levels and/or modified blade angle settings.

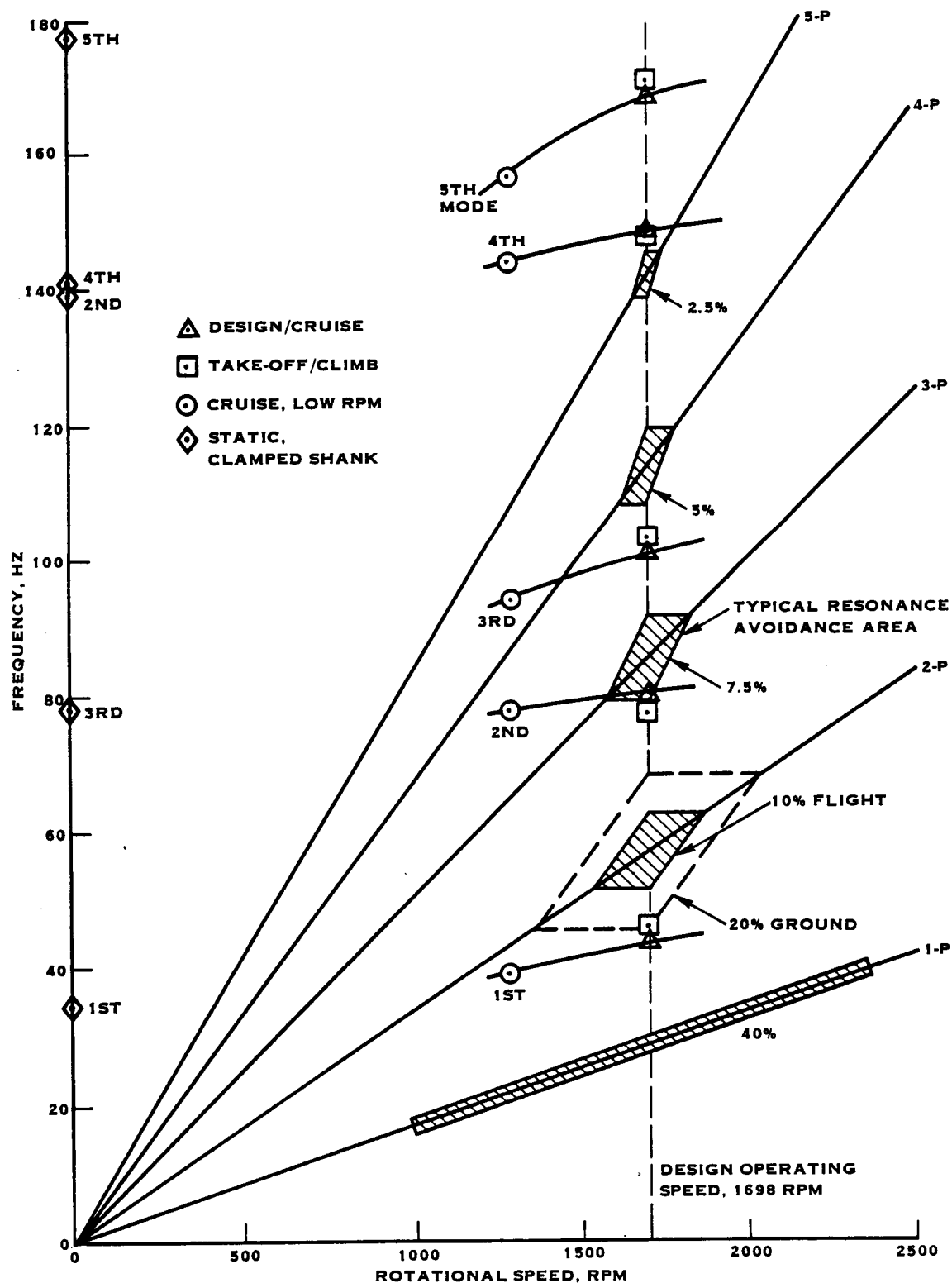


FIGURE 9-1. CALCULATED MODAL FREQUENCIES

ORIGINAL PAGE IS  
OF POOR QUALITY

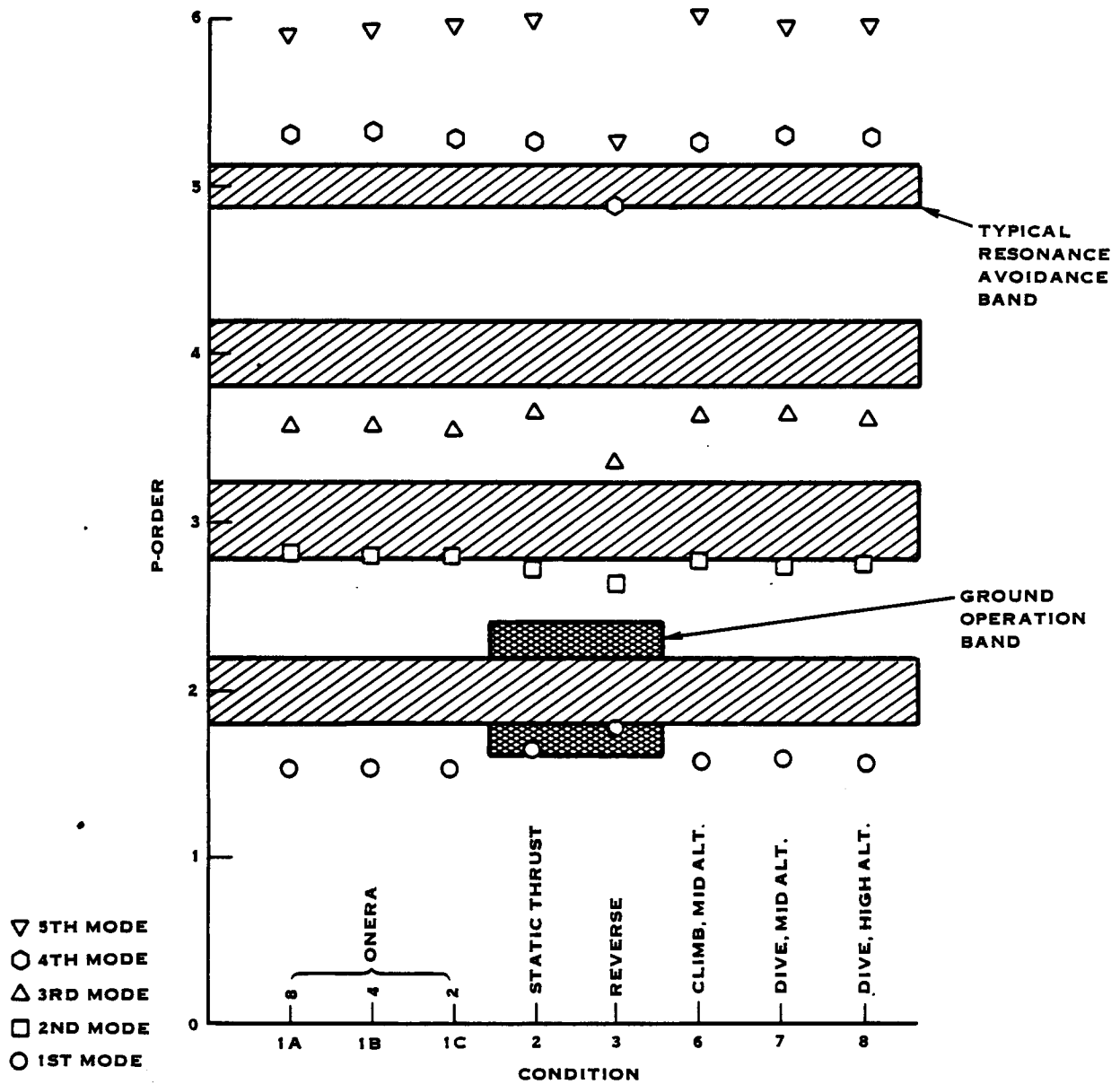


FIGURE 9-2. SR-7L BLADE RESONANT FREQUENCIES  
(FOR ADDITIONAL 8 CONDITIONS ANALYZED)



Figures 9-3 through 9-7 show the normalized mode shape of each of the five modes for the design/cruise condition. The mode shape deflections are resolved normal to the chord line of the three-quarter radius station (see section 5.1 for a description of this station) for the contour plotting.

### 9.3 Characterization of Mode Shapes

For a structure as complex as a Prop-Fan blade, most of the mode shapes corresponding to the natural frequencies of vibration are difficult to characterize. Much of the complexity in mode shapes is due to coupling of bending and torsional deflection characteristics caused by the sweep of the blade, first forward in the mid-blade region, then rearward at the tip. However, some of the lower resonant frequencies of the SR-7L blade can be characterized by their mode shapes.

#### 9.3.1 First Mode

The first mode is a flatwise bending mode. The downward slant towards the trailing edge of the iso-deflection contours indicates a small amount of torsional coupling is present.

#### 9.3.2 Second Mode

The second mode is similar to the third mode in that it appears to be a combination of flatwise beam bending at the outer third of the blade and local bending at the leading edge of the inner two-thirds of the blade. One difficulty of resolving all motions to a flatwise direction, however, is that edgewise motions are not visible. A check of shank reaction forces reveals that the second mode is predominantly an edgewise mode, but because of the twist and sweep of the blade, and the resolved flatwise motion plotted, it takes on the appearance of the second flatwise mode.

#### • 9.3.3 Third mode

This is the second flatwise bending mode with torsional coupling again evident from the slope of the node line and tip contours.

#### 9.3.4 Fourth Mode

Mode four is the first torsional mode. The blade does not vibrate about the pitch change axis but rather about a swept line which approximates the locus of section shear centers.

ORIGINAL PAGE IS  
OF POOR QUALITY

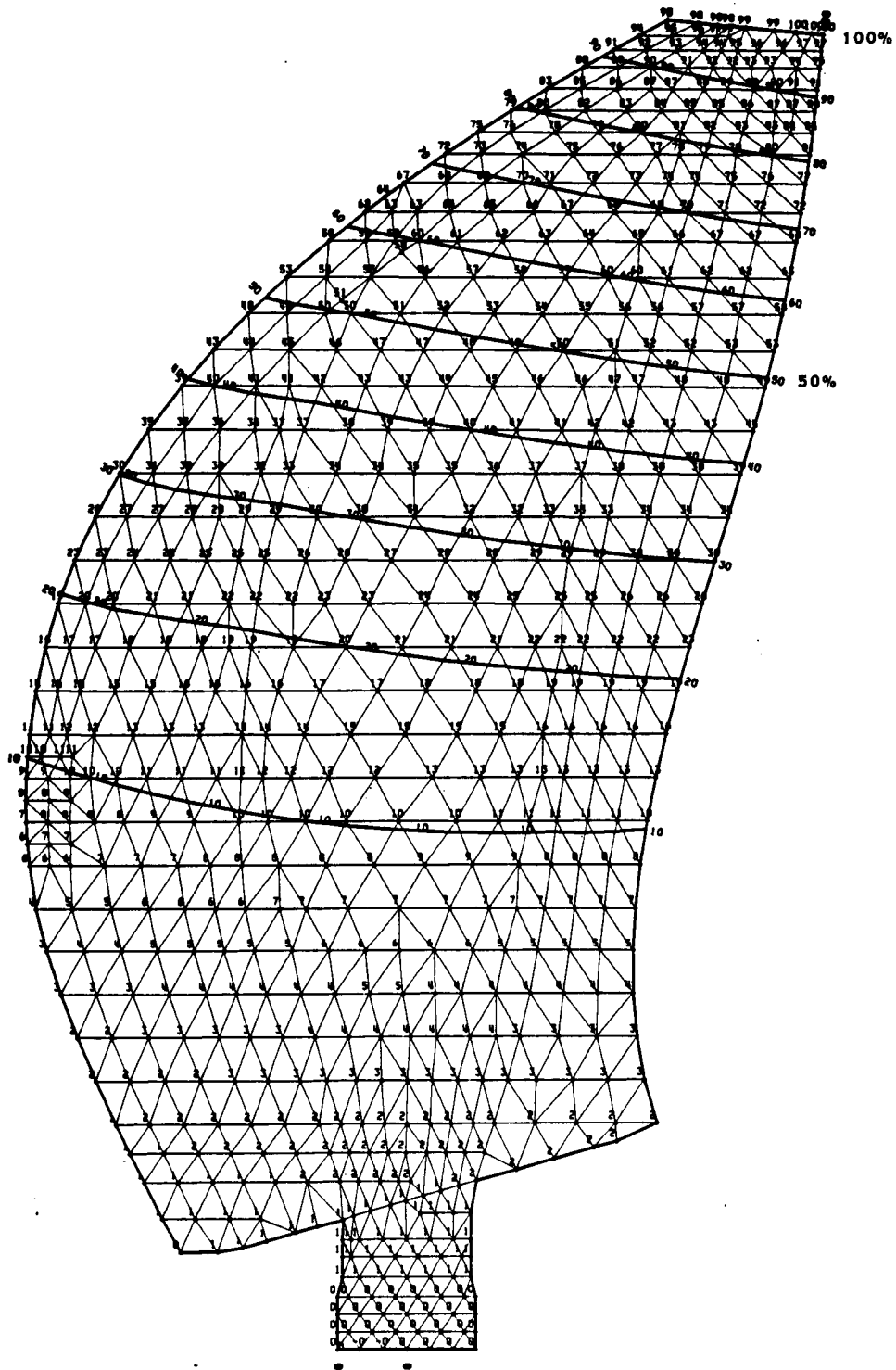


FIGURE 9-3. NORMALIZED MODE SHAPE  
CRUISE CONDITION SR-7L MODE 1

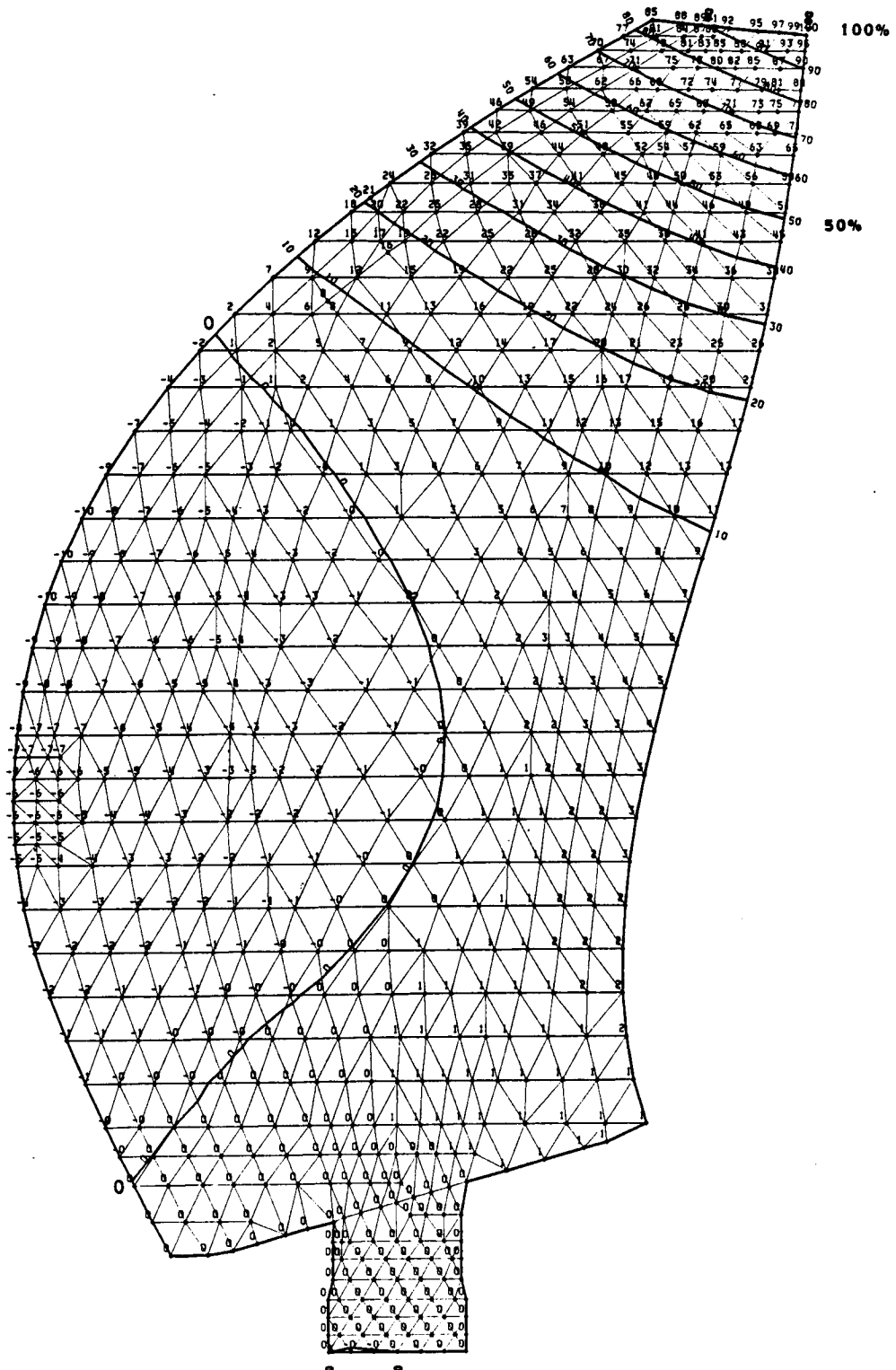


FIGURE 9-4. NORMALIZED MODE SHAPE  
CRUISE CONDITION SR-7L MODE 2

ORIGINAL PAGE IS  
OF POOR QUALITY

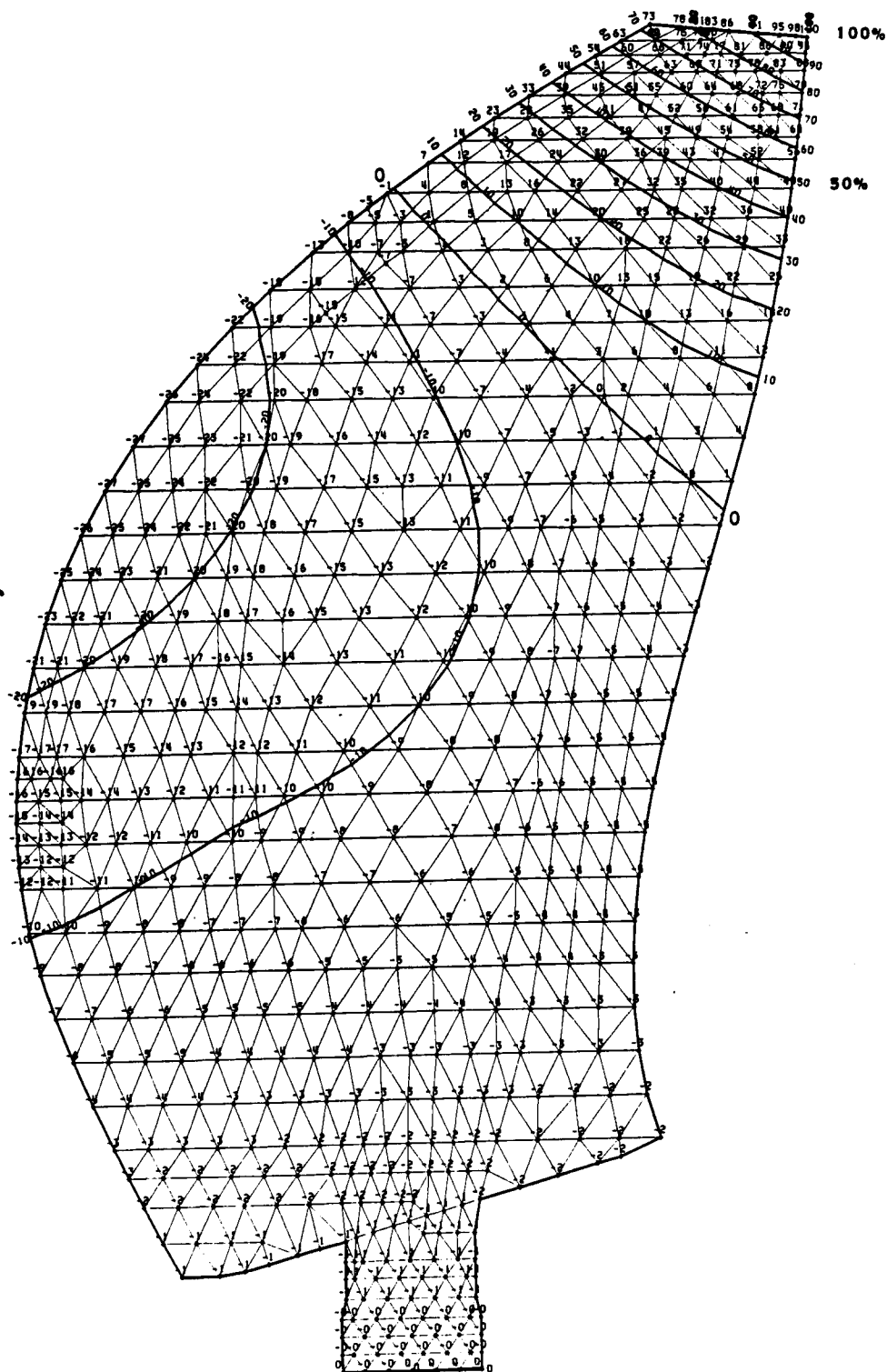


FIGURE 9-5. NORMALIZED MODE SHAPE  
CRUISE CONDITION SR-7L MODE 3

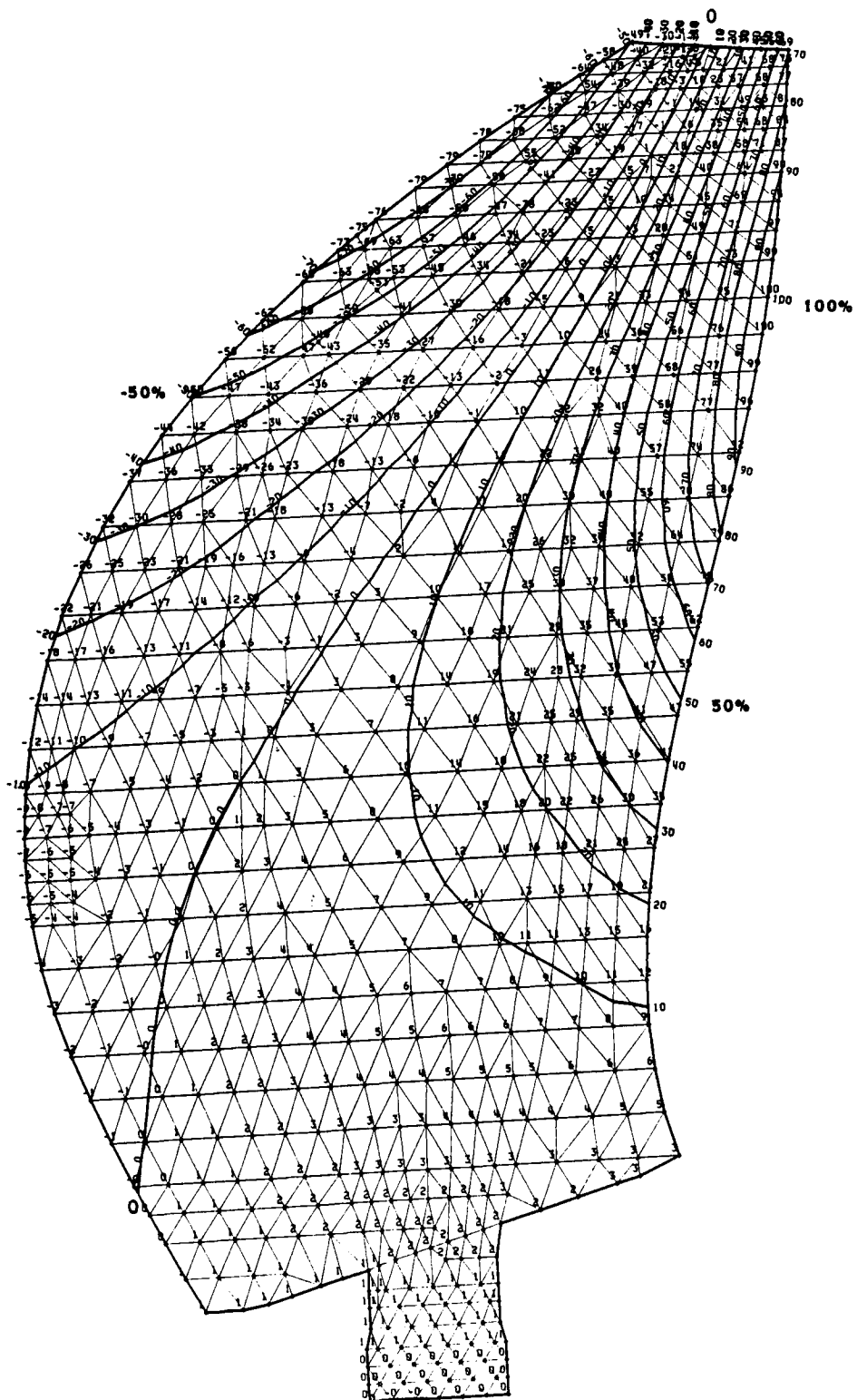


FIGURE 9-6. NORMALIZED MODE SHAPE  
CRUISE CONDITION SR-7L MODE 4

ORIGINAL PAGE IS  
OF POOR QUALITY

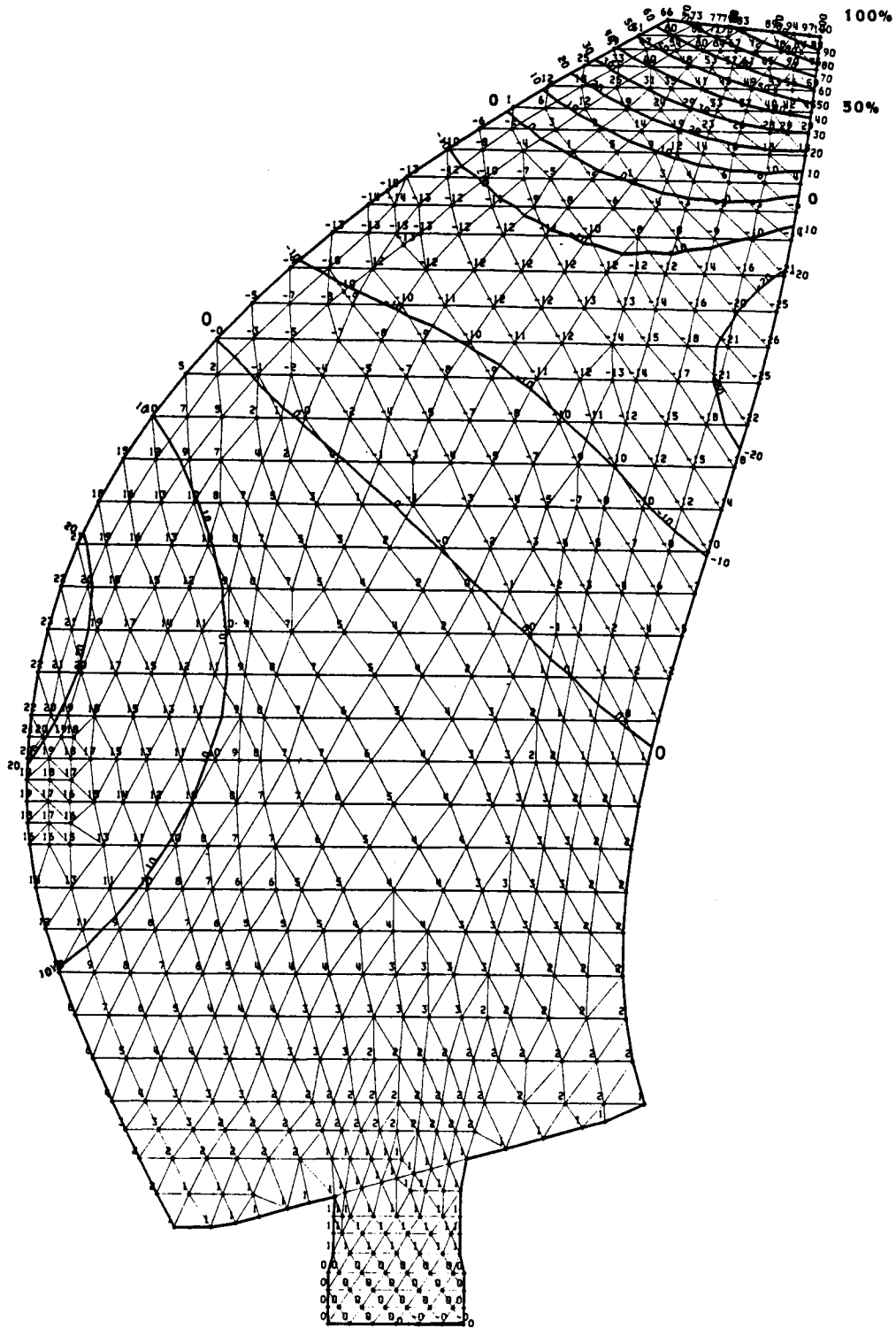


FIGURE 9-7. NORMALIZED MODE SHAPE  
CRUISE CONDITION SR-7L MODE 5

Most of the torsional movement is near the blade tip while the inboard area of the blade shows little deflection. The fact that the node line falls off the inboard leading edge is probably due to the resolution of deflections normal to the three-quarters radius station. Resolution normal to an inboard station should show the node line to be concentric to the shank.

#### 9.3.5 Fifth Mode

The fifth mode is the third flatwise bending mode. Again torsional coupling is evident from the slope of the contours.

## 10.0 Stability

A stability analysis of the SR-7L blade was performed to assure structural integrity in terms of aeroelastic stability over the entire flight envelope and wind tunnel test conditions. The requirements divide flutter into two categories: unstalled flutter and stalled flutter. These categories were established because there is a distinct difference in aerodynamics during unstalled and stalled operation. Unstalled flutter can occur when the Prop-Fan operates in an unstalled condition, such as during cruise at high forward speed. Stall flutter can occur when the Prop-Fan operates in a stalled condition, such as during take-off under high power and low forward speed. The combination of high power and low speed gives rise to a high airfoil angle of attack, causing the air to separate from the aerodynamic surface and to stall the blade. For this reason, stall flutter is often called separated flow flutter. Because each category of flutter involves a unique aerodynamic condition, they are examined using different analytical approaches.

### 10.1 Unstalled Flutter Analysis

The unstalled flutter stability of the SR-7L blade was examined using an aeroelastic stability analysis that was specifically developed to model the structural and aerodynamic complexities of a Prop-Fan.

Briefly, the analysis is a linear modal formulation in which the structure is modeled with fully-coupled mode shapes obtained from finite element analysis and the unsteady aerodynamic loads are based on linear, compressible, two-dimensional theory (ref. 8). Because the aeroelastic analysis uses two-dimensional aerodynamic theory to model the three-dimensional flow about the blade, the application of the theory has been guided by existing model test results to give consistent and accurate predictions. This tailoring has taken the form of programmed options selected to best model the installation. Three basic options exist in the analysis that perform the following functions:

- a) isolated and cascade unsteady airfoil data can be combined to account for large blade spacing effects,
- b) a blade tip load reduction (tip loss factor) can be implemented to model the three-dimensional flow about the tip of an unducted fan, and
- c) steady state empirical airfoil lift and moment curve slopes can be used to model the actual airfoil section and to account for some transonic effects.



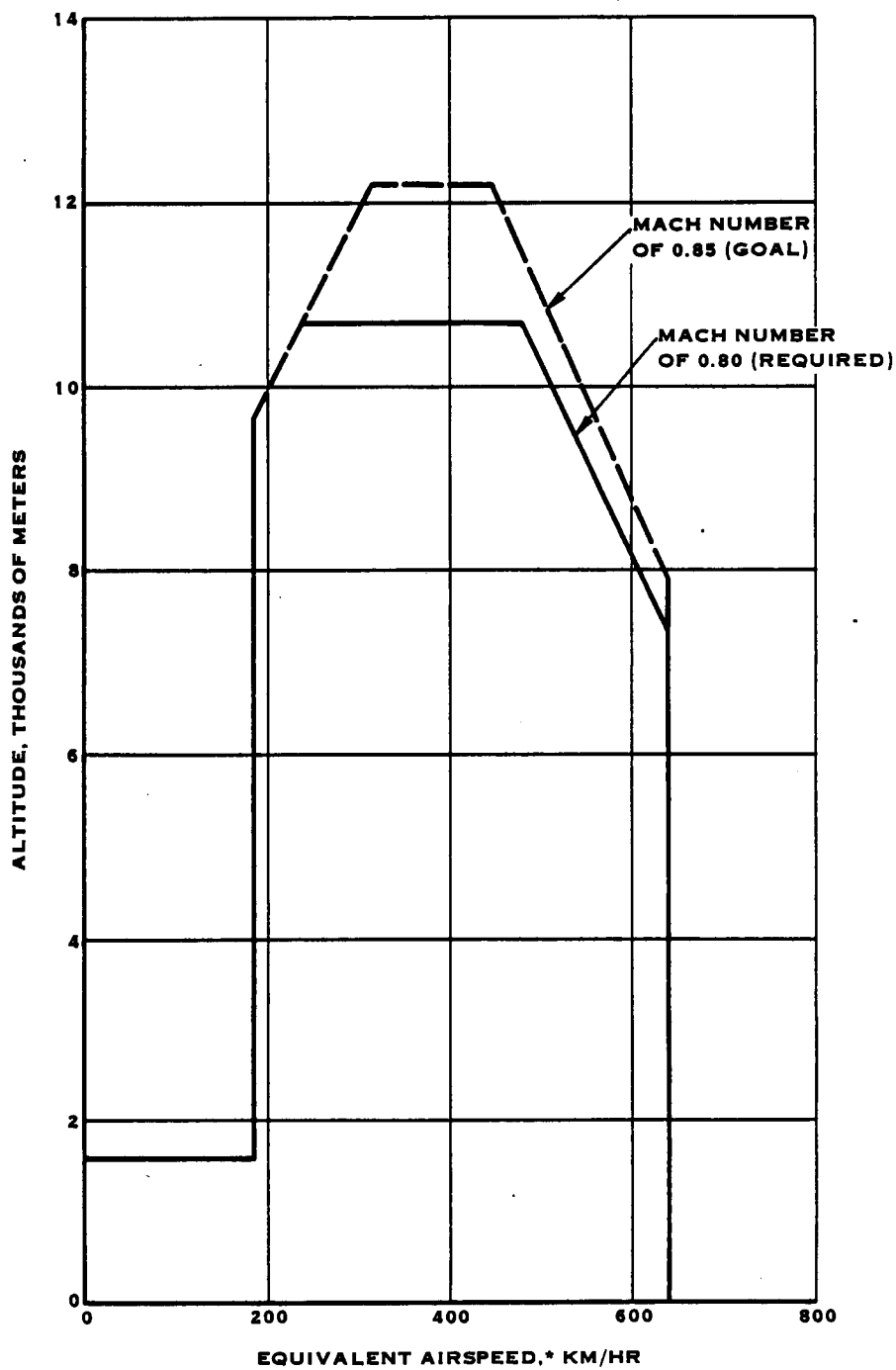
The SR-7L calculations were based on a conservative combination of these options. The calculations were carried out using theoretical airfoil data, no blade tip losses, and combined cascade and isolated aerodynamic data to account for the close blade spacing at the root and high blade spacing at the tip. Specifically, the combined cascade/isolated airfoil option (called the partial cascade option) uses cascade data for blade gap-to-chord ratios of two or less, and isolated data for blade gap-to-chord ratios greater than two. For the SR-7L blade this results in the using cascade effects out to 80 percent of the blade radius, and isolated effects for the remaining outboard 20 percent.

#### 10.1.1 Unstalled Flutter Requirements and Results

The design requirement for unstalled flutter is that no instability should occur in the operating flight envelope shown in figure 10-1. Also shown in figure 10-1 is the goal of an extended flutter-free flight envelope used for the SR-7L design. The same flight profile is shown in figure 10-2 in terms of altitude versus Mach number (see also figure 3-1), with the ONERA S1 Wind Tunnel condition indicated.

To ensure that the entire operating regime is free of instability, many operating conditions were analyzed.

Initially, ten operating conditions were studied for stability. These conditions are listed in table 10-1, along with the calculated flutter Mach number.



\*AIRSPEED CALCULATED WITH AIR DENSITY AT SEA LEVEL

FIGURE 10-1. SR-7L FLIGHT ENVELOPE AIRSPEED VS. ALTITUDE

ALTITUDE, THOUSANDS OF METERS

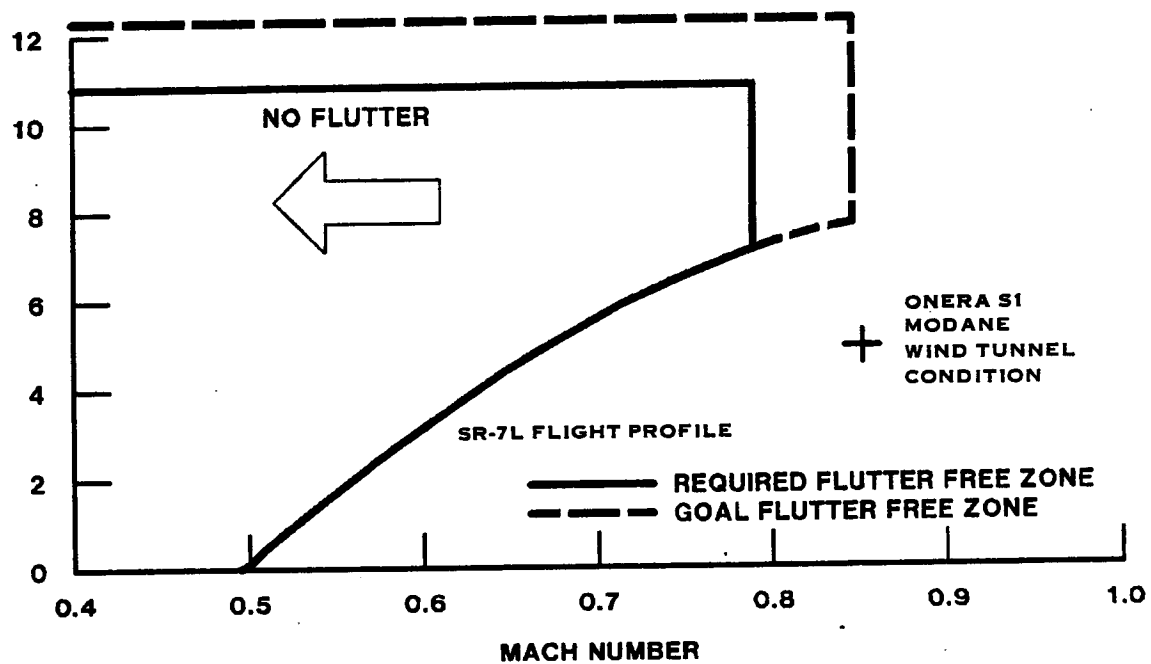


FIGURE 10-2. SR-7L DESIGN REQUIREMENTS UNSTALLED FLUTTER

Table 10-1

## PREDICTED FLUTTER MACH NUMBER FOR TEN SR-7L OPERATING CONDITIONS

<u>Case</u>	<u>Condition</u>	<u>Operating Mach no.</u>	<u>Altitude, meters (feet)</u>	<u>RPM</u>	<u>Flutter Mach no.</u>	<u>Flutter mode</u>
D1	Design/Cruise	.80	10,675 (35,000)	1,698	.95	3
D2	Take-off/Climb	.20	0 (0)	1,698	.60	3
1A	ONERA, 8 blades	.80	4,270 (14,000)	1,698	.85	3
1B	ONERA, 4 blades	.80	4,270 (14,000)	1,698	1.00	2
1C	ONERA, 2 blades	.80	4,270 (14,000)	1,698	.95	2
4	Cruise, Low RPM	.80	10,675 (35,000)	1,273	1.00	-
5	Cruise, High RPM	.85	10,675 (35,000)	1,783	.92	3
6	Climb, Mid Altitude	.50	3,050 (10,000)	1,698	.76	3
7	Dive, Mid Altitude	.60	6,100 (20,000)	1,698	.92	3
8	Dive, High Altitude	.80	10,675 (35,000)	1,698	1.00	3

For each condition, the flutter Mach number was greater than the required Mach number for that condition, indicating a stable configuration. Figure 10-3 shows in summary that all stability requirements and the .85 Mach number goal were exceeded with regard to unstalled flutter.

#### 10.1.2 Stability Determination

Each flutter Mach number point listed in table 10-1 was obtained using the following calculation procedure. At each condition, a set of stability calculations were performed over a range of Mach numbers to arrive at the typical damping plot shown in figure 10-4. This plot illustrates the 10,675 meter (35,000 foot) cruise condition (case D1 in table 10-1), and shows that mode three becomes unstable at .95 Mach number which is well above the .80 Mach number requirement. Each point on the damping curve represents the least stable inter-blade phase angle of a mode at the analyzed Mach number.

For multi-bladed rotors where blade-to-blade interaction is important, the phase relationship between blades (called the inter-blade phase angle) becomes an important parameter affecting system stability. For the eight-bladed SR-7L Prop-Fan, eight phase angles are significant: 0, 45, 90, 135, 180, 225, 270 and 315 degrees. The least stable angle is determined by examination of the damping prediction at each angle, as shown by the root locus plot in figure 10-5. This plot shows the imaginary portion of the root locus of the solution eigenvalue, which is the damped natural frequency, plotted against the real portion of the eigenvalue, which is the indicator of stability. The least stable inter-blade phase angle shown in this figure occurs at 315 degrees.

#### 10.1.3 Stability Discussion

The predicted blade instability, which occurs well above the required Mach number for the design/cruise condition, does not involve frequency coalescence as is typical of fixed-wing unstalled flutter. The lack of frequency change with increasing Mach number is illustrated by the flat frequency curves in figure 10-6.

The predicted high Mach number instability occurs in the third mode at nearly the third mode natural frequency. This mode can be characterized loosely as a second flatwise mode. The predicted flutter mode is dominated by the third natural frequency mode of the blade as shown in table 10-2, which lists the percent contribution of the natural modes to the flutter prediction. The lack of mode coupling shown in table 10-2 would suggest single mode flutter, if the mode shape of the flutter mode was not considered.

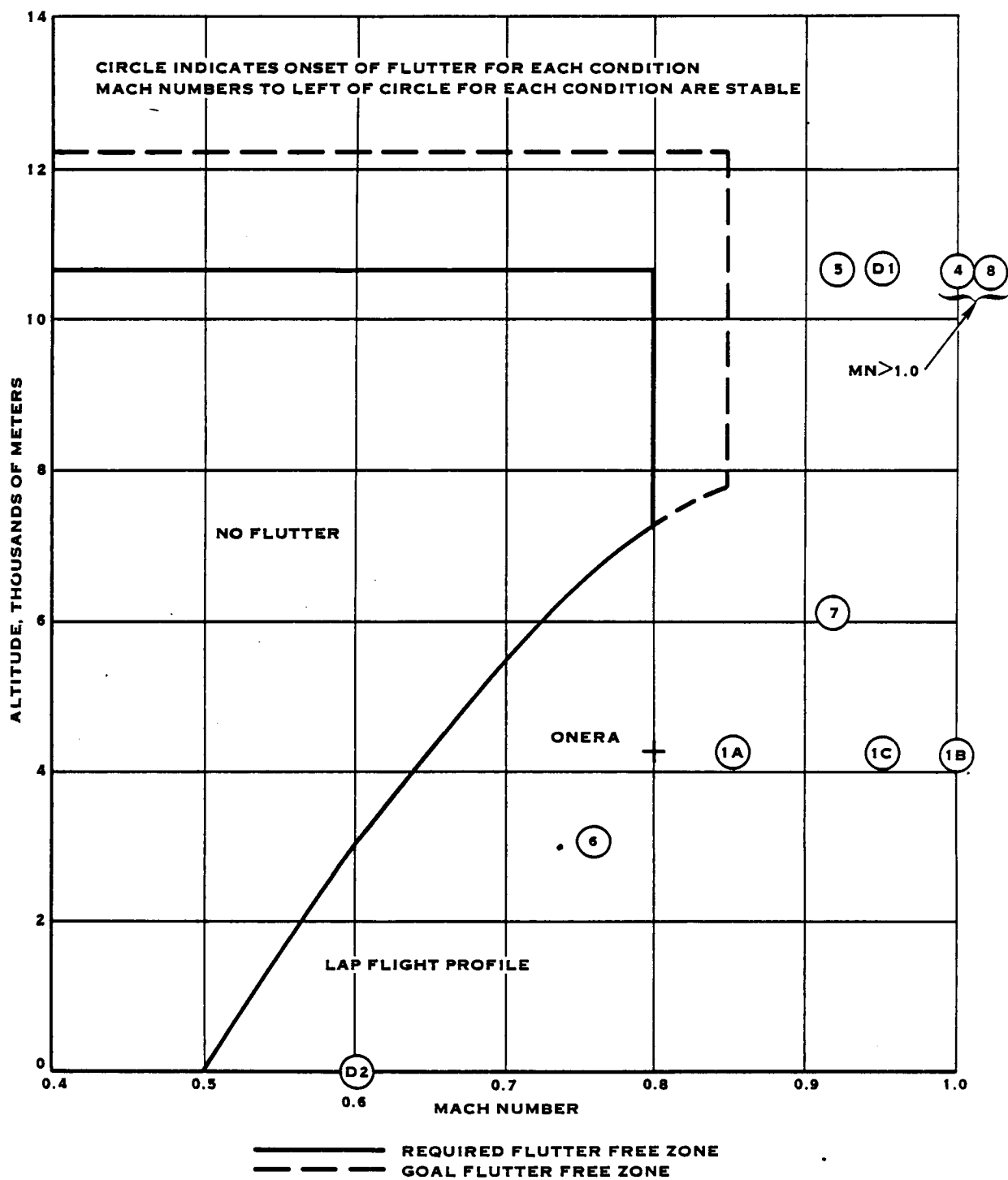


FIGURE 10-3. UNSTALLED FLUTTER STABILITY SUMMARY BY CONDITION NUMBER

# VISCOUS DAMPING RATIO

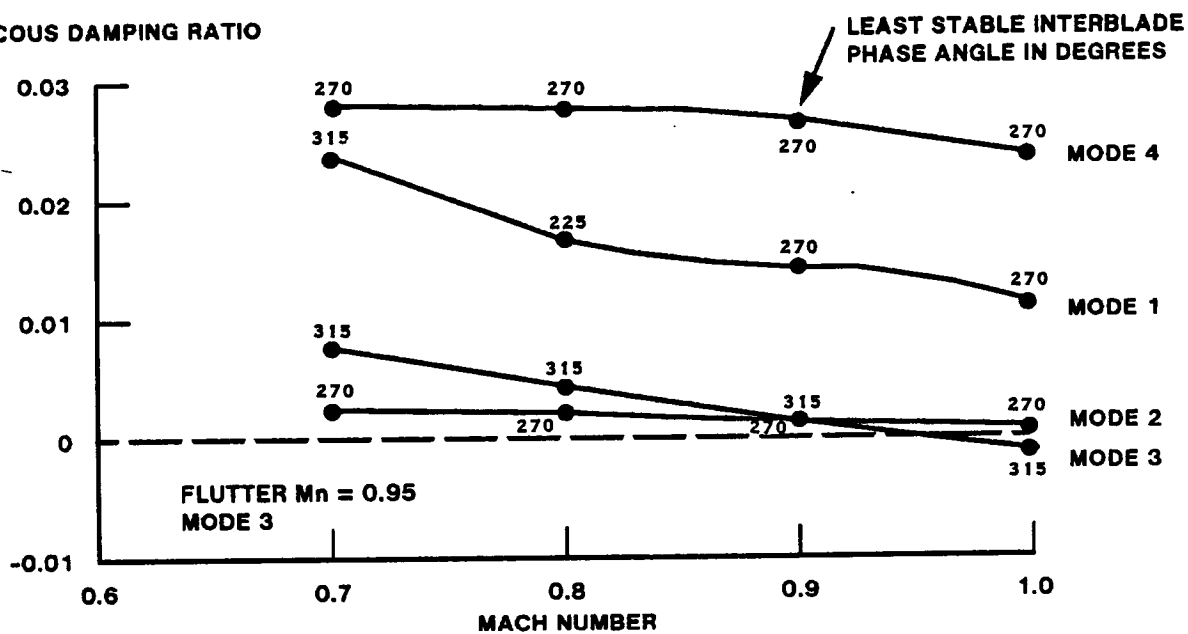


FIGURE 10-4. SR-7L DAMPING PREDICTION AT THE D1 CONDITION

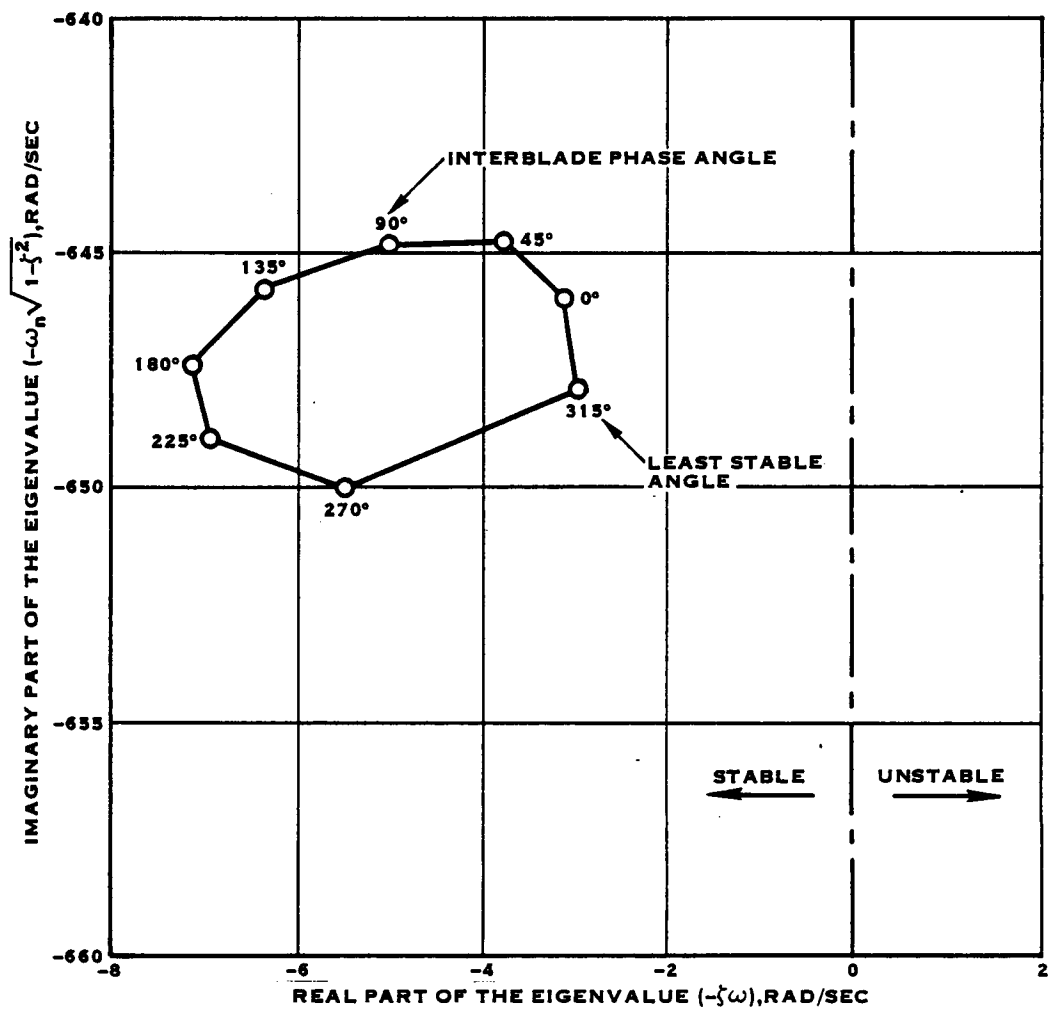


FIGURE 10-5. SR-7L ROOT LOCUS PLOT FOR MODE 3 AT CONDITION D1



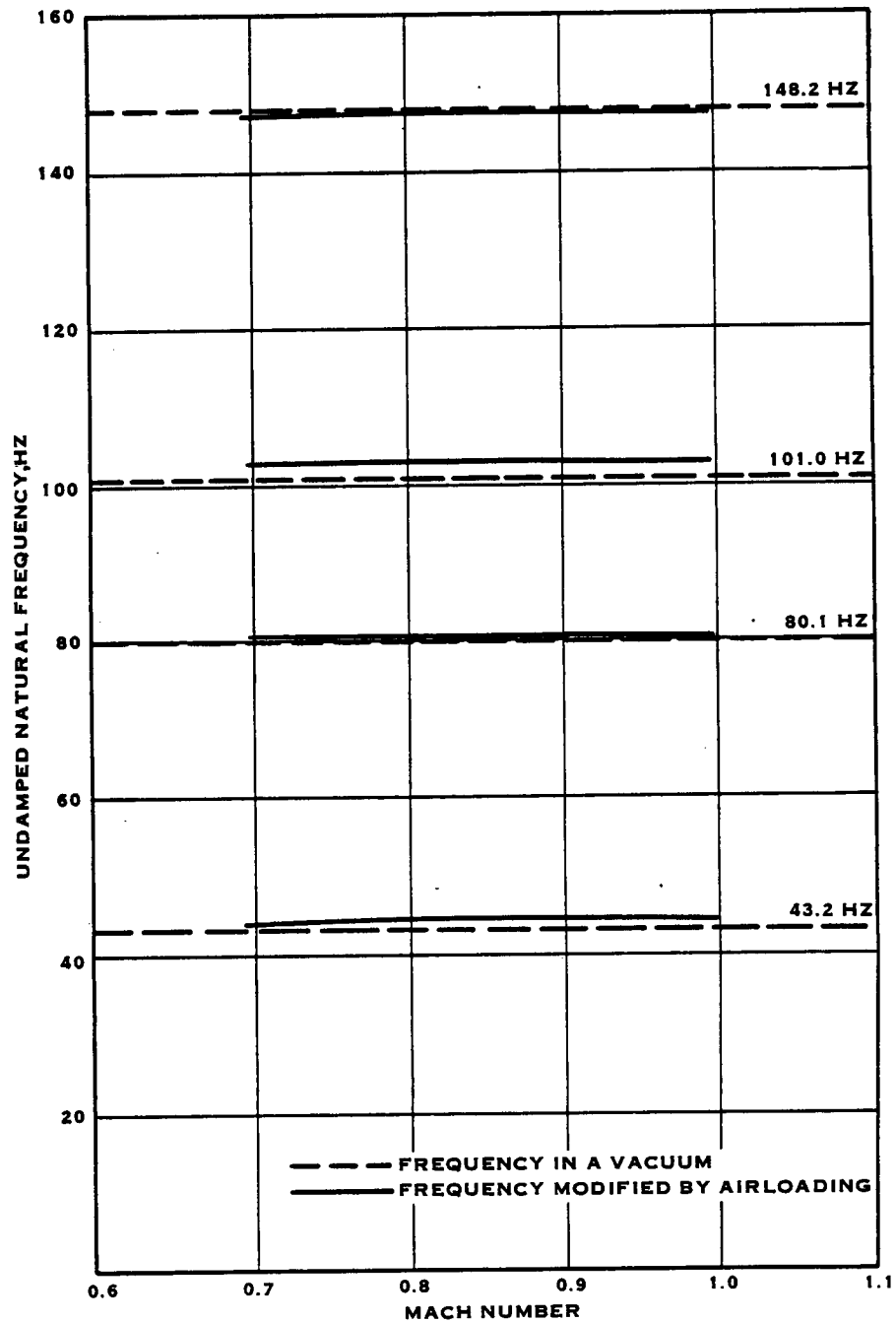


FIGURE 10-6. EFFECT OF UNSTEADY AIRLOADS ON SR-7L FREQ. FOR CONDITION D1

Table 10-2

CONTRIBUTION OF THE NATURAL MODES TO THE THIRD COUPLED  
AEROELASTIC MODE FOR CASE D1

Condition: Design/Cruise  
10,675 meter (35,000 feet)  
1698 revolutions per minute  
0.8 Mach number  
57.57 degrees Beta three-quarter angle

<u>Mode</u>	<u>Percent Contribution</u>
1	3.0
2	3.2
3	84.8
4	2.6
5	3.0
6	1.6
7	0.8
8	0.9

The coupling that does exist modifies the third natural mode at the blade tip as shown in figure 10-7. This coupling reduces the tip torsional motion and causes it to be out of phase with the blade bending, resulting in a destabilizing condition. This change in mode shape at the blade tip is significant because the loads and mode shape displacements are highest at the tip. Therefore, the predicted high Mach number instability is a second flatwise flutter controlled by the blade tip loads.

#### 10.1.4 Stability Modal Evaluation at Nine Other Conditions

Damping plots for the other nine conditions listed in table 10-1 are shown in figures 10-8 through 10-16.

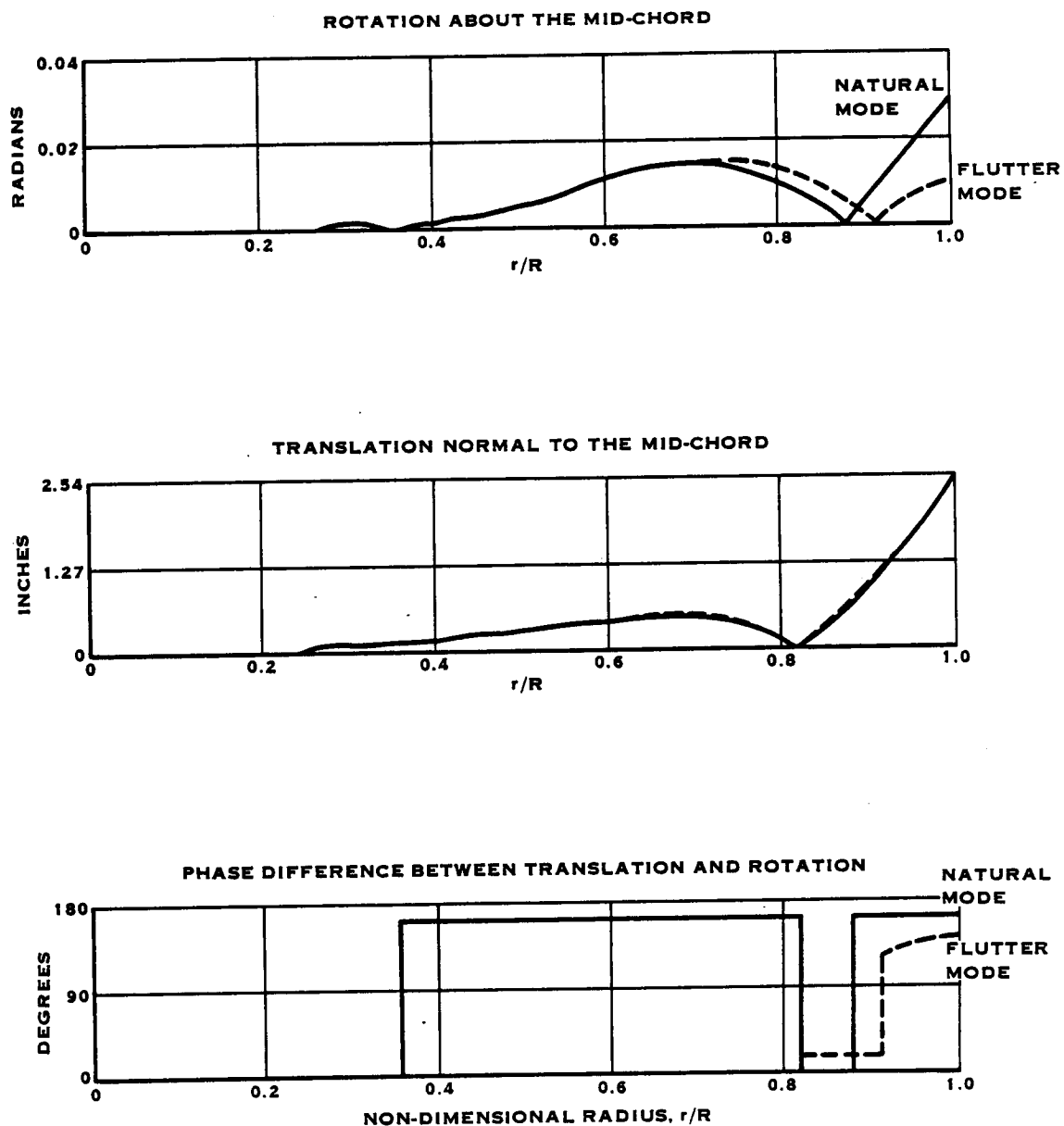


FIGURE 10-7. THE EFFECT OF UNSTEADY AIRLOADS ON THE THIRD NATURAL MODE SHAPE FOR THE D1 FLIGHT CONDITION

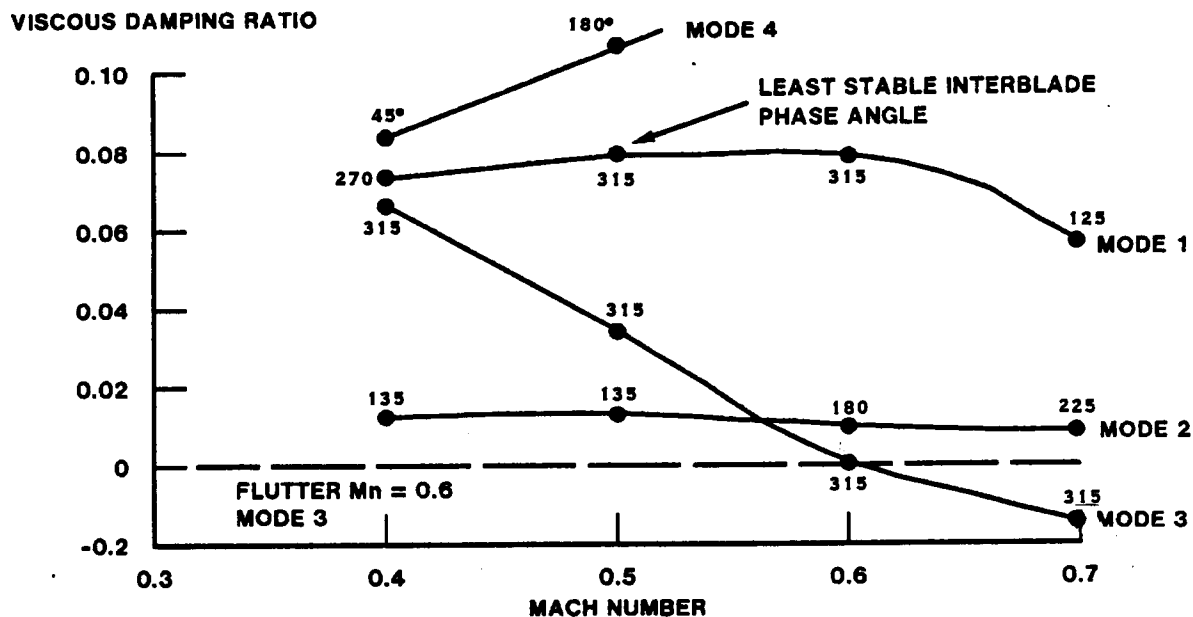


FIGURE 10-8. SR-7L DAMPING AT CONDITION D2

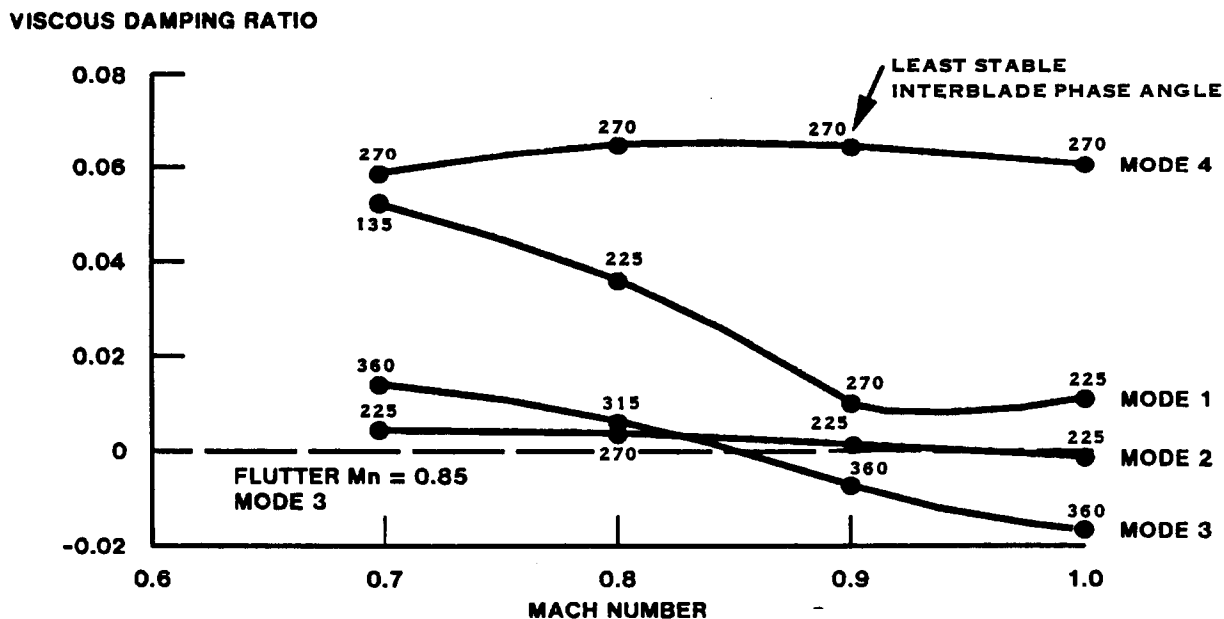


FIGURE 10-9. SR-7L DAMPING AT CONDITION 1A.

# VISCOUS DAMPING RATIO

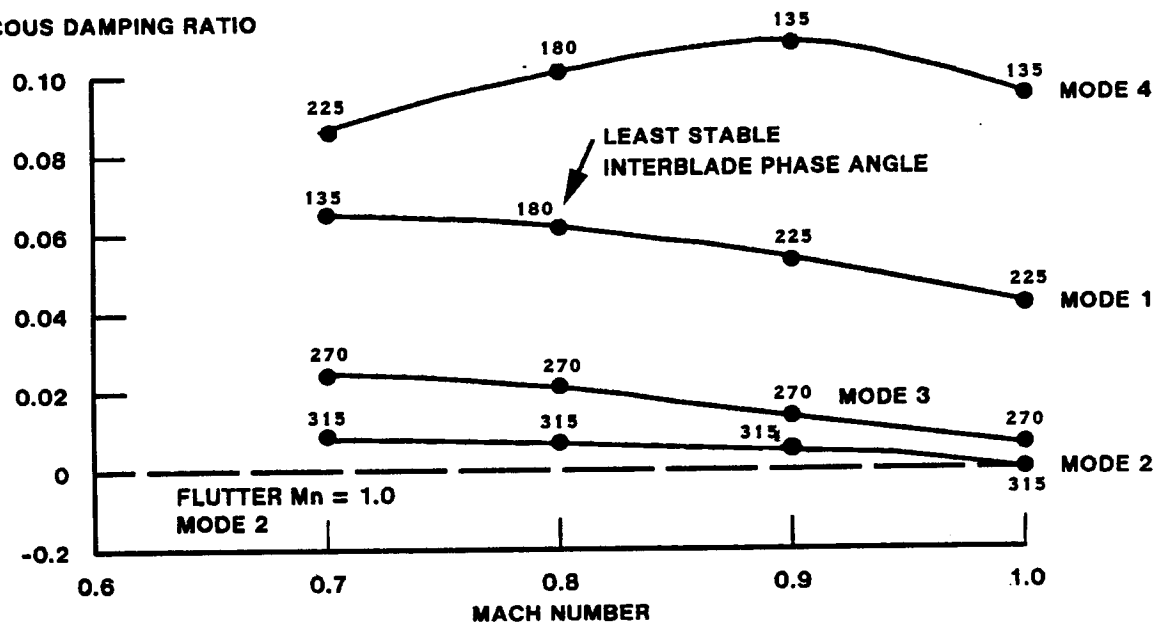


FIGURE 10-10. SR-7L DAMPING AT CONDITION 1B

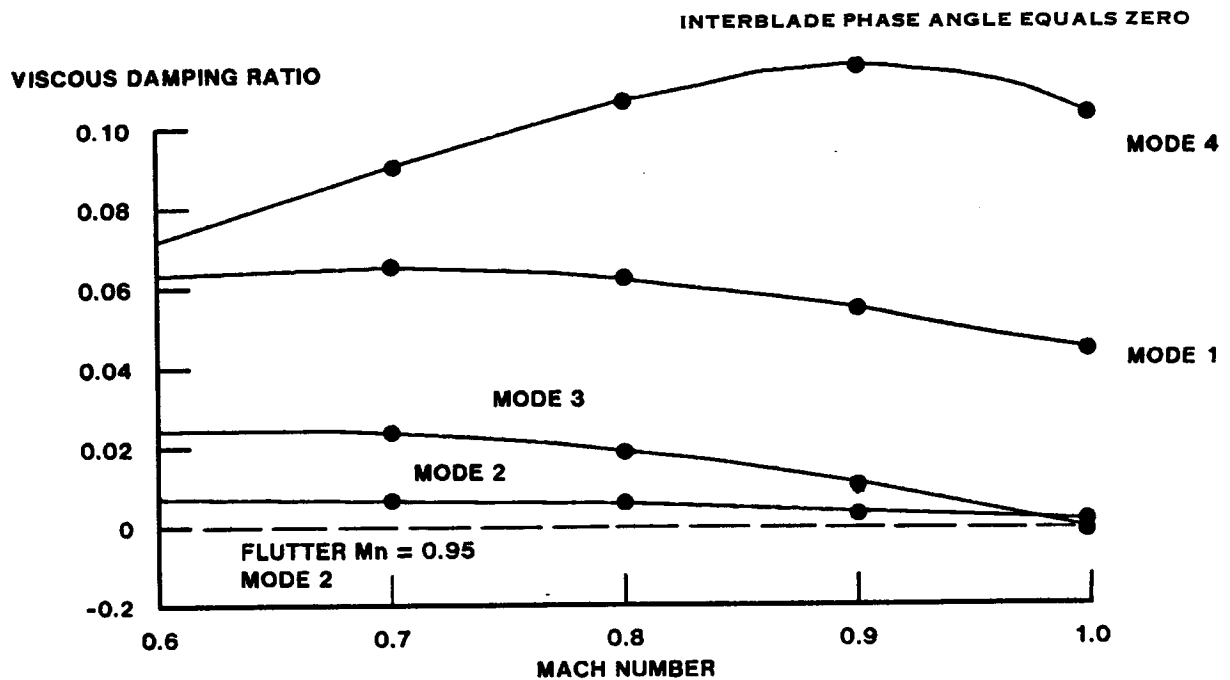


FIGURE 10-11. SR-7L DAMPING AT CONDITION 1C

# VISCOUS DAMPING RATIO

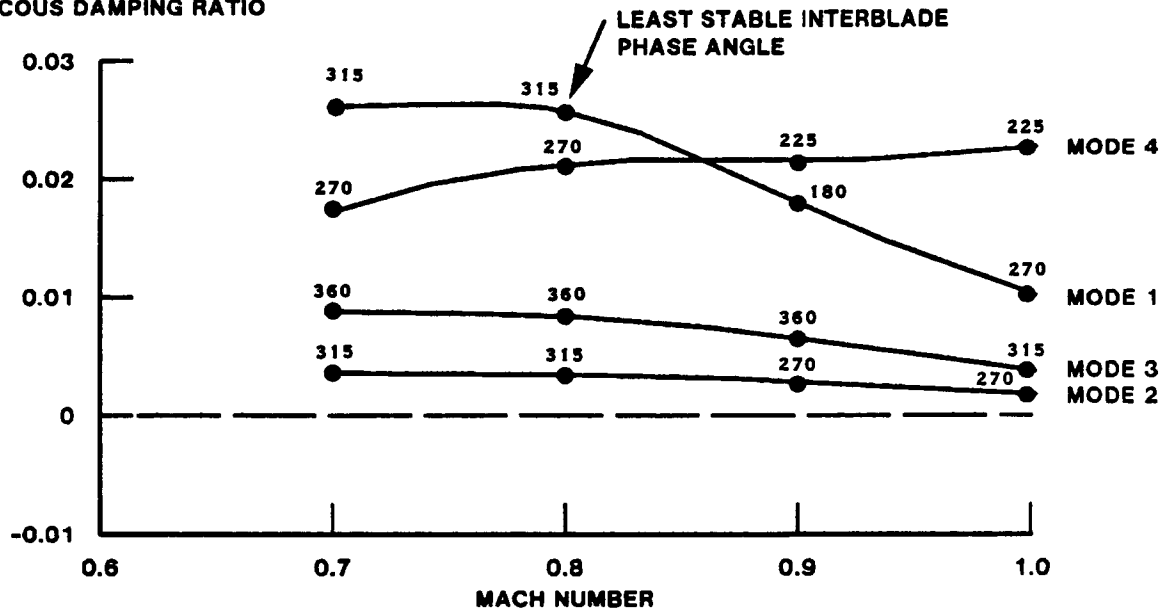


FIGURE 10-12.SR-7L DAMPING AT CONDITION

# VISCOUS DAMPING RATIO

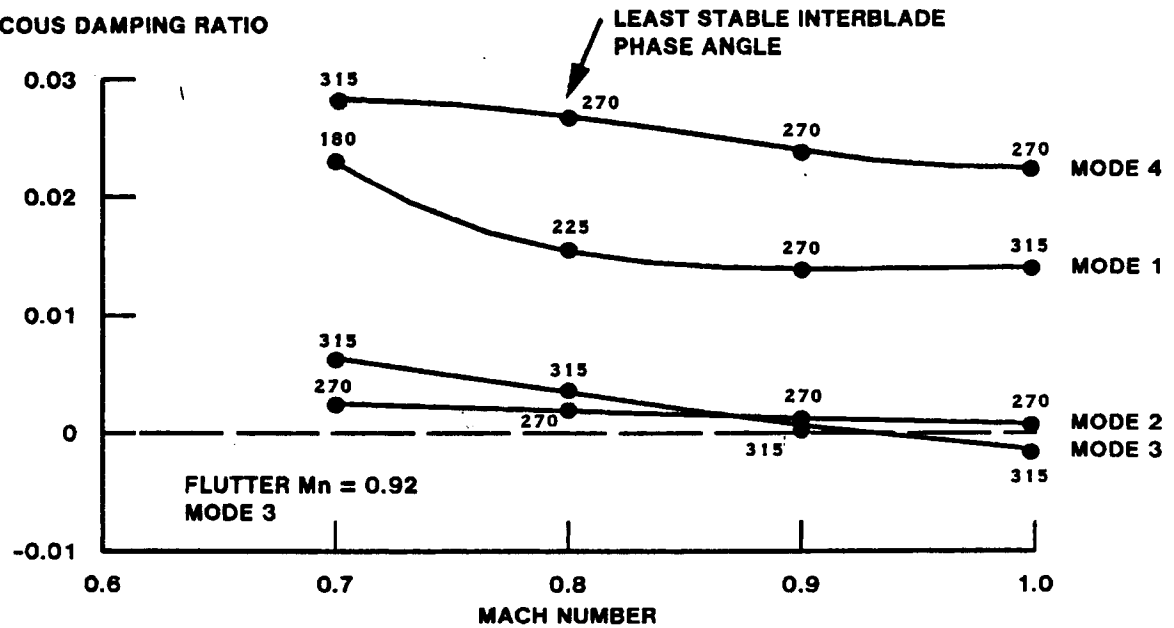


FIGURE 10-13. SR-7L DAMPING AT CONDITION 5

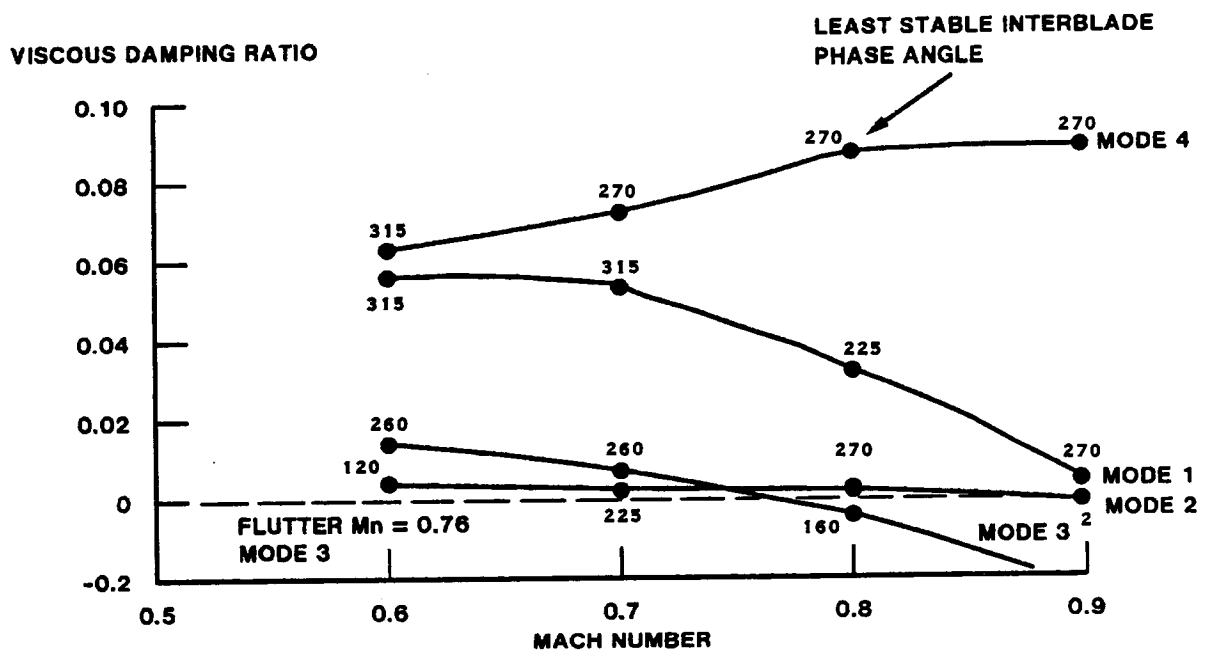


FIGURE 10-14. SR-7L DAMPING AT CONDITION 6

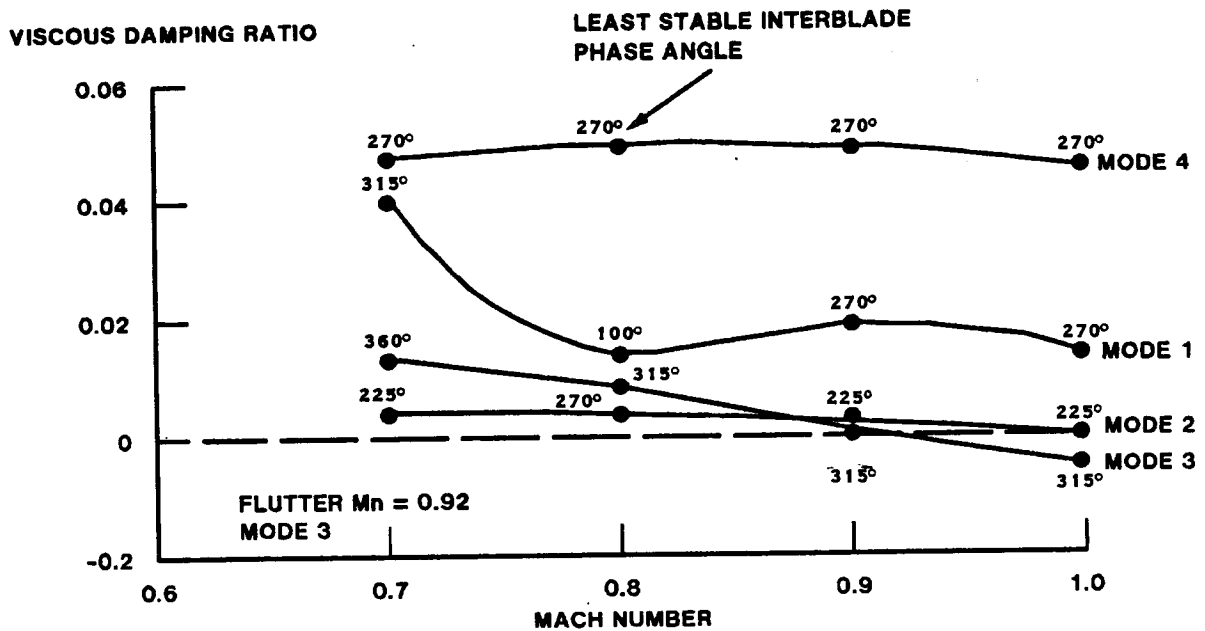
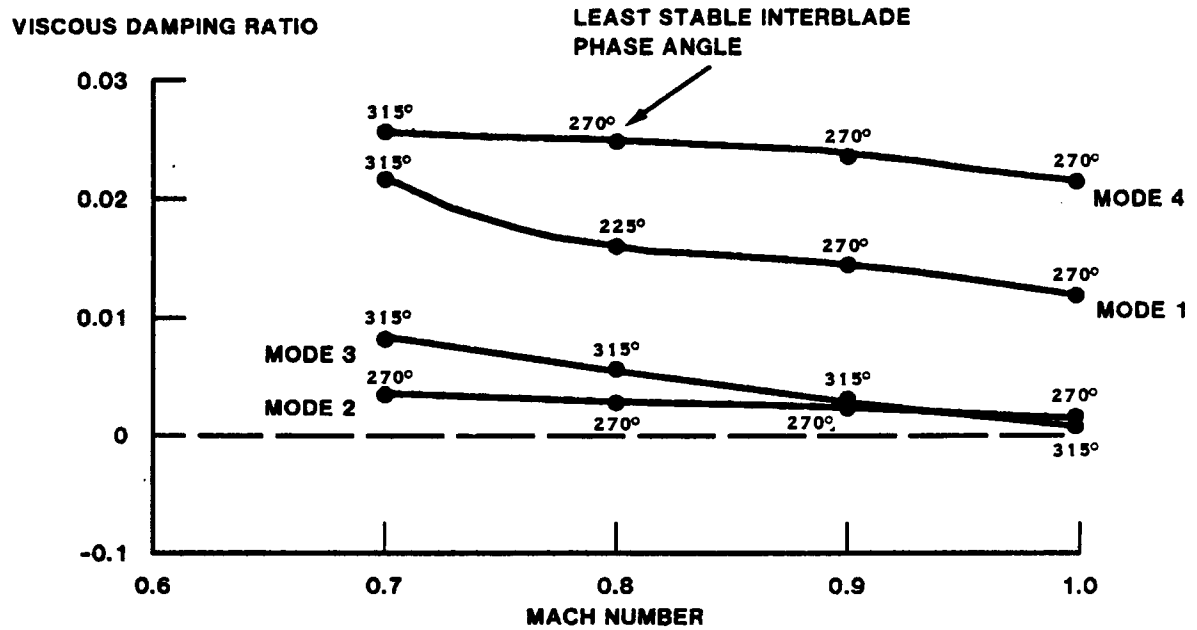


FIGURE 10-15. SR-7L DAMPING AT CONDITION 7



**FIGURE 10-16. SR-7L DAMPING AT CONDITION 8**



A comparison of the stability results for the three ONERA S1 Wind Tunnel conditions (figures 10-9 through 10-11) offers further insight into the SR-7L blade stability. Because of tunnel operating restrictions, the blade cannot be operated at full power in the tunnel in an eight-bladed configuration. Therefore, two- and four-bladed configurations with higher loading per blade will be tested. The larger spacing between the blades in the two and four-bladed configurations eliminates any aerodynamic cascade effects and increases the stability. The four-bladed configuration has an even further increase in stability over the two-bladed configuration because it has a lower power loading per blade. This lower loading causes the blade to deflect less, resulting in a more stable set of mode shapes since mode shape is dependent on the spatial position of the blade. Although the eight-bladed configuration has the lowest loading per blade, the stability decreases due to the close blade proximity, which causes destabilizing cascade effects.

#### 10.1.5 Effects of Aerodynamic and Structural Variations

The stability of the SR-7L blade was further examined to determine the effects of variability in the aerodynamics and structure. Initially, an overall flutter boundary was established using the 10,675 meter (35,000 foot), .8 Mach number cruise condition (case D1) mode shape.

The same analysis was then performed assuming that cascade effects exist over the entire span of the blade. The resulting change in aerodynamics decreased the stability prediction to below the design goal, but the design requirements were still satisfied, as shown in figure 10-17.

The next variation was to assess the effect of frequency degradation on the stability prediction. Using a 15 percent across-the-board frequency reduction of the original frequencies, the required flight profile was not met. This is also shown in figure 10-17. Both of these additional checks are severe, but they demonstrate the sensitivity of the blade stability to changes in structure and aerodynamics.

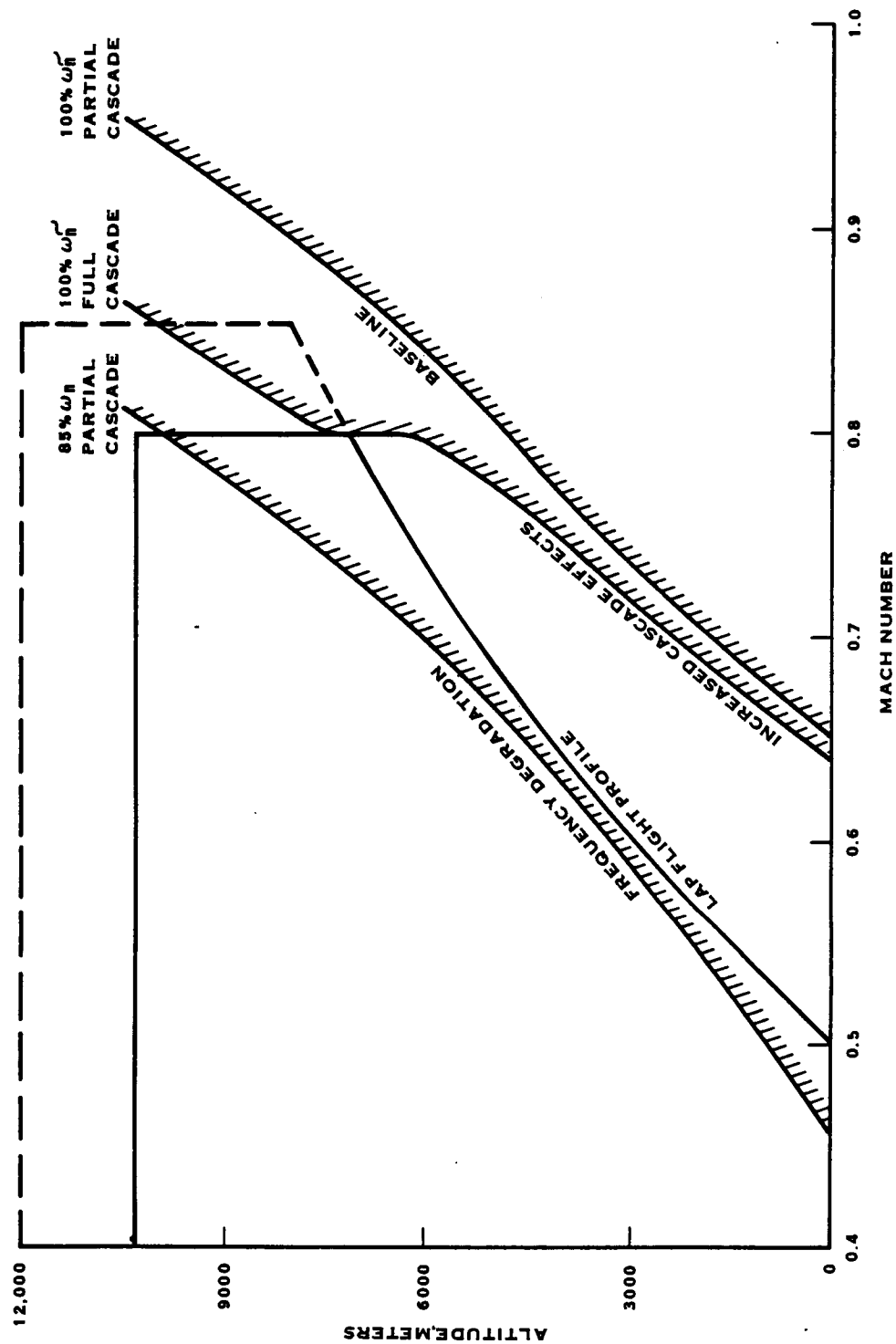


FIGURE 10-17. EFFECT OF CHANGES IN THE STRUCTURE AND AERODYNAMICS ON THE STABILITY OF THE SR-7L PROP-FAN

An additional note of importance is that the third mode instability predicted for the blade has never been confirmed experimentally, even where model Prop-Fan predictions have indicated that this instability should occur. Because this type of flutter is unconfirmed experimentally and because it is controlled by the high loads at the blade tip, an aerodynamic tip loss factor was incorporated into the analysis. With this tip loss factor, the aeroelastic stability analysis program gives results that show higher stability of the third mode and better correlation with experimental data. Figure 10-18 shows that the use of this tip loss factor on the design/cruise condition, case D1, eliminates the previous instability found in the third mode. This demonstrates the conservatism of the analytical procedure discussed in section 10.1.

## 10.2 Stall Flutter Evaluation

To study stall flutter, two methods of analysis were used. One was a semi-empirical formulation that has been incorporated in the aeroelastic stability analysis computer program. The other method was a purely empirical method used for conventional propeller stall flutter analysis. Two methods were chosen for stall flutter analysis because the theoretical analysis of stall flutter is not a well-established procedure due to the complexity of the air flow about a stalled blade section.

### 10.2.1 Semi-Empirical Method

The semi-empirical method uses combined bending and torsion modes, but does not couple the modes since stall flutter is generally a single mode phenomenon. The unsteady airfoil coefficients are developed from steady-state empirical airfoil data. The results from this analysis give the onset of stall flutter, not the magnitude of the response, because large amplitude stall flutter response is non-linear while the analysis assumes a linear response.

Table 10-3 lists the conditions examined for stall flutter along with the resulting predictions. The predictions are in terms of blade angle because stall flutter occurs at high power when the blade is stalled and increasing power corresponds to increasing blade angle.

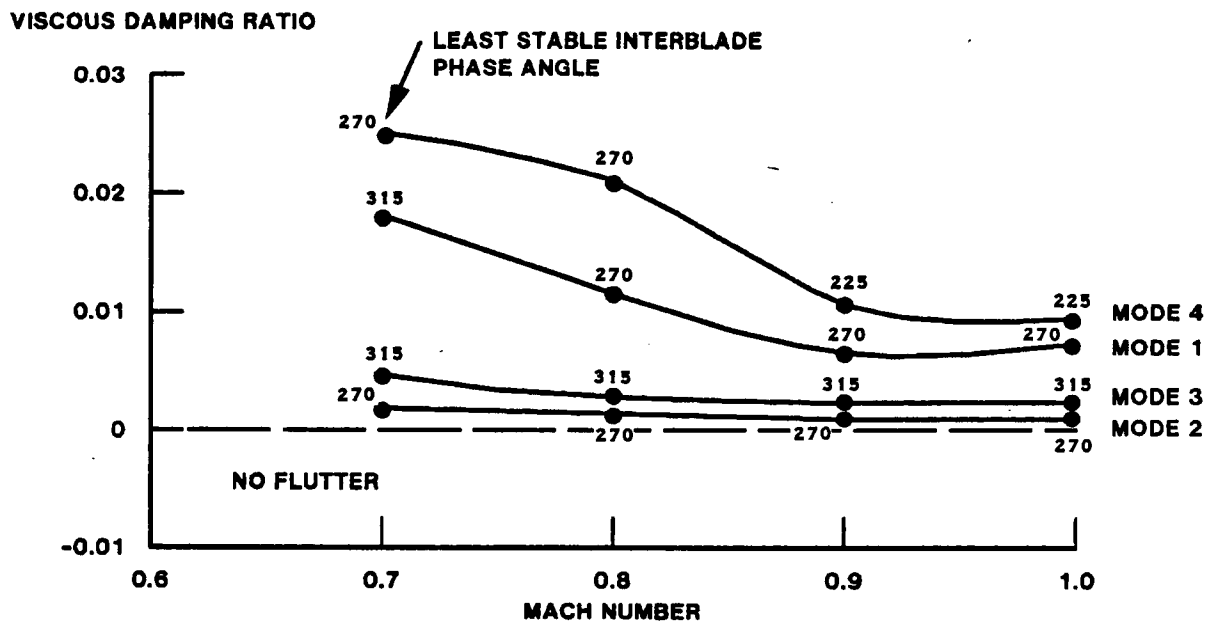


**FIGURE 10-18. DAMPING PREDICTION INCLUDING THE EFFECT OF AN AERODYNAMIC BLADE TIP LOSS ON CONDITION D1**

Table 10-3

STALL FLUTTER ONSET PREDICTION SUMMARY			
	<u>Take-off/Climb</u>	<u>Static Thrust</u>	<u>Reverse</u>
Speed, RPM	1698	1698	1698
Mach no.	0.2	0.0	0.0
Nominal blade angle, deg	38.0	33.0	-10.0
Flutter blade angle, deg	40.0	31.0	No flutter
Flutter mode of vibration	4	4	No flutter

The predictions show that stall flutter occurs at a lower blade angle than required by the static thrust condition. This prediction is illustrated by the predicted damping plot, figure 10-19. The fourth mode, which is the first torsional mode, becomes unstable at a 31 degree blade angle.

When the blade is subjected to a small amount of forward flight speed, the stall flutter stability is greatly improved, as seen by the take-off/climb condition damping predictions shown in figure 10-20.

This improvement in stability indicates that with the proper pitch change schedule, stall flutter will not be a problem at take-off, even though stall flutter is predicted statically at full power.

As seen in figure 10-21, no flutter was found for the reverse thrust condition. Therefore, no flutter problems would be encountered during landing.

#### 10.2.2 Empirical Method

Since the SR-7L blade has a distinct torsional mode, and stall flutter was predicted for this mode, a stall flutter parameter was applied to the blade. The stall flutter parameter is an empirical design factor that was developed for conventional propeller design to prevent the occurrence of torsional stall flutter. This parameter is calculated for a given configuration and plotted on a stall flutter design chart to see if torsional stall flutter is possible. The calculated stall flutter parameter for the SR-7L blade for a blade angle of 33.0 degrees is 1.35, which is well inside the stable region of a stall flutter design chart shown in figure 10-22, indicating that no flutter will occur in the torsional mode.

The two methods used to predict the stall flutter stability of the SR-L blade give different results. The first method, the semi-empirical method which predicted the blade angle when flutter would occur, shows stall flutter occurring in a mode that the second method, using the stall parameter, showed to be stable. Therefore, the stall flutter results are inconclusive. The best procedure for determining stall flutter stability is testing the

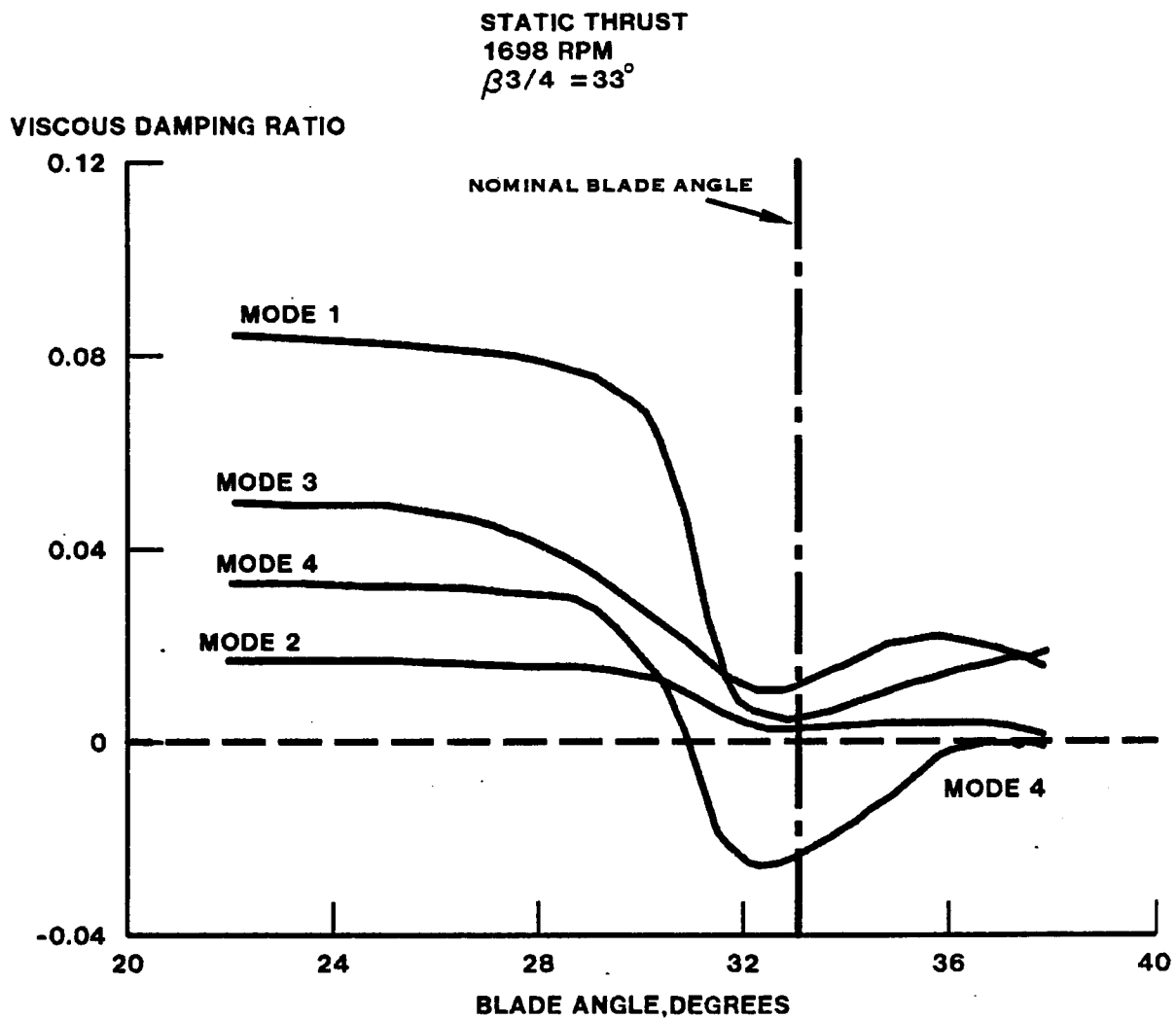


FIGURE 10-19. SR-7L STALL FLUTTER STABILITY

TAKE-OFF/CLIMB  
1698 RPM  
 $\beta_{3/4} = 38.3^\circ$

VISCOUS DAMPING RATIO

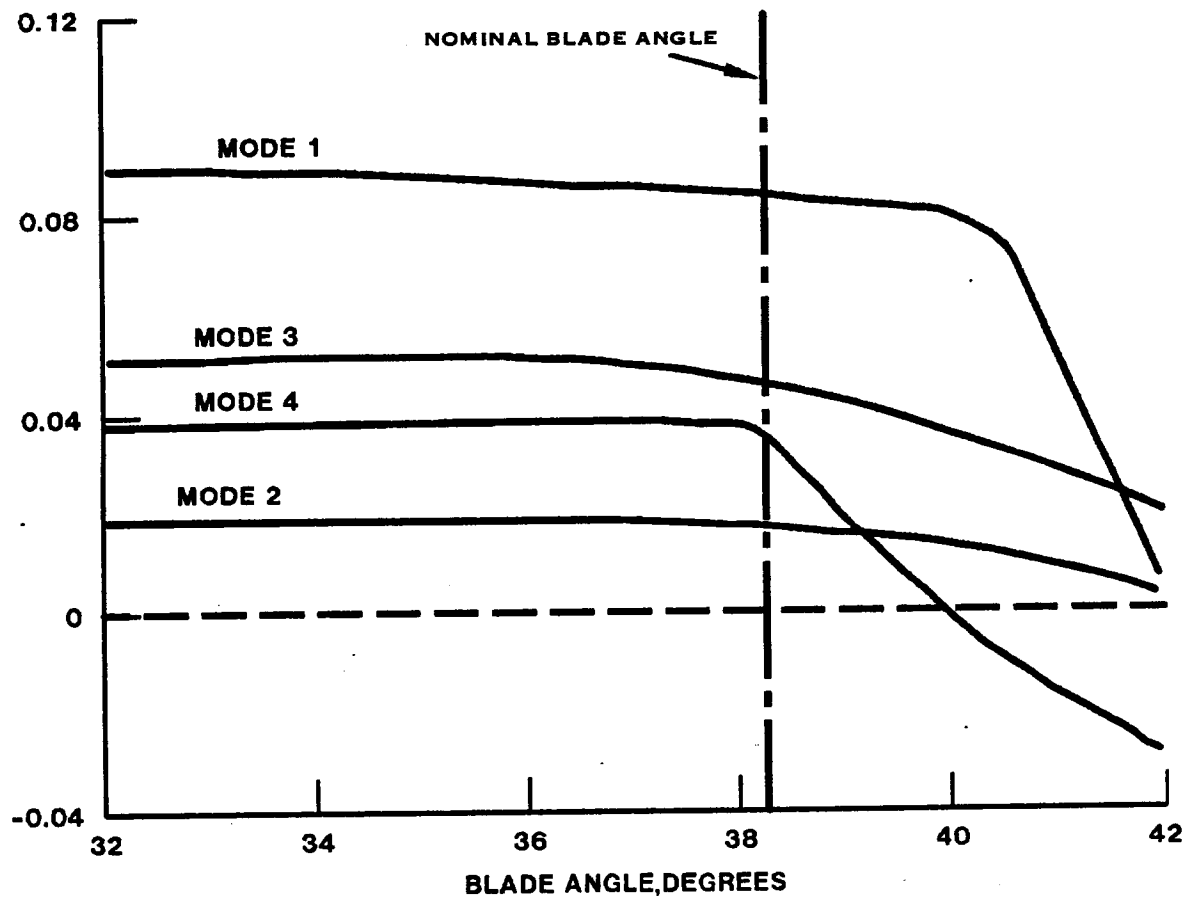


FIGURE 10-20. SR-7L STALL FLUTTER STABILITY

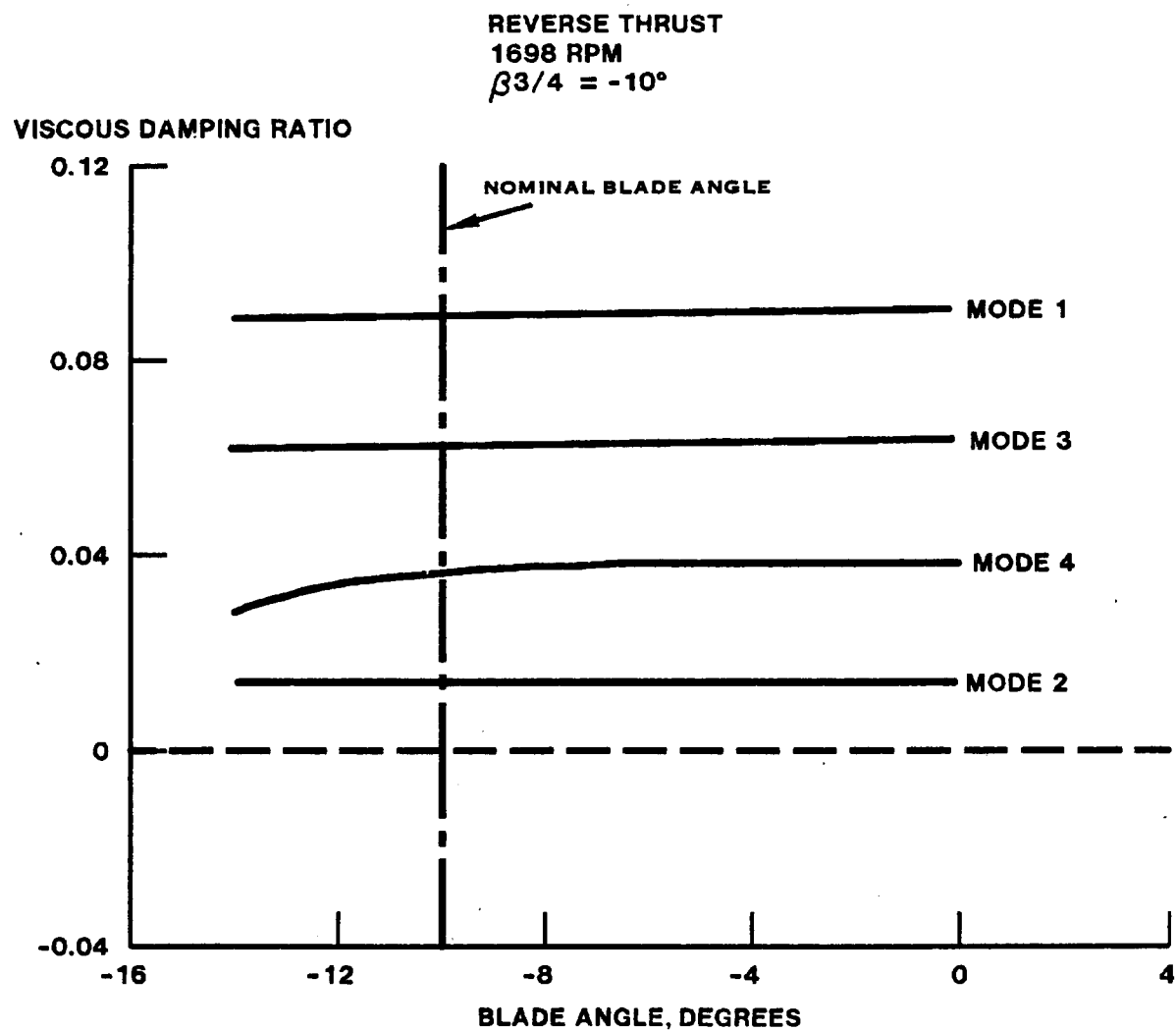


FIGURE 10-21. SR-7L STALL FLUTTER STABILITY



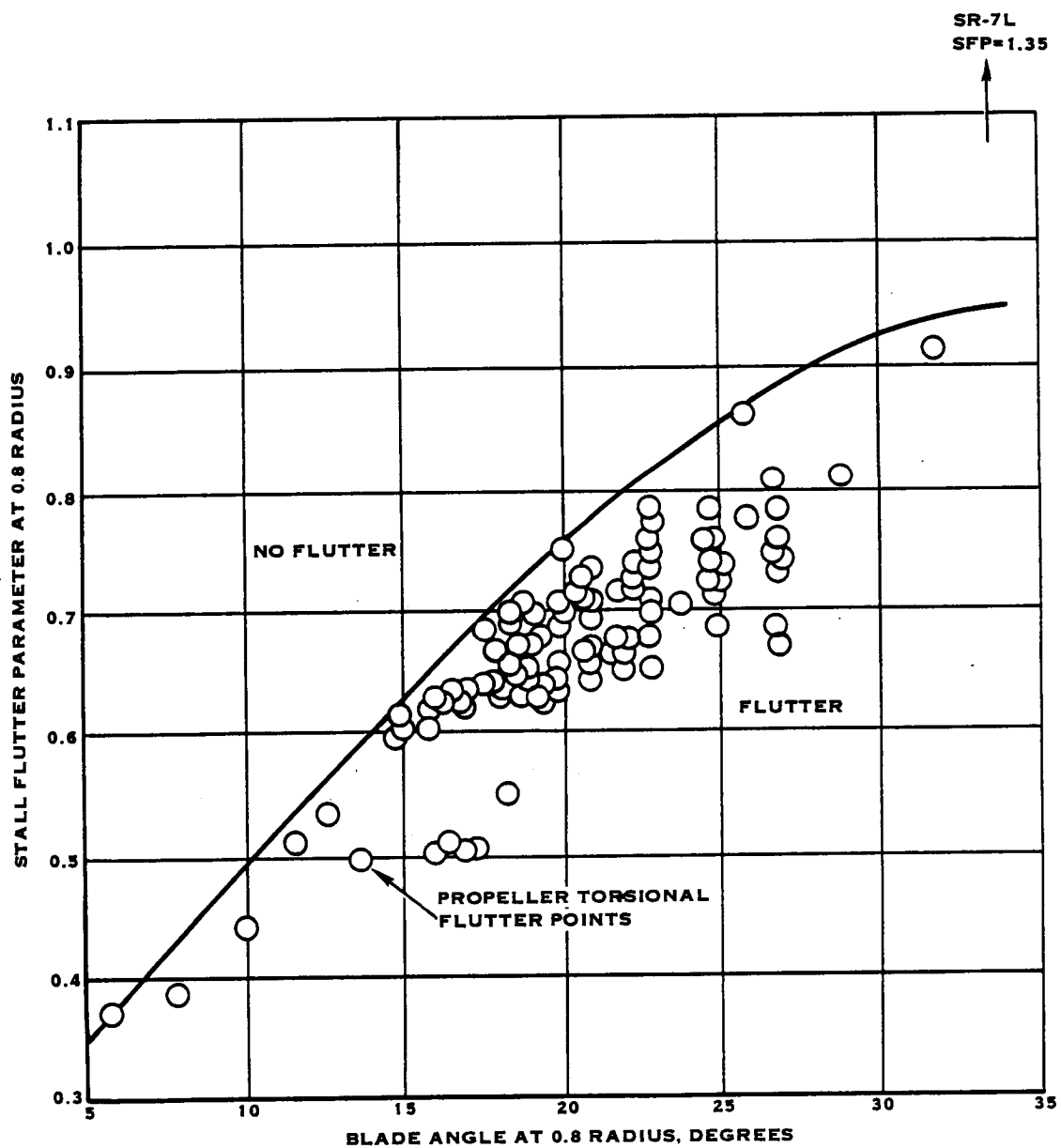


FIGURE 10-22. STALL FLUTTER DESIGN CHART

full-scale blade with careful monitoring of the stresses. Stall flutter boundaries for model Prop-Fan blades were successfully determined by monitoring stresses during testing. The stress rise during stall flutter is gradual and reaches a limit amplitude. For this reason, the stall flutter phenomenon is non-destructive when studied with careful test procedures.

## 11.0 Foreign Object Damage

To assess the FOD tolerance design goals of section 3.2.4, gross blade stresses resulting from moderate and major impacts have been calculated for the SR-7L blade. A moderate impact is one with a bird of up to .907 kilogram (two pounds) while a major impact involves a bird of up to 1.814 kilogram (four pounds).

### 11.1 Calculation Procedure

A three-dimensional, computerized, impact analysis program (ref. 9) was used to calculate the gross blade stresses due to a 1.814 kilogram (four pound) bird impact.

The moment and deflection mode shapes are assumed to be uncoupled, and are based on beam calculations of the SR-7L blade. However, the beam frequencies were replaced with frequencies calculated using finite element techniques. A comparison of the beam analysis frequencies with those of the finite element analysis is shown in table 11-1.

Table 11-1

<u>Method</u>	Mode 1	Mode 2	Mode 4
	<u>First Bending, Flatwise</u>	<u>First Bending, Edgewise</u>	<u>Torsion</u>
Beam Analysis	42.1	83.3	131.4
Finite Element Analysis	43.7	80.1	146.7

The comparison shows that agreement between the beam and finite element analysis bending mode frequencies is quite good, whereas the torsional mode frequencies are significantly different. To neglect the higher torsional frequency of the finite element analysis could have produced significantly different results from the foreign object impact analysis. Therefore, all beam frequencies were revised to those of the FEA.

#### 11.1.1 Flight Condition

A single flight condition was analyzed: 185 kilometers per hour (100 knots) take-off at a blade angle of 37 degrees, measured at the three-quarter radial station of the blade. Impact was assumed to occur at 80 percent of blade span, as shown in figure 11-1, resulting in an impact angle of 20 degrees and a relative impact velocity of 210 meters per second (689 feet per second).

PRECEDING PAGE BLANK NOT FILMED

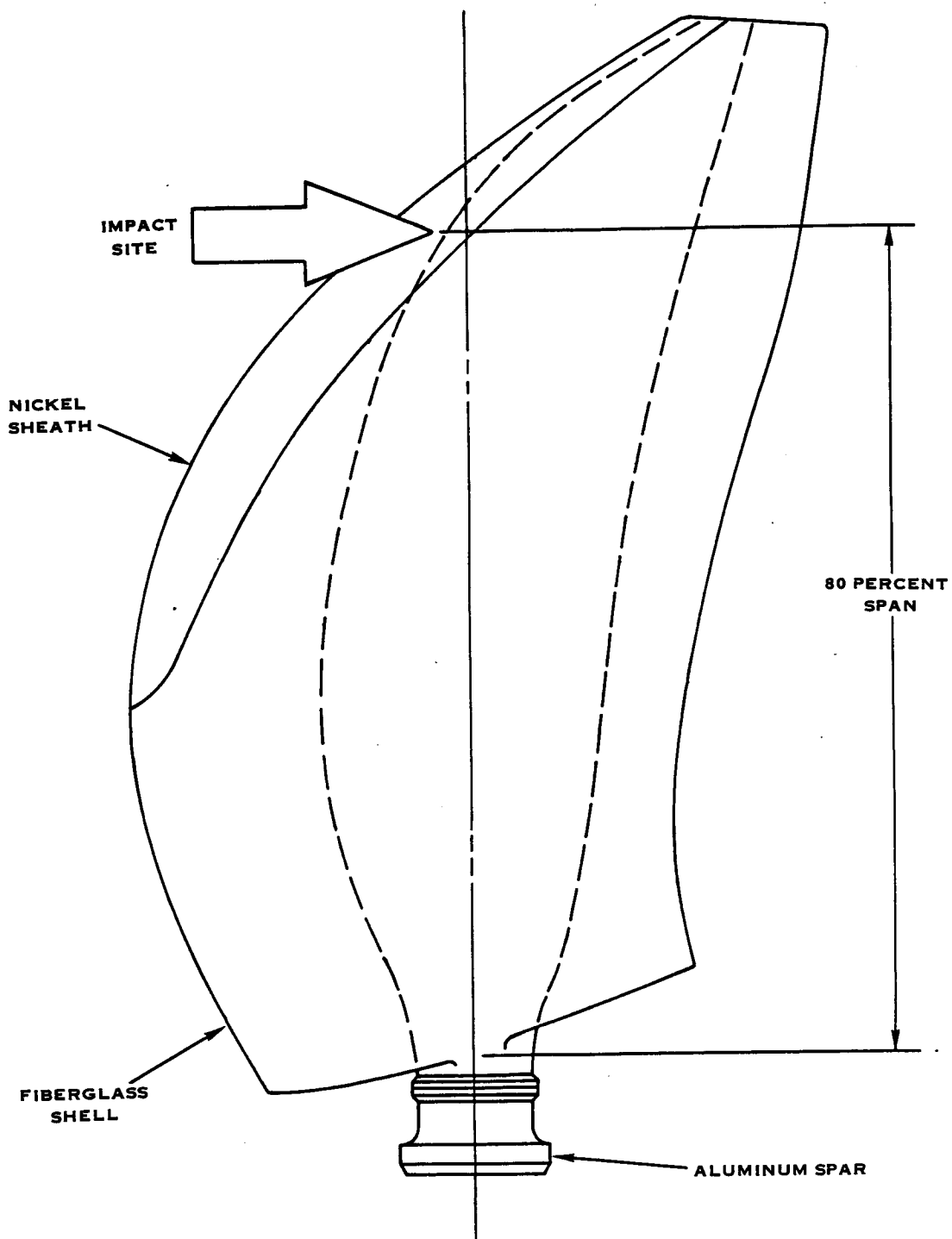


FIGURE 11-1. SPANWISE BIRD IMPACT LOCATION

### 11.1.2 Bird Impact Model

Figure 11-2 shows a typical geometry impact model used for analysis of the major impact resulting from a 1.814 kilogram (four pound) bird. Similar models were used for smaller size birds to determine stress variations relative to bird size. It is felt that the model illustrated is most typical of actual impact conditions.

### 11.2 Effect of Sweep

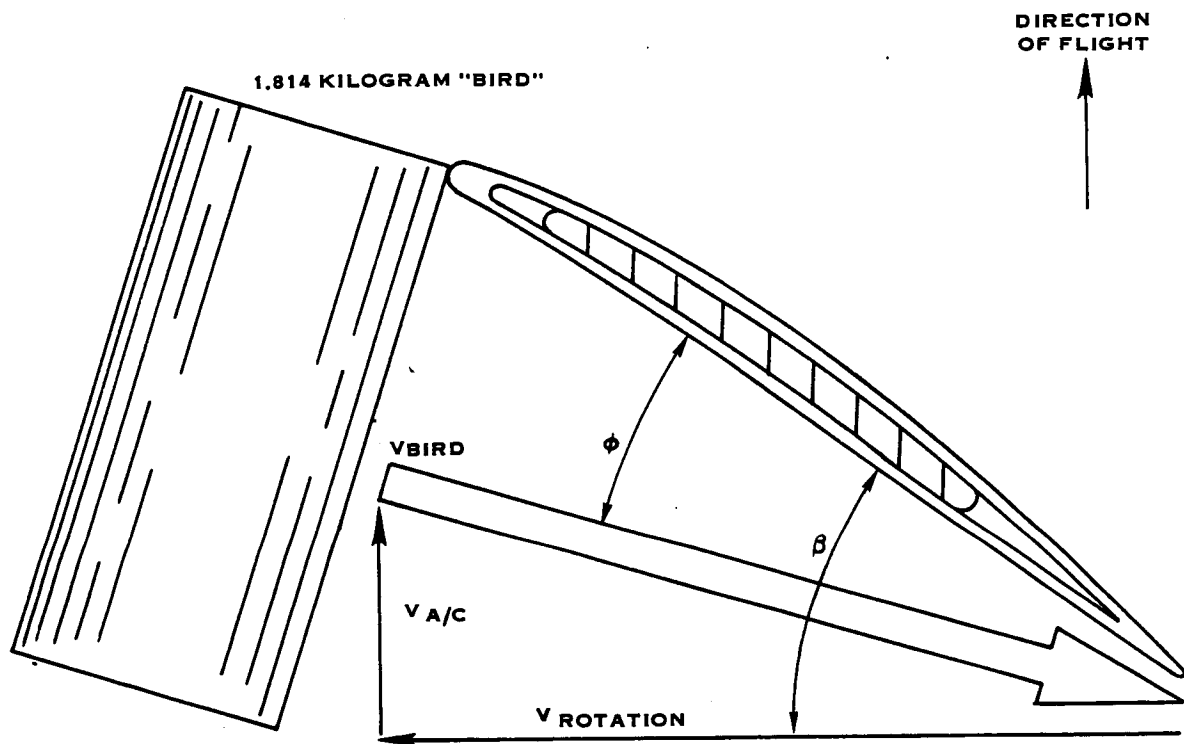
The effect of sweep on the foreign object damage of the blade was accounted for in the beam model by redefining the chordwise locations of the elastic axis and the center of mass at the impact site of the blade. The chordwise locations of the elastic axis and the center of mass were determined to be about 25 and 40 percent of the chord, respectively, measured from the leading edge of the blade. These are also shown in figure 11-1.

A small separate study was performed to evaluate the effect of sweep on FOD by also analyzing the blade without sweep, that is, the section mass center and the elastic axis at the impact station were assumed to be coincident at 40 percent of chord. The non-swept blade showed a slight increase of ten percent in gross blade stressing, which is within the tolerance band of the analysis, and probably should not be taken as an absolute trend.

### 11.3 Deflection and Stress Results

To illustrate the perturbation effects shown by the analysis and the dependence of deflection on impact load and time, the results of the 1.814 kilogram (four pound) bird impact case are reproduced in figures 11-3 through 11-6.

The peak impact load lasts only 1.75 millisecond and reaches a peak of 109,000 newtons (24,500 pounds) as shown in figure 11-3. After about seven milliseconds, the maximum flatwise tip deflection is predicted to reach about 24.6 centimeters (9.69 inches) as shown in figure 11-5, while the maximum torsional deflection is about 19 degrees and occurs at the impact site after approximately four milliseconds, as shown in figure 11-6.



$V_{A/C} = 51$  METERS PER SECOND

$V_{ROTATION} = 207$  METERS PER SECOND

$V_{BIRD} = 213$  METERS PER SECOND

$\beta = 33.6$  DEGREES ( $\beta_{3/4} = 37$  DEGREES)

$\phi = 20.0$  DEGREES

A/C = AIRCRAFT

FIGURE 11-2. BIRD IMPACT MODEL FOR TAKE-OFF CONDITION

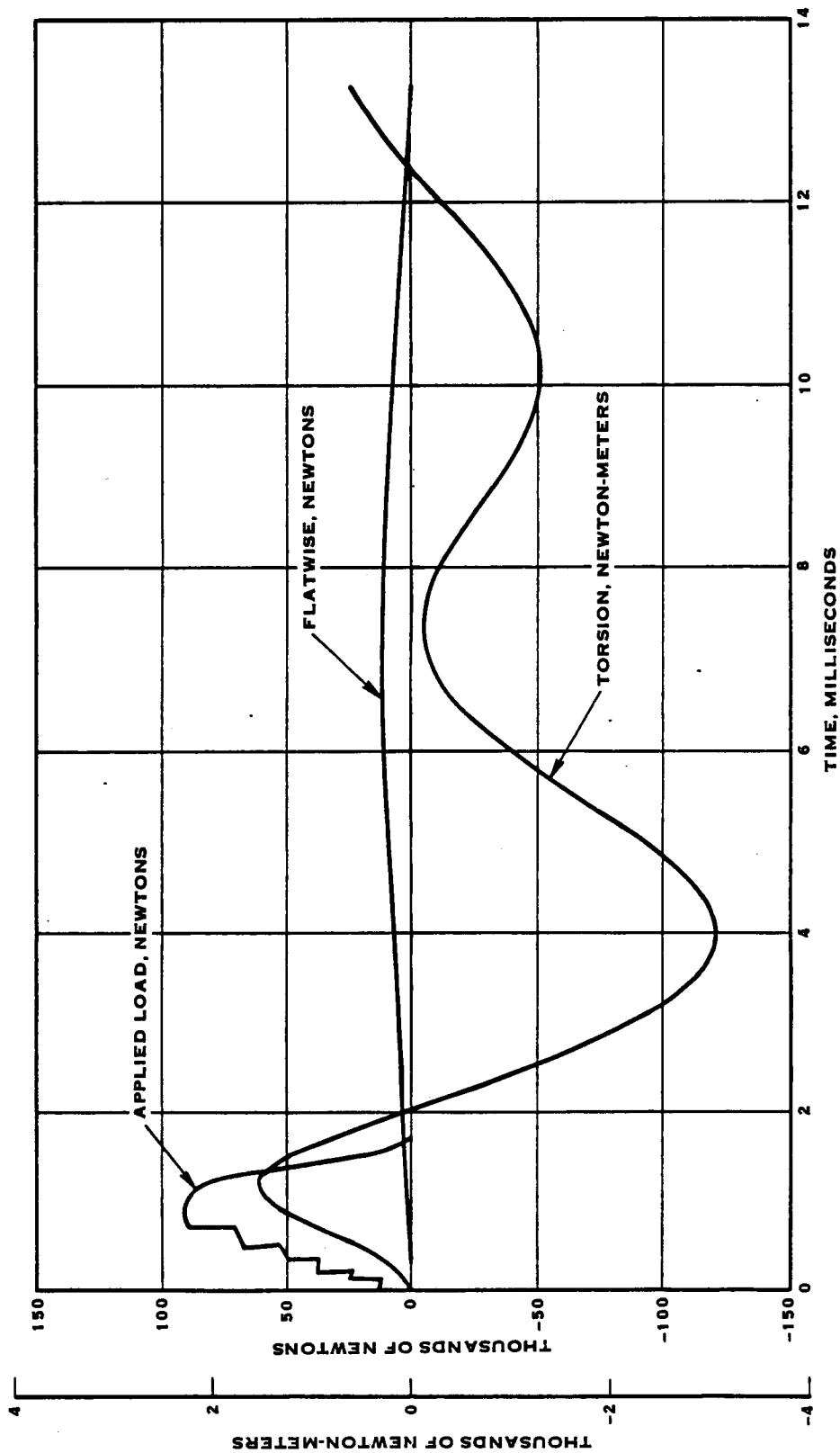


FIGURE 11-3. LOAD AT IMPACT SITE VS. TIME AFTER IMPACT

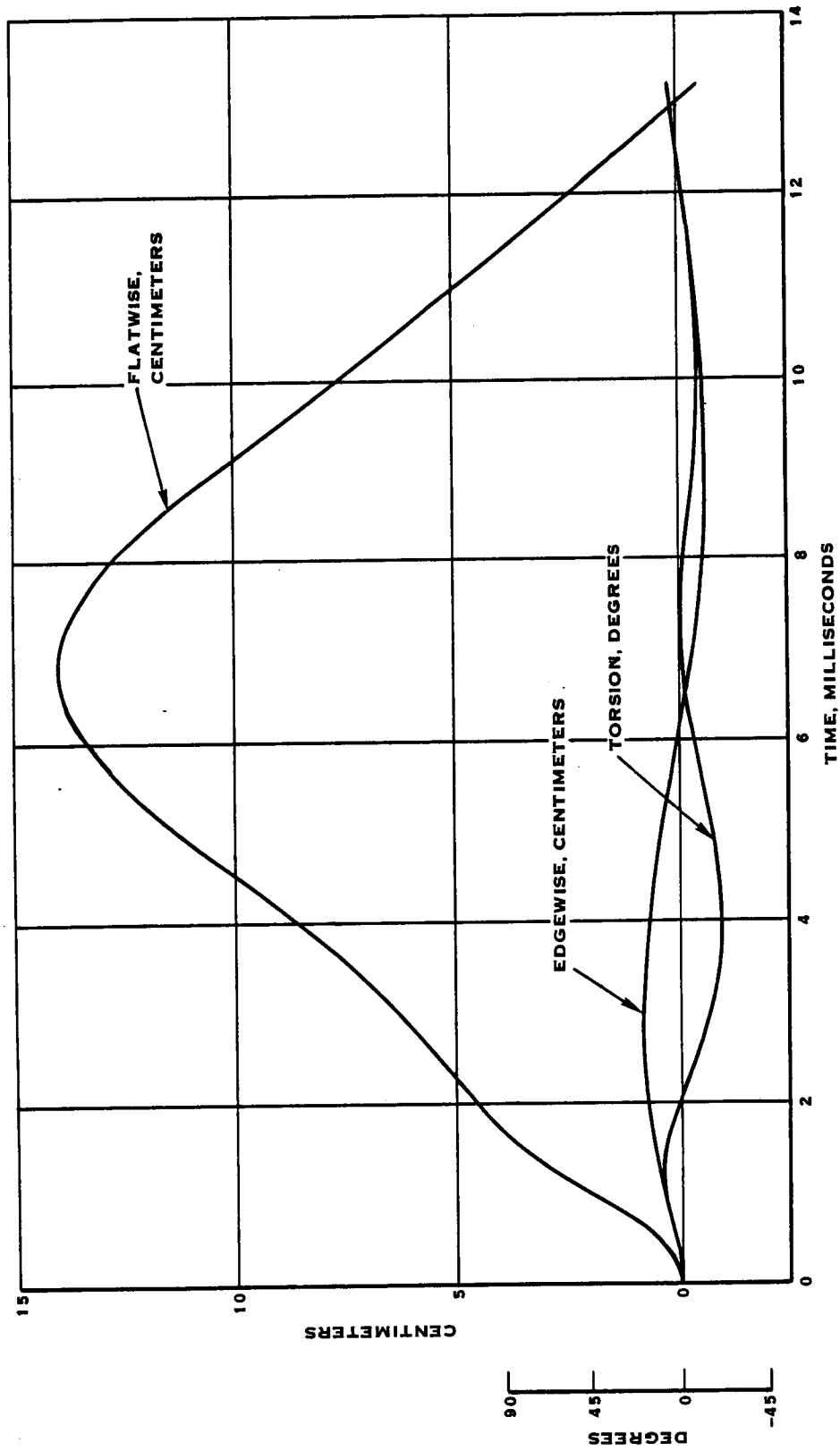


FIGURE 11-4. DEFLECTION AT IMPACT SITE VS. TIME AFTER IMPACT



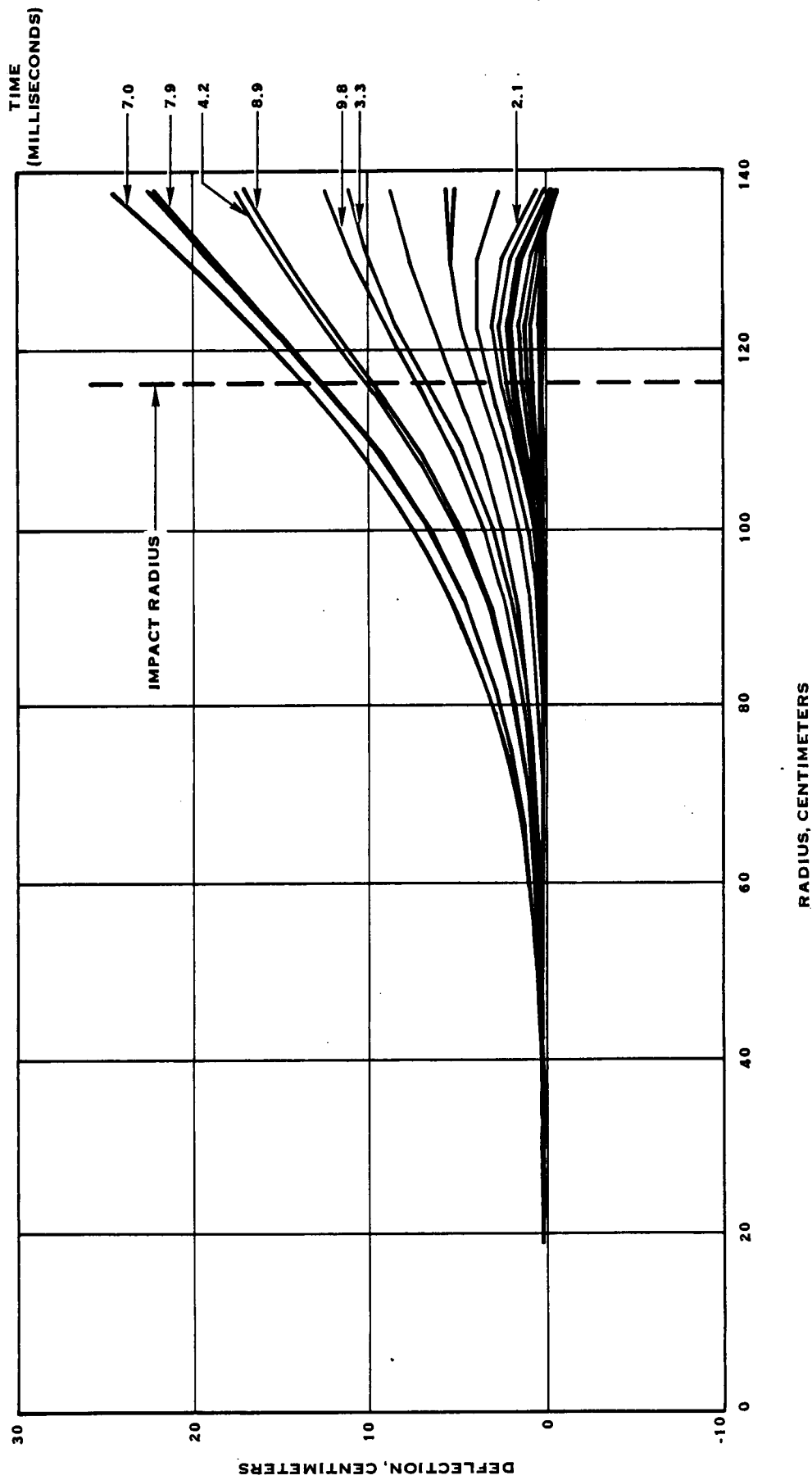


FIGURE 11-5. FLATWISE DEFLECTION VS. BLADE RADIUS  
AT VARIOUS TIMES AFTER IMPACT

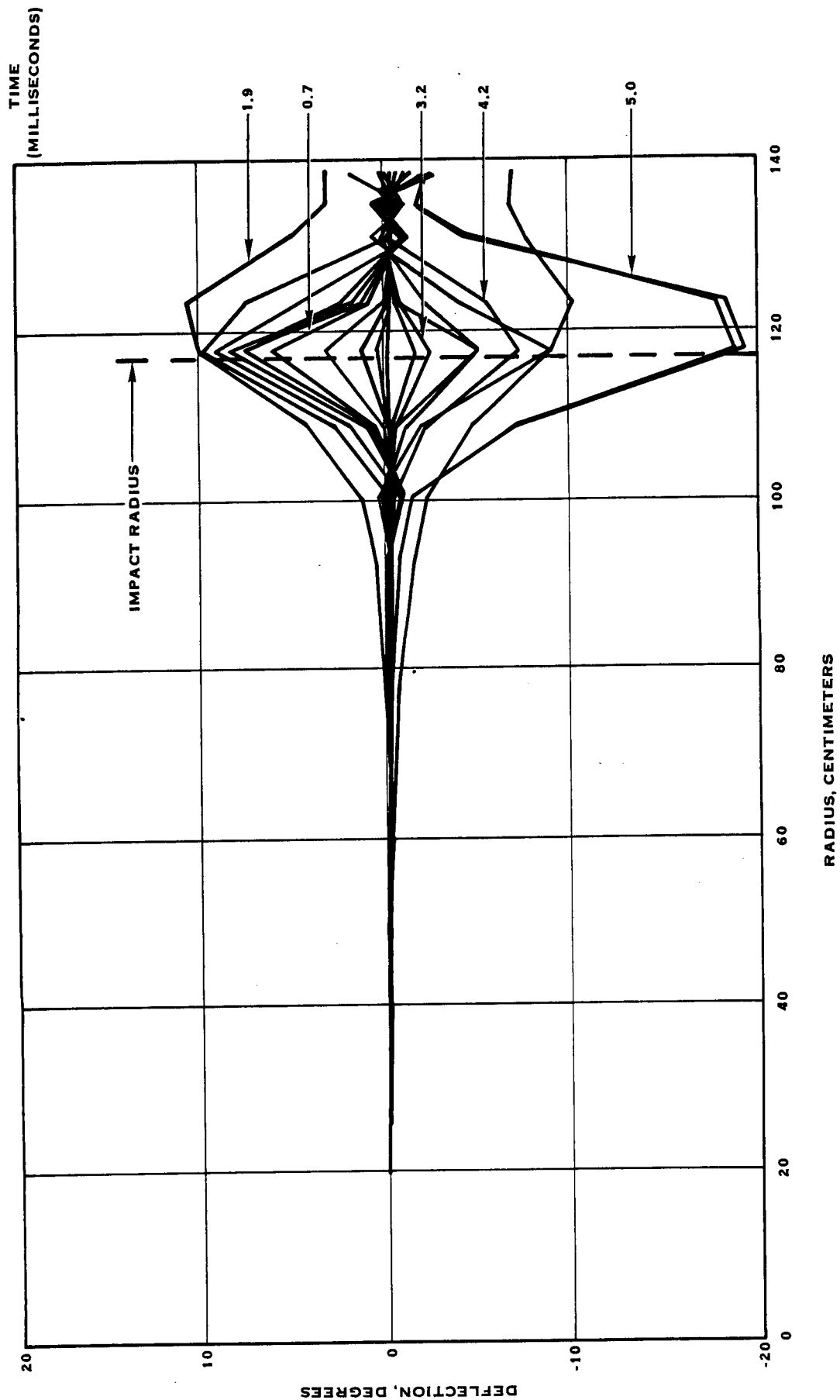


FIGURE 11-6. TORSIONAL DEFLECTION VS. BLADE RADIUS  
AT VARIOUS TIMES AFTER IMPACT

To assess blade stresses, both the spanwise normal stresses and the torsional shear stresses must be determined so that a combined effective stress, including normal blade operating stresses, could be obtained. The spanwise normal stresses were calculated directly by the foreign object impact analysis computer program. However, the torsional shear stresses must be determined from the maximum twist and displacement predicted by the program. First, the maximum twist and displacement were corrected to account for the low thickness-to-chord ratio of Prop-Fan blades.

Second, the maximum gross torsional shear stress near the foreign object impact site was estimated as a function of this corrected twist and displacement, the maximum blade or spar thickness, and the blade or spar shear modulus. The resulting maximum shear stress was then combined with the spanwise bending stress in order to obtain the maximum Von Mises effective stress defined by the following:

$$\sigma_{\text{EFFECTIVE VON MISES}} = \frac{1}{\sqrt{2}} \sqrt{2(\sigma_{\text{FOD}} + \sigma_{\text{OPER}})^2 + 6(\tau_{\text{FOD}})^2}$$

Results calculated with the above equation are summarized in table 11-2 for the case of a 1.814 kilogram (four pound) bird ingestion.

Table 11-2

FOD 1.814 KILOGRAM (FOUR POUND) BIRD

Stress, Thousands of Newtons per Square Centimeter  
(Thousands of Pounds per Square Inch)

<u>Maximum Bending</u>		<u>Maximum Torsional</u>		<u>Operating stdy. + cyc.*</u>		<u>Effective Von Mises @ max. bend.</u>	
<u>Spar</u>	<u>Shell</u>	<u>Spar</u>	<u>Shell</u>	<u>Spar</u>	<u>Shell</u>	<u>Spar</u>	<u>Shell</u>
42.0	17.1	11.6	7.5	-3.1	-1.9	40.2	16.5
(61.0)	(24.8)	(16.8)	(10.9)	(-4.5)	(-2.8)	(58.4)	(24.0)

\* Camber steady stress is negative

#### 11.4 Establishing "True" Ultimate Spar Strength

Since the foreign object impact loading is a suddenly applied shock load, the effective ultimate strength, or "true ultimate", of the blade spar must be consistent with the typical strain rates or impact times for the specific material analyzed. Therefore, the "true ultimate" strength of the aluminum spar for these strain or impact rates was estimated to be a function of the minimum value of the reduction in area ( $\Delta A/A$  for a tensile specimen), equal to two times the material elongation. This is consistent with the fact that the maximum ultimate strength will not be realized due to the high impact or strain rates which limit the full yielding prior to fracture. The "true ultimate" strength is a function of:

- 1) the engineering Ultimate Tensile Strength (UTS engrg),
- 2) the plastic capacity for pure bending stress (F), which is 1.5 for a rectangular section, and
- 3) the material elongation ( $\Delta l/l$ ), which is taken to be .13 for hard aluminum alloys.

$$\text{UTS "true" @ impact time} = F \left[ \frac{\text{UTS engrg}}{1 - 2(\Delta l/l)} \right] = 2.03 \left[ \text{UTS engrg} \right]$$

For the spar aluminum material (7075-T73) the "true ultimate" is 92,300 n/cm<sup>2</sup> (134,000 PSI).

#### 11.5 Stress/Strength Comparison

The maximum spar and shell gross blade stress for .454, .907, and 1.814 kilogram (one, two, and four pound) bird impacts, along with the maximum effective stress, are compared to their respective material yield and ultimate strengths on the plot in figure 11-7.

##### 11.5.1 Effect On Blade

For the bird impact, the blade appears to be in good shape. A sizeable portion of the bird hits the blade, while the remaining portion is separated. The portion which strikes the blade imparts enough momentum during its sliding path across the width of the blade to cause the spanwise spar and shell stressing shown in figure 11-7. For moderate impacts, birds up to .907 kilogram (two pounds), both the spar and shell spanwise stresses are well below their respective strengths and thus there is no problem meeting the requirements for moderate impacts. For major impacts, birds up to 1.814 kilogram (four pounds), the spar begins to yield, spanwise, at about the 1.814 kilogram (four pound) level, while the shell is still slightly below its tensile strength. Again, there is no problem meeting the requirements.

STRESS, THOUSANDS OF NEWTONS PER CENTIMETER<sup>2</sup>

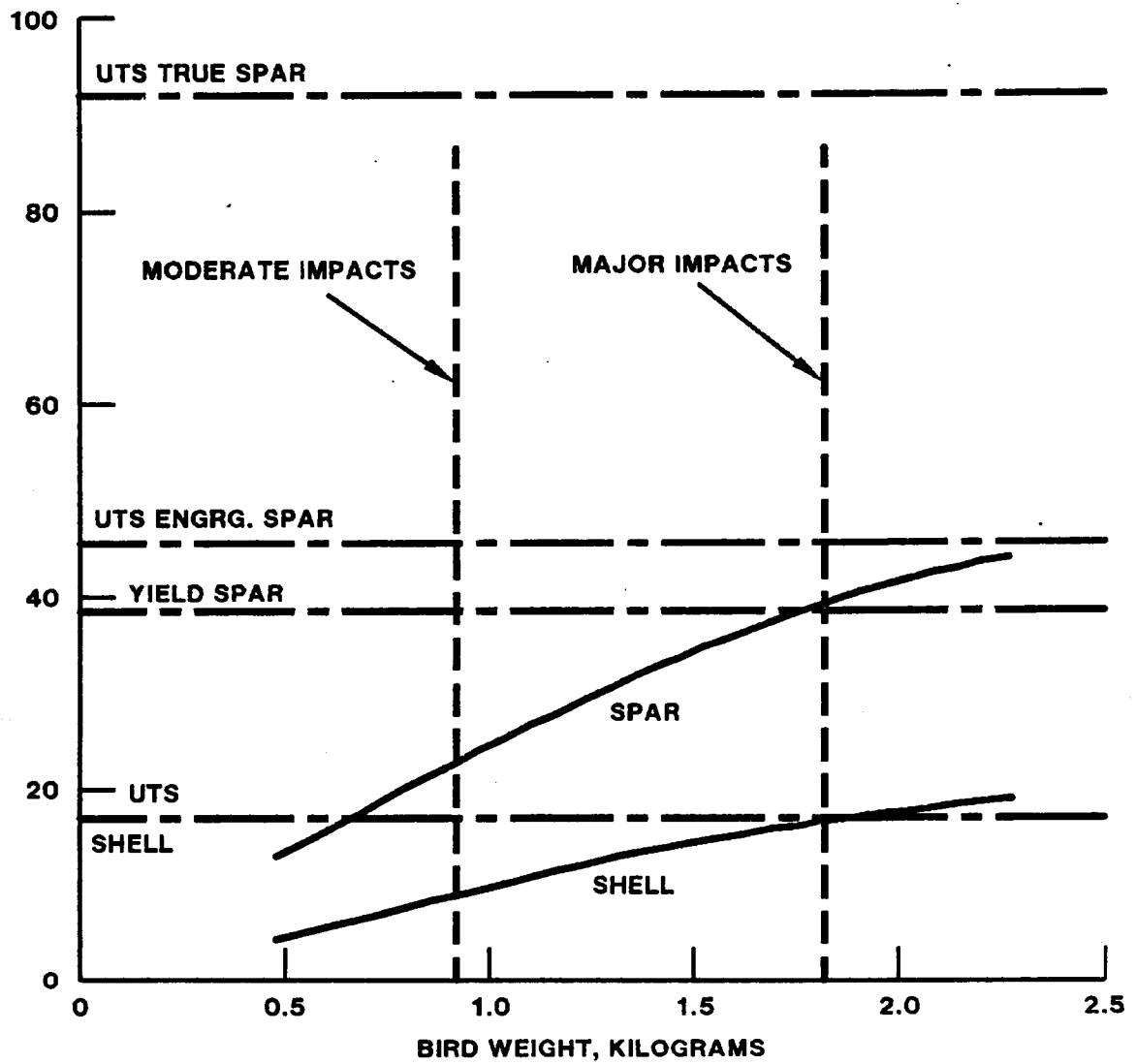


FIGURE 11-7. MAXIMUM BLADE STRESS VS BIRD WEIGHT

### 11.5.2 Effect On Retention

A cursory review of the retention loads was made by comparing the retention moment caused by the 1.814 kilogram (four pound) bird to the moment capacity, or the initiation of rocking of the retention, which is approximately equal to  $LR/2$ , where  $L$  is the centrifugal load and  $R$  is one-half of the bearing pitch diameter. The results indicated that the maximum moment for the 1.814 kilogram (four pound) strike is about 75 percent of capacity or rocking initiation, assuming steady and 1-P moments add directly.

## 12.0 Aerodynamic and Acoustic Performance

A major objective of the Advanced Turboprop Program was to develop an efficient Prop-Fan while maintaining acceptable noise levels. During the evolution of the SR-7L (see section 4.1), the efficiency and noise level of each design iteration were calculated. The final SR-7L design achieves high efficiency and satisfactory noise levels while possessing the necessary stress, stability and frequency characteristics.

The results of the performance calculation are listed in table 12-1. The efficiency and the noise level for the design/cruise condition meet the design goal requirements. The efficiency at take-off/climb is 0.4% below the design goal. Modification of the blade geometry may permit increasing this efficiency without adversely affecting other characteristics.

The far-field noise design goal is to satisfy FAR-36, minus 10 dB, which is 79 dB. The take-off condition at full power is above this noise level; however, a take-off at cut-back power will meet the design goal. The far-field noise for an approach condition also satisfies the design goal.

TABLE 12-1

### SR-7L AERODYNAMIC AND ACOUSTIC PERFORMANCE

Design/cruise condition	
Efficiency	79.4%
Near-field noise	143 dB
Take-off/climb	
Efficiency	51.6%
Far-field noise (full power)	86.7 dB
(cut-back power)	76.3 dB
Approach condition	
Far-field noise	77.3 dB

### 13.0 Conclusions

It has been demonstrated, in detail, in the preceding sections of this report that the final design of the SR-7 blade is structurally adequate to meet the test requirements and goals of the planned test program. The metal spar/composite shell design is a service-proven concept which is representative of future full-size Prop-Fan designs, while utilizing today's manufacturing technology. Analytical techniques used to evaluate structural adequacy are state-of-the-art, and have been correlated with test results as well as with other comparable analyses. Blade stresses have been compared to material design strengths which were appropriately adjusted to reflect years of blade test and flight experience. Further conclusions about the four primary structural aspects of the blade are presented below.

#### 13.1 Stress/Strength Evaluation

All blade components easily meet High-Cycle Fatigue (HCF) and Low-Cycle Fatigue (LCF) stress requirements for the four primary conditions analyzed, which include design/cruise, take-off/climb, and two overspeed conditions: 25 percent and 40 percent.

The blade is also adequate in that it meets its stress goals for almost all of the ten other design conditions analyzed, including three multi-bladed tests to be run in the ONERA S1 Wind Tunnel to simulate design/cruise conditions. All HCF goals are satisfied for the ten additional operating conditions. Some LCF limitations exist for four of the conditions, but most of these can be discounted as unimportant for the proposed test program.

Only the LCF shell stress on the camber side in the reverse operating condition has the potential of limiting testing to 600 cycles. This prediction may not be a serious limitation, but should be monitored during testing. It should be noted that reaching 600 cycles implies only a potential reduction in fiberglass modulus, and not a shell failure. The effect on the blade properties would be minimal since the area in question is over the spar in the mid-blade camber zone, and the shell is secondary structure.

#### 13.2 Resonant Frequencies

Resonant frequency requirements for the design/cruise and take-off/climb primary design conditions have been met, except for a minor infringement of the second mode into the lower portion of the 3-P (third multiple of operating speed) avoidance band at the design/cruise rotational speed. This should in no way limit the design because:

- 1) no source of 3-P excitation is envisioned in the test installation;
- 2) vibratory stresses will be continuously monitored such that dynamic magnification, if detected, could be alleviated by a change in rotational speed;



3) early test of static resonant frequencies will help identify potential problems;

4) measured resonant frequencies tend to be lower than predicted;

5) the second mode is first edgewise, and is closely tied to retention stiffness, which also tends to be lower than predicted.

Most resonant frequency goals for eight other conditions analyzed have also been met. The only notable exception is the first mode frequency in reverse which is predicted to climb into an expanded avoidance zone for ground operation. This is because the blade angle setting orients the blade to a flat-pitch setting, in the plane of rotation. This orientation results in maximum centrifugal stiffening for flatwise bending. Very little can be done to alter the characteristics of this mode without major design revision. Therefore, careful stress monitoring should be exercised, and testing in reverse in moderate to high cross-wind conditions should be avoided.

### 13.3 Stability

The SR-7L blade meets all design requirements and goals for unstalled flutter. No instability exists in the flight profile or in the ONERA S1 Wind Tunnel. The stall flutter results on the other hand were inconclusive, and no analysis is presently available to confidently predict the blade stability in the complex stalled environment. Therefore, stall flutter stability will have to be determined by tests with the full-scale hardware. If stall flutter should be found in the operating region, it can be eliminated with the appropriate pitch change schedule.

### 13.4 Foreign Object Damage

A three-dimensional, interactive, blade impact analysis of the SR-L blade shows that both the aluminum spar and fiberglass shell meet the requirements for major impacts. During a major impact, the maximum spar stress will be at the material yield point, and the shell stress will be slightly below the tensile strength. Although some permanent airfoil distortion could occur, no shell or spar material should be lost.

### 13.5 Aerodynamic and Acoustic Performance

The SR-7L blade exceeds the efficiency and noise level design goals for the design/cruise condition. The efficiency at take-off/climb is slightly less than the design goal, however, the noise level at take-off/climb meets the design goal for a cut-back power condition.


### 13.6 Weight

The calculated weight of the SR-7L blade, from the finite element analysis, is 41.65 pounds. The breakdown of this weight by components is:

- spar                    33.8 pounds
- shell                  6.75 pounds
- sheath                0.3 pounds
- fill                    0.8 pounds

#### 14.0 References

1. "Fuel Savings Potential of NASA Advanced Turboprop Program", J.B. Whitlow, Jr, and G.K. Sievers, NASA Tech. Mem. 83736, Sept, 1984.
2. "Large Scale Prop-Fan Blade Structural Design Study -  
NASA CR174992 Vol 1 - Initial Concepts  
NASA CR174993 Vol 2 - Preliminary Design of SR-7.
3. "Prop-Fan Test Assessment Program," NASA Contract NAS 3-24339.
4. "Parametric Flutter Stability Study and F203 Code Verification," J.E. Turnberg, H.S. Internal Memo V#1072, July 8, 1982.
5. "Bestran User's Guide: Auxiliary Program ST570," D.C. Jennings, Dec. 14, 1977.
6. Large Scale Advanced Prop-Fan (LAP) Hub and Blade Retention Design Report, NASA CR174786.
7. "Excitation Studies for Proposed Mach .8 Prop-Fan," A.S. Dale, H.S. Internal Memo V#629, Feb. 1976.
8. "Classical Flutter Stability of Swept Propellers," J.E. Turnberg, AIAA, ASME/ASCE/AHS 24th Structures, Structural Dynamics and Materials Conf, May, 1983.
9. "Elementary Three-Dimensional Interactive Rotor Blade Impact Analysis," ASME #75-WA/GT-15, Jan. 5, 1976.

1. Report No. CR-174790		2. Government Accession No.		3. Recipient's Catalog No.	
4. Title and Subtitle Large-Scale Advanced Prop-Fan (LAP), Blade Design				5. Report Date	
				6. Performing Organization Code 73030	
7. Author(s) John A. Violette, William E. Sullivan, Jay E. Turnberg				8. Performing Organization Report No. HSER 9246	
9. Performing Organization Name and Address Hamilton Standard Division United Technologies Corporation P.O. Box 1000 Windsor Locks, Connecticut 06096				10. Work Unit No.	
				11. Contract or Grant No. NAS 3-23051	
12. Sponsoring Agency Name and Address National Aeronautical and Space Administration Washington, D.C. 20546				13. Type of Report and Period Covered Contractor Report Sept '83 - Mar '84	
				14. Sponsoring Agency Code	
15. Supplementary Notes Project Manager, David A. Sagerser, Advanced Turboprop Project Office, NASA Lewis Research Center, Cleveland, Ohio 44135					
16. Abstract This report covers the design analysis of a very thin, highly swept, propeller blade to be used in the Large-scale Advanced Prop-Fan (LAP) test program. The report includes: design requirements and goals, a description of the blade configuration which meets requirements, a description of the analytical methods utilized/developed to demonstrate compliance with the requirements, and the results of these analyses. The methods described include: finite element modeling, predicted aerodynamic loads and their application to the blade, steady-state and vibratory response analyses, blade resonant frequencies and mode shapes, bird impact analysis, and prediction of stall and unstalled flutter phenomena. Summarized results include deflections, retention loads, stress/strength comparisons, foreign object damage resistance, resonant frequencies and critical speed margins, resonant vibratory mode shapes, calculated boundaries of stalled and unstalled flutter, and aerodynamic and acoustic performance calculations.					
17. Key Words (Suggested by Author(s)) Prop-Fan Blade Structural Design				18. Distribution Statement 	
19. Security Classif. (of this report) Unclassified		20. Security Classif. (of this page) Unclassified		21. No. of Pages 168	
22. Price*					